

UNIVERSITÉ DU QUÉBEC À CHICOUTIMI

MÉMOIRE PRÉSENTÉ À  
L'UNIVERSITÉ DU QUÉBEC À CHICOUTIMI  
COMME EXIGENCE PARTIELLE  
DE LA MAÎTRISE EN INGÉNIERIE

BY  
ZHENG LI

PARAMETERS CONTROLLING THE PRECIPITATION AND  
DISSOLUTION OF  $\text{CuAl}_2$  PHASE IN 319-TYPE ALLOYS AND THEIR  
INFLUENCE ON THE ALLOY PERFORMANCE

MAY 2003



### Mise en garde/Advice

Afin de rendre accessible au plus grand nombre le résultat des travaux de recherche menés par ses étudiants gradués et dans l'esprit des règles qui régissent le dépôt et la diffusion des mémoires et thèses produits dans cette Institution, **l'Université du Québec à Chicoutimi (UQAC)** est fière de rendre accessible une version complète et gratuite de cette œuvre.

Motivated by a desire to make the results of its graduate students' research accessible to all, and in accordance with the rules governing the acceptance and diffusion of dissertations and theses in this Institution, the **Université du Québec à Chicoutimi (UQAC)** is proud to make a complete version of this work available at no cost to the reader.

L'auteur conserve néanmoins la propriété du droit d'auteur qui protège ce mémoire ou cette thèse. Ni le mémoire ou la thèse ni des extraits substantiels de ceux-ci ne peuvent être imprimés ou autrement reproduits sans son autorisation.

The author retains ownership of the copyright of this dissertation or thesis. Neither the dissertation or thesis, nor substantial extracts from it, may be printed or otherwise reproduced without the author's permission.

*Dedicated to my parents*

謹以此獻給我的父母

## RÉSUMÉ

Les alliages aluminium-silicium-cuivre (Al-Si-Cu), particulièrement les alliages du type 319, sont couramment employés dans les applications automobiles en raison de leurs excellentes propriétés mécaniques et caractéristiques de coulabilité. Une étude approfondie reliée à l'investigation du comportement de la précipitation de la phase  $\text{CuAl}_2$  dans divers alliages de type 319 contenant des éléments alliés dont les strontium (Sr), fer (Fe) et phosphore (P), et sa dissolution durant la mise en solution à 505 °C pour des temps allant jusqu'à 100 heures, fut effectuée dans le présent travail. De plus, l'effet du  $\text{CuAl}_2$  et d'autres intermétalliques sur la performance de l'alliage soumis à deux conditions de traitements thermiques différentes (*i.e.*, T5 et T6) a aussi été investigué à travers un examen des propriétés de traction et d'impact. En comparant les résultats expérimentaux, des conclusions furent tirées en termes des paramètres de solidification optimaux des éléments alliés, et des conditions de traitement thermiques (*viz.*, modification au Sr, contenu en Fe, taux de refroidissement et condition T6). Les comportements de fracture des alliages 319 de base et des alliages 319 modifiés au Sr et contenant ~1.2% Fe furent aussi comparés à travers une étude des surfaces des échantillons d'alliages correspondants.

Les résultats révèlent explicitement que le traitement de mise en solution joue un rôle critique dans la dissolution de la phase  $\text{CuAl}_2$ . La modification au strontium mène à la ségrégation de la phase  $\text{CuAl}_2$  à l'extérieur des régions eutectiques des alliages Al-Si, ce qui ralentit sa dissolution durant la mise en solution. De plus, le phosphore a un effet négatif sur la dissolution du  $\text{CuAl}_2$  en raison de sa solubilité dans les particules de  $\text{CuAl}_2$  et la formation de particules d'oxydes  $(\text{Al,P})\text{O}_2$  qui agissent en tant que sites de germination pour la précipitation de la phase  $\text{CuAl}_2$  de type bloc. Cependant les plaquettes de la phase de fer  $\beta\text{-Al}_5\text{FeSi}$  présentes dans la structure agissent en tant que sites préférentiels de précipitation pour les particules de la phase de cuivre, et ainsi diminue le degré de ségrégation et accélère leur dissolution.

Le taux de refroidissement est le paramètre le plus efficace pour contrôler les propriétés mécaniques des alliages 319 étudiés. Les propriétés de traction et d'impact augmentent toutes deux avec une augmentation du taux de refroidissement (*i.e.*, une diminution de la valeur de l'espace inter dendritique secondaire (DAS) peu importe la composition de l'alliage ou le traitement de mise en solution (T5 et T6). Les alliages modifiés au strontium montrent des valeurs beaucoup plus élevées de limite ultime et de ductilité en raison du changement de morphologie des particules de silicium eutectiques à

partir d'une forme grossière de flocon jusqu'à une forme fibreuse fine. Des additions de fer et de phosphore ont toutes deux un effet préjudiciable sur les valeurs de limite élastique et de ductilité, en raison de la présence des plaquettes de  $\beta$ - $\text{Al}_5\text{FeSi}$  et des particules d'oxydes  $(\text{Al,P})\text{O}_2$ , respectivement.

L'addition de fer mène à une précipitation accentuée de plaquettes fragiles de  $\beta$ - $\text{Al}_5\text{FeSi}$  qui agissent en tant que sites préférentiels de fissuration et qui réduisent dramatiquement les propriétés d'impact, peu importe la valeur de l'espace inter dendritique (DAS). La modification au strontium et la sphéroidisation des particules de silicium peuvent compenser pour la perte en énergie d'impact causée par la présence de grandes plaquettes aciculaires de  $\beta$ - $\text{Al}_5\text{FeSi}$  résultant de l'addition de  $\sim 1.2\%$  Fe. Comparativement au traitement T5, les alliages étudiés révèlent des valeurs plus grandes de propriétés mécaniques sous des conditions T6 en raison de la sphéroidisation partielle des particules de silicium et la dissolution et redistribution de la plupart des particules de  $\text{CuAl}_2$  à l'intérieur de la matrice aluminium. Ainsi, plus de cuivre est disponible pour agir comme agent de renforcement durant le vieillissement artificiel.

L'initiation des fissures se produit habituellement par la fragmentation des particules de silicium et des plaquettes de  $\beta$ - $\text{Al}_5\text{FeSi}$ , et la fissure se propage à travers le clivage des plaquettes de  $\beta$ - $\text{Al}_5\text{FeSi}$ , la fracture du  $\text{CuAl}_2$  non dissous ou d'autres intermétalliques de cuivre, aussi bien que par les particules de silicium fracturées. Dans les alliages 319 modifiés au strontium, les fissures sont principalement initiées par la fragmentation ou le clivage de la phase  $\beta$ -Fe, en plus de celle des particules grossières de silicium et d'intermétalliques de cuivre non dissous.

## ABSTRACT

Aluminum-silicon-copper (Al-Si-Cu) alloys, particularly 319-type alloys are popularly employed in automotive applications due to their excellent mechanical properties and casting characteristics. An extensive study related to the investigation of the precipitation behavior of the  $\text{CuAl}_2$  phase in various 319-type alloys containing strontium (Sr), iron (Fe) and phosphorus (P) alloying elements, and its dissolution during solution heat treatment at 505 °C for times up to 100 hours was carried out in the present work. Furthermore, the effect of  $\text{CuAl}_2$  and other intermetallics on the alloy performance under two different heat treatment conditions (*i.e.*, T5 and T6) was also investigated through an examination of the tensile and impact properties. By comparing the experimental results, conclusions were drawn in terms of the optimum alloying elements, solidification parameters and heat treatment conditions (*viz.*, Sr modification, Fe content, cooling rate and T6 condition). The fracture behaviors of the 319 base alloy and the Sr-modified 319 alloy containing ~1.2% Fe were also compared through a study of the fracture surfaces of the corresponding alloy samples.

The results explicitly reveal that solution heat treatment plays a critical role in the dissolution of the  $\text{CuAl}_2$  phase. Strontium modification leads to the segregation of the  $\text{CuAl}_2$  phase away from the Al-Si eutectic regions, which slows down its dissolution during solution heat treatment. In addition, phosphorus has a negative effect on  $\text{CuAl}_2$  dissolution due to its solubility in the  $\text{CuAl}_2$  particles and the formation of  $(\text{Al,P})\text{O}_2$  oxide particles which act as nucleation sites for the precipitation of the block-like  $\text{CuAl}_2$  phase. However, the  $\beta\text{-Al}_5\text{FeSi}$  iron phase platelets present in the structure act as preferred precipitation sites for the copper phase particles and, hence, lessen the degree of segregation and accelerate their dissolution.

The cooling rate is the most efficient parameter controlling the mechanical properties in the studied 319 alloys. Both tensile and impact properties increase with an increase in the cooling rate (*i.e.*, a decrease in the secondary dendrite arm spacing (or DAS) value) regardless of alloy composition or solution heat treatment (T5 and T6). The Sr-modified alloys display much higher UTS and ductility values due to the change in morphology of the eutectic Si particles from a coarse, flake-like form to a fine fibrous one. Both iron and phosphorus additions have a detrimental effect on UTS and ductility values, due to the presence of  $\beta\text{-Al}_5\text{FeSi}$  platelets and  $(\text{Al,P})\text{O}_2$  oxide particles, respectively.

Iron addition leads to an increased precipitation of brittle  $\beta$ - $\text{Al}_5\text{FeSi}$  platelets which act as preferred crack sites and dramatically reduce the impact properties, regardless of the value of DAS. Strontium modification and spheroidization of the Si particles can compensate for the loss in impact energy caused by the presence of large acicular  $\beta$ - $\text{Al}_5\text{FeSi}$  platelets resulting from the  $\sim 1.2\%$  Fe addition. Compared to T5 treatment, the studied alloys reveal higher values of mechanical properties under T6 condition due to partial spheroidization of the Si particles and the dissolution and redistribution of most of the  $\text{CuAl}_2$  particles within the aluminum matrix. Thus, more copper is available to act as a strengthening agent during aging.

Crack initiation usually occurs through the fragmentation of Si particles and  $\beta$ - $\text{Al}_5\text{FeSi}$  platelets, and the crack propagates through the cleavage of  $\beta$ - $\text{Al}_5\text{FeSi}$  platelets, the fracture of undissolved  $\text{CuAl}_2$  or other Cu-intermetallics, as well as through fractured Si particles. In Sr-modified 319 alloys, cracks are mostly initiated by the fragmentation or cleavage of the  $\beta$ -iron phase, in addition to that of coarse Si particles and undissolved Cu-intermetallics.

## **ACKNOWLEDGEMENTS**

It is a great pleasure to finally have a chance to express my gratefulness to all those who were involved, directly or indirectly, in making this work a success. It is my pleasure to convey my sincere thanks to my supervisors, Professors F. H. Samuel and C. Ravindran, for their invaluable guidance in each stage of my study. I would like to express my gratitude to Dr. Agnes Samuel for her help and guidance during different stages of my work.

Financial assistance (in the form of scholarships) and in-kind support received from the Natural Sciences and Engineering Research Council of Canada (NSERC), General Motors Powertrain Group (U.S.A.), and Corporation Nematik (Mexico) is gratefully acknowledged.

I would like to express my appreciation to several colleagues, particularly Mr. Alain Bérubé at UQAC and Dr. Florence Paray at McGill University, for their help and for creating an enjoyable working atmosphere. Many thanks go to Dr. Zheyuan Ma who recommended me to join UQAC and also for his enthusiastic help during these two years.

Finally, I would like to record my deep gratitude to the members of my family, especially my parents and grandfather. Without their encouragement and support, I would not have been able to fulfill my goal of completing my Master's Degree successfully.

## PUBLICATIONS

Three research articles have been published and two others prepared and submitted from this work. The details are provided below. The third article was also given in the form of a presentation at the 107<sup>th</sup> AFS Casting Congress to be held in Milwaukee, WI, April 26-29, 2003.

1. Effect of Alloying Elements on the Segregation and Dissolution of CuAl<sub>2</sub> Phase in Al-Si-Cu 319 Alloys.  
Z. Li, A. M. Samuel, F. H. Samuel, C. Ravindran, and S. Valtierra.  
Journal of Materials Science, Vol. **38** (2003), pp. 1203-1218.
2. Role of P and Fe on the Precipitation of Copper Intermetallics in 319 Alloys.  
Z. Li, A. M. Samuel, and F. H. Samuel.  
Journal of Materials Science Letters, Vol. **22(8)** (2003), pp. 585-587.
3. Factors Affecting Dissolution of CuAl<sub>2</sub> Phase in 319 Alloys.  
Z. Li, A. M. Samuel, F. H. Samuel, C. Ravindran, S. Valtierra, and H. W. Doty.  
AFS Transactions, Vol. **111** (2003), Paper **03-100**, pp. 1-14.
4. Parameters Controlling the Performance of 319-Type Alloys, Part I: Tensile Properties.  
Z. Li, A. M. Samuel, F. H. Samuel, C. Ravindran, S. Valtierra, and H. W. Doty.  
Materials Science & Engineering A (2003), Submitted (May 23, 2003).
5. Parameters Controlling the Performance of 319-Type Alloys, Part II: Impact Properties and Fractography.  
Z. Li, A. M. Samuel, F. H. Samuel, C. Ravindran, S. Valtierra, and H. W. Doty.  
Materials Science & Engineering A (2003), Submitted (May 23, 2003).

### Conference Presentation

Paper 03-100, Monday, April 28 – Aluminum Session (2:00 PM)

Factors Affecting Dissolution of CuAl<sub>2</sub> Phase in 319 Alloys.

Z. Li, A. M. Samuel, F. H. Samuel, C. Ravindran, S. Valtierra, and H. W. Doty.

107<sup>th</sup> AFS Casting Congress, Milwaukee, Wisconsin, April 26-29, 2003.

## TABLE OF CONTENTS

RÉSUMÉ.....	i
ABSTRACT.....	iii
PUBLICATIONS.....	v
ACKNOWLEDGEMENTS.....	vi
TABLE OF CONTENTS.....	vii
LIST OF TABLES.....	x
LIST OF FIGURES.....	xii
<b>CHAPTER 1 DEFINITION OF THE PROBLEM .....</b>	<b>1</b>
1.1 INTRODUCTION.....	2
1.2 OBJECTIVES.....	5
<b>CHAPTER 2 LITERATURE SURVEY .....</b>	<b>6</b>
2.1 COMMON Al-Si CASTING ALLOYS .....	7
2.2 319 Al-Si-Cu ALLOYS.....	10
2.3 SOLIDIFICATION CHARACTERISTICS OF 319 ALLOYS .....	12
2.4 ROLE OF MODIFICATION .....	15
2.5 ROLE OF GRAIN REFINEMENT.....	18
2.6 THE COPPER INTERMETALLIC $\text{CuAl}_2$ PHASE IN 319 ALLOYS.....	21
2.6.1 Precipitation and Segregation of $\text{CuAl}_2$ .....	21
2.6.2 Dissolution and Melting of $\text{CuAl}_2$ .....	23

2.7	THE IRON INTERMETALLIC PHASE $\beta$ -Al <sub>5</sub> FeSi PHASE .....	24
2.7.1	Iron Intermetallics in Al-Si Alloys .....	25
2.7.2	The Formation of the $\beta$ -Al <sub>5</sub> FeSi Phase.....	26
2.7.3	Effect of Sr Addition on the $\beta$ -Al <sub>5</sub> FeSi Phase .....	27
2.8	HEAT TREATMENT OF Al-Si ALLOYS .....	28
2.8.1	Solution Heat Treatment.....	28
2.8.2	Quenching.....	29
2.8.3	Precipitation Heat Treatment (Aging) .....	30
2.8.4	Effect of Solution Heat Treatment on 319 Alloys .....	32
2.9	TWO IMPORTANT MECHANICAL PROPERTIES — TENSILE AND IMPACT PROPERTIES.....	33
2.9.1	Tensile Properties .....	33
2.9.1.1	Effect of alloy composition.....	35
2.9.1.2	Effect of solidification time .....	36
2.9.1.3	Effect of heat treatment.....	36
2.9.1.4	Effect of modification .....	38
2.9.2	Impact Properties .....	39
2.9.2.1	Effect of alloy composition.....	39
2.9.2.2	Effect of solidification time .....	40
2.9.2.3	Effect of heat treatment.....	40
2.9.2.4	Effect of modification .....	41
2.9.2.5	Effect of porosity .....	42
2.10	FRACTOGRAPHY .....	43
2.10.1	Fracture Behavior of Al-Si Base Alloys.....	43
2.10.1.1	Effect of Si particles .....	45
2.10.1.2	Effect of iron intermetallics .....	45
2.10.1.3	Effect of solidification rate .....	46
<b>CHAPTER 3 SEGREGATION AND DISSOLUTION OF THE CuAl<sub>2</sub> PHASE.....</b>		<b>48</b>
3.1	INTRODUCTION .....	49
3.2	EXPERIMENTAL PROCEDURE.....	51
3.3	RESULTS AND DISCUSSION.....	55
3.3.1	Thermal Analysis.....	55
3.3.2	Optical Microscopy.....	58
3.3.3	Dissolution of CuAl <sub>2</sub> During Solution Heat Treatment.....	64
3.3.4	Electron Probe Microanalysis (EPMA).....	72
3.3.5	Role of (Al,P)O <sub>2</sub> Oxide on CuAl <sub>2</sub> Precipitation .....	84
3.3.6	Precipitation of Cu <sub>2</sub> FeAl <sub>7</sub> Phase.....	87

<b>CHAPTER 4</b>	<b>TENSILE AND IMPACT PROPERTIES OF 319 ALLOYS</b>	<b>90</b>
4.1	INTRODUCTION	91
4.2	EXPERIMENTAL PROCEDURE	93
4.2.1	Casting Material	93
4.2.2	Heat Treatment	96
4.2.3	Tensile Testing	97
4.2.4	Impact Testing	99
4.2.5	Image Analysis	101
4.3	RESULTS AND DISCUSSION	102
4.3.1	Microstructure	102
4.3.1.1	T5 heat treatment	102
4.3.1.2	T6 heat treatment	107
4.3.1.3	Porosity	112
4.3.2	Tensile Properties	114
4.3.2.1	T5 heat treatment	114
4.3.2.2	T6 heat treatment	121
4.3.2.3	Correlation between ultimate tensile strength and %elongation	127
4.3.3	Impact Properties	130
4.3.3.1	Load-time curves	130
4.3.3.2	T5 heat treatment	132
4.3.3.3	T6 heat treatment	136
4.3.4	Relationship Between Tensile and Impact Properties	141
4.3.4.1	T5 heat treatment	141
4.3.4.2	T6 heat treatment	144
<b>CHAPTER 5</b>	<b>FRACTOGRAPHY</b>	<b>148</b>
5.1	INTRODUCTION	149
5.2	FRACTOGRAPHY RESULTS	150
5.2.1	T5 Heat Treatment	151
5.2.2	T6 Heat Treatment	159
<b>CHAPTER 6</b>	<b>CONCLUSIONS</b>	<b>168</b>
	<b>SUGGESTIONS FOR FURTHER WORK</b>	<b>175</b>
	<b>REFERENCES</b>	<b>176</b>

## LIST OF TABLES

### Chapter 2

Table 2.1.	AA-standard composition (wt%) of 319 alloys <sup>6</sup> .....	11
------------	--	----

### Chapter 3

Table 3.1.	Chemical compositions (wt%) of the experimental base alloy (coded ASC) and industrial 319 alloy .....	52
Table 3.2.	List of the alloys used in the present work and their respective codes .....	52
Table 3.3.	Actual alloying element additions (wt%) in the alloys studied obtained from chemical analysis.....	54
Table 3.4.	Precipitation temperatures of the Al+CuAl <sub>2</sub> eutectic in the alloys studied.....	56
Table 3.5.	Expected reactions in ASC, ASCS and ASCF alloys.....	58
Table 3.6.	Al and Cu concentrations (at%) of the CuAl <sub>2</sub> phase in the experimental Al-7%Si-3.5%Cu alloy (as-cast condition; cooling rate ~0.8 °C/s).....	64
Table 3.7.	Summary of the dissolution of the CuAl <sub>2</sub> phase at 505°C as a function of alloy composition and solution treatment time .....	72
Table 3.8.	Al and Cu concentrations (at%) in CuAl <sub>2</sub> phase particles during solution heat treatment at 505 °C.....	80
Table 3.9.	Maximum Cu counts obtained from WDS analysis for ASCFS alloy after different solution heat treatment times .....	84
Table 3.10.	Spot analysis of the new copper phase .....	89

### Chapter 4

Table 4.1.	Codes of the alloys used in the present work.....	93
Table 4.2.	Actual chemical composition (wt%) of the alloys studied in the present work.....	95
Table 4.3.	DAS values obtained at various levels of the end-chilled castings for the six alloys studied.....	96
Table 4.4.	Eutectic Si particle characteristics observed in AW, CW and DW alloy samples (T5 condition) .....	105

Table 4.5.	Eutectic Si particle characteristics observed in AW, CW and DW alloy samples (T6 condition) .....	111
Table 4.6.	Amount of undissolved $\text{CuAl}_2$ phase observed at the highest and lowest cooling rates in the six studied alloys.....	111
Table 4.7.	Area percentage of porosity in the alloys studied.....	112
Table 4.8.	Impact test results of T5 heat-treated alloys .....	133
Table 4.9.	Impact test results of T6 heat-treated alloys .....	137

## LIST OF FIGURES

### Chapter 2

Figure 2.1.	Part of the Al-Si phase diagram showing composition ranges of various alloy types. <sup>3</sup> .....	9
Figure 2.2.	This illustration shows a typical cooling curve and its first derivative of unmodified 319.2 at 0.8 °C/s <sup>-1</sup> for 1) Primary Al phase nucleation, 2) Al-Si eutectic reaction, 3) Reaction 1 and 4) Reaction 2. <sup>8</sup> .....	13
Figure 2.3.	(a) Microstructure of a sample from 319.1 alloy cooled at a rate of 0.3 °C/s, X560: 1) $\beta$ -Al <sub>5</sub> FeSi, 2) blocky CuAl <sub>2</sub> phase, and 3) Al <sub>5</sub> Mg <sub>3</sub> Cu <sub>2</sub> Si <sub>6</sub> phase; (b) Microstructure of a sample from 319.1 alloy cooled at a rate of 0.6 °C/s, X560: 4) Chinese script Al <sub>15</sub> (Fe,Mn) <sub>3</sub> Si <sub>2</sub> phase and 5) acicular Si phase. <sup>3</sup> .....	14
Figure 2.4.	Optical microstructures of 319.2 alloy samples (Mag: X200 for both samples): a) 0.8% Fe, DAS 83 $\mu$ m, unmodified; b) 0.8% Fe, DAS 83 $\mu$ m, Sr-modified.....	17
Figure 2.5.	a) First part of a cooling curve and its derivative obtained from the melt near to the mold wall of a casting; b) Cooling curve and its derivative from a sample to which titanium boride particles have been added. The nucleation temperature (T <sub>N</sub> ) here is above the actual growth temperature of the melt. The recalescence function shows a very low value of (dT/dt) <sub>max</sub> , indicating a grain refined sample. <sup>3</sup> .....	19
Figure 2.6.	DSC run for a powdered sample obtained from the experimental 319 alloy solidified at 10 °C/s. The open arrow in the enlarged circled area indicates the onset of melting of the CuAl <sub>2</sub> phase. <sup>31</sup> .....	23
Figure 2.7.	Representative isothermal aging curves for alloy 2014-T4. <sup>5</sup> .....	31
Figure 2.8.	The engineering stress-strain curve. <sup>55</sup> .....	34
Figure 2.9.	Two main types of fracture observed in the Al-Si alloys under tensile overloading: (a) Dimple rupture <sup>75</sup> and (b) cleavage fracture of intermetallics. <sup>76</sup> .....	44
<b>Chapter 3</b>		
Figure 3.1.	Schematic diagram of the graphite mold used for thermal analysis. ....	53
Figure 3.2.	Cooling curves and first derivatives obtained from ASC, ASCS and ASCF alloys.....	57

Figure 3.3.	(a) Microstructure of the experimental base alloy (ASC) in the as-cast condition; (b) High magnification micrograph showing the eutectic-like copper phase marked A in (a). .....	59
Figure 3.4.	As-cast microstructure of ASCS alloy (Sr modified base alloy) showing Al-Si eutectic (A), and $\text{CuAl}_2$ segregation (B). .....	60
Figure 3.5.	As-cast microstructure of ASCF alloy (base alloy containing 1 wt% Fe) showing an $\beta\text{-Al}_5\text{FeSi}$ platelet (A), and eutectic ( $\text{Al}+\text{CuAl}_2$ ) precipitated along the sides of the $\beta$ -platelets (circled area). .....	61
Figure 3.6.	As-cast microstructure of ASCFS-1 alloy (base alloy containing 0.9 wt% Fe and modified with Sr. Note how the $\beta$ - and Cu-phases occur away from the Al-Si eutectic regions. ....	61
Figure 3.7.	As-cast microstructure of ASCFS-2 alloy (base alloy containing 1.2 wt% Fe and modified with Sr). Note the larger amount of $\beta$ -platelets compared to Figure 3.6. ....	62
Figure 3.8.	As-cast microstructure of H4T1 alloy (industrial 319 alloy containing 60 ppm P and modified with Sr), showing the precipitation of the $\text{CuAl}_2$ phase along the dendrite cell boundaries. ....	63
Figure 3.9.	As-cast microstructure of H20T1 alloy (industrial 319 alloy containing 90 ppm P, 0.7 wt% Fe and modified with Sr), showing a structure similar to that of Figure 3.7. ....	63
Figure 3.10.	$\text{CuAl}_2$ phase dissolution in ASC alloy during solution heat treatment at 505 °C as a function of solution treatment time. ....	66
Figure 3.11.	$\text{CuAl}_2$ phase dissolution in ASCS alloy during solution heat treatment at 505 °C as a function of solution treatment time. ....	67
Figure 3.12.	$\text{CuAl}_2$ phase dissolution in ASCF alloy during solution heat treatment at 505 °C as a function of solution treatment time. ....	68
Figure 3.13.	$\text{CuAl}_2$ phase dissolution in ASCFS-1 alloy during solution heat treatment at 505 °C as a function of solution treatment time. ....	69
Figure 3.14.	$\text{CuAl}_2$ phase dissolution in ASCFS-2 alloy during solution heat treatment at 505 °C as a function of solution treatment time. ....	69
Figure 3.15.	$\text{CuAl}_2$ phase dissolution in H4T1 alloy during solution heat treatment at 505 °C as a function of solution treatment time. ....	71
Figure 3.16.	$\text{CuAl}_2$ phase dissolution in H20T1 alloy during solution heat treatment at 505 °C as a function of solution treatment time. ....	71
Figure 3.17.	Backscattered images of (a) eutectic copper phase, (b) blocky copper phase, and (c) EDX spectrum obtained from $\text{CuAl}_2$ particles shown in (b), where strong reflections due to Al and Cu can be seen. ....	73
Figure 3.18.	(a) Backscattered image of $\text{CuAl}_2$ phase distribution in as-cast H4T1 alloy, (b) high magnification micrograph of the Cu phase segregation area shown in (a), and (c) fine $\text{CuAl}_2$ particles scattering on the modified Si particles in as-cast H20T1 alloy. ....	75

Figure 3.19.	(a) Backscattered image, and X-ray images of (b) Al and (c) P underneath $\text{CuAl}_2$ particles observed in H20T1 alloy (ASC alloy containing Fe, P and Sr).....	76
Figure 3.20.	Microstructure of $\text{CuAl}_2$ particles precipitated on the $\beta$ -plate in the as-cast ASCFS alloy. ....	77
Figure 3.21.	Backscattered image showing the dissolution process of $\text{CuAl}_2$ particles in ASCFS alloy after 8 hours of solution heat treatment at 505 °C: (1) separation of $\text{CuAl}_2$ from $\beta$ -plate, (2) necking of $\text{CuAl}_2$ cluster, (3) spheroidization of $\text{CuAl}_2$ and reduction in the size of $\text{CuAl}_2$ fragments. ....	78
Figure 3.22.	Backscattered image showing $\text{CuAl}_2$ dissolution in H4T1 alloy after 8 hours of solution heat treatment at 505 °C. ....	78
Figure 3.23.	Backscattered image taken from H4T1 alloy after 100 hours of solution heat treatment at 505 °C.....	79
Figure 3.24.	(a) Backscattered image of a $\text{CuAl}_2$ particle in ASCFS alloy after 8 hours of solution heat treatment; (b) the concentration profile of Cu along the path AB in (a).....	81
Figure 3.25.	(a) Backscattered image of a $\text{CuAl}_2$ particle in ASCFS alloy after 100 hours of solution heat treatment; (b) the concentration profile of Cu along the path AB in (a).....	82
Figure 3.26.	X-ray image of Cu in ASCFS alloy after a: (a) 0-hour, (b) 8-hour and (c) 100-hour solution heat treatment at 505 °C. ....	83
Figure 3.27.	(a) Backscattered image of $\text{CuAl}_2$ phase with phosphorus oxide particle, (b) corresponding X-ray image of P obtained from this sample. ....	85
Figure 3.28.	High magnification secondary electron image of a phosphorus oxide particle. ....	86
Figure 3.29.	(a) Backscattered image of a $\text{Cu}_2\text{FeAl}_7$ particle precipitating on the $\beta$ - $\text{Al}_5\text{FeSi}$ platelet, and corresponding X-ray images of (b) Cu and (c) Fe in (a).....	88

#### Chapter 4

Figure 4.1.	Schematic diagram of the end-chilled mold used to prepare the castings.....	94
Figure 4.2.	End-chill casting showing specimen blanks sectioning scheme (mm).....	96
Figure 4.3.	a) Schematic diagram of blanks used for preparing tensile test specimens, b) dimensions of the tensile test specimen (All dimensions are in mm).....	98
Figure 4.4.	Impact machine connected to a data acquisition system. ....	99
Figure 4.5.	a) Schematic diagram of the blanks used for preparing the impact testing specimens, b) dimensions of the impact testing specimen. (mm).....	100

Figure 4.6.	Photographs showing typical microstructures in AW alloy with T5 heat treatment: a) 23 $\mu\text{m}$ DAS, b) 83 $\mu\text{m}$ DAS. ....	103
Figure 4.7.	Photographs showing typical microstructures in CW alloy with T5 heat treatment: a) 23 $\mu\text{m}$ DAS, b) 83 $\mu\text{m}$ DAS. ....	104
Figure 4.8.	Photographs showing typical microstructures in DW alloy with T5 heat treatment: a) 23 $\mu\text{m}$ DAS, b) 83 $\mu\text{m}$ DAS. ....	106
Figure 4.9.	Photographs showing typical microstructures in AW alloy with T6 heat treatment: a) 23 $\mu\text{m}$ DAS, b) 83 $\mu\text{m}$ DAS. ....	108
Figure 4.10.	Photographs showing typical microstructures in CW alloy with T6 heat treatment: a) 23 $\mu\text{m}$ DAS, b) 83 $\mu\text{m}$ DAS. ....	109
Figure 4.11.	Photographs showing typical microstructures in DW alloy with T6 heat treatment: a) 23 $\mu\text{m}$ DAS, b) 83 $\mu\text{m}$ DAS. ....	110
Figure 4.12.	Tensile properties of the six alloys studied (T5 condition) as a function of DAS: a) ultimate tensile strength, b) yield strength, c) %Elongation.....	118
Figure 4.13.	Tensile properties of the six alloys studied (T6 condition) as a function of cooling rate: a) ultimate tensile strength, b) yield strength, c) %Elongation.....	125
Figure 4.14.	a) Plot of ultimate tensile strength vs. percent elongation for studied alloys with different solution heat treatments (T5 & T6), b) plot of logUTS vs. log%El for studied alloys with different heat treatments (T5 & T6).....	129
Figure 4.15.	a) Load-time curve of T6 heat-treated CW alloy (at 23 $\mu\text{m}$ DAS), b) load-time curve of T5 heat-treated EW alloy (at 83 $\mu\text{m}$ DAS). ....	131
Figure 4.16.	Total absorbed energy of the studied alloys as a function of DAS after T5 heat treatment.....	135
Figure 4.17.	Total absorbed energy of the alloys studied as a function of DAS (T6 condition).....	140
Figure 4.18.	Relationship between %El and $E_t$ for the six alloys studied (T5 condition).....	142
Figure 4.19.	Relationship between UTS and $E_t$ for the six alloys studied (T5 condition).....	143
Figure 4.20.	Relationship between %El and $E_t$ for the six alloys studied (T6 condition).....	145
Figure 4.21.	Relationship between UTS and $E_t$ for the six alloys studied (T6 condition).....	147

## Chapter 5

Figure 5.1.	(a) BS micrograph showing fracture surface of base alloy (DAS 23 $\mu\text{m}$ , unmodified, T5 condition, center), (b) high magnification BS showing the fracture of Si and $\text{CuAl}_2$ in (a).....	152
-------------	--	-----

Figure 5.2.	BS micrograph showing fracture surface of base alloy (DAS 23 $\mu\text{m}$ , unmodified, edge).....	153
Figure 5.3.	High magnification BS micrograph showing fracture surface of base alloy (DAS 83 $\mu\text{m}$ , unmodified, center).....	153
Figure 5.4.	High magnification BS micrograph showing fracture surface of base alloy (DAS 83 $\mu\text{m}$ , unmodified, edge).....	154
Figure 5.5.	BS micrograph showing fracture surface of DW alloy (1.2% Fe, DAS 23 $\mu\text{m}$ , Sr-modified, center).....	155
Figure 5.6.	BS micrograph showing fracture surface of DW alloy (1.2% Fe, DAS 23 $\mu\text{m}$ , Sr-modified, center).....	155
Figure 5.7.	(a) BS micrograph showing fracture surface of DW alloy (1.2% Fe, DAS 83 $\mu\text{m}$ , Sr-modified, edge), (b) high magnification of $\beta\text{-Al}_5\text{FeSi}$ particle in (a).....	157
Figure 5.8.	(a) BS micrograph showing fracture surface of DW alloy (1.2% Fe, DAS 83 $\mu\text{m}$ , Sr-modified, center), (b) high magnification of the pore existing in (a).....	158
Figure 5.9.	(a) BS micrograph showing fracture surface of base alloy (DAS 23 $\mu\text{m}$ , unmodified, T6 condition, edge), (b) high magnification BS showing the crack initiation passing through the undissolved Cu-containing phase and fibrous Si particles.....	160
Figure 5.10.	BS micrograph showing fracture surface of the intermetallics in base alloy (DAS 23 $\mu\text{m}$ , unmodified, T6 condition, center).....	161
Figure 5.11.	(a) BS micrograph showing fracture surface of base alloy (DAS 83 $\mu\text{m}$ , unmodified, T6 condition, center), (b) high magnification of BS showing the crack propagation through the undissolved $\text{CuAl}_2$ phase.....	162
Figure 5.12.	(a) BS micrograph showing fracture surface of DW alloy (1.2% Fe, DAS 23 $\mu\text{m}$ , Sr-modified, T6 condition, edge), (b) high magnification of BS showing the fracture behavior of $\beta\text{-Al}_5\text{FeSi}$ during crack initiation.....	165
Figure 5.13.	(a) BS micrograph showing fracture surface of DW alloy (1.2% Fe, DAS 83 $\mu\text{m}$ , Sr-modified, T6 condition, edge), (b) high magnification of BS showing the fracture behavior of $\beta\text{-Al}_5\text{FeSi}$ during crack initiation.....	166
Figure 5.14.	BS micrograph showing fragmentation of $\text{Cu}_2\text{FeAl}_7$ on the fracture surface of DW alloy (1.2% Fe, DAS 83 $\mu\text{m}$ , Sr-modified, T6 condition, center).....	167

## **CHAPTER 1**

### **DEFINITION OF THE PROBLEM**

# CHAPTER 1

## DEFINITION OF THE PROBLEM

### 1.1 INTRODUCTION

The excellent castability and mechanical properties of 319-type alloys are among the reasons why this alloy is used for the production of engine blocks by the automotive industry. Based on the Al-Si system, the alloy contains copper as the main alloying element (3.5 wt%), magnesium in the range 0.04 to 0.3 wt%, and varying amounts of iron, manganese and zinc as impurity elements. During the solidification of 319 alloys, the main precipitation of  $\text{CuAl}_2$  is a multicomponent eutectic reaction at about 525 °C. Finely dispersed  $\text{CuAl}_2$  and coexisting  $\beta\text{-Al}_3\text{FeSi}$  needles are formed through this reaction, along with some deposition of Si.

Modification is one of the melt treatments normally carried out for Al-Si alloys, where modifying agents (Sr, Na, *etc.*) are added to the alloy melt in the form of master alloys to alter the structure of the eutectic silicon particles from a coarse flake-like morphology to a fine fibrous form, in order to improve the mechanical properties, particularly ductility. It is now widely accepted that strontium atoms which are incorporated into the crystal structure of silicon, enhance the formation of growth twins and allow the silicon to bend and twist into a fibrous morphology. Unlike sodium, which is

rapidly lost from a melt through vaporization, strontium is lost primarily through slow oxidation, and the action of Sr can be retained for a long period of time. Furthermore, from the experimental operation standpoint, the addition of strontium via a master alloy is easier to control.

The presence of strontium also leads to the segregation of the copper phases and, hence, slows their dissolution during solution treatment. Due to the segregation, the copper phase  $\text{CuAl}_2$  precipitates more often in the block-like form (coarse  $\text{CuAl}_2$  precipitates, copper content  $\sim 40$  wt%) rather than in the fine eutectic form (fine  $\text{CuAl}_2$  particles interspersed with Al, copper content  $\sim 24$  wt%). Most of the recommended heat treatments restrict the solution temperature to below the final solidification point, in order to avoid the melting of the copper-containing phases. In order to enhance the dissolution of  $\text{CuAl}_2$  in the aluminum matrix, a two-step heat treatment was proposed for 319 alloys, where the alloy samples were heated to a temperature of  $495^\circ\text{C}$ , followed by a second solution treatment at a temperature above the  $\text{CuAl}_2$  eutectic phase melting point, in order to accelerate its dissolution. However, this can lead to the incipient melting of the copper phase ( $\sim 507^\circ\text{C}$ ), resulting in the formation of shrinkage cavities when the samples are quenched after solution heat treatment.

Thus, control of the solution treatment temperature is very critical because, if the melting point is exceeded, localized melting can occur at the grain boundaries and the mechanical properties are reduced. Compared to the eutectic  $\text{CuAl}_2$  phase, the coarser block-type form of the phase is found to be much harder to dissolve. It is also found that Sr modification leads to the segregation of the  $\text{CuAl}_2$  phase to areas free of eutectic silicon

particles, resulting from a divorced eutectic reaction. The increased number of the modified silicon particles serves as nucleation sites for the precipitation of very fine individual  $\text{CuAl}_2$  particles. At the same time, the presence of Fe – in the form of iron intermetallics, in particular the  $\beta\text{-Al}_5\text{FeSi}$  plate-like phase, acts as a nucleant for the  $\text{CuAl}_2$  phase. Grain refining plays an important role in reducing the degree of the  $\text{CuAl}_2$  segregation and in refining the block-like  $\text{CuAl}_2$  particles in the Sr-modified alloys, particularly at low cooling rates. It is a well-established fact that the addition of small quantities of  $\text{TiB}_2$  refines the grain size and reduces pore sizes, which improves the mechanical properties. In addition,  $\text{TiB}_2$  also has a significant influence on reducing the degree of the  $\text{CuAl}_2$  phase segregation.

As strontium is commonly employed in Al-Si-Cu type alloys to modify the eutectic silicon in order to improve the properties, the various problems associated with its addition (*viz.*, segregation of the copper phase and the consequent slowing down of its dissolution during solution treatment; precipitation of the block-like rather than the finer eutectic-like  $\text{CuAl}_2$  phase; and the danger of incipient melting) will need to be overcome in order to maintain the mechanical properties of the alloy. This has been the main focus of my study.

## 1.2 OBJECTIVES

The present research work was undertaken to achieve the following objectives related to 319 Al-Si-Cu alloys:

- (i) Study the effect of the  $\beta$ -iron phase on the nucleation of the  $\text{CuAl}_2$  phase in 319 alloys and the severity of  $\text{CuAl}_2$  segregation with respect to different alloying elements, *viz.*, Sr, Fe, and P.
- (ii) Dissolution of  $\text{CuAl}_2$  during solution heat treatment (at 505 °C for times up to 100 h) with emphasis on the role of Sr, Fe and P additions.
- (iii) The exact dissolution process of the segregated  $\text{CuAl}_2$  particles during the heat treatment process (T6).
- (iv) Effect of the intermetallic, namely  $\text{CuAl}_2$  in the T5 and T6 treatments, on the tensile and impact properties under directional solidification.
- (v) Fracture behavior of impact samples at different cooling rates and heat treatments.

**CHAPTER 2**  
**LITERATURE SURVEY**

## CHAPTER 2

### LITERATURE SURVEY

#### 2.1 COMMON Al-Si CASTING ALLOYS

Worldwide, the use of cast aluminum components in automotive applications has become a key focus area. To date, cast aluminum components have been used primarily in engine components, including blocks, cylinder heads, pistons, intake manifolds, and brackets. Also, in order to reduce weight, strong interest has been generated in using cast aluminum instead of cast iron for suspension control arms, steering gear components, front strut support bearings, and wheels.<sup>1,2</sup>

Although most metals will alloy with aluminum, comparatively few have sufficient solid solubility to serve as major alloying additions. Of the commonly used elements, only zinc, magnesium, copper and silicon have significant solubilities. In contrast, with the exception of hydrogen, elemental gases have no detectable solubility in either liquid or solid aluminum.

Alloys with silicon as the major alloying addition are the most important of the aluminum casting alloys, mainly because of the high fluidity imparted by the presence of relatively large volumes of the Al-Si eutectic. Aluminum-silicon castings constitute 85% to 90% of the total aluminum cast parts produced. Furthermore, there are many other reasons

justifying the commercial importance of these alloys, including a high resistance to corrosion, good weldability and the fact that the silicon phase reduces both shrinkage during solidification and the coefficient of thermal expansion of the cast products.

The Al-Si alloys obtain extensive applications in the automobile industry where there has been a continuing demand for greater fuel efficiency and higher performance materials. Higher fuel efficiency can be achieved by reducing the weight of vehicles. Since Al-Si alloys possess the same mechanical properties as cast iron for particular parts, Al-Si alloys have made considerable inroads into applications in automobiles formerly monopolized by cast iron, such as: transmission cases, intake manifolds, and some engine blocks and cylinder heads. Cast iron used for these parts is three times heavier than aluminum-silicon alloys. Cast Al-Si alloy substitutes for cast iron have proven to be very cost-effective, especially in the case of cylinder heads.

The main feature of aluminum-silicon alloys is that a eutectic is formed between aluminum and silicon at a silicon content of 11.5-12% (see the phase diagram in Figure 2.1). Depending on the amount of silicon, the alloys are divided into three groups: hypo-eutectic alloys with a Si content between 5-10% Si, eutectic alloys with 11-13% Si, and hyper-eutectic alloys, with a Si content normally between 14% and 20%.

During the solidification process of Al-Si alloys, the following main sequence of phase precipitation will occur:

- (1) Formation of a dendritic network of  $\alpha$ -aluminum.
- (2) The aluminum-silicon eutectic reaction.
- (3) Precipitation of a secondary eutectic phase such as  $Mg_2Si$  or  $CuAl_2$ .

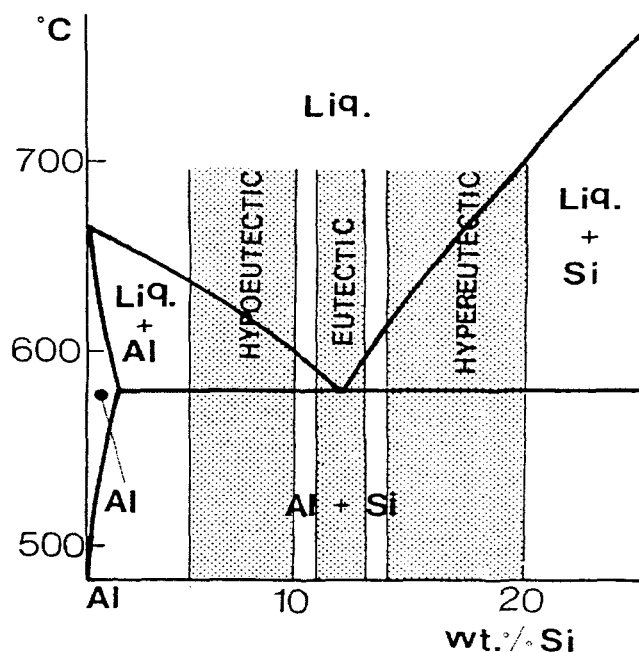


**Figure 2.1.** Part of the Al-Si phase diagram showing composition ranges of various alloy types.<sup>3</sup>

In eutectic alloys the pre-eutectic reaction may be missing and in hypereutectic alloys, the primary reaction involves the precipitation of silicon particles until the eutectic composition is reached. In addition to the main reactions, precipitation of the iron- and manganese-containing phases will take place. The most common of such phases in foundry alloys are  $\text{Al}_5\text{FeSi}$  and  $\text{Al}_{15}(\text{Mn,Fe})_3\text{Si}_2$ . Toward the end of the solidification process  $\text{Mg}_2\text{Si}$ ,  $\text{CuAl}_2$  and other more complex phases will precipitate from the remaining liquid.<sup>3</sup>

The eutectic is formed between an aluminum solid solution containing just over 1% silicon and virtually pure silicon as the second phase. The eutectic composition has been accepted as being close to Al-11.6%Si. Slow solidification of a pure Al-Si alloy produces a very coarse microstructure in which the eutectic comprises large plates or needles of silicon in a continuous aluminum matrix. The eutectic itself is composed of individual cells in

which the silicon particles appear to be interconnected. Alloys having this coarse eutectic exhibit low ductility because of the brittle nature of the large silicon plates. Rapid cooling, as occurs during permanent mold casting, greatly refines the microstructure and the silicon phase assumes a fibrous form with the result that both ductility and tensile strength are much improved. The eutectic may also be refined by a process known as modification.

Generally, the microstructure of Al-Si alloys is characterized by two phases, *i.e.* Al and Si. Thus, these alloys are a combination of the high strength-brittle phase (Si) and low strength-ductile phase (Al). The addition of copper to Al-Si alloys leads to a slight increase in alloy ductility and substantially improves strength and hardness in as-cast and heat-treated conditions. At the same time, a depression in the Si eutectic temperature of  $\sim 1.8$  °C for every 1 wt% Cu added can be detected. On an atomic basis, copper and manganese are the most effective strengtheners. Some of the mechanical properties obviously benefit from the addition of Cu as an alloying element (such as YS and UTS).<sup>4</sup> However, copper additions to the non-heat-treatable alloys are normally held to a maximum of 0.3 wt% to avoid the possible formation of insoluble Al-Cu-Fe constituents.

## **2.2 319 Al-Si-Cu ALLOYS**

The 319 (Al-Si-Cu) casting alloys are being widely used in many of the automotive components mentioned previously. These alloys have good casting characteristics, excellent mechanical properties, and are heat-treatable. Moreover, the low specific gravity of 319 alloys is essential in reducing energy consumption, and its excellent corrosion resistance and low recycling costs are also important considerations from an environmental

point of view.<sup>5</sup> Due to its important application and high demand in the automotive industry, which is the largest consumer of cast aluminum-silicon alloys, the 319 alloy demands detailed information on how the mechanical properties are affected by alloying elements and different heat treatments.

The composition of common 319 aluminum alloys is listed in Table 2.1. This table shows that, except for Al, the main components in 319 alloys are Si and Cu, in quantities of 5.5-6.5% and 3.0-4.0%, respectively.

**Table 2.1.** AA-standard composition (wt%) of 319 alloys<sup>6</sup>

Alloy Code	Elements								
	Si	Fe	Cu	Mn	Mg	Zn	Ti	Ni	Others
319.0	5.5-6.5	1.0	3.0-4.0	0.50	0.10	1.0	0.25	0.35	bal.
319.1	5.5-6.5	0.8	3.0-4.0	0.50	0.10	1.0	0.25	0.35	bal.
B319.1	5.5-6.5	0.9	3.0-4.0	0.80	0.15-0.50	1.0	0.25	0.35	bal.
319.2	5.5-6.5	0.6	3.0-4.0	0.10	0.10	0.10	0.20	0.10	bal.

In the present work, the 319 alloy was selected for study due to its popularity among Al-Si alloys which contain high levels of iron (1.2% max). Also, 319 alloy is a general-purpose foundry alloy that is moderately responsive to heat treatment. It contains both copper and magnesium as the hardening elements. It is well known that at ~548 °C, the amount of Cu usually in the form of a solid solution in Al is about 5.7 wt%. This value decreases with a decreasing temperature, reaching 0.1~0.2 wt% at 250 °C.<sup>7</sup> Copper forms an intermetallic phase with aluminum that precipitates during solidification either as block-like  $\text{CuAl}_2$  or in eutectic form as  $(\text{Al} + \text{CuAl}_2)$ . As a result of its chemical composition, it

has excellent casting characteristics, good mechanical properties and its strength at elevated or low temperatures is very good.

### 2.3 SOLIDIFICATION CHARACTERISTICS OF 319 ALLOYS

Typical cooling curves are presented in Figure 2.2<sup>8</sup> for an unmodified 319 alloy in the temperature-time and derivative format. It is characterized by the following reactions:

- (1) formation of primary aluminum at about 608 °C;
- (2) the main silicon-forming eutectic reaction at about 563 °C;
- (3) a CuAl<sub>2</sub>-forming reaction at about 550 °C (reaction 1);
- (4) a complex eutectic reaction at about 525 °C (reaction 2);

Reaction 1 occurs close to the formation temperature of CuAl<sub>2</sub> through the reaction:



It is likely that this is the main formation reaction of CuAl<sub>2</sub> particularly in the blocky form, which is probably primary. Reaction 2 is a multicomponent eutectic reaction reported by Mondolfo<sup>9</sup> as:



Finely dispersed small CuAl<sub>2</sub> particles and the coexisting  $\beta$ -Al<sub>5</sub>FeSi needles are formed through this reaction, accompanied by some deposition of the Si phase.

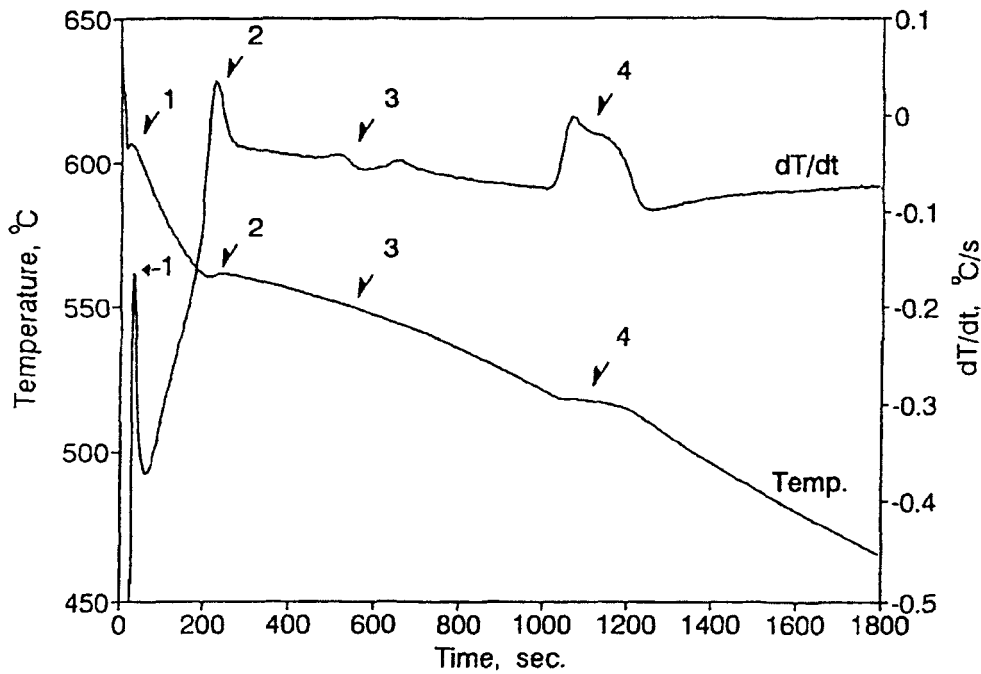


**Figure 2.2.** Diagram of a typical cooling curve and its first derivative obtained from unmodified 319.2 at  $0.8\text{ }^{\circ}\text{C/s}^{-1}$  showing 1) Primary Al phase nucleation, 2) Al-Si eutectic reaction, 3) Reaction 1 and 4) Reaction 2.<sup>8</sup>

The solidification rate during casting is perhaps the most important of the various parameters influencing microstructure, as it directly or indirectly affects almost all the microstructural parameters, such as dendrite arm spacing (DAS), the degree of eutectic silicon modification and grain refinement, and the amount of microporosity, intermetallics and inclusions observed in the microstructure. The two microstructures of Figure 2.3 depict the main typical phases appearing in 319.1 alloy at different solidification rates.<sup>3</sup> Figure 2.3(a) shows how  $\text{Al}_5\text{FeSi}$  needles (1) actually serve as nucleating sites for silicon crystals (5). Blocky  $\text{CuAl}_2$  particles (2) are also observed and with them particles of the  $\text{Al}_5\text{Mg}_2\text{Si}_6\text{Cu}_2$  phase (3). Figure 2.3(b) exhibits a eutectic area where  $\text{Al}_{15}(\text{Mn,Fe})_3\text{Si}_2$  and  $\text{Al}_5\text{FeSi}$  phases coexist.

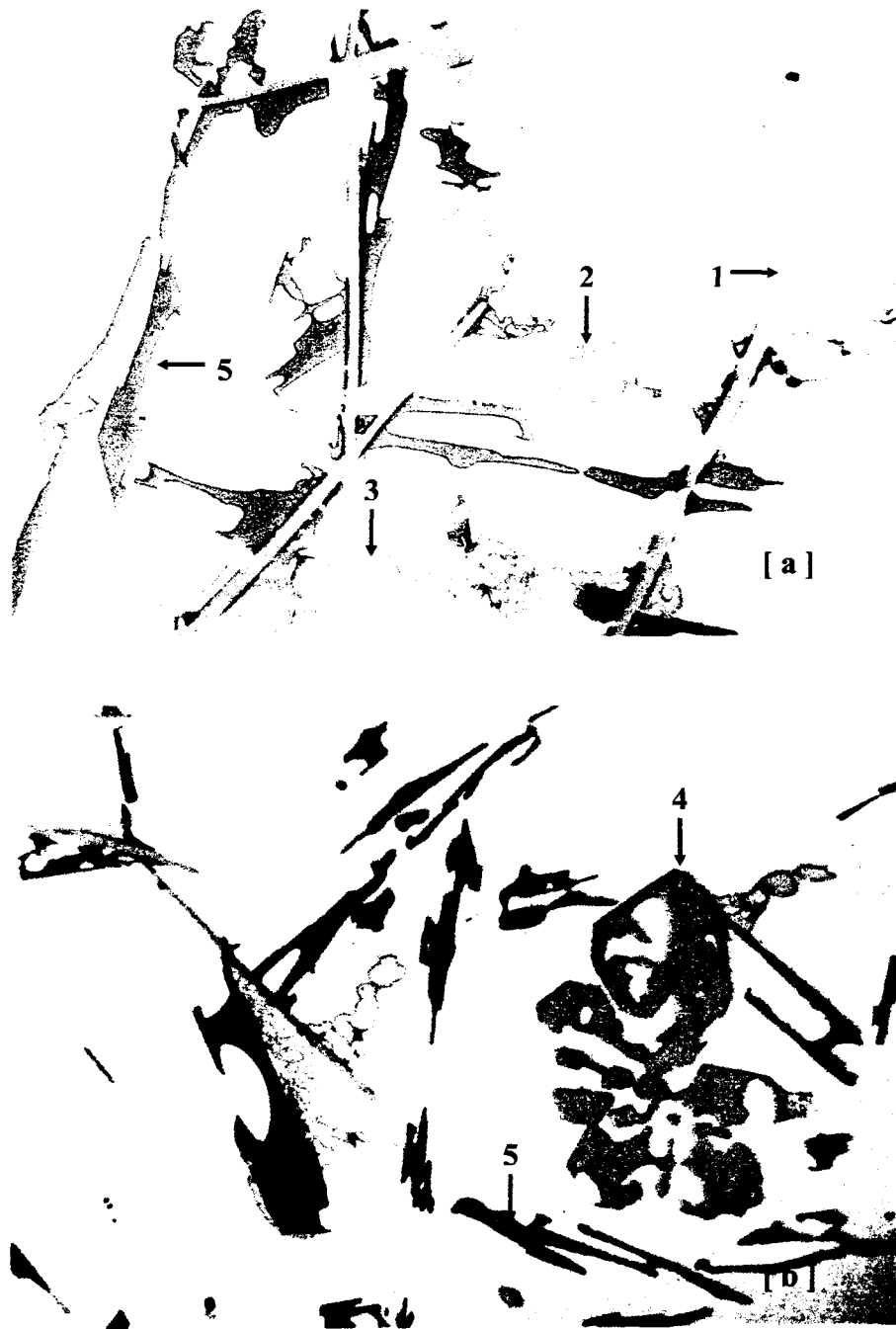


**Figure 2.3.** (a) Microstructure of a sample from 319.1 alloy cooled at a rate of 0.3 °C/s, X560: 1)  $\beta$ - $\text{Al}_5\text{FeSi}$ , 2) blocky  $\text{CuAl}_2$  phase, and 3)  $\text{Al}_5\text{Mg}_8\text{Cu}_2\text{Si}_6$  phase; (b) Microstructure of a sample from 319.1 alloy cooled at a rate of 0.6 °C/s, X560: 4) Chinese script  $\text{Al}_{15}(\text{Fe},\text{Mn})_3\text{Si}_2$  phase and 5) acicular Si phase.<sup>3</sup>

## 2.4 ROLE OF MODIFICATION

Modification is one of the melt treatments normally carried out for Al-Si alloys, to alter the structure of the eutectic silicon particles in order to improve the mechanical properties, particularly ductility.

Modification occurs naturally at rapid solidification rates (quenching modification), but requires a modifying agent at the slower solidification rates typical of sand casting (impurity modification). Fast solidification rates are used to reduce the size and the distance between eutectic silicon particles, rather than their shape or morphology.<sup>10</sup> Modification was originally attributed to the repeated nucleation of the eutectic silicon phase at a reduced temperature.<sup>11,12</sup> It has been established that, although the nucleation temperature is depressed, the silicon phase grows continuously without repeated nucleation with increased undercooling.<sup>13</sup> During the modification procedure, the aluminum phase is not affected structurally. For the silicon phase, however, modification results in a change from a faceted to a more isotropic growth morphology.

It is well known that the eutectic structure can be greatly refined by the addition of sodium. For many years, sodium has been the predominant modifying agent for hypoeutectic Al-Si casting alloys. Apart from atomic size, there are several other factors that control the efficiency of a modifier. A low melting point and a high vapor pressure promote rapid dispersion of the modifier in the melt, but a high vapor pressure will encourage fading by evaporation. Moreover, oxidation loss will be a problem with modifiers having a free energy of oxide formation higher than that of aluminum. A low solid solubility and a wide miscibility gap having a monotectic point at a very low

concentration of modifier, as in the aluminum-silicon system, produce a large increase in modifier concentration at the growth front and a powerful modifying effect. Therefore, sodium dissolves and disperses rapidly in the melt without oxidation, but fades quickly (<20 min) because of evaporation, and within this time, provides a powerful modifying action. However, the undesirable problems<sup>14</sup> associated with the use of sodium led to the search for alternative elements for modifying Al-Si alloys.

Currently, in order to improve mechanical properties, the use of strontium as a modifier has become a widely accepted practice. Compared to sodium, strontium, as a modifier, has similar effects, and the key attributes of strontium are its greater resistance to loss from a melt and great tolerance (in terms of amount) to over-modification. It alters the morphology of the eutectic silicon particles from a coarse flake-like form to a fine fibrous one. Figure 2.4 clearly shows the difference in the microstructures of alloys with or without Sr-modification. The change in the Si morphology, in turn, improves the mechanical properties of the alloy, particularly ductility.<sup>15</sup>

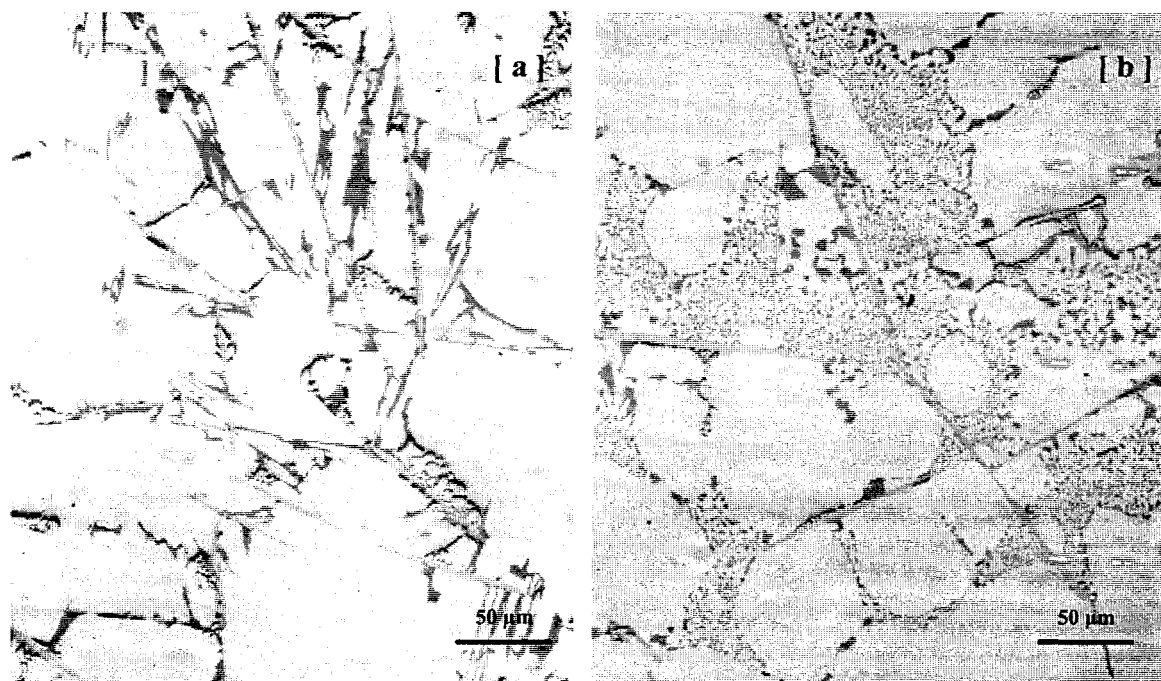


**Figure 2.4.** Optical microstructures of 319.2 alloy samples (Mag: X200 for both samples): a) 0.8% Fe, DAS 83 μm, unmodified; b) 0.8% Fe, DAS 83 μm, Sr-modified.

It is now widely accepted that Sr atoms that are incorporated into the crystal structure of silicon enhance the formation of growth twins and allow the silicon to bend and twist into a fibrous morphology.<sup>16</sup> It reacts with and neutralizes aluminum-phosphide (AlP) nuclei, an effective nucleant for silicon, and changes the growth kinetics of silicon crystallizing from the melt to produce a fibrous eutectic. Also, Sr oxidizes slightly and has a greater resistance to fading than sodium, producing a more permanent but weaker modifying action. However, when Al-Si alloys contain more than 0.05 wt% Sr, the formation of undesirable Sr-compounds such as  $\text{Al}_2\text{SrSi}_2$  contribute to a decrease in mechanical properties.<sup>17</sup> Depending on the alloy grade, concentrations of Sr in commercial alloys commonly range from 80-600 ppm. It has also been reported by some foundrymen that Sr has an “incubation time” of one to two hours at 730 °C.<sup>14,18</sup>

Another aspect that should be mentioned is that modification with Sr considerably lowers the actual eutectic reaction temperature. The depression in the eutectic temperature can be used as an indicator of the extent of Si structure modification expected in the casting: the lower the eutectic temperature, the greater the modification effect.<sup>19-21</sup> However, some previously published results reveal that the eutectic temperature decreases until ~0.016 wt% Sr is reached, then it increases again with a further increase in strontium concentration.<sup>22</sup> On the other hand, Sr modification also results in a larger area fraction of the interdendritic blocky  $\text{CuAl}_2$  structure in 319 aluminum alloys.<sup>23</sup> Furthermore, recent studies have indicated that Sr modification can be used effectively to lower heat treatment times substantially.<sup>24,25</sup> The data of Parker *et al.*<sup>26</sup> indicates that even solution times of less than 1 h may be sufficient to spheroidize silicon particles in modified alloys.

## 2.5 ROLE OF GRAIN REFINEMENT

It is standard practice to refine the grain structure as well as the eutectic structure of aluminum-silicon casting alloys in order to improve the mechanical properties. The most common way to promote the formation of fine grains is to add certain chemical agents that facilitate the nucleation of new aluminum crystals. This is most conveniently done by the addition of specially prepared master alloys.

Grain refinement is, however, the result of two separate processes: nucleation of new crystals from the melt, and subsequent growth of the new crystals into a limited size. Both these processes need a driving force that has to be supplied to the system via undercooling ( $\Delta T$ ) and/or supersaturation ( $\Delta C$ ) in relation to the equilibrium conditions of the actual

system. Figure 2.5(a)<sup>3</sup> shows that in a real casting, during the very first period of the solidification process, only those parts of the liquid metal in contact with the mold walls are undercooled to such a degree that the nucleation of new aluminum grains can occur. However, Figure 2.5(b) shows that nucleation starts above the steady state growth temperature. This means that new crystals can form, not only at the first contact of the melt with the cold walls of the mold, but also in the liquid ahead of the growing crystal front all the way from the walls to the center of the casting. This phenomenon is due to the fact that particles of high nucleating potency – like titanium-boride particles which already become active at an undercooling of only 0.1-0.2 °C – are added.

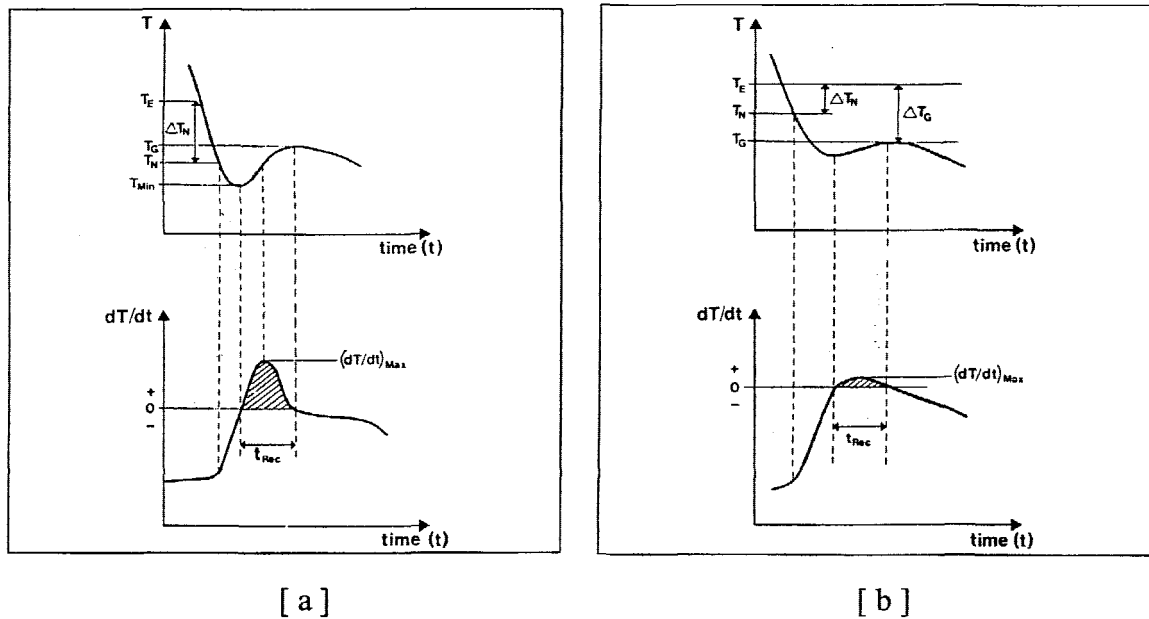


**Figure 2.5.** a) First part of a cooling curve and its derivative obtained from the melt near to the mold wall of a casting; b) Cooling curve and its derivative from a sample to which titanium boride particles have been added. The nucleation temperature ( $T_N$ ) here is above the actual growth temperature of the melt. The recalescence function shows a very low value of  $(dT/dt)_{max}$ , indicating a grain refined sample.<sup>3</sup>

Other temperature parameters shown in Figure 2.5 correspond to:

- $T_E$  = Equilibrium liquidus temperature.
- $T_G$  = Steady state growth temperature of the melt under the cooling conditions prevailing.
- $T_N$  = Start of nucleation temperature.  $T_N$  is called the “potency” of the nucleating particles present in the melt. This point is most easily recognized by a sudden change in the derivative, as indicated in the figure.
- $T_{Min}$  = The temperature at which the newly nucleated crystals have grown to such an extent that the latent heat liberated balances the heat extracted from the sample. After this moment, the melt is actually heating up to the steady state growth temperature. The time period needed for this heating up is called the “recalescence” period ( $t_{Rec}$ ).

An efficient heterogeneous nucleus for  $\alpha$ -aluminum is one that will provide a surface for growth at, or just above, the liquidus temperature of the alloy. It is well established that the addition of small quantities of  $TiB_2$  can meet all the necessary criteria, and thus refine grain size and reduce pore size, which results in improving the mechanical properties.<sup>27</sup> Also,  $TiB_2$  has a significant influence on reducing the degree of the  $CuAl_2$  phase segregation in both modified and unmodified alloys, resulting in a better distribution of the  $CuAl_2$  precipitated particles.

Recent studies have shown that commercial aluminum-titanium-boron master alloys contain  $(Al,Ti)B_2$  particles that are effective centers for the surface concentration of titanium atoms.<sup>28</sup> Titanium boride ( $TiB_2$ ) particles are not effective nuclei, and the successful master alloys contain an excess of titanium exceeding the quantity required to form  $TiB_2$  stoichiometrically. Thus, when an aluminum-titanium-boron master alloy is added to molten aluminum, soluble and insoluble particles are released into the melt. As the

soluble aluminide phase releases titanium into the melt, the (Al,Ti)B<sub>2</sub> particles become increasingly active nuclei for  $\alpha$ -aluminum.

## 2.6 THE COPPER INTERMETALLIC CuAl<sub>2</sub> PHASE IN 319 ALLOYS

As a secondary phase, CuAl<sub>2</sub> is usually formed in the temperature interval of 520 °C to 500 °C at a critical concentration during the precipitation of 319 alloys. This critical concentration depends on the efficiency of the nucleation sites. In the 319 alloys, there are two different morphologies of the CuAl<sub>2</sub> phase present, one is the blocky CuAl<sub>2</sub> type, the other is the finer eutectic (Al+CuAl<sub>2</sub>) type.

### 2.6.1 Precipitation and Segregation of CuAl<sub>2</sub>

The mechanism of CuAl<sub>2</sub> precipitation has been proposed by Samuel *et al.*<sup>29</sup> as follows: during the first stages of solidification, the formation of the  $\alpha$ -Al dendritic network is associated with the segregation of Si and Cu in the melt, ahead of the processing dendrite interfaces. When the solidification temperature approaches the eutectic temperature, rounded/fibrous Si particles precipitate, leading to a local concentration of Cu in the remaining areas. Depending on the cooling rate, CuAl<sub>2</sub> may precipitate as a mixture of eutectic-like and block-like forms, or mainly in the block-like form in the presence of  $\beta$ -Al<sub>5</sub>FeSi needles.

According to the observation of Reiso *et al.*,<sup>30</sup> one character of the eutectic CuAl<sub>2</sub> phase formed on subsequent solidification of the melt is the high Cu content. The chemical composition could reach a value of 43 wt% Cu higher than the equilibrium eutectic composition of 33 wt% Cu. The most likely explanation of this observation is the difficulty

in nucleation of the  $\text{CuAl}_2$  particles during solidification. At a critical Cu concentration,  $\text{CuAl}_2$  particles are nucleated, and the eutectic is formed. This critical concentration depends on the efficiency of the nucleation sites.

When the alloy is cooled at a high rate, the  $\text{CuAl}_2$  phase occurs mainly in the form of pockets of fine eutectics ( $\text{Al}+\text{CuAl}_2$ ) in the interdendritic regions, together with Si particles. As the cooling rate decreases, there is the possibility for simultaneous precipitation of the  $\text{CuAl}_2$  phase in the form of coarse particles and as a network. In the solidification process,  $\beta\text{-Al}_5\text{FeSi}$  platelets are very active sites for the nucleation of the  $\text{CuAl}_2$  phase. Yet, it should be noted that there is also a cooling rate effect involved, in that the precipitation and resulting size of the  $\beta$ -iron platelets are solidification rate-dependent. Thus, the available sites for nucleation of the Cu phase – determined by the amount and nature of the  $\beta$ -iron phase precipitation – will also be influenced by the cooling rate.

It has been observed that the presence of Sr also leads to segregation of the copper phase in areas free of eutectic Si particles during precipitation, resulting in the slowing of its dissolution during solution heat treatment. Furthermore, due to the segregation, the  $\text{CuAl}_2$  phase more often precipitates in the blocky form rather than in the fine eutectic form.<sup>29</sup> Compared with the latter, the blocky phase is more difficult to dissolve into the aluminum matrix. In low cooling rate cases, where precipitation of  $\text{CuAl}_2$  takes place mostly along the long sides of the  $\beta$ -platelets, it can be reasonably presumed that the mechanism of  $\text{CuAl}_2$  precipitation is caused by a divorced eutectic reaction that is coupled with segregation in the remaining areas shaped by the advancing eutectic Si-containing interdendritic regions.<sup>16</sup>

The purpose of the present study was to investigate the different aspects involved in the casting of Sr-modified 319 alloys in order to overcome the problems related to the segregation of the  $\text{CuAl}_2$  phase. At the same time, in order to study the role of different alloying elements (e.g., Fe, Sr and P) on the mechanical properties of 319 alloy, tensile and impact tests were carried out.

### 2.6.2 Dissolution and Melting of $\text{CuAl}_2$

Heat treatment is normally employed after the castings have been produced. Different types of heat treatment sequences or tempers are used to attain various mechanical properties.

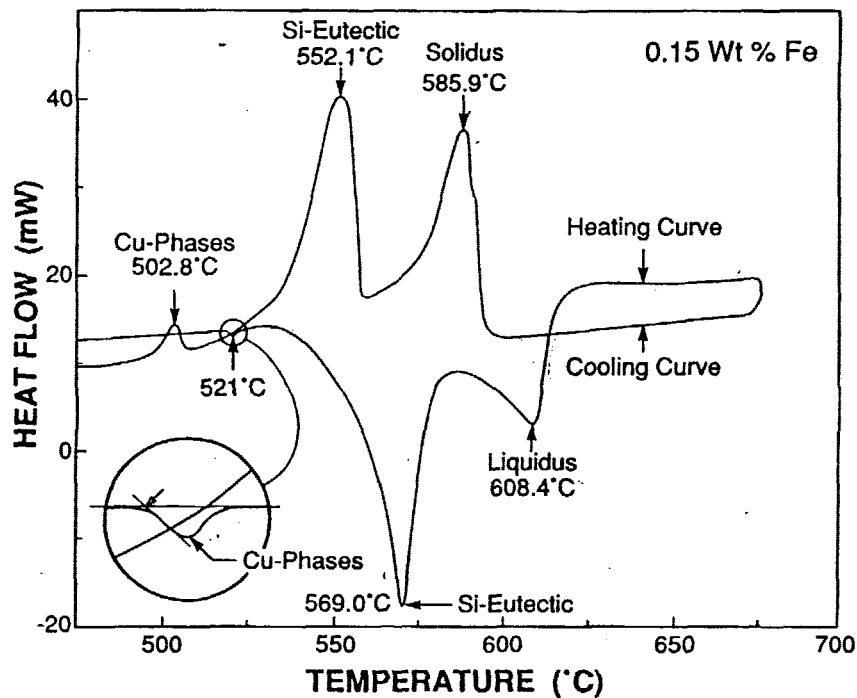


**Figure 2.6.** DSC run for a powdered sample obtained from the experimental 319 alloy solidified at  $10\text{ }^\circ\text{C/s}$ . The open arrow in the enlarged circled area indicates the onset of melting of the  $\text{CuAl}_2$  phase.<sup>31</sup>

In the case of 319 alloy, as Figure 2.6<sup>31</sup> indicates, during heat treatment, when the alloy is heated above 521 °C, the melting of the CuAl<sub>2</sub> phase will be expected to occur. Below this temperature, the CuAl<sub>2</sub> particles undergo dissolution in the Al matrix. Nevertheless, if heated at temperatures below the final solidification temperature, the dissolution of the CuAl<sub>2</sub> phase will be very sluggish.

Samuel *et al.*<sup>31</sup> found that the dissolution of CuAl<sub>2</sub> is accelerated as soon as the solution temperature is increased to 505 °C, where the dissolution exhibits a relatively linear behavior with the solution time. Fragmentation of the CuAl<sub>2</sub> eutectic phase occurs when the alloy is heated to 505 °C for 4 hours and progresses with an increase in solution time. The fragmentation process is followed by the dissolution of the broken particles in the aluminum matrix. At 515 °C, a temperature recommended for solution heat treatment, about 80% of the CuAl<sub>2</sub> has dissolved after 8 hours.

According to the studies of Gauthier *et al.*,<sup>32,33</sup> during solution heat treatment, incipient melting of the CuAl<sub>2</sub> phase can occur when the composition exceeds the critical composition and the 319 alloy is annealed at a temperature higher than the melting point of the eutectic (Al + CuAl<sub>2</sub>), *e.g.*, 540 °C. This results in the formation of a structureless form of the CuAl<sub>2</sub> phase and related porosity on quenching, and a consequent deterioration of the tensile properties.

## 2.7 THE IRON INTERMETALLIC PHASE $\beta$ -Al<sub>5</sub>FeSi PHASE

In addition to silicon structure control, another important consideration from the microstructural point of view is controlling the iron content of the alloy. Together with

aluminum and other alloying elements, iron forms several intermetallic compounds, among which the brittle, plate-like  $\beta$ - $\text{Al}_5\text{FeSi}$  phase is particularly deleterious to the mechanical properties. The plate-like nature of this phase leads to feeding difficulties during solidification, increasing the tendency for porosity formation. So, it is very important to minimize the amount and the size of the  $\beta$ - $\text{Al}_5\text{FeSi}$  phase platelets during solidification.

### 2.7.1 Iron Intermetallics in Al-Si Alloys

The complete literature on intermetallic phases has been reviewed by Pearson.<sup>34</sup> Intermetallic phases in aluminum alloy systems have also been discussed by Mondolfo.<sup>9</sup> The conclusion has been drawn that iron is the most deleterious impurity element normally present in aluminum-silicon alloys. Depending upon alloy composition and solidification conditions, iron can form various intermetallic compounds, such as  $\alpha$ - $\text{Al}_{15}(\text{Fe},\text{Mn})_3\text{Si}_2$  or  $\text{Al}_8\text{Fe}_2\text{Si}$  (in Al-Si-Mg alloys),  $\beta$ - $\text{Al}_5\text{FeSi}$ , or  $\pi$ - $\text{Al}_8\text{FeMg}_3\text{Si}_6$ . Another negative effect of iron is that it reacts with Cu to form  $\text{Cu}_2\text{FeAl}_7$ , thus reducing the effective Cu content of the alloy. As this compound is not affected by solution heat treatment,<sup>35</sup> its formation reduces the amount of Cu available for hardening. Indeed, 1% Fe removes approximately 2% Cu from solid solution.<sup>36</sup>

According to the previously established data, during the solidification process of Al-Si alloys, the formation of  $\beta$ - $\text{Al}_5\text{FeSi}$  depends on the cooling rate of the casting, on the degree of modification of the alloy and the alloying elements, such as Mn and Cr present in the alloy. At cooling rates normally employed in permanent and sand mold castings, the intermetallic compound  $\beta$ - $\text{Al}_5\text{FeSi}$  is generally formed. This compound tends to form hard

brittle platelets (appearing as needles in the microstructure), which have a relatively low bonding strength with the matrix.<sup>37</sup> Due to their brittle nature and under conditions of high stress intensity, these platelets often act as stress raisers and fracture or separate from the aluminum matrix, providing preferential crack paths ahead of the advancing crack, and thereby decreasing the energy required for crack propagation. Thus, the  $\beta$ -Al<sub>5</sub>FeSi intermetallic significantly reduces the ductility and fracture strength of the alloy, the reduction depending on the amount present and on the size and type of crystals existing in the aluminum matrix.<sup>38</sup>

The volume percent and size of the  $\beta$ -platelets formed is strongly dependent on the iron content, solidification rate and melt superheat temperature.<sup>39,40</sup> As the iron content of the alloy increases, the number of  $\beta$ -Al<sub>5</sub>FeSi platelets does not increase appreciably, but their size does. Thus, when the iron content is above 0.7 pct, the  $\beta$ -Al<sub>5</sub>FeSi compound tends to crystallize as extremely large platelets.<sup>41</sup> In general, the length of the  $\beta$ -Al<sub>5</sub>FeSi platelets increases with increasing iron content and decreasing cooling rate.<sup>42</sup>

### 2.7.2 The Formation of the $\beta$ -Al<sub>5</sub>FeSi Phase

The  $\beta$ -Al<sub>5</sub>FeSi crystal phase grows in lateral or faceted crystal growth mode. These crystals are bounded by slowly growing planes of low indices. On the atomic scale, any further atoms from the liquid find few possibilities to join the interface due to these relatively “smooth” surfaces, so their growth is restricted and therefore slow. This type of growth occurs at low driving forces or slow cooling rates, *i.e.* low degrees of undercooling  $\Delta T$ .<sup>43,44</sup>

Cooling rate influences both the formation and size of the  $\beta$ -platelets in the alloy, with hardly any  $\beta$ -platelets being observed in the microstructure obtained at the highest cooling rate (DAS  $\sim 15 \mu\text{m}$ ). As the cooling rate decreases, the  $\beta$ - $\text{Al}_5\text{FeSi}$  platelets are observed in relative abundance (DAS  $\sim 90 \mu\text{m}$ ).<sup>45</sup> The effect of cooling rate on the aspect ratio of  $\beta$ - $\text{Al}_5\text{FeSi}$  platelets has been explained by referring to the growth mechanics of this phase,<sup>46</sup> *i.e.* the phase is non-metallic, and consequently solidifies with a faceted interface, which is comparable to silicon growth in aluminum alloys. However, while silicon has the ability to branch and to keep up with the more kinetically mobile aluminum phase, the  $\beta$ -iron intermetallic does not show any such characteristics and is therefore expected to be overgrown by the aluminum phase.

In a word, a low cooling rate is helpful to the precipitation of the  $\beta$ -phase mainly at grain boundaries, causing serious alloy embrittlement and the  $\beta$ -phase platelets to be thick.<sup>47</sup> By contrast, at high cooling rates, the undercooling developed is large. Thus, the  $\beta$ -phase platelets are fine and well distributed in the microstructure, or the rigid growth of this phase is replaced by the less rigid growth of the script-like  $\alpha$ -iron phase, which has no preferential growth directions.

### 2.7.3 Effect of Sr Addition on the $\beta$ - $\text{Al}_5\text{FeSi}$ Phase

The microstructure of Al-Si alloys often shows the branching of the  $\beta$ -iron platelets, particularly at high Fe content. This is referred to as sympathetic nucleation. The addition of strontium vastly reduces the phenomenon of sympathetic nucleation of the  $\beta$ -phase, through its poisoning action on the  $\beta$ -needle nucleation sites; this reduces the number of

sites available for nucleation, and a lower  $\beta$ -needle density is obtained (albeit somewhat larger-sized needles), compared to that in the unmodified alloy. Dissolution of the  $\beta$ -needles is also observed with strontium addition, resulting in the fragmentation of the needles.

Samuel *et al.*<sup>45</sup> have studied the effect of strontium (Sr) on the formation of the  $\beta$ -phase in 319-type alloys. The addition of 300 ppm Sr seems to accelerate the dissolution of the  $\beta$ -phase through the fragmentation of the long intercepted needles into small pieces. For such concentrations of Sr, the average  $\beta$ -needle length decreases from 130  $\mu\text{m}$  to 70  $\mu\text{m}$ . Thus, Sr can be suggested to act as a  $\beta$ -phase nucleation inhibitor. All of the observations have been supported by the microstructural analysis carried out by Pennors *et al.*<sup>48</sup>

## 2.8 HEAT TREATMENT OF Al-Si ALLOYS

Al-Si-Cu alloys are heat-treated to obtain an optimum combination of strength and ductility. The heat treatment consists of solutionizing at temperatures close to, but below, the eutectic temperature, quenching, and a combination of natural and artificial aging processes. Under practical heat treatment conditions for alloys such as 319, the solutionizing temperature is often selected below 495 °C, *i.e.* the Cu binary eutectic reaction temperature for commercial alloys such as 319 containing Mg and other alloying and impurity elements.

### 2.8.1 Solution Heat Treatment

Solution heat treatment is achieved by heating cast or wrought products to a suitable temperature, holding at that temperature long enough to allow the constituents to enter into

solid solution, and cooling rapidly enough to hold the constituents in solid solution. By cooling with sufficient rapidity, the solid solution formed at a high temperature may be retained in a supersaturated state to minimize the precipitation of the solute atoms as coarse, incoherent particles.<sup>49</sup>

The purpose of solution heat treatment is to put the maximum practical amount of hardening solutes such as copper, magnesium, silicon, or zinc into the solid solution in the aluminum matrix. For some alloys, the temperature at which the maximum amount is soluble corresponds to a eutectic temperature. Consequently, temperature must be limited to a safe level below the maximum to avoid the consequences of overheating and partial melting. The time required for solution heat treatment depends on the type of product, alloy, the casting or fabricating procedure used, and thickness, as it influences the preexisting microstructure. Sand castings are usually held at the solution temperature for about 12 h; permanent mold castings, because of their finer structure, may require only 8 h.<sup>5</sup>

### **2.8.2 Quenching**

Quenching is in many ways the most critical step in the sequence of heat-treating operations. The objective of quenching is to preserve the solid solution formed at the solution heat-treating temperature, by rapidly cooling to some lower temperature, which is usually near room temperature. This operation is applied not only to retain solute atoms in solution, but also to maintain a certain minimum number of vacant lattice sites to assist in promoting the low-temperature diffusion required for zone formation.<sup>50</sup>

In general, the highest strength attainable and the best combinations of strength and toughness are those associated with the most rapid quenching rates. Some exceptions to this rule have been found, for example, the copper-free 7xxx alloys.

### **2.8.3 Precipitation Heat Treatment (Aging)**

Aging practice after quenching affects the combination of strength and ductility or toughness that are developed. A characteristic feature of elevated-temperature aging (artificial aging) effects on tensile properties is that the increase in yield strength is more pronounced than the increase in tensile strength. Alloy hardening and softening attributable to precipitation are illustrated by the isothermal aging curves of Figure 2.7 for T4 heat-treated 2014 alloy.<sup>5</sup> These curves show typical effects of time and temperature that are basic to the heat-treating process and influence the selection of conditions required to achieve various mechanical properties. Some of the important features that can be observed from the figure are as follows:

- (1) Hardening can be greatly retarded or suppressed indefinitely by lowering the temperature;
- (2) The rates of hardening and subsequent softening increase with increasing temperature;
- (3) Over the temperature range in which a maximum strength can be observed, the level of the maximum generally decreases with increasing temperature;
- (4) At sufficiently high temperatures no hardening is observed, and precipitation causes an initial and continued softening.

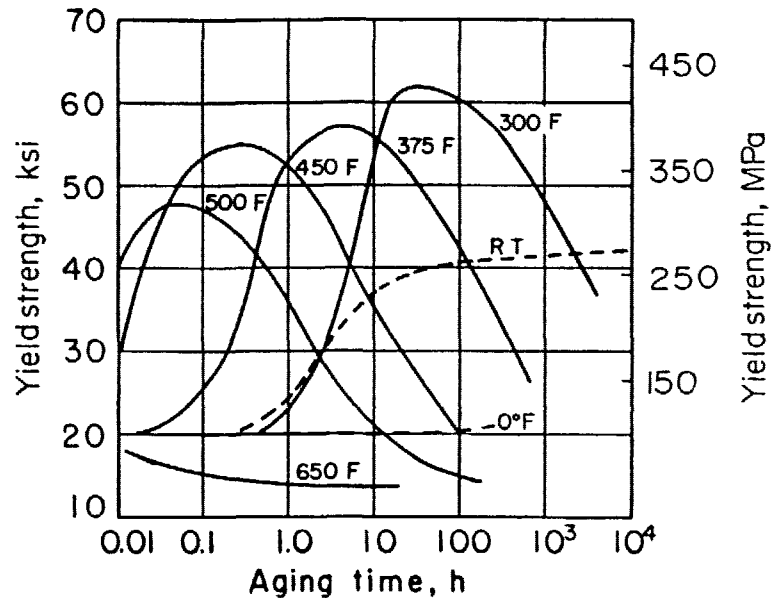


**Figure 2.7.** Representative isothermal aging curves for alloy 2014-T4.<sup>5</sup>

In most precipitation-hardenable systems, a complex sequence of time and temperature-dependent changes are involved. At relatively low temperatures and during initial periods of artificial aging at moderately elevated temperatures, the principal change is a redistribution of solute atoms within the solid-solution lattice to form clusters or GP (Guinier-Preston) zones that are considerably enriched in the solute. This local segregation of solute atoms produces a distortion of the lattice planes, both within the zones and extending for several atom layers into the matrix. With an increase in the number or density of the zones, the degree of disturbance of the regularity and periodicity of the lattice increases. The strengthening effect of the zones results from the additional interference with the motion of dislocations when they cut the GP zones.<sup>5</sup>

The precipitation heat treatment can also reduce the residual stress developed during quenching from solution heat treatment. The degree of relaxation of stresses is highly

dependent upon the time and temperature of the precipitation treatment and alloy composition. In general, precipitation treatments used to obtain the T6 tempers provide only a modest reduction in stresses, ranging from about 10 to 35%.<sup>51</sup>

#### 2.8.4 Effect of Solution Heat Treatment on 319 Alloys

Solution heat treatment in Al-Si-Cu alloys is used to homogenize the alloy, change the morphology of the interdendritic phases and dissolve precipitation-hardening constituents, such as  $\text{CuAl}_2$ ,  $\text{AlMgCu}$ , and  $\text{Mg}_2\text{Si}$ .<sup>52</sup> During solution heat treatment, the Si particles fragment, spheroidize and then gradually coarsen with time.

When the solution heat treatment temperature applied to 319 alloys exceeds the melting point of the copper phase, there will be localized incipient melting of the phase at the grain boundaries, resulting in the formation of shrinkage cavities when the alloy samples are quenched after solution heat treatment. This process is expected to lead to a reduction in the mechanical properties.

Studies by Gauthier *et al.*<sup>32,33</sup> on the solution heat treatment and aging behavior of 319 alloy over a temperature range of 480 °C to 540 °C, for solution times of up to 24 hours, showed that the best combination of tensile strength and ductility was obtained when the as-cast material was solution-heat-treated at 515 °C for 8 to 16 hours, followed by quenching in warm water at 60 °C. A higher solution temperature was seen to result in the partial melting of the copper phase, the formation of a structureless form of the phase and related porosity on quenching, with a consequent deterioration of the tensile properties. A two-stage solution heat treatment suggested by Sokolowski *et al.*<sup>53</sup> is reported to significantly reduce the amount of the copper-rich phase in the 319 alloys, giving rise to

better homogenization prior to aging and improving mechanical properties. Also, Crowell *et al.*<sup>54</sup> stated that the blocky Cu phase in Al-Si-Cu alloys dissolves with increasing solution time at the recommended solution temperature of 495 °C. The rate of dissolution increases with Sr concentration.

## **2.9 TWO IMPORTANT MECHANICAL PROPERTIES — TENSILE AND IMPACT PROPERTIES**

For a special application, the selection of an alloy usually depends on the required mechanical and physical properties. The mechanical properties of aluminum-silicon alloys are strongly dependent on the casting process used, the chemical additions made to control the eutectic structure, primary silicon and grain structure, and the melt treatments used to reduce hydrogen gas content and remove inclusions from the molten metal. Tensile and impact tests are the most commonly used methods to quantify the mechanical properties of aluminum alloys.

### **2.9.1 Tensile Properties**

The engineering tensile test is widely used to provide basic design information on the strength of materials and as an acceptance test for the specification of materials. In the tensile test, a specimen is subjected to a continually increasing uniaxial tensile force while simultaneous observations are made of the elongation of the specimen. An engineering stress-strain curve is constructed from the load-elongation measurements shown in Figure 2.8.<sup>55</sup> The stress used in this stress-strain curve is the *average* longitudinal stress in the tensile specimen. It is obtained by dividing the load by the *original area* of the cross section of the specimen.

$$s = \frac{P}{A_0}$$

The strain used for the engineering stress-strain curve is the *average* linear strain, which is obtained by dividing the elongation of the gage length of the specimen,  $\delta$ , by its original length.

$$e = \frac{\delta}{L_0} = \frac{\Delta L}{L} = \frac{L - L_0}{L_0}$$

Since both the stress and the strain are obtained by dividing the load and elongation by constant factors, the load-elongation curve will have the same shape as the engineering stress-strain curve. So these two curves are frequently used interchangeably.

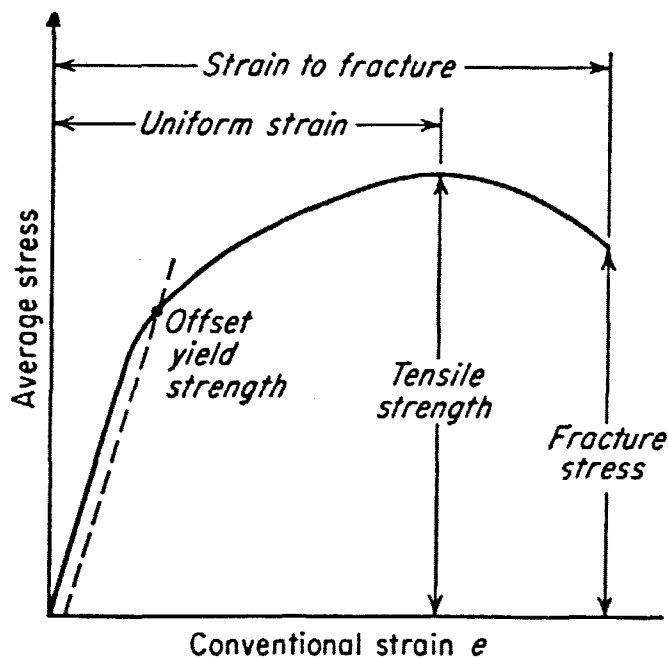


Figure 2.8. The engineering stress-strain curve.<sup>55</sup>

### 2.9.1.1 Effect of alloy composition

For aluminum alloy castings, both copper and magnesium act as the hardening elements. The tensile strengths, or ultimate tensile strengths (UTS), of silicon and aluminum are of the order of 1520 MPa and 546 MPa, respectively. Therefore, parameters such as the percentage of Si, and its shape and distribution, play an important role in determining the mechanical properties. The higher the silicon content, the harder and stronger the Al-Si alloy, but the lower its ductility.

In Al-Si-Mg alloys, Mg combines with Si to form the age-hardening compound  $Mg_2Si$ . The increase in strength with Mg content becomes evident after heat treatment, and the improvement in strength properties is accompanied by a corresponding reduction in ductility. DasGupta *et al.*<sup>56</sup> studied the effect of increasing the magnesium content from ~0.07% to ~0.59% on the mechanical properties of sand-cast 319 aluminum alloy. The authors concluded that an increase in magnesium content in this range has a negligible effect on the mechanical properties of such alloys.

Grand studied the influence of Fe on Al-Si-Cu alloy test bars cast in sand and in shell molds.<sup>35</sup> The results revealed that iron increases hardness but greatly decreases elongation. Also it markedly decreases tensile strength in some cases but not in others. For example, iron from 0.4 to 1.0%, does not affect the castability of Al-12Si-Cu, Al-10Si-4Cu and Al-5Si-4Cu alloys. It does not change the hot-tearing resistance of Al-5Si-4Cu, but decreases that of Al-12Si-Cu and of Al-10Si-4Cu alloys. The author also observed that slow cooling increases the size of the  $Al_5FeSi$  particles if enough Fe is present, and that such particles may develop to the point where they will reduce feeding and thus the soundness of the

casting. Dornauf<sup>57</sup> states that, in Al-Si alloys, Fe up to 0.8% does not appreciably affect the tensile strength, but with over 1% of Fe, the tensile strength and ductility are drastically reduced. However, at all concentrations, Fe drastically reduces elongation.

### **2.9.1.2 Effect of solidification time**

Solidification times have a strong influence on the microstructure, especially in terms of the resulting secondary dendrite arm spacing (SDAS, commonly also referred to simply as DAS), intermetallic content, and the porosity size and distribution. Thus, they have a large effect on the ultimate tensile strength and ductility of the aluminum alloy. In general, all of the mechanical properties decrease as solidification time increases.

According to the study of Meyer *et al.* on 319 alloy,<sup>58</sup> as the DAS increased, the tensile strengths and ductility decreased. In one case, for samples with a peak-aged (T64) heat-treatment, increasing the DAS from 20 to 50  $\mu\text{m}$  caused a 20% decrease in the UTS and YS and a 15% decrease in the ductility. Similar trends were found for the tensile properties in 319.2 alloy,<sup>59</sup> in this study, as the DAS increased from 28 to 95  $\mu\text{m}$ , the UTS decreased by  $\sim 20\%$ , while the elongation decreased by as much as 80%. However, the yield strength was observed to remain constant regardless of solidification time.

### **2.9.1.3 Effect of heat treatment**

Meyer *et al.*<sup>58</sup> also revealed that heat-treatment had an effect on the tensile properties of 319 alloy. For example, changing from the no heat-treatment to peak-aged condition caused a 25-45% increase in UTS, 30-35% increase in 0.2% YS, and up to a 25% increase in ductility, depending upon the DAS of the tested alloy sample.

Another study<sup>54</sup> examined the effect of solution time on the room temperature tensile properties of a high Si (~ 8%) 319 alloy. In this study, separately-cast tensile bars in the T6 heat-treated condition were employed. It was found that, as the solution time was increased from 2 to 64 hours at 495 °C, the tensile strengths increased slightly (UTS by ~10%, YS by ~7%) while the ductility was substantially increased (~40%). This study also examined the effect of a 505 °C solution temperature on the resulting room temperature tensile properties. As the solution treatment time increased from 2 to 20 hours at 505 °C, there was a significant decrease in all the tensile properties, especially the ductility (~91% decrease). The cause of the decrease was found to be incipient melting of the CuAl<sub>2</sub> phase, which flowed to and weakened the grain boundaries in the 319 Al alloy.

The effect of solution time and temperature on the room temperature tensile properties of 319.2 aluminum alloy were also studied by Gauthier *et al.*,<sup>32</sup> using separately-cast tensile bars with an DAS range of 20 ~ 30 μm. As the solution time was increased from 0 to 4 hours at 490 °C, the UTS increased slightly (~16%) while the ductility was substantially increased (~70%); no improvement was seen in the yield strength. Further, as the solution time was increased from 4 to 24 hours, no improvements were observed in any of the tensile properties. Unlike the results reported in reference [54], increasing the solution temperature to 505 °C did not cause a decrease in the tensile properties for times up to 24 hours; improvements in tensile properties were noted until the solution temperature reached 515 °C.

In the second part of their study, Gauthier *et al.*<sup>33</sup> focused on the effect of aging time and temperature on the 319.2 alloy, (separately-cast tensile bars with a DAS range of 20 ~

30  $\mu\text{m}$  were again employed). They found that as aging temperature increased from 155 to 220 °C, the time needed to obtain peak tensile strengths decreased from 24 to 2 hours. Both Gauthier *et al.*<sup>33</sup> and DasGupta *et al.*<sup>56</sup> observed that the tensile yield strength is more sensitive to changes in aging time and temperature compared to the ultimate tensile strength.

#### 2.9.1.4 Effect of modification

Regardless of casting conditions, a significant improvement in the ultimate tensile strength and a substantial increase in elongation can be achieved with Sr modification. In unmodified as-cast Al-Si alloys, coarse, acicular plates of silicon act as internal stress builders in the microstructure and provide easy paths for fracture. After modification with sodium or strontium, these silicon particles are transformed or “modified” to a finer, fibrous form. In this case, the tensile properties of the modified alloys are affected appreciably by the fibrous morphology of the eutectic Si particles.

Hafiz *et al.*<sup>60</sup> pointed out that for steel mold-cast Al-Si alloy, the ultimate tensile strength was improved from 177.2 MPa for non-modified alloy to 225.6 MPa for the modified one (0.024 mass% Sr). In addition, percent elongation increased dramatically from 8.03% in the non-modified state, to 18.2% with 0.012 mass% of Sr addition, and a value of 22.2 at a strontium level of 0.024 mass%. In contrast, the ultimate tensile strength and elongation of graphite mold-cast Al-Si alloy showed increases of about 21.8% and 266.3%, respectively, due to a Sr addition of  $\sim 0.028$  mass%. The remarkable improvement in elongation associated with the addition of strontium can be related to its effect on the microstructure of the Al-Si alloy.

## 2.9.2 Impact Properties

The impact strength is of importance in certain applications and can provide a useful estimation of the ductility of an alloy under conditions of rapid loading. The Charpy impact test measures the energy absorbed by the high strain rate fracture of a standard specimen. The specimen is broken by the impact of a heavy pendulum hammer, falling through a fixed distance (constant potential energy) to strike the specimen at a fixed velocity (constant kinetic energy). Tough materials absorb a lot of energy when fractured, and brittle materials absorb very little. The Charpy impact energy therefore includes the elastic strain energy, the plastic work done during yielding and the work done to create the fracture surface. The elastic energy is usually not a significant fraction of the total energy, which is dominated by the plastic work. The total impact energy depends on the size of the test specimen.

### 2.9.2.1 Effect of alloy composition

Komatsu *et al.*<sup>61</sup> reported that the impact strength of as-cast Al-Si alloys decreased with increasing Si content. Tsukuda *et al.*<sup>62</sup> studied the impact strength of an Al-Si-0.15%Sb alloy containing different amounts of Si from 1% to 13%. They found that the Charpy impact value decreased rapidly at Si contents of 6% to 8% or more. The effects of Mg and Fe on the impact strength of Al-7%Si-Mg alloy were also investigated. Increase in Mg levels up to 0.4% rapidly decrease the impact strength in both the as-cast and T6 conditions. The impact strength is exponentially reduced as the Fe content increases. The latter results were confirmed by Voren *et al.*<sup>40</sup> who found that the fracture toughness (calculated from the Charpy energy) increases with a decrease in the iron content.

### 2.9.2.2 Effect of solidification time

Impact strength is drastically affected by the fact that the solidification time essentially controls the secondary dendrite arm spacing (DAS) and the silicon particle morphology.

Boileau *et al.*<sup>63</sup> showed that a three-fold decrease in fatigue life of A356-T6 was observed when the solidification time increased from 40 seconds (~30  $\mu\text{m}$  DAS) to 1290 seconds (~90  $\mu\text{m}$  DAS).

Clearly, an increased solidification rate has a beneficial effect on impact value. This is why we can notice that a metallic mold-cast sample has a higher impact energy than a sand-cast one. Richard<sup>64</sup> reported that impact strength is more sensitive to very small variations in the microstructure than elongation. Similar observations were made by Tsukuda<sup>65</sup> who indicated that impact values were more sensitive to the as-cast microstructure of Al-Si alloys than were the tensile test results.

### 2.9.2.3 Effect of heat treatment

Various heat treatment procedures will produce a wide range of mechanical and physical properties. In the two main aluminum alloys, 356 and 319, the uniform distribution and dissolution of  $\text{Mg}_2\text{Si}$  and  $\text{CuAl}_2$ , respectively, can be obtained through a solution heat treatment, quenching, and aging procedure. As a result, the impact energy can be increased greatly.

Komatsu *et al.*<sup>61</sup> reported that the impact strength of heat treated Al-Si alloys remained constant in the range of 5~12%. Drouzy *et al.*<sup>66</sup> found that the cooling rate of the hypereutectic alloy specimens from the solution heat treatment temperature (*i.e.* quenched

in water or cooled inside the furnace) affected the impact energy. In the case of both unmodified and modified samples, the values were higher for samples which had been solution heat-treated, with the highest values obtained for the samples which were furnace cooled. Tsukuda *et al.*<sup>67</sup> Examined the impact energies of Al-6.85%Si-0.30%Mg-0.20%Fe-0.12%Ti-0.006%Na alloy castings in the T6 conditions. The Charpy impact energy value was reduced by quenching in hot water or quenching after prolonged delay over time. From these results, the optimum solution heat treatment was identified as 9 hours at 540 °C, followed by quenching in cold water (15 °C) as soon as possible. Aging parameters (time and temperature) also influenced the impact strength, and aging at 140 °C for 4 hours was recommended.

#### 2.9.2.4 Effect of modification

Strontium is commonly added to most Al-Si alloys as a modifier for the eutectic silicon to obtain a finely dispersed eutectic structure. According to the research of Shivkumar *et al.*,<sup>68</sup> in the as-cast condition, strontium modification increases the impact energy from 1.1 J to 2.3 J in sand castings. Similarly, in metallic mold castings, the impact energy of the as-cast alloy increases from 2 J to 10.8 J upon strontium modification.

Closset *et al.*<sup>69</sup> found that modification improved the unnotched impact strength of both as-cast and heat-treated A356.0 and 413.0 alloys. For the as-cast A356.0 alloy, the impact value increased from 9.5 J/cm<sup>2</sup> for an unmodified structure (0% Sr) to 18.7 J/cm<sup>2</sup> for a modified structure (0.016% Sr), *viz.*, an improvement of 96% was achieved with modification. The increase was 40%, from 23.7 J/cm<sup>2</sup> at 0% Sr to 33.7 J/cm<sup>2</sup> at 0.02% Sr

for samples solution heat treated for 13 hours at 538 °C and artificially aged at 154 °C for 8 hours.

#### **2.9.2.5 Effect of porosity**

Several researchers<sup>70,71</sup> studied the effect of porosity on the fatigue properties of an A356 alloy and concluded that the pore size had a greater effect on fatigue life than the pore volume fraction. It was found that, while fatigue life was sensitive to the maximum pore size, no relationship between pore size (as observed on random metallographic surfaces) and fatigue life was obtained. Boileau *et al.*<sup>63</sup> found that porosity had a more profound effect on the fatigue life of the A356-T6 alloy. Samples with internal porosity had an approximate ten-fold decrease in fatigue life compared to porosity-free samples.

In their study, Skallerud *et al.*<sup>72</sup> showed that multiple small pores located close together (~0.7 mm apart) could initiate failure just as frequently as a single, large pore. They found that cracks initiate from each of the pores and grow in a manner that allows the individual cracks to combine into one large crack that eventually causes final failure. They also classified the porosity according to the importance in initiation as follows: a single shrinkage pore close to or at the surface being the most critical and a series of shrinkage pores at the surface or a gas pore at the surface being the least critical. The effect of porosity on fatigue life was summarized as follows: pores reduce the time of crack initiation by creating a high stress concentration in the material adjacent to the pores. Because of this, most of the fatigue life is spent in crack growth.

## 2.10 FRACTOGRAPHY

Fractography is defined as the study and documentation of fracture surfaces. The purpose of fractography is to analyze the fracture features and to attempt to relate the topography of the fracture to the causes and/or basic mechanisms of fracture.<sup>73</sup> The knowledge of fracture behavior is important in upgrading material specifications, improving product design, and analyzing failures for improved reliability.<sup>74</sup>

A study of the characteristics of fracture surfaces is often carried out using optical microscopy. However, when very fine details of the fracture surface, *e.g.*, dimples and microvoids are required to be observed, a scanning electron microscope (*viz.*, SEM fractography) is employed instead. The choice of using a scanning electron microscope for fractography studies is generally made due to the fact that it allows for a direct examination of the fracture surface without the need for a replica, as in the case of transmission electron microscopy (TEM). One of the great advantages of the SEM is its ability to examine specimens at low magnifications of about 50 diameters, and then enlarge regions of special interest to very high magnifications.

### 2.10.1 Fracture Behavior of Al-Si Base Alloys

Four major types of fracture (or failure) modes have been discussed in the literature. Briefly, these modes and the sources of their occurrence are as follows:<sup>74</sup>

- (1) Dimpled rupture (or microvoid coalescence) caused by ductile fracture or rapid overload fracture;
- (2) Cleavage or quasi-cleavage caused by brittle fracture or premature or overload failure by catastrophic rapid fracture;

- (3) Intergranular fracture caused by stress corrosion cracking, hydrogen embrittlement, or subcritical growth under sustained load; and
- (4) Ductile striations caused by fatigue cracking or subcritical growth under cyclic load.

Figure 2.9 shows the two main types of fracture observed in Al-Si alloys under tensile overloading. Figure 2.9(a) illustrates a rupture mode of fracture, where the particles are observed at the bottom of the dimples. These particles are seen to have decohered from the surrounding matrix. Figure 2.9(b) represents an example of the cleavage fracture of intermetallics. Cleavage is a low-energy fracture that propagates along well-defined low-index crystallographic planes known as cleavage planes. As Al-Si alloys are complicated combinations of various microconstituents after solidification, their fracture behavior is affected by the microstructural features of these constituents, *i.e.*, Si particles, iron and other intermetallic phases, and the solidification rate, *etc.*

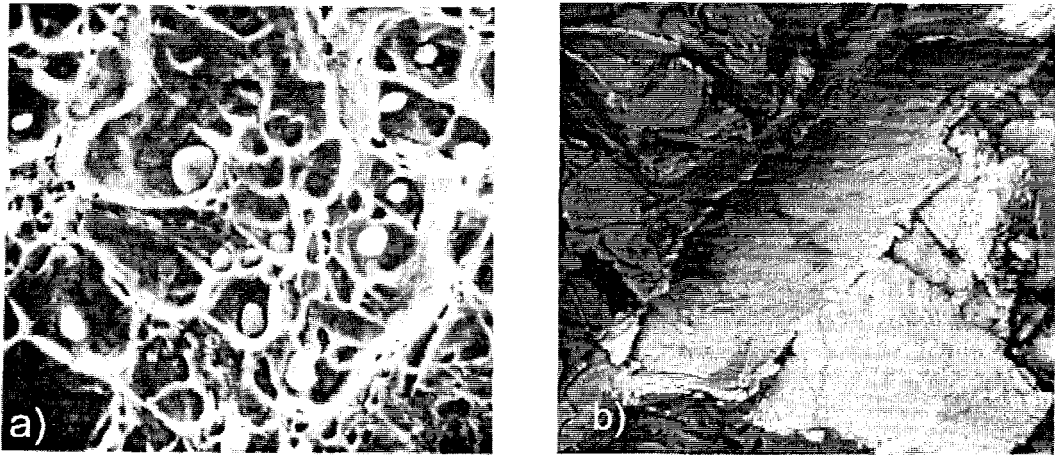


**Figure 2.9.** Two main types of fracture observed in Al-Si alloys under tensile overloading: (a) Dimple rupture<sup>75</sup> and (b) cleavage fracture of intermetallics.<sup>76</sup>

### 2.10.1.1 Effect of Si particles

Voigt and Bye<sup>77</sup> studied the fracture behavior of Al-Si-Mg (A356) alloys using tensile samples of different section sizes and under different conditions (as-cast/heat-treated, unmodified/Sr-modified). Cracks were found to initiate with the fracture of Si particles at relatively low strain values. Crack propagation also proceeded by the same mechanism, preferably through the eutectic region of the microstructure, avoiding the primary  $\alpha$ -Al dendrite cores where possible. Continued strain resulted in localized plastic deformation around the fractured Si particles, which eventually led to the formation of microcracks in the eutectic region.

According to the study of Hafiz and Kobayashi<sup>10</sup>, in general, the voids formed as a result of the decohesion of non-fractured Si particles from the surrounding matrix were found to initiate on silicon particles. The individual voids then grew and coalesced, creating microcracks in the eutectic region. These microcracks linked up to form the main crack, resulting in the final fracture.

### 2.10.1.2 Effect of iron intermetallics

Hrong *et al.*<sup>78</sup> studied the fracture behavior of A356 alloys with different iron contents under resonant vibration. According to them, the cracks were found to initiate and grow along the eutectic Si and Fe-rich intermetallic particles. The crack paths propagated predominantly through the Si particles and occasionally through the Fe-rich intermetallics. When the iron content was above 0.57 wt%, the Fe-intermetallics occurred mostly as  $\beta$ - $\text{Al}_3\text{FeSi}$ , which was found to be detrimental to the fracture resistance.

Kato<sup>79</sup> examined the microstructure of Al-7%Si-1%Fe alloys during tensile deformation and found that the plate-like  $\beta$ -iron intermetallics are cracked easily in the earlier stages of deformation, whereas the  $\alpha$ -iron Chinese script intermetallics can withstand a higher stress. Villeneuve and Samuel<sup>80</sup> found that in Al-13%Si-Fe alloy castings, cracks appeared within the  $\beta$ -Al<sub>5</sub>FeSi platelets rather than at the  $\beta$ /Al interface. This is due to the brittle nature of the  $\beta$ -phase, whereby the platelets are easily split into two halves. They also observed that in Al-Si-Cu (319) cast alloys, fragmentation of the  $\beta$ -Al<sub>5</sub>FeSi needles (with the addition of Sr, or Sr + Be) or their transformation into  $\alpha$ -Al<sub>15</sub>(Fe,Mn)<sub>3</sub>Si<sub>2</sub> in the form of Chinese script (with Mn/Fe ratio ~0.7) or sludge (with the addition of 1% Cr) results in a dimpled rupture surface.<sup>81</sup>

#### 2.10.1.3 Effect of solidification rate

The work of Cáceres *et al.*<sup>82</sup> on the fracture behavior of A356 casting alloy shows that under low cooling rate conditions, when coarse structures are observed, the cell boundaries are distinct, the cracked particles are located with equal probability in the cell and grain boundaries, and the fracture mode is of a transgranular type. At a high cooling rate (*viz.*, in fine structures), the cracked particles are preferentially located in the grain boundaries, and the fracture mode is of an intergranular type.

The research studies of Wang *et al.*<sup>83</sup> show that in large cell-size material, the fracture tends to occur along the dendritic cell boundaries (transgranular fracture), whereas in smaller cell-size material, the fracture path runs along grain boundaries in an increasing proportion (intergranular fracture).

Samuel *et al.*<sup>84</sup> found that, even though the Sr-modified eutectic silicon microstructure is considerably finer than the unmodified one, the pre-fracture and fracture events observed in the modified alloys are similar to those observed in the unmodified case. However, the amount of strain required for microcrack initiation and propagation is increased with Sr modification.

## **CHAPTER 3**

### **SEGREGATION AND DISSOLUTION OF THE $\text{CuAl}_2$ PHASE**

## CHAPTER 3

### SEGREGATION AND DISSOLUTION OF THE $\text{CuAl}_2$ PHASE

#### 3.1 INTRODUCTION

Strontium (Sr) is commonly added to Al-Si casting alloys in very small amounts to modify the eutectic silicon morphology from a coarse, flake-like form to a fine fibrous one. The change in the Si morphology, in turn, enhances the mechanical properties, particularly ductility.<sup>15</sup> However, it has been observed that the presence of Sr also leads to the segregation of the copper phase in areas away from the Al-Si eutectic regions during the solidification process, resulting in slowing its dissolution during solution heat treatment. Also, due to the segregation, the  $\text{CuAl}_2$  phase precipitates in the blocky form rather than in the fine eutectic form. Thus, the addition of strontium leads to an increase in the amount of blocky type  $\text{CuAl}_2$  observed in the structure.<sup>85</sup> Compared with the eutectic-like copper phase, the blocky  $\text{CuAl}_2$  particles are more difficult to dissolve into the aluminum matrix during solution heat treatment.

Iron is the most common and detrimental impurity in cast aluminum, which forms hard, brittle intermetallic phases that reduce ductility and, to a lesser extent, strength. The most detrimental Fe-rich phase is  $\beta\text{-Al}_5\text{FeSi}$ , which occurs as platelets. In addition to acting

as stress raisers in the matrix, the  $\beta$ -phase also increases porosity by blocking feeding channels between solidifying dendrites. The resulting porosity decreases fatigue strength.<sup>86</sup>

Kato *et al.*<sup>87</sup> clarified the effect of the phosphorus as a site of heterogeneous nucleation during the Al-Si hypoeutectic solidification. The coarse needle-like silicon particles are nucleated on the AlP microconstituents. And the solidification time becomes shorter by the addition of phosphorus than that of without phosphorus. If phosphorus is contained in the molten metal, the quantity of the primary crystal of  $\alpha$ -dendrite increases, whereas the length of it is short. So the microstructure of eutectic silicon depends on the level of phosphorus content.

When the solution temperature applied to 319 alloys exceeds the melting point of the  $\text{CuAl}_2$  phase, one problem associated with the homogenization process is localized incipient melting of the phase at the grain boundaries, resulting in the formation of shrinkage cavities when the alloy samples are quenched after solution heat treatment. The plastic deformation of the 319 alloys in this condition is problematic due to low ductility. As mentioned in the literature survey, studies by Gauthier *et al.*<sup>32,33</sup> on the solution heat treatment and aging behavior of 319 alloys over a temperature range 480 °C – 540 °C, for solution times of up to 24 hours, showed that the best combination of tensile strength and ductility was obtained when the as-cast material was solution-heat-treated at 515 °C for 8 – 16 hours, followed by quenching in warm water at 60 °C. A higher solution temperature was seen to result in the partial melting of the copper phase, the formation of a structureless form of the phase and related porosity on quenching, with a consequent deterioration of the tensile properties. A two-stage solution heat treatment suggested by Sokolowski *et al.*<sup>53</sup> is

reported to significantly reduce the amount of the copper-rich phase in 319 alloys, giving rise to better homogenization prior to aging, and improving the mechanical properties.

A part of the present study was undertaken to investigate the precipitation behavior of the  $\text{CuAl}_2$  phase in various 319-type alloys containing Sr, Fe and P, individually or in combination, and its dissolution during solution heat treatment at 505 °C for times up to 100 h. The solution temperature was selected as 505 °C because it is in the temperature range suggested by Gauthier *et al.* and is lower than the melting temperature of  $\text{CuAl}_2$  phase (~507 °C). And the times were ranged from 0 to 100 h to cover a wide range of dissolution degree.

### 3.2 EXPERIMENTAL PROCEDURE

Measured quantities of pure aluminum, silicon and Al-33% Cu master alloy were used to prepare the experimental Al-7% Si-3.5% Cu base alloy. The melting temperature was kept at 725 °C  $\pm$  5 °C. Prior to casting, the melt was degassed for ~15 minutes to remove the hydrogen and the inclusions. And then the melt was poured into ingots. The chemical composition is shown in Table 3.1.

The base alloy ingots were cut into small pieces, dried, and melted in a 1-kg capacity SiC crucible, heated by means of an electric resistance furnace. The melting temperature was kept at 725 °C  $\pm$  5 °C. Strontium was added in the form of an Al-10% Sr master alloy (~ 200 ppm). Iron was introduced in the form of an Al-25% Fe master alloy. The melt was degassed for ~15 minutes to ensure homogeneous mixing of the additions. The different experimental alloys and their respective codes are listed in Table 3.2.

**Table 3.1.** Chemical compositions (wt%) of the experimental base alloy (coded ASC) and industrial 319 alloy

Alloy	Element Concentration (wt%)					
	Si	Fe	Cu	Mn	Mg	Zn
ASC	6.50	0.1245	3.054	<0.0005	0.0018	<0.0017
319 alloy	5.95	0.11	3.56	0.02	0.043	<0.01
	Al	Cr	Ti	Sr	B	Ni
ASC	90.3	<0.0005	<0.0013	<0.0000	<0.0002	<0.0016
319 alloy	90.16	0.001	0.145	–	–	0.01

Similar experiments were carried out using industrial 319 alloy, the chemical composition of which is also shown in Table 3.1. In this case, phosphorus was also added (in addition to Sr and Fe) using Cu-8% P brazing alloy. The corresponding alloy codes are shown in Table 3.2.

**Table 3.2.** List of the alloys used in the present work and their respective codes

Alloy Type	Alloy Code	Nominal Composition
Experimental Alloy	ASC	Al-7%Si-3.5%Cu (Base Alloy)
	ASCS	Base Alloy + Sr*
	ASCF	Base Alloy + 1%Fe
	ASCFS-1	Base Alloy + 0.9%Fe + Sr
	ASCFS-2	Base Alloy + 1.2%Fe + Sr
Industrial Alloy	H4T1	319 Alloy + Sr + 60 ppm P
	H20T1	319 Alloy + Fe + Sr + 90 ppm P

\* Sr additions: 150-200 ppm.

In order to determine the possible reactions that could take place during solidification under conditions close to equilibrium ( $\sim 0.8 \text{ }^\circ\text{C s}^{-1}$ ), the liquid metal was poured into a

graphite crucible (length: 10 cm, diameter: 6 cm) that was preheated to 600 °C. Thermal analysis was carried out simultaneously, using a K-type thermocouple (chromel-alumel) placed vertically within the mold (through a hole in the bottom of the mold) with its tip at ~30 mm above the bottom, and interfaced with a computer as shown in Figure 3.1.

The temperature-time data was recorded by means of a data acquisition system attached to the computer (at a rate of 0.2 sec). From the thermal analysis data, the cooling curves and their first derivatives were plotted using Microsoft Excel software. Samplings for chemical analysis were also taken simultaneously for each melt condition. The actual alloying element additions for the various alloys, as obtained from the chemical analysis are listed in Table 3.3.

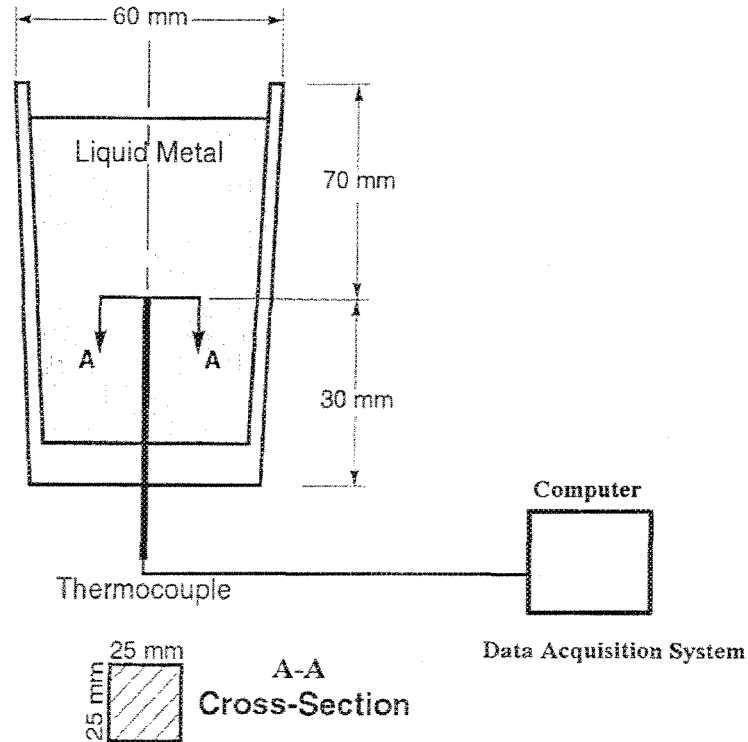


**Figure 3.1.** Schematic diagram of the graphite mold used for thermal analysis.

**Table 3.3.** Actual alloying element additions (wt%) in the alloys studied obtained from chemical analysis

Alloy Code	Main Alloying Elements (wt%)			
	Cu	Fe	Sr	P
ASC	3.054	0.1245	<0.0000	–
ASCS	2.990	0.1190	0.0060	–
ASCF	2.970	1.015	<0.0000	–
ASCFS-1	3.080	0.862	0.0063	–
ASCFS-2	2.820	1.200	0.0140	–
H4T1	3.56	0.11	0.0140	0.0019
H20T1	3.39	0.68	0.0126	0.0033

Eight samples (2.5 cm x 2.5 cm) for metallographic examination were sectioned from each alloy casting (from a bigger section sliced from the central part containing the thermocouple tip). One of these (as-cast condition) was mounted in bakelite, and polished to a fine finish (1 $\mu$ m diamond paste). The other samples were solution heat-treated at 505 $^{\circ}$ C in a forced-air furnace (where the temperature could be controlled to within  $\pm 2$   $^{\circ}$ C) for different solution times, *i.e.*, 4, 8, 12, 24, 48, 72 and 100 hours. After solutionizing, the samples were immediately quenched in warm water ( $\sim 60$   $^{\circ}$ C) to stop any further reaction of the copper phase. These samples were then mounted and polished. Optical micrographs were taken at magnifications of 200X and 750X for each sample.

Microstructural changes were examined and quantified using a Leco 2001 image analyzer in conjunction with the optical microscope (Olympus PMG3), to measure the amount of the undissolved CuAl<sub>2</sub> phase following the different solution treatment times applied. For every sample, fifty fields were measured over the entire sample surface (in a

systematic fashion) and the percentage area of the  $\text{CuAl}_2$  phase was measured in each field. From these readings, the average area percent of the undissolved  $\text{CuAl}_2$  phase was determined for the corresponding sample. In addition, the dissolution behavior was also studied using a JEOL electron probe microanalyzer (EPMA, model JXA-8900R) equipped with energy dispersive X-ray (EDX) and wavelength dispersion spectroscopy (WDS) facilities, operating at 20 kV (the size of the analyzed zone was  $\sim 2 \mu\text{m}$ ).

### 3.3 RESULTS AND DISCUSSION

#### 3.3.1 Thermal Analysis

From the first derivative curves obtained from the cooling curves of each of the alloys studied, the precipitation temperatures of the  $\text{Al}+\text{CuAl}_2$  eutectic were noted and are listed in Table 3.4. The precipitation temperature of the  $\text{CuAl}_2$  phase in the ASCF alloy (containing 1 wt% Fe) is lower than those obtained in the Sr-containing or (P+Sr)-containing alloys (*viz.*, ASCS, H4T1, H20T1 alloys). This difference can be due to the fact that the  $\beta\text{-Al}_5\text{FeSi}$  phase precipitates first at  $\sim 564^\circ\text{C}$ , before the  $\text{Al}+\text{CuAl}_2$  eutectic reaction, which could lead to an increase in the nucleation sites for the copper phase.

The cooling curves and first derivatives obtained from ASC, ASCS and ASCF alloys are shown in Figure 3.2, while the corresponding reactions expected to occur are listed in Table 3.5 (based on Bäckerud *et al.*<sup>3</sup>). Apparently, the precipitation of the  $\beta$ -iron phase prevents the segregation of the  $\text{CuAl}_2$  phase through its nucleation along the long sides of the  $\beta$ -phase platelets. This mechanism of precipitation may explain why the precipitation temperature of  $\text{CuAl}_2$  is low in the ASCF alloy. In the Sr-modified base alloy (*viz.*, ASCS

**Table 3.4.** Precipitation temperatures of the Al+CuAl<sub>2</sub> eutectic in the alloys studied

Alloy Code	Temperature (°C)
ASC	509
ASCS	516
ASCF	509
ASCFS-1	516
ASCFS-2	515
H4T1	517
H20T1	518

alloy), however, the solidification temperature increases to 516 °C, where the strontium pushes the (Al+CuAl<sub>2</sub>) eutectic particles away from the well-modified silicon particles *i.e.*, segregates them into clusters. In this case, the CuAl<sub>2</sub> particles solidify earlier compared to the base alloy (*viz.*, ASC alloy). At the same time, it is interesting to note that the precipitation temperature of CuAl<sub>2</sub> is almost stable even when iron and phosphorus are added to the Sr-modified base alloy (*cf.* ASCS and ASCFS alloys). Thus, it can be reasonably deduced that the modification function of strontium is fundamental in Al-Si-Cu 319-type alloys, as it is observed to dominate the segregation of the copper phase in all the alloys studied.

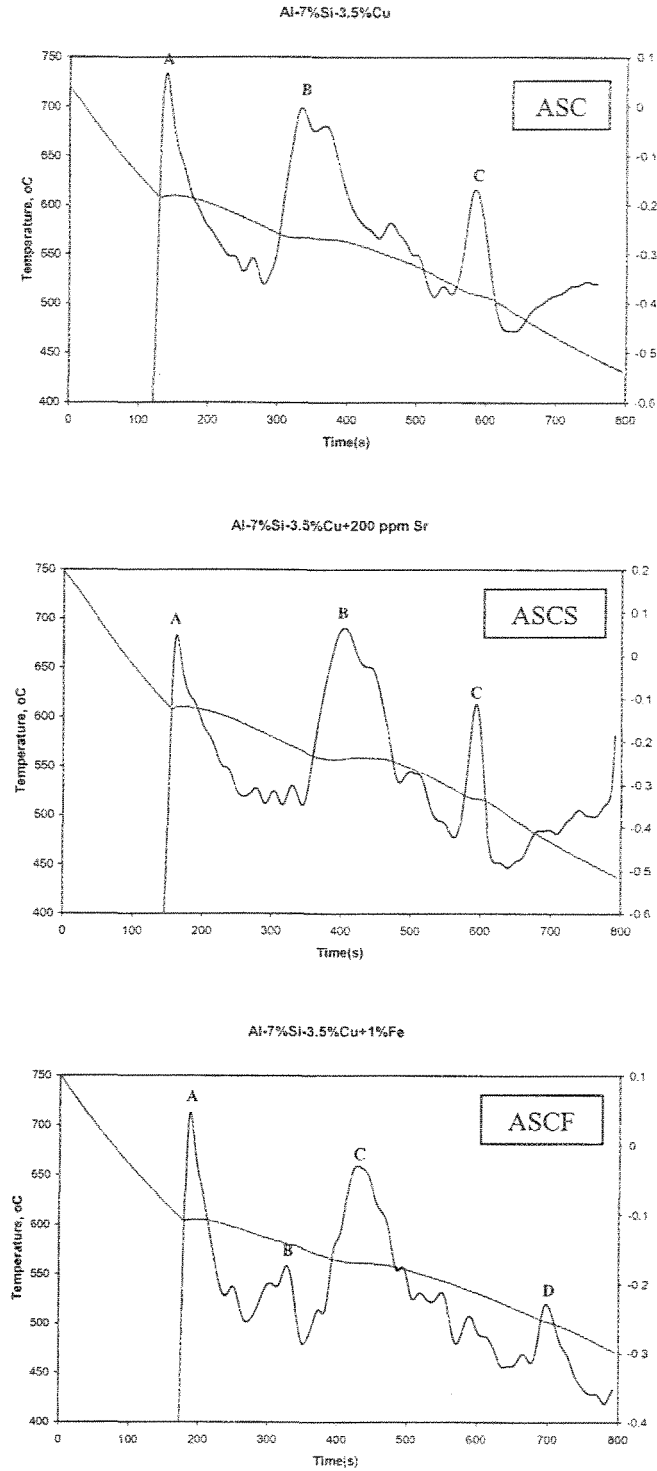


**Figure 3.2.** Cooling curves and first derivatives obtained from ASC, ASCS and ASCF alloys.

**Table 3.5.** Expected reactions in ASC, ASCS and ASCF alloys

Alloy Code	Peak	Temperature (°C)	Reaction <sup>3</sup>
ASC	A	608	Precipitation of $\alpha$ -Al dendrite network
	B	566	Al-Si eutectic reaction
	C	509	Al-CuAl <sub>2</sub> eutectic reaction
ASCS	A	609	Precipitation of $\alpha$ -Al dendrite network
	B	558	Al-Si eutectic reaction
	C	516	Al-CuAl <sub>2</sub> eutectic reaction
ASCF	A	605	Precipitation of $\alpha$ -Al dendrite network
	B	581	Precipitation of $\beta$ -Al <sub>5</sub> FeSi phase
	C	564	Al-Si eutectic reaction
	D	509	Al-CuAl <sub>2</sub> eutectic reaction

### 3.3.2 Optical Microscopy

Figure 3.3(a) shows the as-cast microstructure of the base ASC alloy, in which the copper phase is seen mainly as small pockets of the (Al+CuAl<sub>2</sub>) eutectic or the blocky CuAl<sub>2</sub> phase, nucleating on preexisting particles, *i.e.* coarse Si particles or  $\beta$ -Al<sub>5</sub>FeSi platelets. Similar observations have been reported by Samuel *et al.*<sup>31</sup> The arrows marked B and C indicate two instances of such Si particle nucleation sites on which the (Al+CuAl<sub>2</sub>) particles are seen to occur. A high magnification micrograph, Figure 3.3(b), shows the details of the (Al+CuAl<sub>2</sub>) eutectic particle marked A in Figure 3.3(a). When strontium is added to the alloy (*viz.* ASCS alloy), the eutectic silicon particles become much finer compared to those observed in the base alloy, Figure 3.4. The addition of Sr also leads to the clustering of the CuAl<sub>2</sub> particles in regions away from the growing Al-Si eutectic colonies. Figure 3.4 depicts that the CuAl<sub>2</sub> phase solidifies in the blocky form rather than in the eutectic one due to Sr-modification.

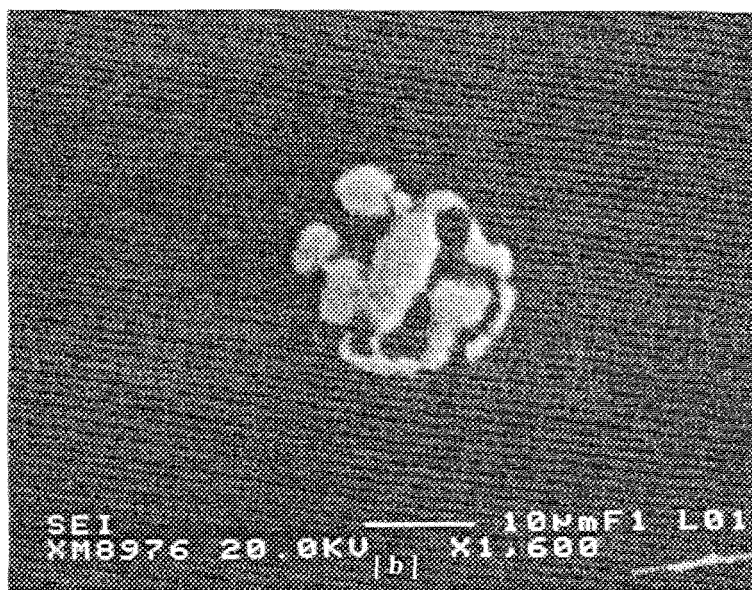
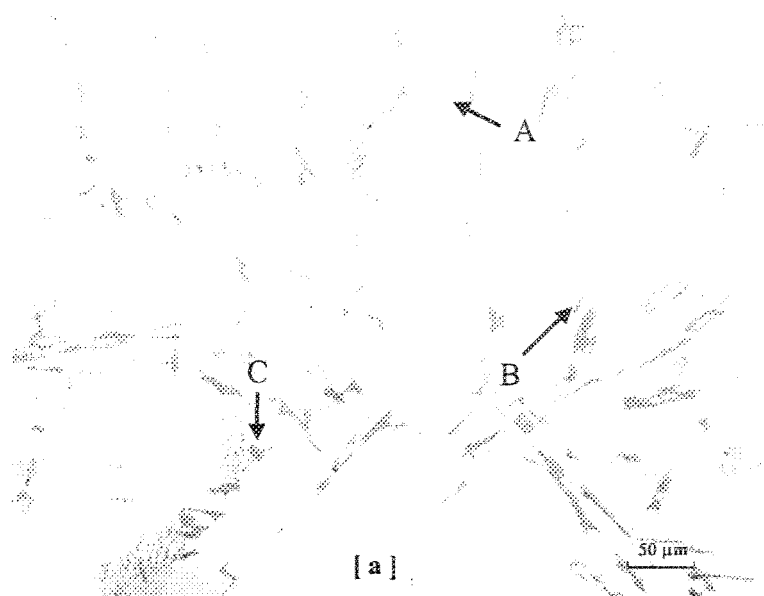


**Figure 3.3.** (a) Microstructure of the experimental base alloy (ASC) in the as-cast condition; (b) High magnification micrograph showing the eutectic-like copper phase marked A in (a).

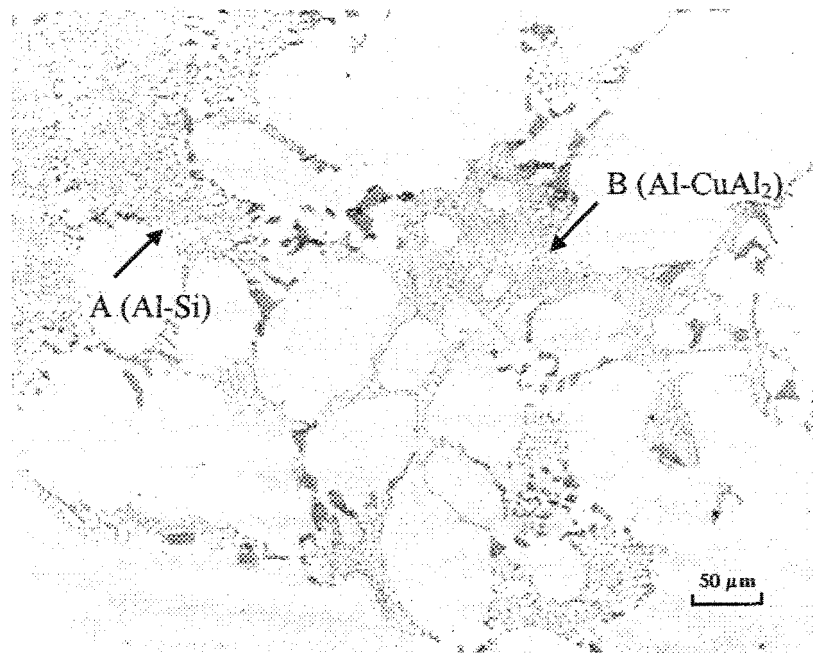


**Figure 3.4.** As-cast microstructure of ASCS alloy (Sr-modified base alloy) showing Al-Si eutectic (A), and  $\text{CuAl}_2$  segregation (B).

The microstructure of the ASCF alloy (with  $\sim 1.0\%$  Fe) is exhibited in Figure 3.5, where a large number of  $\beta\text{-Al}_5\text{FeSi}$  platelets are also seen in the matrix, decorated by  $(\text{Al}+\text{CuAl}_2)$  particles. The microstructures of ASCFS-1 (Figure 3.6) and ASCFS-2 (Figure 3.7) alloys show that the  $\beta$ -phase and the blocky  $\text{CuAl}_2$  phase are connected to each other, *viz.* the  $\beta$ -platelets act as nucleation sites for the copper phase particles. Due to the presence of Sr in the alloy, the two phases occur in regions away from those occupied by the (well-modified) Al-Si eutectic. Also, on account of its higher Fe content, the ASCFS-2 alloy (Figure 3.7) displays a larger amount of the  $\beta\text{-Al}_5\text{FeSi}$  phase compared to ASCFS-1 alloy.

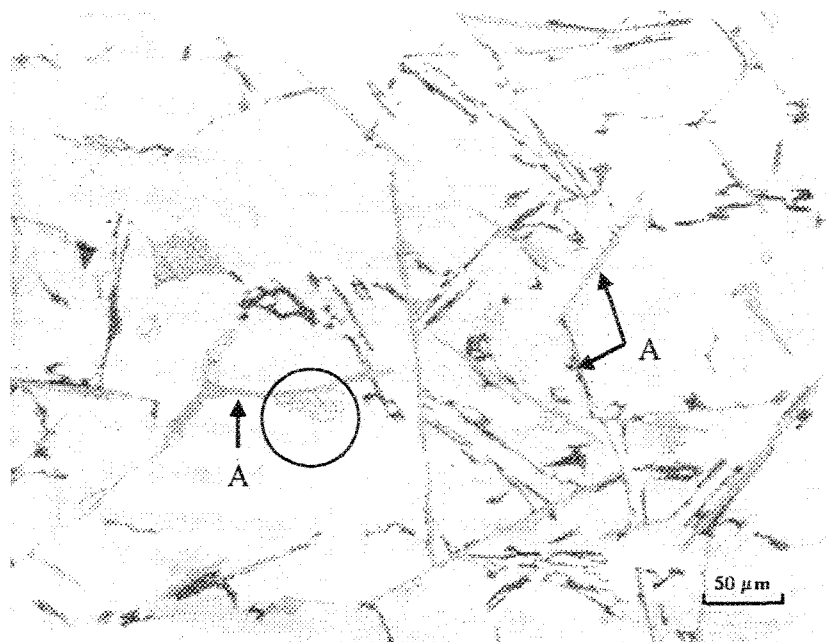


**Figure 3.5.** As-cast microstructure of ASCF alloy (base alloy containing 1 wt% Fe) showing a  $\beta$ -Al<sub>5</sub>FeSi platelet (A), and eutectic (Al+CuAl<sub>2</sub>) precipitated along the sides of the  $\beta$ -platelet (circled area).

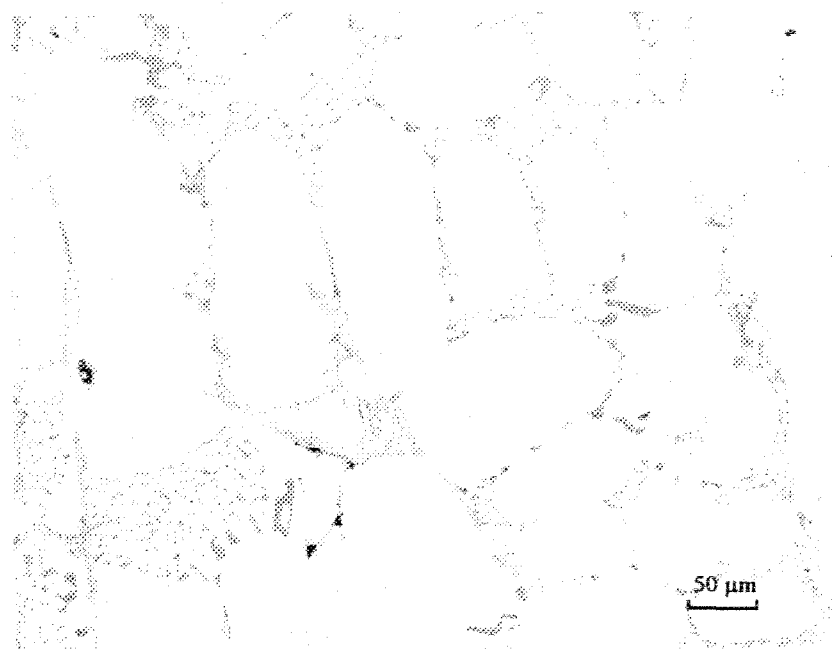


**Figure 3.6.** As-cast microstructure of ASCFS-1 alloy (base alloy containing 0.9 wt% Fe and modified with Sr). Note how the  $\beta$ - and Cu-phases occur away from the Al-Si eutectic regions.

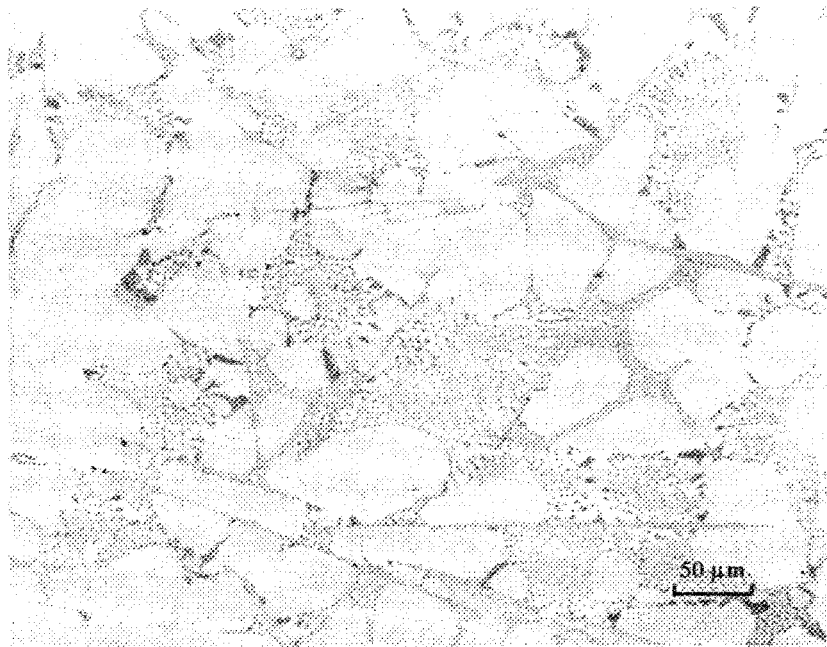


**Figure 3.7.** As-cast microstructure of ASCFS-2 alloy (base alloy containing 1.2 wt% Fe and modified with Sr). Note the larger amount of  $\beta$ -platelets compared to Figure 3.6.

Figure 3.8 shows the microstructure of H4T1 alloy (industrial 319 alloy with Sr and P additions), where  $\text{CuAl}_2$  and AlP particles are observed along the dendrite cell boundaries. When the Fe level of the alloy is increased (*viz.* H20T1 alloy), the corresponding microstructure (Figure 3.9) shows no obvious differences when compared to that of the ASCFS-2 alloy (Figure 3.7). Consequently, from Figure 3.7, Figure 3.8 and Figure 3.9, it can be concluded that the changes in the microstructure of 319 alloys brought out by the addition of P are not very obvious in the presence of other element additions such as Fe and Sr. However, the  $\text{CuAl}_2$  particles still have the tendency to precipitate on the  $\beta\text{-Al}_3\text{FeSi}$  platelets.

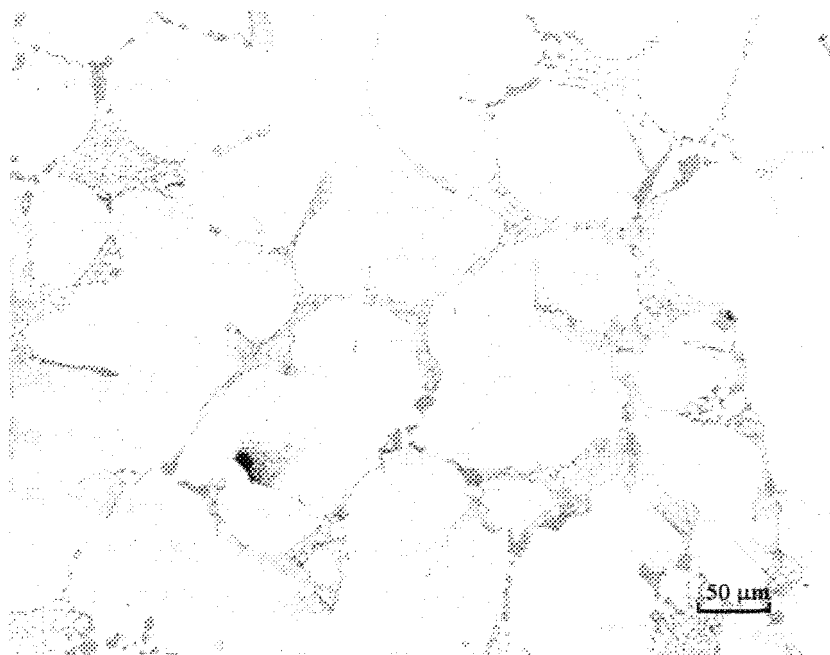


**Figure 3.8.** As-cast microstructure of H4T1 alloy (industrial 319 alloy containing 60 ppm P and modified with Sr), showing the precipitation of the CuAl<sub>2</sub> phase along the dendrite cell boundaries.

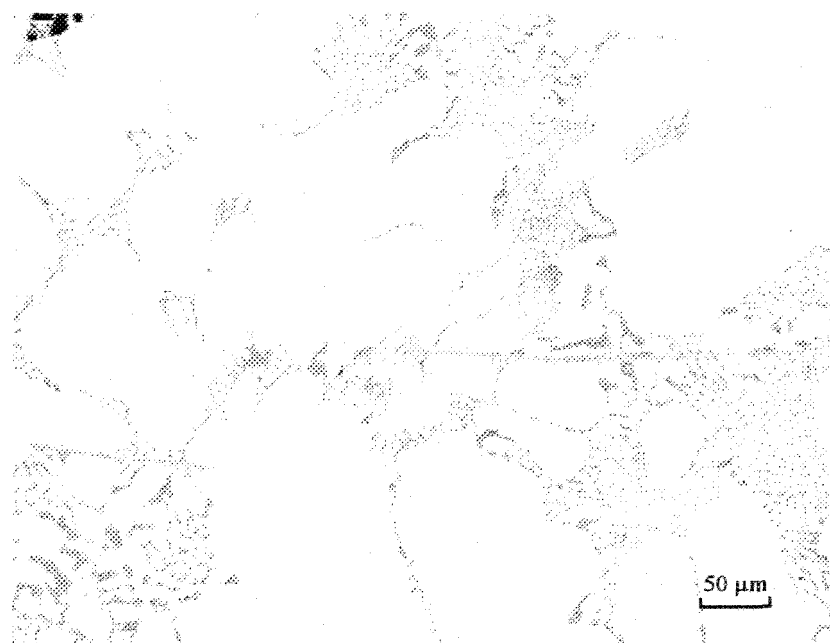


**Figure 3.9.** As-cast microstructure of H20T1 alloy (industrial 319 alloy containing 90 ppm P, 0.7 wt% Fe and modified with Sr), showing a structure similar to that of Figure 3.7.

### 3.3.3 Dissolution of $\text{CuAl}_2$ During Solution Heat Treatment

Solution heat treatment causes fragmentation and spheroidization of the silicon particles which are beneficial to the resultant alloy mechanical properties. At the same time, strontium modification has also been found to considerably lower solution treatment times.<sup>88</sup>

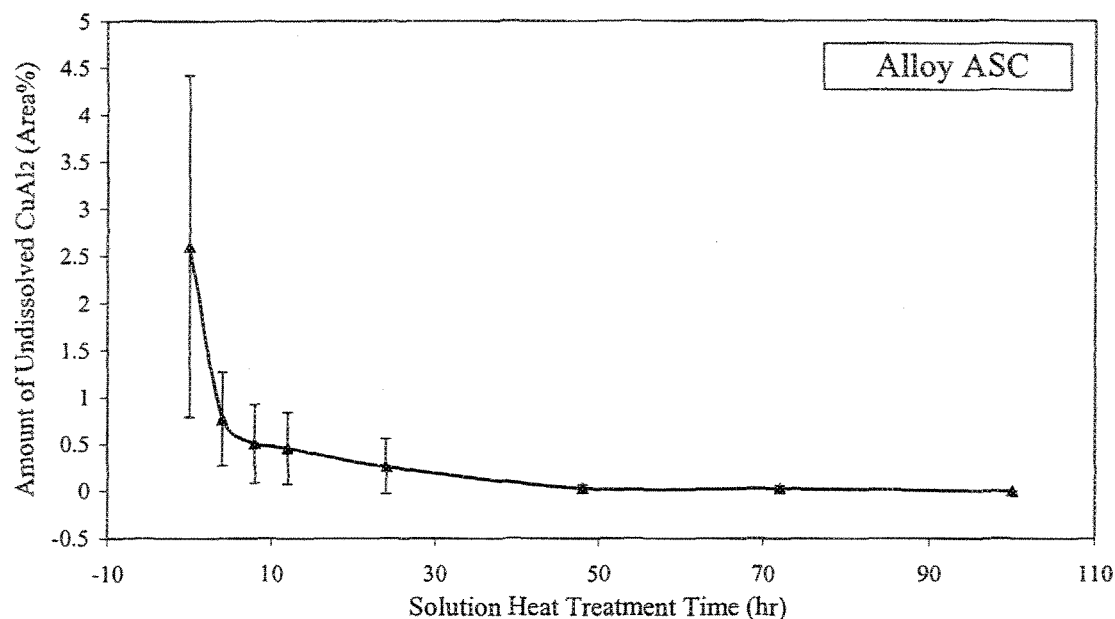
Table 3.6 shows the Al and Cu concentrations obtained in  $\text{CuAl}_2$  particles observed in the experimental Al-7% Si-3.5% Cu alloy in the as-cast condition ( $\sim 0.8$  °C/s). The six spots listed include all the possible  $\text{CuAl}_2$  morphologies existing in the sample. The data shows that the composition of  $\text{CuAl}_2$  is nearly stable regardless of its form. Again, it is necessary to point out that the morphology of the  $\text{CuAl}_2$  particles will depend on the segregation or dispersion caused by the presence of the added elements, with no significant effect on the stoichiometric composition of the  $\text{CuAl}_2$  phase itself.

**Table 3.6.** Al and Cu concentrations (at%) of the  $\text{CuAl}_2$  phase in the experimental Al-7%Si-3.5%Cu alloy (as-cast condition; cooling rate  $\sim 0.8$  °C/s)

Spot No.	Al	Cu
1	68.994	29.850
2	68.702	30.194
3	72.106	27.021
4	63.765	27.469
5	69.117	29.799
6	75.002	23.031

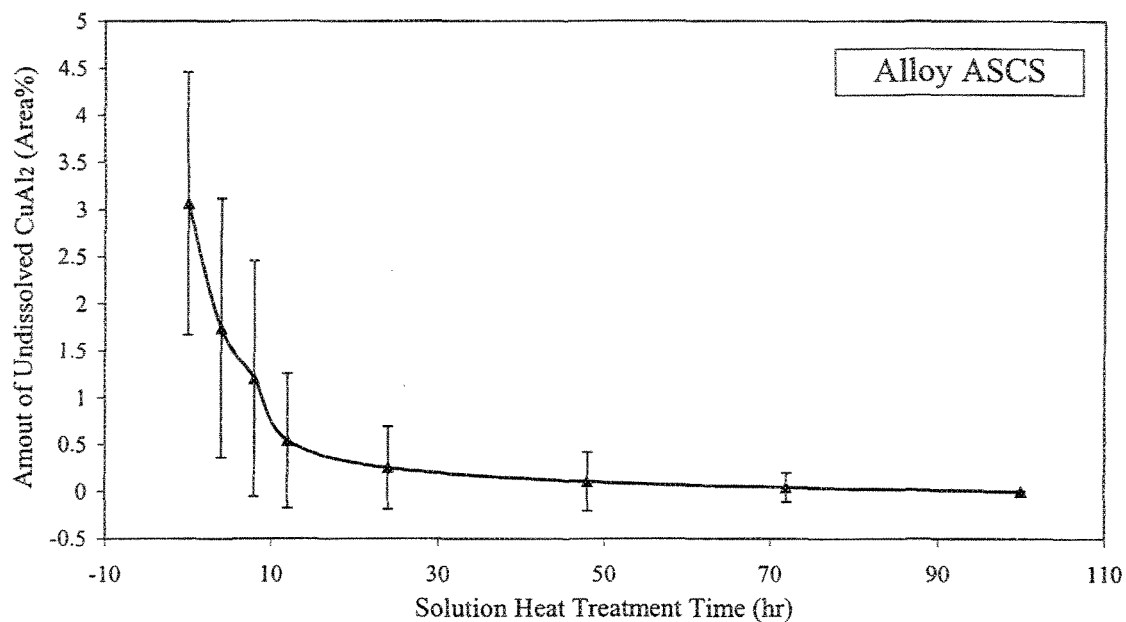
As mentioned previously, copper forms an intermetallic phase with aluminum that precipitates during solidification either as block-like  $\text{CuAl}_2$  or in eutectic form as  $(\text{Al}+\text{CuAl}_2)$ . These phases are easily distinguishable under an optical microscope. In order to study the effect of solution heat treatment, the percentage area of the undissolved copper phase was measured for the various alloy samples/conditions. A Leco 2001 image analyzer was used in conjunction with the optical microscope for quantitative analysis. The amounts of the undissolved copper phase so determined were plotted as a function of solution heat treatment time and are presented in Figure 3.10 through Figure 3.16. The error bars in these figures represent  $\pm\sigma$ , where  $\sigma$  is the standard deviation obtained with respect to the average values that are plotted in the figures.

Figure 3.10 reveals the progress of the  $\text{CuAl}_2$  phase dissolution in the experimental ASC base alloy. After 4 hours of solution treatment at 505 °C, the quantity of the  $\text{CuAl}_2$  phase decreases abruptly from 2.6% to 0.77%, *i.e.*, about 70% of the total  $\text{CuAl}_2$  phase has been dissolved in the matrix. With further solution treatment, up to 48 h, the  $\text{CuAl}_2$  phase dissolves very slowly, reaching 0.03%. Prolonged solution treatment, *i.e.* 100 h, tends to put the rest of the copper into the surrounding aluminum matrix. It should be mentioned here that the term “complete dissolution” is taken to mean that the  $\text{CuAl}_2$  particles cannot be detected in the matrix by optical means (at X500 magnification).



**Figure 3.10.** CuAl<sub>2</sub> phase dissolution in ASC alloy during solution heat treatment at 505°C as a function of solution treatment time.

In the case of the modified alloy (*viz.*, ASCS alloy), Figure 3.11, most of the CuAl<sub>2</sub> (~2.7%) is dissolved after 12 hours. Thereafter, the percentage of the remaining CuAl<sub>2</sub> phase (~0.5%) reduces slowly with a further increase in solution time. Compared to the base alloy (ASC), the amount of undissolved CuAl<sub>2</sub> phase in the ASCS alloy was about 20% higher in the as-cast condition. This is to be expected, as the Sr-modification should obviously slow down the rate of CuAl<sub>2</sub> dissolution due to its effect on the segregation of the CuAl<sub>2</sub> phase during solidification.



**Figure 3.11.** CuAl<sub>2</sub> phase dissolution in ASCS alloy during solution heat treatment at 505°C as a function of solution treatment time.

Comparing Figure 3.12 (ASCF alloy) with Figure 3.10 (ASC alloy), the addition of Fe is seen to shorten the time needed for the dissolution of the CuAl<sub>2</sub> phase to 24 hours, *i.e.* almost half of the time needed for the base alloy to reach the same level of dissolution. The addition of Fe to the base alloy assists in the dispersion of the CuAl<sub>2</sub> particles, since the  $\beta$ -Al<sub>5</sub>FeSi phase, which precipitates before the Al+CuAl<sub>2</sub> eutectic (as inferred from the corresponding cooling curve) provides nucleation sites for the CuAl<sub>2</sub> particles. Consequently, CuAl<sub>2</sub> phase segregation is much less likely to occur, reducing the size of the CuAl<sub>2</sub> particles. Thus, during solution heat treatment, these CuAl<sub>2</sub> particles will be much more easily dissolved.

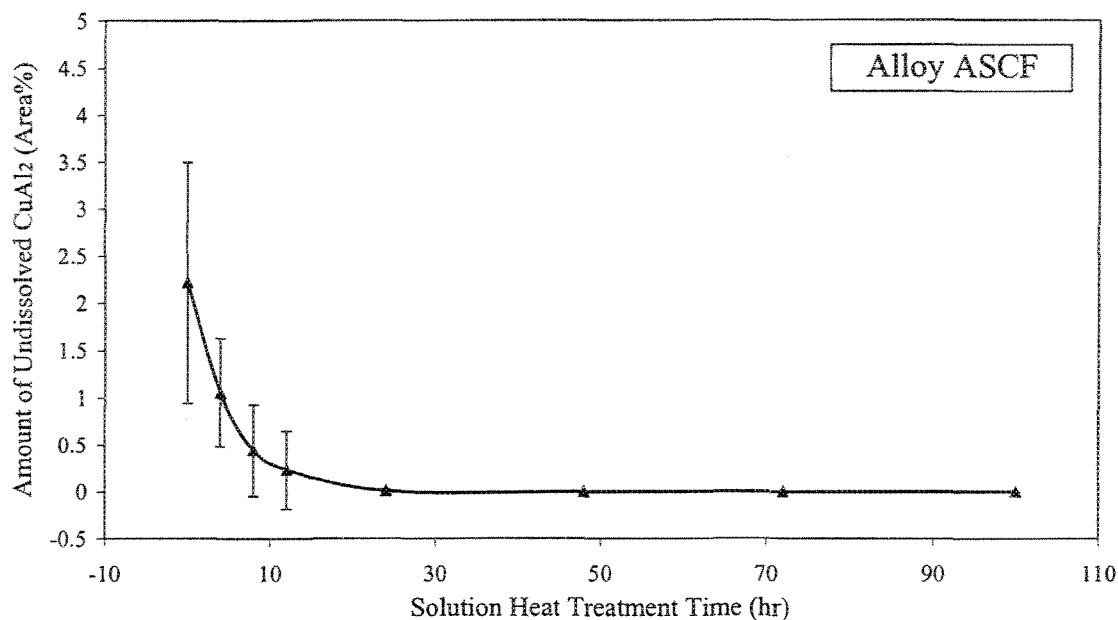


**Figure 3.12.** CuAl<sub>2</sub> phase dissolution in ASCF alloy during solution heat treatment at 505°C as a function of solution treatment time.

The ASCFS-1 alloy and the ASCFS-2 alloy (Figure 3.13 and Figure 3.14, respectively) have compositions that are more or less similar. The differences between the two dissolution curves are caused by the difference in their Fe concentrations. The somewhat higher Fe level in the ASCFS-2 alloy will increase the dispersion and thus accelerate the dissolution of the CuAl<sub>2</sub> particles under the same conditions of solution heat treatment. It is also interesting to note how the effects of Sr and Fe addition on the CuAl<sub>2</sub> phase counteract one another by comparing Figure 3.12, Figure 3.13 and Figure 3.14 for ASCF, ASCFS-1 and ASCFS-2 alloys, respectively.

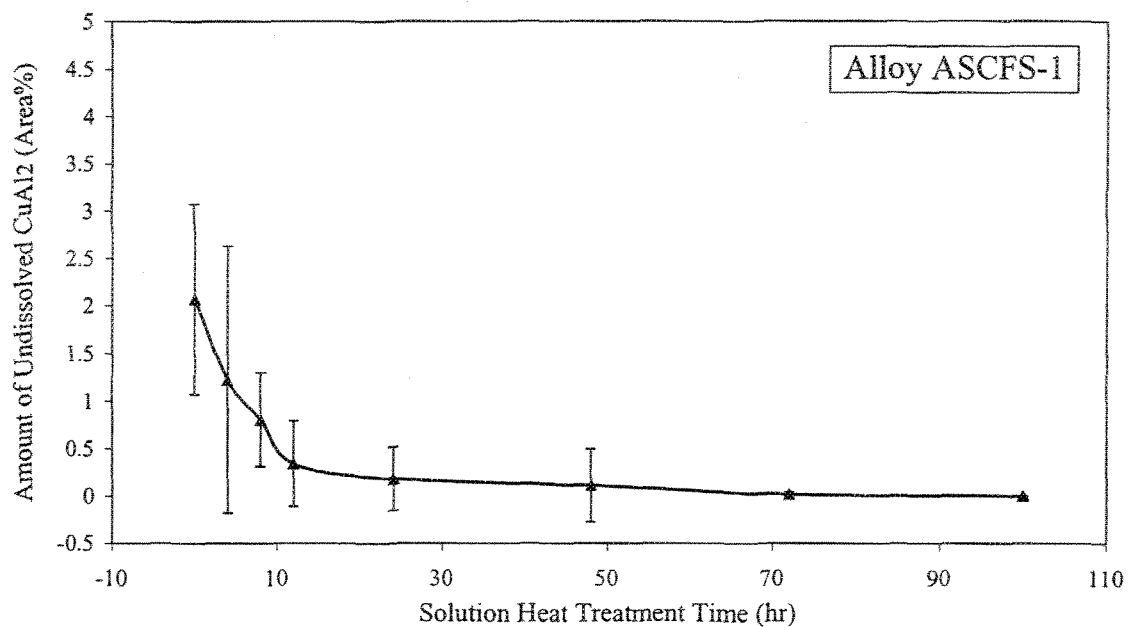


**Figure 3.13.** CuAl<sub>2</sub> phase dissolution in ASCFS-1 alloy during solution heat treatment at 505°C as a function of solution treatment time.

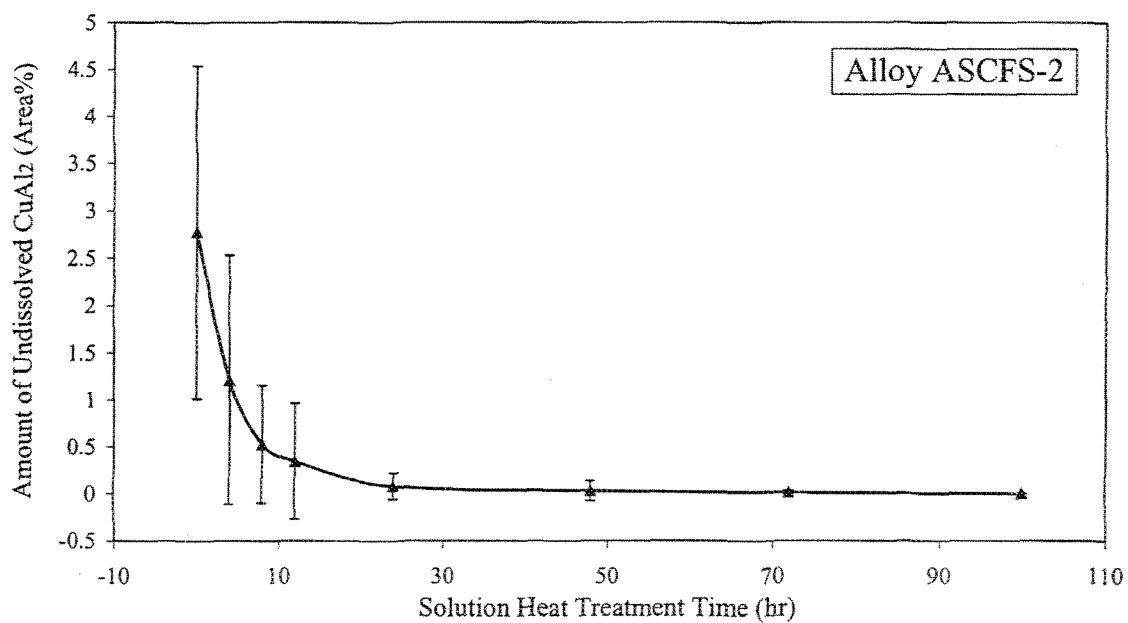


**Figure 3.14.** CuAl<sub>2</sub> phase dissolution in ASCFS-2 alloy during solution heat treatment at 505°C as a function of solution treatment time.

The results obtained for the H4T1 alloy (industrial 319 alloy with Sr and P additions), Figure 3.15, showed a different behavior, in that the dissolution of the  $\text{CuAl}_2$  phase was found to be very sluggish in this alloy. After 8 hours of solution heat treatment, only 60% of the original amount of the  $\text{CuAl}_2$  phase observed in the structure was dissolved. Even after 100 hours, about 0.41% of the  $\text{CuAl}_2$  phase remained undissolved. This observation is attributed to the presence of AlP particles that reinforce the segregation of  $\text{CuAl}_2$  at the dendrite cell boundaries. The data for H20T1 alloy presented in Figure 3.16 exhibits clearly that iron has the ability to neutralize this negative effect of phosphorus.

A summary of the above results is presented in Table 3.7, in which the effects of the various element additions on the dissolution of  $\text{CuAl}_2$ , as a function of solutionizing time are provided for the seven alloys studied, in terms of the amount of time required to reach (i) 0.5% remaining  $\text{CuAl}_2$  phase, and (ii) complete dissolution. These results were obtained from image analysis measurements. The Si particles were also observed to undergo morphological changes with increasing solution heat treatment time. However, while the  $\beta$ -iron phase essentially retained its plate-like morphology, dissolution of the  $\beta$ -platelets with increasing solution heat treatment time was also observed. These observations are in good agreement with the conclusions drawn by Crowell and Shivkumar.<sup>54</sup>

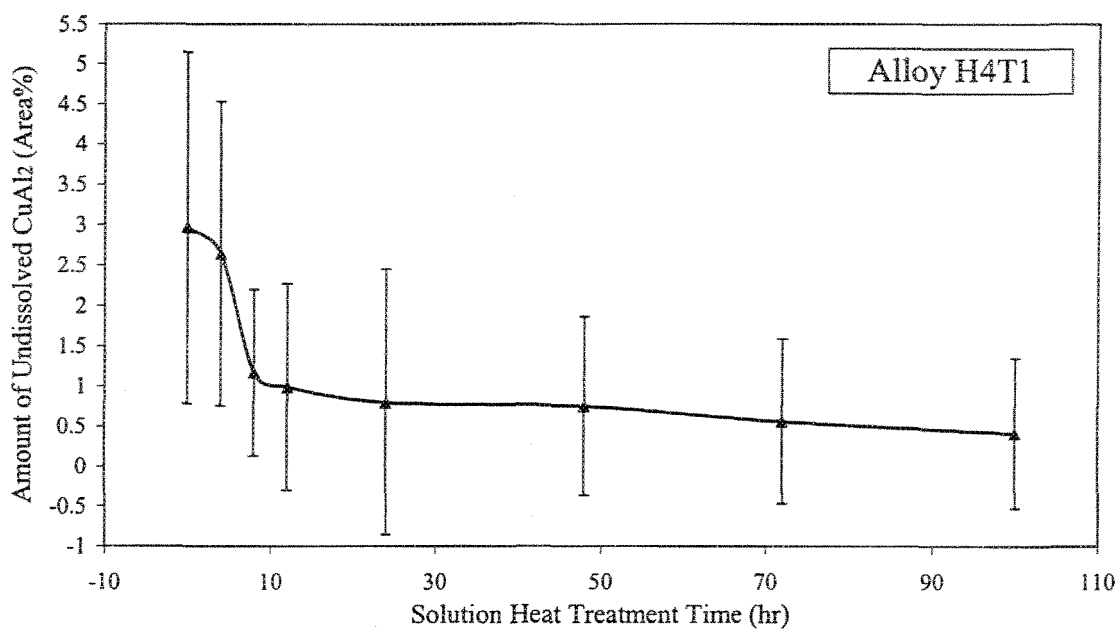


**Figure 3.15.** CuAl<sub>2</sub> phase dissolution in H4T1 alloy during solution heat treatment at 505°C as a function of solution treatment time.

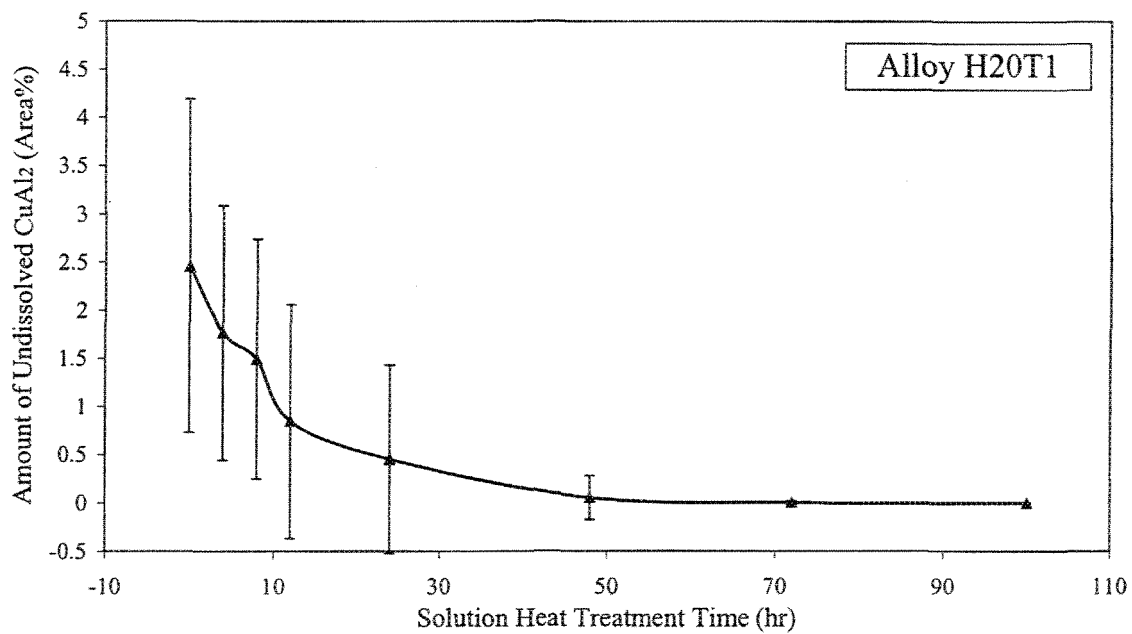


**Figure 3.16.** CuAl<sub>2</sub> phase dissolution in H20T1 alloy during solution heat treatment at 505°C as a function of solution treatment time.

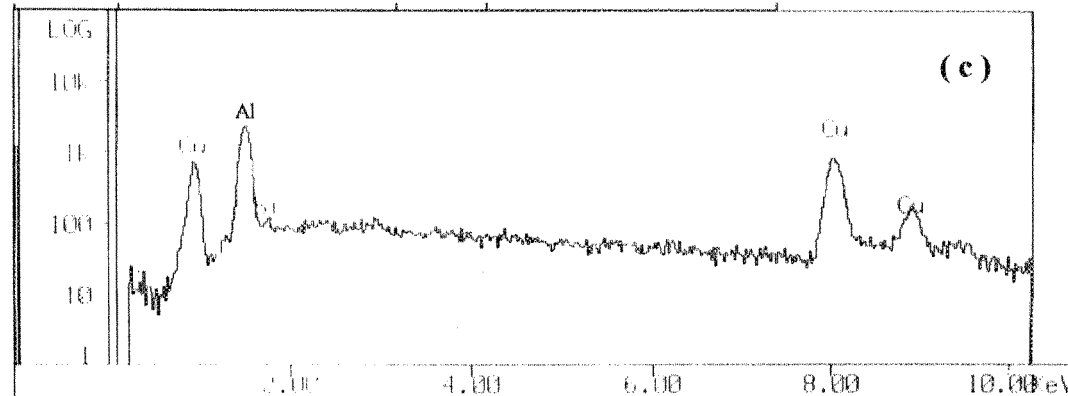
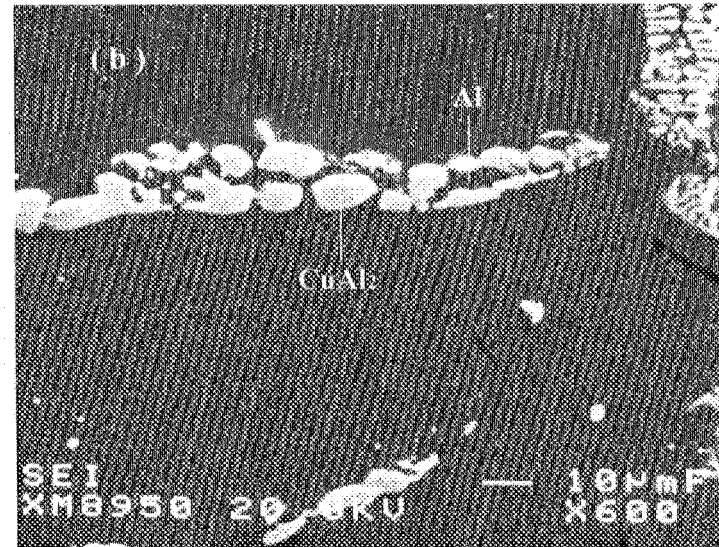
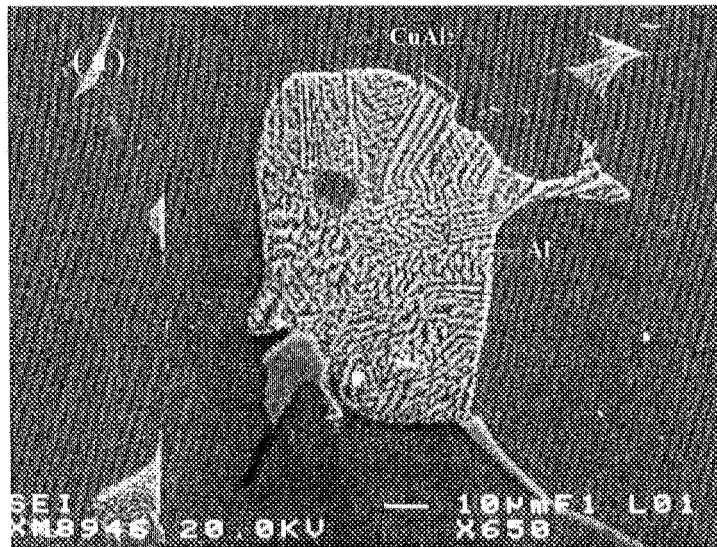
**Table 3.7.** Summary of the dissolution of the  $\text{CuAl}_2$  phase at  $505^\circ\text{C}$  as a function of alloy composition and solution treatment time

Alloy	Time to Reach 0.5% of Undissolved $\text{CuAl}_2$ Phase (hr)	Time to Reach Approx. Complete Dissolution of $\text{CuAl}_2$ Phase (hr)
ASC	8	48
ASCS	12	~100
ASCF	4-8	24
ASCFS-1	8-12	~72
ASCFS-2	8	~24
H4T1	>72	>100
H20T1	~20	~48

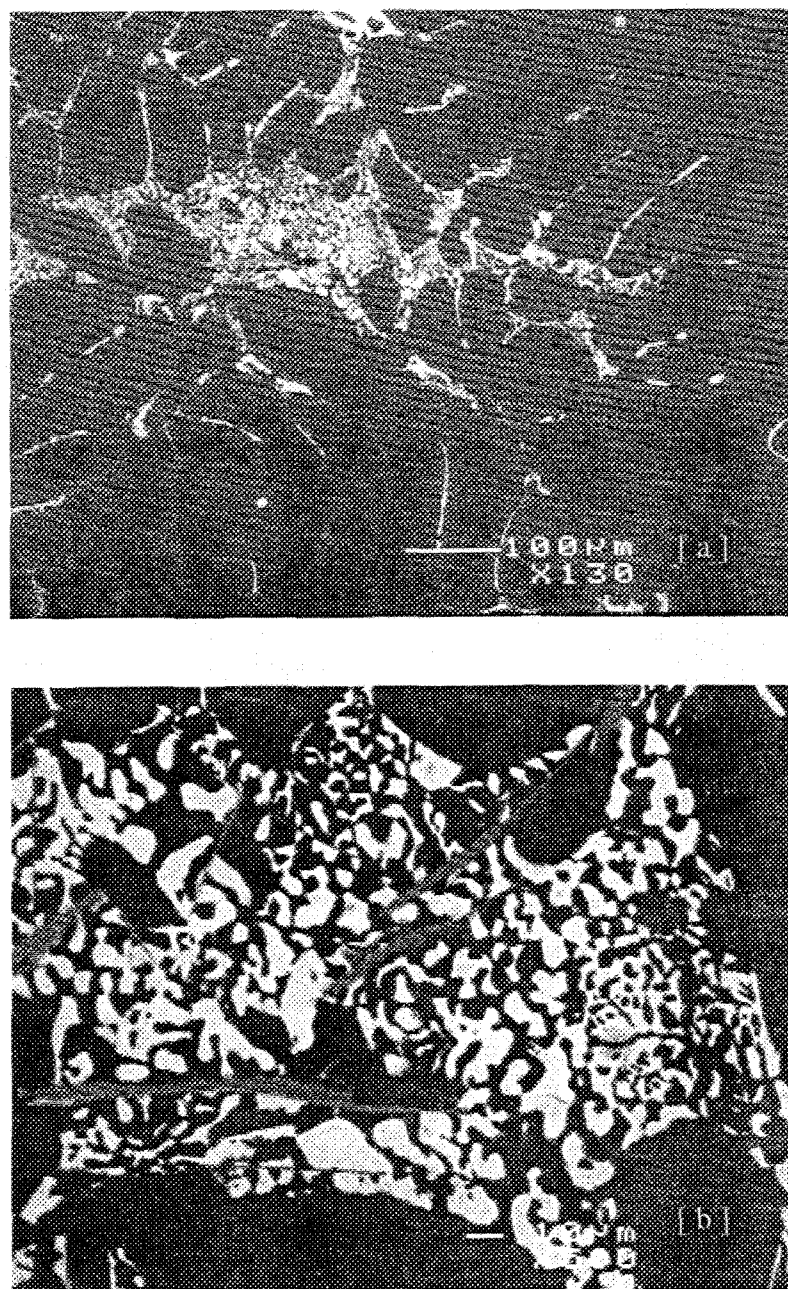
### 3.3.4 Electron Probe Microanalysis (EPMA)

Figure 3.17 exhibits the two distinct forms of the copper phase: (a) the eutectic-like ( $\text{Al}+\text{CuAl}_2$ ) phase, and (b) the blocky  $\text{CuAl}_2$  phase, which were observed in the present alloys. The EDX spectrum obtained from the  $\text{CuAl}_2$  particles shown in (b) is given in Figure 3.17(c), in which strong reflections due to Al and Cu can be observed. The block-like morphology of the  $\text{CuAl}_2$  phase particles in Figure 3.17(b) clearly stands out when one compares it to the eutectic-like particles observed at the top right corner of the same micrograph.

The backscattered image of the as-cast microstructure of the Sr-modified H4T1 alloy in Figure 3.18(a) clearly reveals the segregation of the copper phase particles in the interdendritic regions. The high magnification micrograph of Figure 3.18(b) depicts details of the segregated region. It can be noted that due to the presence of Sr, the  $\text{CuAl}_2$  phase particles precipitate mostly in the blocky form along the  $\beta$ -platelet sides.



**Figure 3.17.** Backscattered images of (a) eutectic copper phase, (b) blocky copper phase, and (c) EDX spectrum obtained from  $\text{CuAl}_2$  particles shown in (b), where strong reflections due to Al and Cu can be seen.



**Figure 3.18.** (a) Backscattered image of CuAl<sub>2</sub> phase distribution in as-cast H4T1 alloy, (b) high magnification micrograph of the Cu phase segregation area shown in (a), and (c) fine CuAl<sub>2</sub> particles scattered among the modified Si particles in as-cast H20T1 alloy.

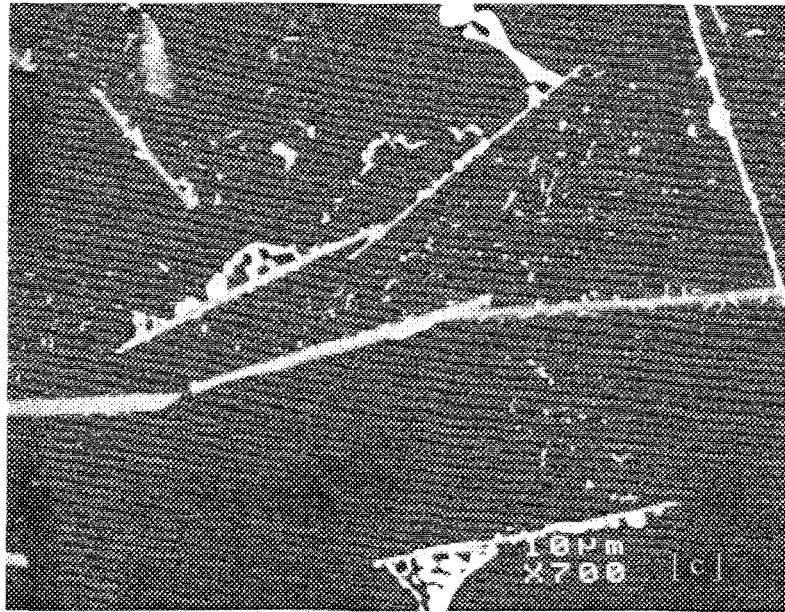


**Figure 3.18.** (a) Backscattered image of  $\text{CuAl}_2$  phase distribution in as-cast H4T1 alloy, (b) high magnification micrograph of the Cu phase segregation area shown in (a), and (c) fine  $\text{CuAl}_2$  particles scattered among the modified Si particles in as-cast H20T1 alloy.

Figure 3.18(c) shows the microstructure of H20T1 alloy (industrial 319 alloy containing Sr, Fe and 90 ppm P) after 8 hours of solution heat treatment. As expected, some blocky  $\text{CuAl}_2$  still exists in the microstructure, together with a scattering of fine  $\text{CuAl}_2$  particles in the modified Si particle regions.

Figure 3.19 shows (a) the backscattered image and the X-ray images of (b) Al, and (c) P taken from the H20T1 alloy sample. The arrows in each case point to segregated block-like  $\text{CuAl}_2$  particles. The presence of AlP particles underneath the copper phase is confirmed from Figure 3.19(b) and Figure 3.19(c). This indicates that the AlP particles also contribute to the segregation of the  $\text{CuAl}_2$  phase.

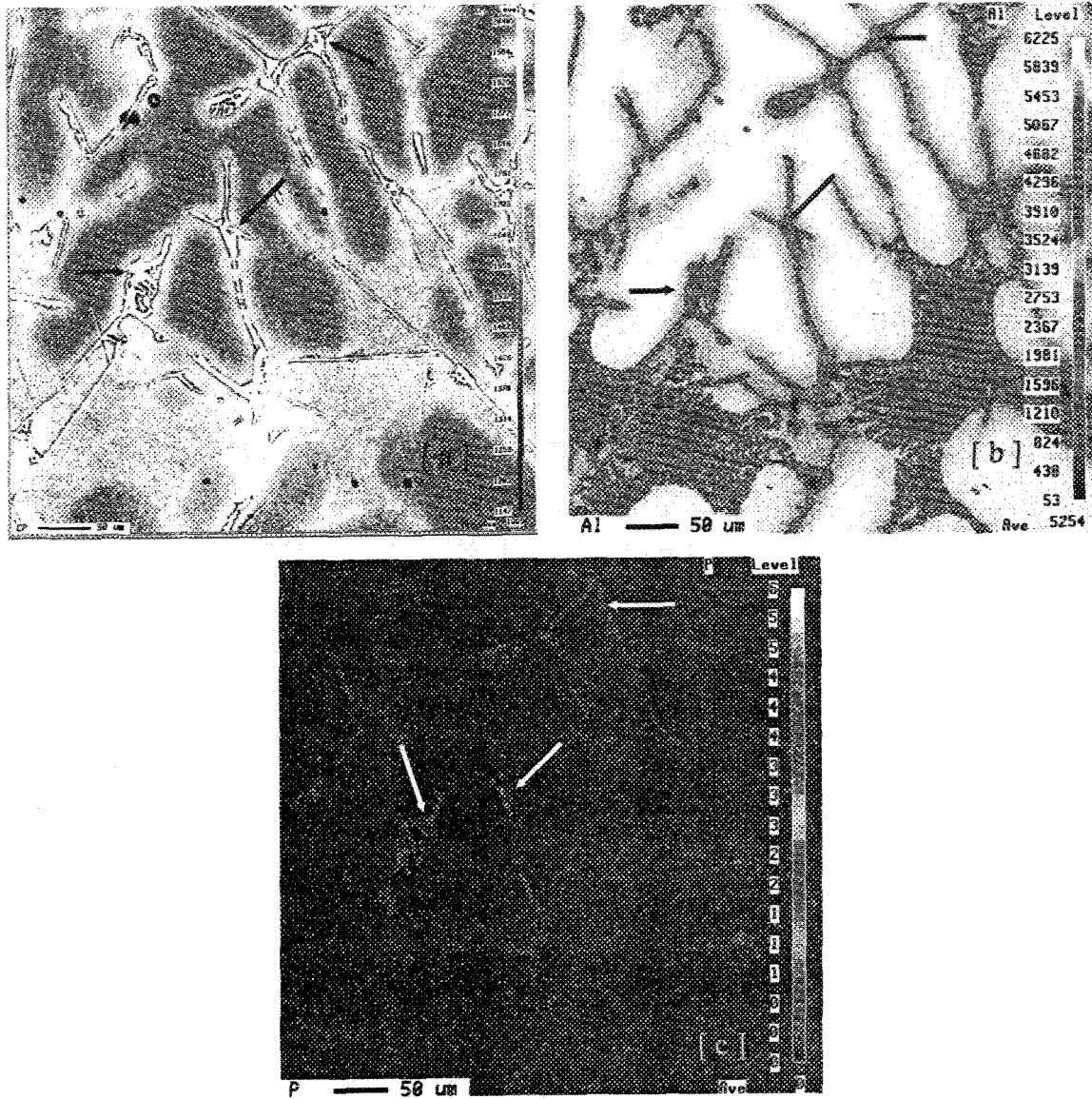


**Figure 3.19.** (a) Backscattered image, and X-ray images of (b) Al and (c) P underneath  $\text{CuAl}_2$  particles observed in H20T1 alloy (ASC alloy containing Fe, P and Sr).

The segregation of blocky  $\text{CuAl}_2$  particles on the  $\beta$ - $\text{Al}_5\text{FeSi}$  platelets in the as-cast ASCFS alloy is shown in Figure 3.20. A high magnification backscattered image taken from ASCFS alloy (Figure 3.21) illustrates the main process of fragmentation and dissolution of the  $\text{CuAl}_2$  particles, which involves: (a) separation of the  $\text{CuAl}_2$  particles from the  $\beta$ -phase after 8 hours of solution heat treatment, followed by (b) necking and spheroidization of the fragmented  $\text{CuAl}_2$  particles, and (c) radial diffusion of Cu atoms into the surrounding aluminum matrix.

The backscattered image taken from H4T1 alloy subjected to 8 hours of solution heat treatment at 505 °C reveals undissolved spheroidized  $\text{CuAl}_2$  particles in a segregated region away from the Al-Si eutectic area (Figure 3.22). It is interesting to note how the fine  $\text{CuAl}_2$  particles scattered over the Si particles in Figure 3.18(c) for the as-cast 319 alloy are almost absent after an 8-hour solution treatment.

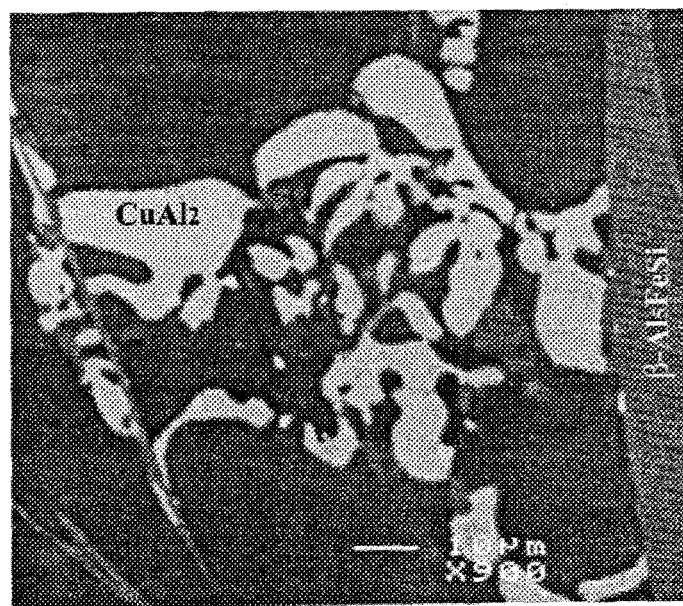


**Figure 3.20.** Microstructure of  $\text{CuAl}_2$  particles precipitated on the  $\beta$ -plate in as-cast ASCFS alloy.

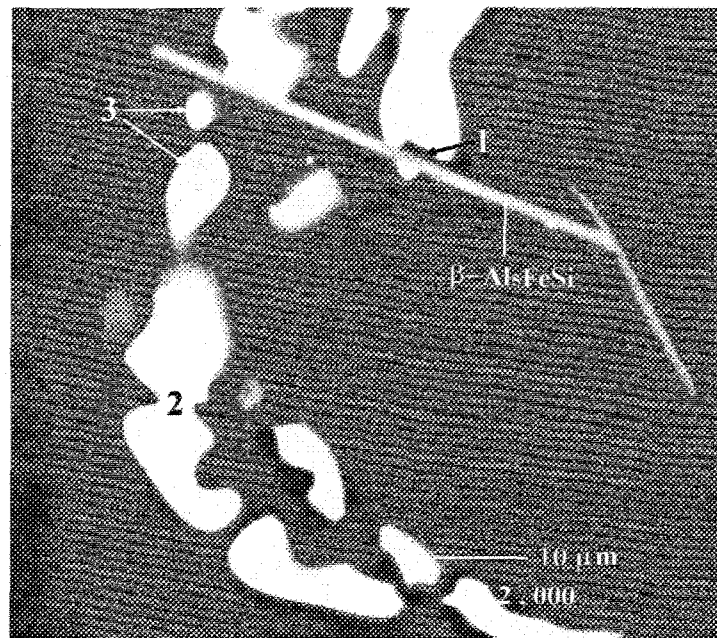


**Figure 3.21.** Backscattered image showing the dissolution process of  $\text{CuAl}_2$  particles in ASCFS alloy after 8 hours of solution heat treatment at  $505^\circ\text{C}$ : (1) separation of  $\text{CuAl}_2$  from  $\beta$ -plate; (2) necking of  $\text{CuAl}_2$  cluster; (3) spheroidization of  $\text{CuAl}_2$  and reduction in the size of  $\text{CuAl}_2$  fragments.

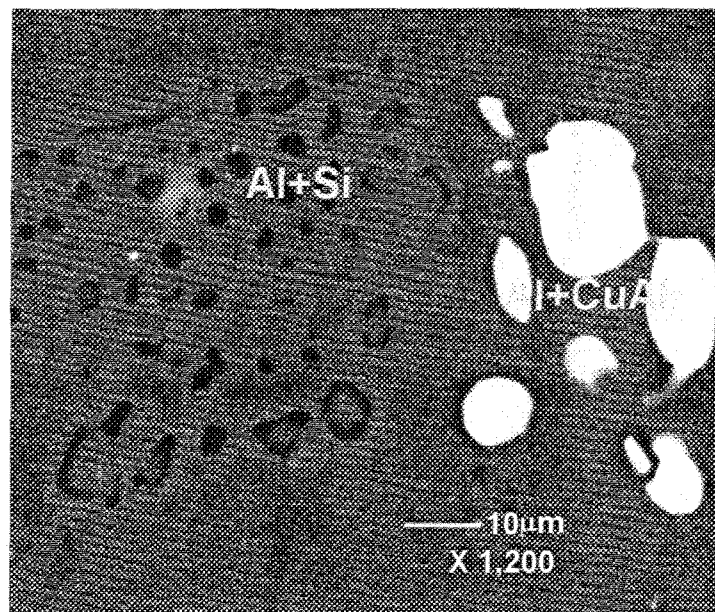


**Figure 3.22.** Backscattered image showing  $\text{CuAl}_2$  dissolution in H4T1 alloy after 8 hours of solution heat treatment at  $505^\circ\text{C}$ .

Figure 3.23 is a general view of the microstructure of H4T1 alloy after a 100-hour solution treatment at 505 °C, revealing the almost complete dissolution of the  $\text{CuAl}_2$  phase, although a few particles are still observed in the matrix. At the same time, it is also noticed that, during the process of dissolution, the Al and Cu concentrations in the  $\text{CuAl}_2$  phase remain practically stable, as shown in Table 3.8. Therefore, it may be suggested that the dissolution of the  $\text{CuAl}_2$  phase occurs by diffusion of the Cu atoms in the outer layer of the  $\text{CuAl}_2$  phase particles into the surrounding matrix, without changing the chemical composition of the remaining portions of the particles, even after 100 h at 505 °C.

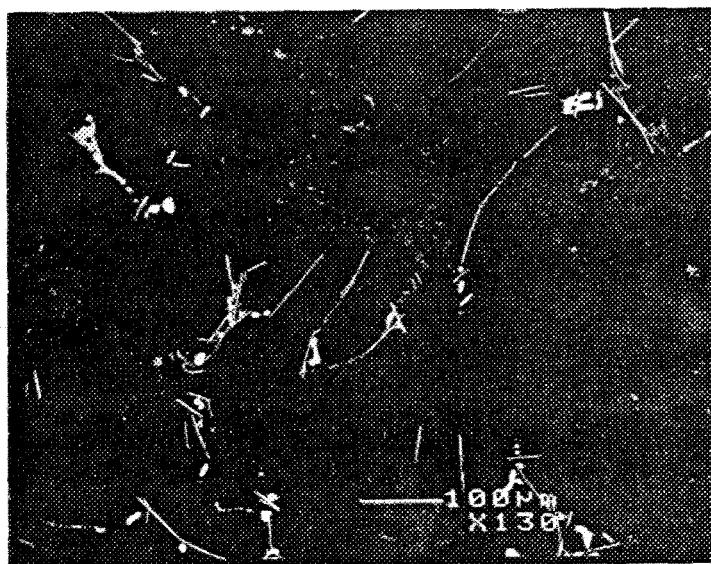


**Figure 3.23.** Backscattered image taken from H4T1 alloy after 100 hours of solution heat treatment at 505 °C.

**Table 3.8.** Al and Cu concentrations (at%) in  $\text{CuAl}_2$  phase particles during solution heat treatment at 505 °C

Sr Concentration (ppm)	Time of Solution Heat Treatment (hr)	Al	Cu
0 (ASC)	0	68.647	29.285
	8	69.764	29.328
	100	69.287	28.267
200 (ASCS)	0	68.691	30.290
	8	68.941	30.118
	100	68.713	30.456

The line scans corresponding to ASCFS alloy following 8 h and 100 h solution heat treatment times are presented in Figure 3.24(b) and Figure 3.25(b), respectively, taken across the paths marked AB in the corresponding Figure 3.24(a) and Figure 3.25(a). These scans reveal the concentration gradients of Cu across the area containing the copper phase particles. The Cu concentration in the matrix around the  $\text{CuAl}_2$  particles in Figure 3.24(b) is ~4 wt% after 8 h of solution treatment — much higher than the Cu concentration (~2 wt%) in the aluminum matrix after a 100-hour solution heat treatment (Figure 3.25(b)). Thus, during the process of solution heat treatment, the Cu atoms diffuse in the matrix, far away from the remaining undissolved  $\text{CuAl}_2$ . This is consistent with the X-ray image for Cu shown in Figure 3.26, corresponding to the (a) as-cast, (b) 8 h solution-treated, and (c) 100 h solution-treated samples of ASCFS alloy. Table 3.9 reveals the maximum Cu counts obtained from a WDS analysis of ASCFS alloy shown in Figure 3.26. Due to the diffusion of Cu during solution heat treatment, the maximum Cu concentration in the  $\text{CuAl}_2$  particle shows a reasonable decrease. It is also interesting to note the sponge-like appearance of the

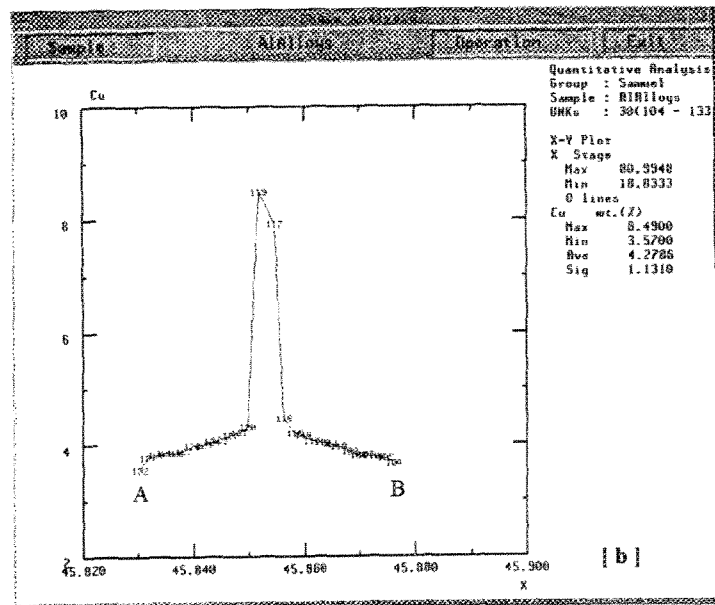
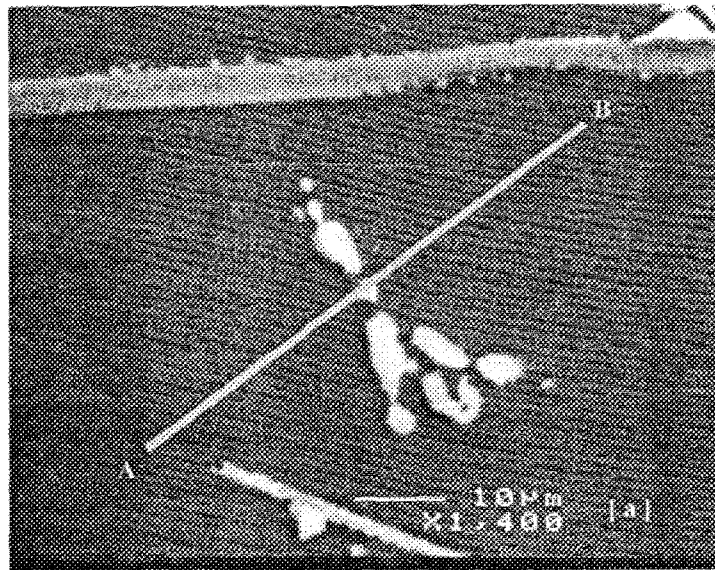


**Figure 3.24.** (a) Backscattered image of a  $\text{CuAl}_2$  particle in ASCFS alloy after 8 hours of solution heat treatment; (b) the concentration profile of Cu along the path AB in (a).

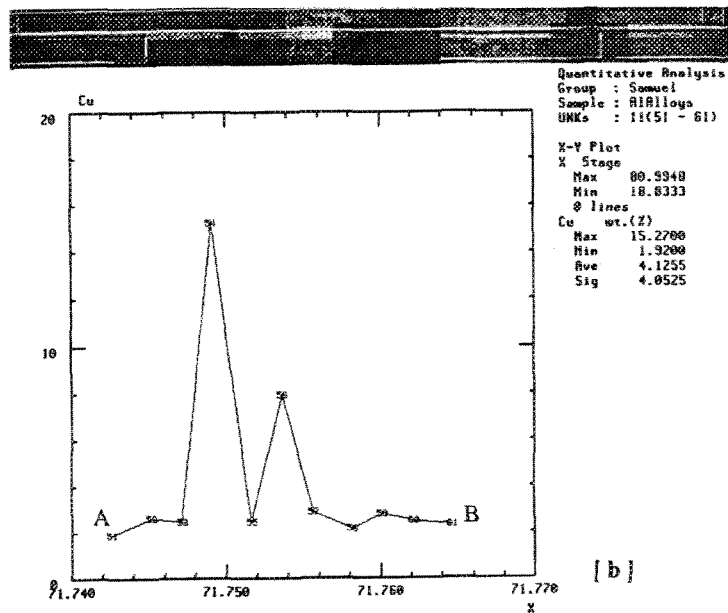
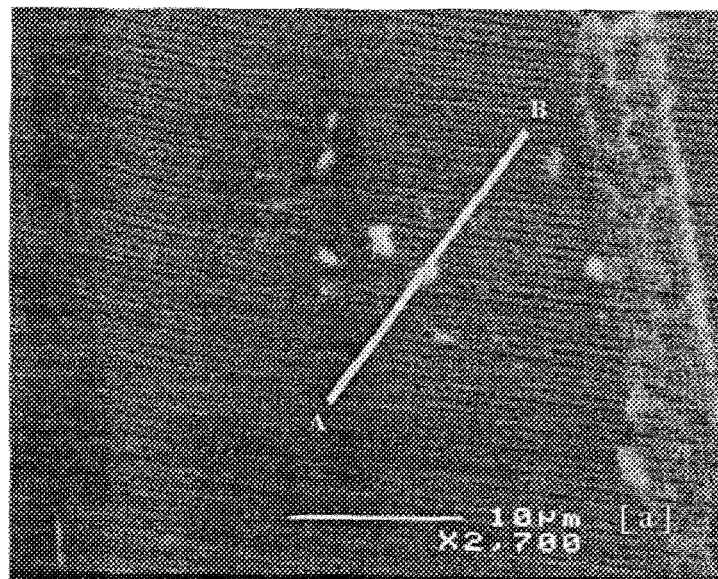


**Figure 3.25.** (a) Backscattered image of a  $\text{CuAl}_2$  particle in ASCFS alloy after 100 hours of solution heat treatment; (b) the concentration profile of Cu along the path AB in (a).

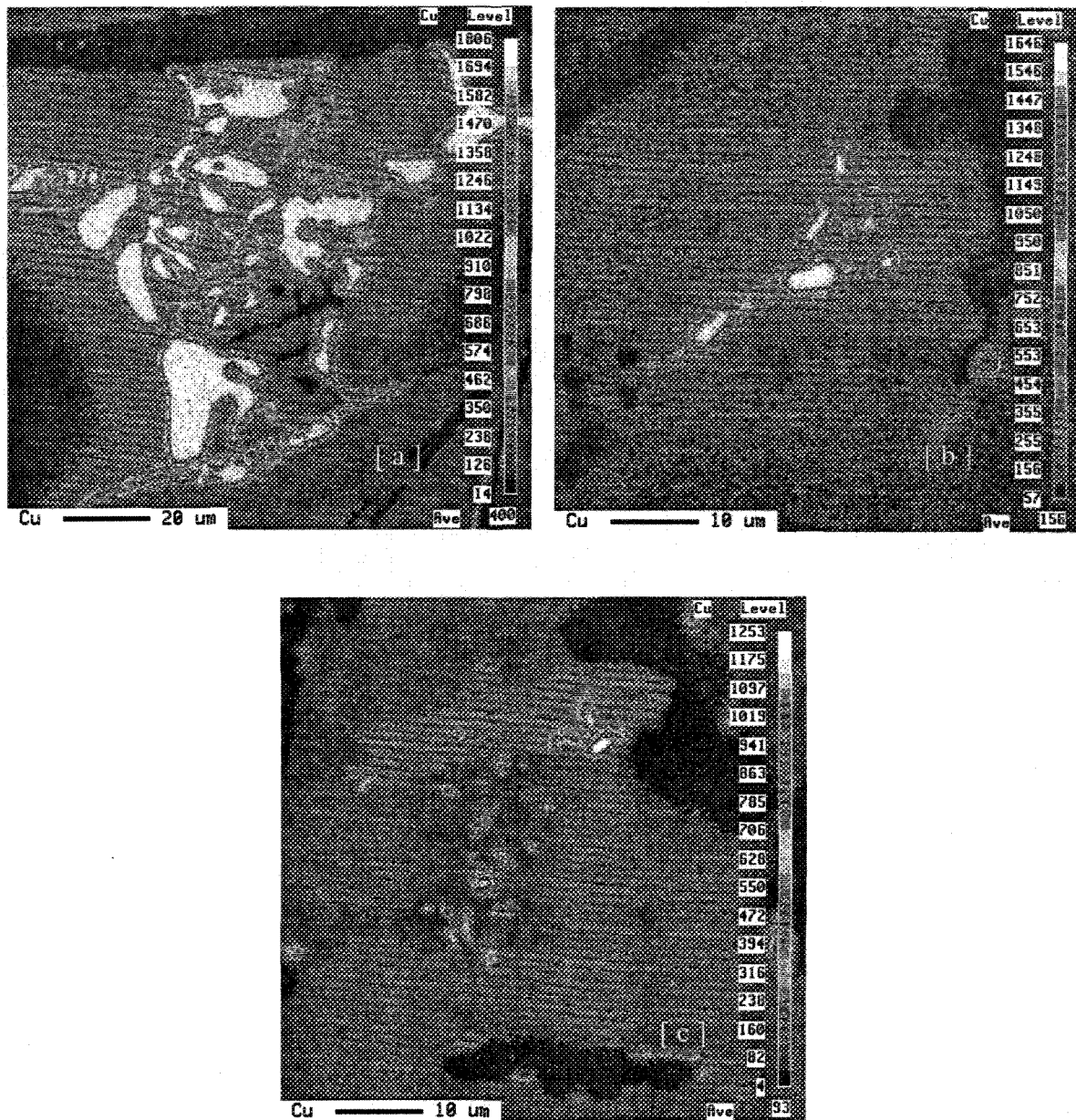


**Figure 3.26.** X-ray images of Cu in ASCFS alloy after (a) 0 h, (b) 8 h, and (c) 100 h solution heat treatment at 505 °C.

**Table 3.9.** Maximum Cu counts obtained from WDS analysis for ASCFS alloy after different solution heat treatment times

Solution Treatment Time (hr)	Counts
0	1806
8	1646
100	1383

$\beta$ -phase shown in Figure 3.25(a), after 100 h of solutionizing at 505 °C, and compare it to the solid platelet seen in Figure 3.20 for the as-cast condition.

### 3.3.5 Role of (Al,P)O<sub>2</sub> Oxide on CuAl<sub>2</sub> Precipitation

In order to understand clearly the exact role of phosphorus with respect to the precipitation of the CuAl<sub>2</sub> phase, a small melt (600 g of unmodified 319 alloy, viz. without any Sr) was prepared to which phosphorus was added in high concentration (1000 ppm), using Cu-8% P brazing alloy. The melt was superheated at 950 °C for 20 min, mechanically stirred, then poured into a preheated graphite mold (600 °C), to obtain near-equilibrium cooling rates. A sample was sectioned from the central part of the casting, mounted in bakelite and polished (1  $\mu$ m diamond finish) for metallographic examination. Figure 3.27 shows the backscattered image (a) and corresponding X-ray image of phosphorus (b) obtained from this sample. The arrows in each case point to an oxide particle. As the X-ray image shows, this particle is concentrated in phosphorus indicating that it is a phosphorus oxide particle.

The corresponding WDS analysis showed that the composition of this particle was 65.4% O, 30.2% Al, 1.5% P and 1.8% Si (in atomic pct), giving an approximate formula of

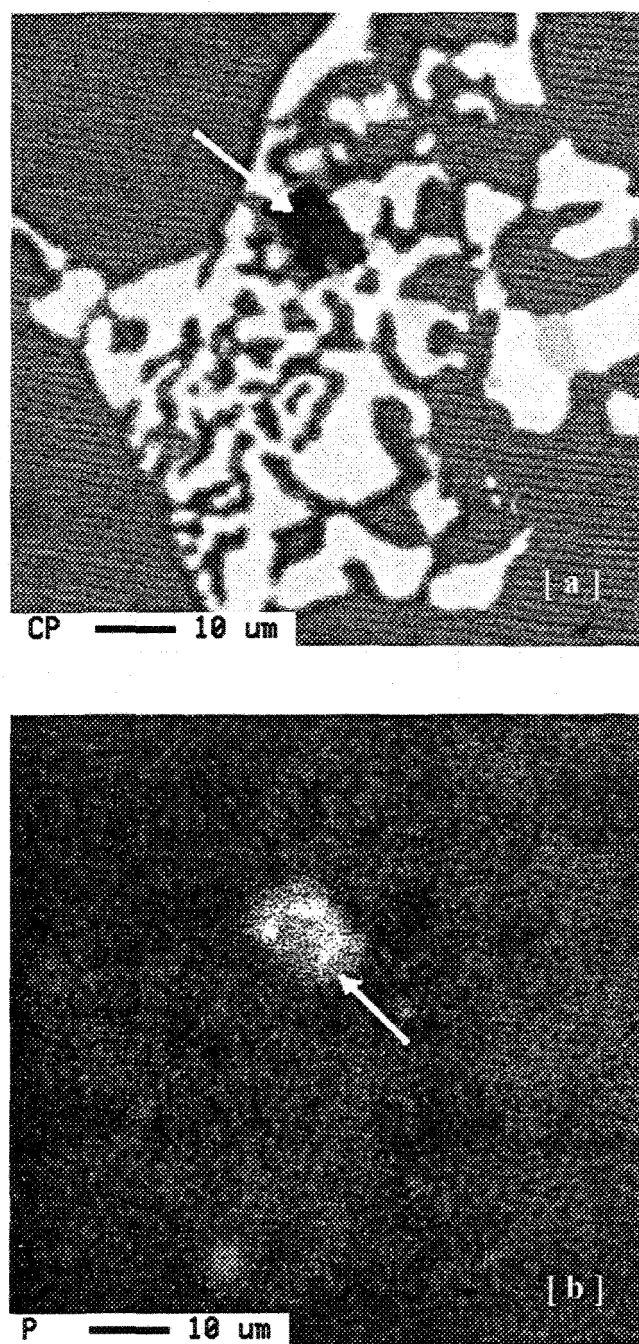


**Figure 3.27.** (a) Backscattered image of  $\text{CuAl}_2$  phase with a phosphorus oxide particle (arrowed), (b) corresponding X-ray image of P obtained from (a), taken from an unmodified 319 alloy sample containing 1000 ppm P.

(Al,P)O<sub>2</sub>, with traces of SiO<sub>2</sub>. The location of the oxide particle (surrounded by the block-like CuAl<sub>2</sub>) indicates that the oxide particle acts as the nucleation site for the precipitation of the copper phase. Figure 3.28 shows a secondary electron image taken at high magnification of such an oxide particle.

It is also interesting to note that elsewhere in Figure 3.27(b), the phosphorus concentration appears to correspond to the CuAl<sub>2</sub> particle areas seen in the backscattered image. This supports our previous observations regarding Figure 3.19 that AlP particles located underneath the copper phase also contribute to CuAl<sub>2</sub> segregation.

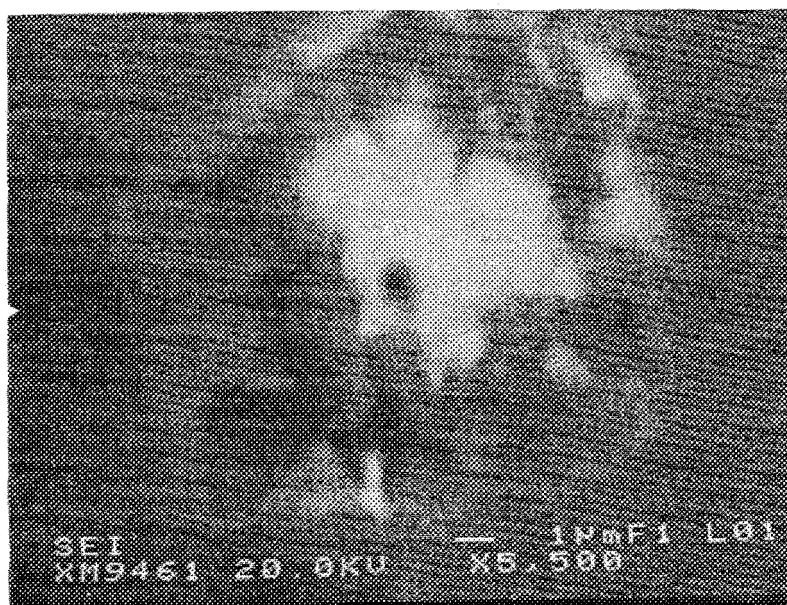


**Figure 3.28.** High magnification secondary electron image of a phosphorus oxide particle.

### 3.3.6 Precipitation of $\text{Cu}_2\text{FeAl}_7$ Phase

As reported in the section 3.3.3, when the 319 alloy containing 1% Fe (ASCF alloy) was annealed at 505 °C, complete dissolution of  $\text{CuAl}_2$  was achieved after 24 h (as determined from optical microscopic observations and image analysis measurements). Figure 3.29(a) shows the backscattered image obtained from the same alloy sample, after a 100-hour annealing time, revealing the presence of another copper phase precipitating on the  $\beta\text{-Al}_5\text{FeSi}$  phase platelets. Figure 3.29(b) and Figure 3.29(c) are the corresponding X-ray images of Cu and Fe.

Table 3.10 shows the chemical composition of the new copper phase that was observed, using spot analysis taken from different such particles in the microstructure. The approximate composition was found to be  $\text{Cu}_{2.1}\text{FeAl}_{7.6}$ , which is very close to the equilibrium composition of  $\text{Cu}_2\text{FeAl}_7$ .

It ought to be mentioned here that, while this copper phase was always observed on the  $\beta\text{-Al}_5\text{FeSi}$  phase, the size and volume fraction of the phase were strongly related to the amount of Fe present in the alloy.

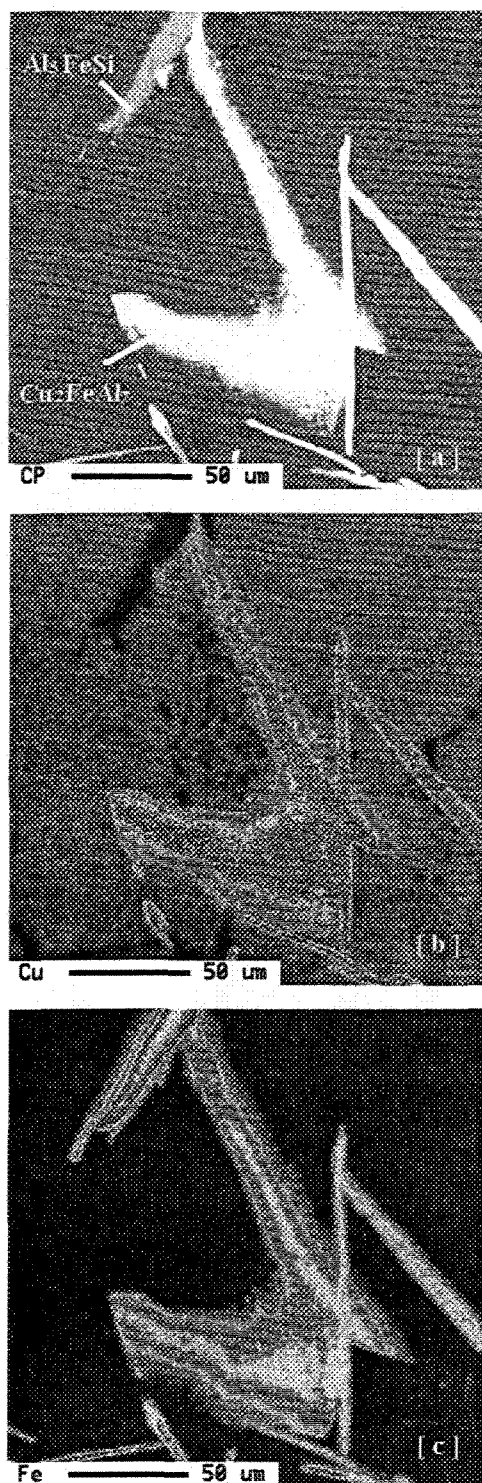


**Figure 3.29.** (a) Backscattered image of a  $\text{Cu}_2\text{FeAl}_7$  particle precipitating on a  $\beta\text{-Al}_5\text{FeSi}$  platelet, and corresponding X-ray images of (b) Cu and (c) Fe.

**Table 3.10.** Spot analysis of the new copper phase

Spot No.	Element	Weight pct	Atomic pct	Approx. Composition
1	Al	55.95	60.08	$\text{Cu}_{2.1}\text{FeAl}_{7.4}$
	Cu	31.28	17.26	
	Fe	12.93	8.12	
2	Al	52.40	69.70	$\text{Cu}_{2.1}\text{FeAl}_{7.7}$
	Cu	34.31	19.38	
	Fe	14.13	9.08	
3	Al	53.46	70.25	$\text{Cu}_{2.1}\text{FeAl}_{7.8}$
	Cu	34.11	19.03	
	Fe	14.12	8.97	
4	Al	52.75	69.75	$\text{Cu}_{2.1}\text{FeAl}_{7.6}$
	Cu	34.39	19.31	
	Fe	14.29	9.18	

## **CHAPTER 4**

# **TENSILE AND IMPACT PROPERTIES OF 319 ALLOYS**

## CHAPTER 4

### TENSILE AND IMPACT PROPERTIES OF 319 ALLOYS

#### 4.1 INTRODUCTION

The 300 series (Al-Si) casting alloys are being widely used in many automotive components. Alloys of this type combine excellent mechanical properties and high corrosion resistance with good castability. There have been a large number of tensile studies on 356-type aluminum alloys reported to date.<sup>40,89</sup> According to these studies, the tensile properties of 356-type alloys are strongly dependent on the effect of secondary dendrite arm spacing (SDAS), porosity level, and the heat treatment given to the alloys. Also, it has been found that the addition of certain elements or modifiers to the Al-Si alloys greatly affects the mechanical properties. Modification treatment results in a finely distributed Si phase throughout the aluminum matrix, with a consequent increase in alloy strength and ductility.

The mechanical properties of 319 alloy castings are essentially controlled by the secondary dendrite arm spacing and silicon particle morphology. Only recently have the users of 319 alloy castings realized the importance of fracture, fatigue, and impact property data in optimizing design parameters, where impact strength can provide a useful estimation of the ductility of an alloy under conditions of rapid loading. While it is well

known that various heat treatment procedures will provide a wide range of mechanical and physical properties. Recent studies have indicated that strontium modification can substantially lower heat treatment times,<sup>25</sup> which can lead to a significant decrease in the overall cost of the finished 319 alloy component. In addition, impact values depend strongly on the testing technique used and in particular on the size and shape of the specimens.<sup>90</sup>

In the present work, impact specimens were tested unnotched in order to increase the accuracy of the measurements and emphasize the effect of the microstructure. For brittle materials, the impact strength is very low and will decrease even further with the presence of a notch which may lower the impact values by up to 50%. Also if a notch is present, the absorbed energy may be more dependent on the notch geometry than on the microstructure.<sup>91</sup>

The use of instrumented impact testing equipment in our work allowed the fracture response of the impact specimen to be studied in terms of the total absorbed fracture energy. The results are discussed in terms of the influence of the microstructure on the impact strength of the alloy. At the same time, in order to obtain a better understanding of the relationship between impact strength and tensile strength, total absorbed energy vs. percent elongation and ultimate tensile strength plots have been presented.

In order to establish the relationship between different element additions (*i.e.* Fe, P, and Sr) and the tensile and impact properties of 319 Al-Si-Cu alloys, two different heat treatments (*i.e.* T5 and T6) were also incorporated in the study.

## 4.2 EXPERIMENTAL PROCEDURE

### 4.2.1 Casting Material

In this part of the work, industrial 319.2 alloy was used as the base alloy. The 319.2 alloy ingots were cut into small pieces and dried. For each casting, 6 kg of base alloy were melted in a 7-kg capacity SiC crucible heated by means of an electrical resistance furnace. At the same time, 28 g of (Al-5%Ti-1%B) master alloy were added to the melt for grain refining purposes. The melting temperature was kept at  $730\text{ }^{\circ}\text{C} \pm 5\text{ }^{\circ}\text{C}$ . Strontium was added in the form of Al-10%Sr master alloy (150-200 ppm Sr). Iron was introduced in the form of Al-25%Fe master alloy (0.4% or 1.2% Fe levels). Phosphorus was added in the form of Cu-8%P brazing alloy (15 ppm P). In order to fully dissolve the phosphorus during melting, the melting temperature was increased to  $850\text{ }^{\circ}\text{C}$  after a Cu-8%P brazing rod was added, maintained for about 10 minutes, then decreased to  $\sim 730\text{ }^{\circ}\text{C}$ . The corresponding alloys thus obtained and their respective codes are listed in Table 4.1. Six castings were prepared for each alloy.

**Table 4.1.** Codes of the alloys used in the present work

Alloy Code	Composition
AW	Al-7%Si-3.5%Cu (base alloy)
BW	Base Alloy + 0.4%Fe + Sr
CW	Base Alloy + Sr
DW	Base Alloy + 1.2%Fe + Sr
EW	Base Alloy + 1.2%Fe
FW	Base Alloy + 1.2%Fe + Sr + P

Prior to casting, each alloy melt was degassed for ~15 minutes using dry argon to ensure a homogeneous mixing of the additions and the removal of hydrogen as well as inclusions. The liquid metal was then poured into a rectangular refractory mold (shown in Figure 4.1). Prior to casting, the mold was dried at 150 °C for 2 h to remove moisture. In order to study the effect of directional solidification, a copper chill was employed at the bottom of the mold through which cold water was circulated. This kind of casting was specifically designed to produce a wide range of solidification times and secondary dendrite arm spacings along the height of the casting above the chill end.

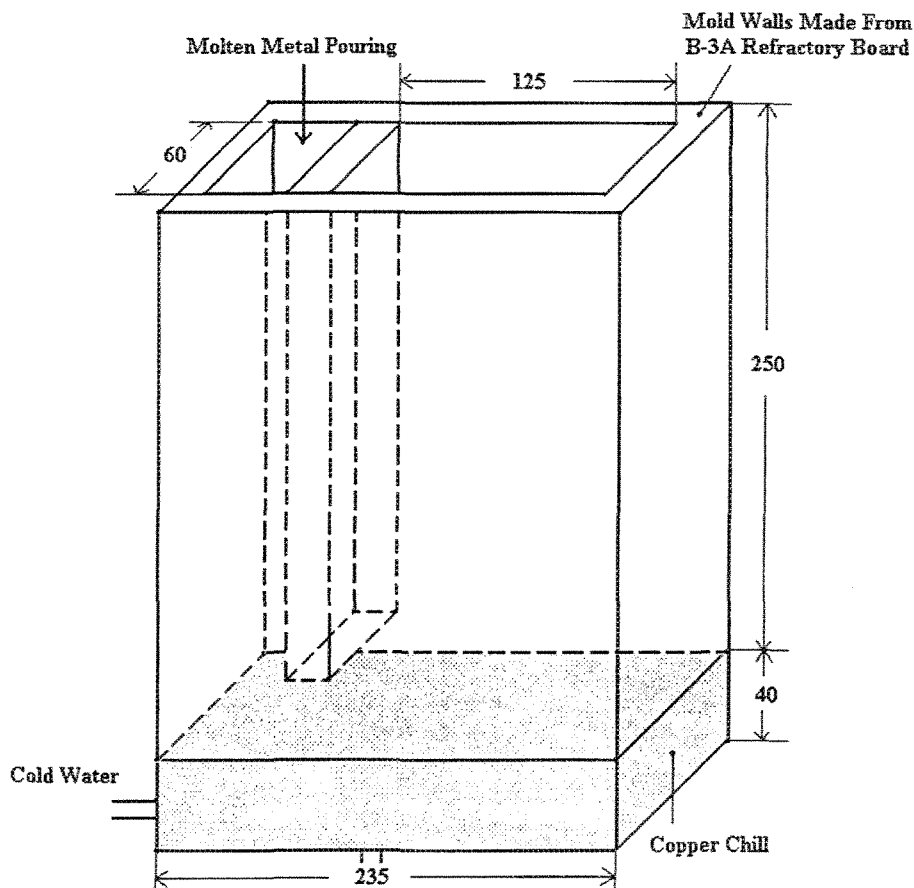


**Figure 4.1.** Schematic diagram of the end-chilled mold used to prepare the castings (All dimensions are in mm).

Samples for chemical analysis were taken for each melt condition. The actual chemical compositions of the studied alloys, as obtained from chemical analysis, are listed in Table 4.2.

**Table 4.2.** Actual chemical composition (wt%) of the alloys studied in the present work

Alloy Code	Main Elements			
	Cu	Fe	Sr	P
AW	3.608	0.105	–	–
BW	3.568	0.406	0.010	–
CW	3.554	0.094	0.022	–
DW	3.355	1.269	0.027	–
EW	3.298	1.360	–	–
FW	3.653	1.408	0.025	0.015

Each casting was machined to obtain 4 rectangular blanks as shown in Figure 4.2. Specimen blanks were sectioned at heights of 10, 30, 50 and 100 mm above the chill end of each casting (referred to as levels 1, 2, 3 and 4, respectively), corresponding to secondary dendrite arm spacings (SDAS) that ranged from 23  $\mu\text{m}$  to 83  $\mu\text{m}$ . The secondary dendrite arm spacings obtained from the different levels are shown in Table 4.3. It should be noted here that the secondary dendrite arm spacing (SDAS) is often quoted in the literature (and in the present case) simply as DAS.

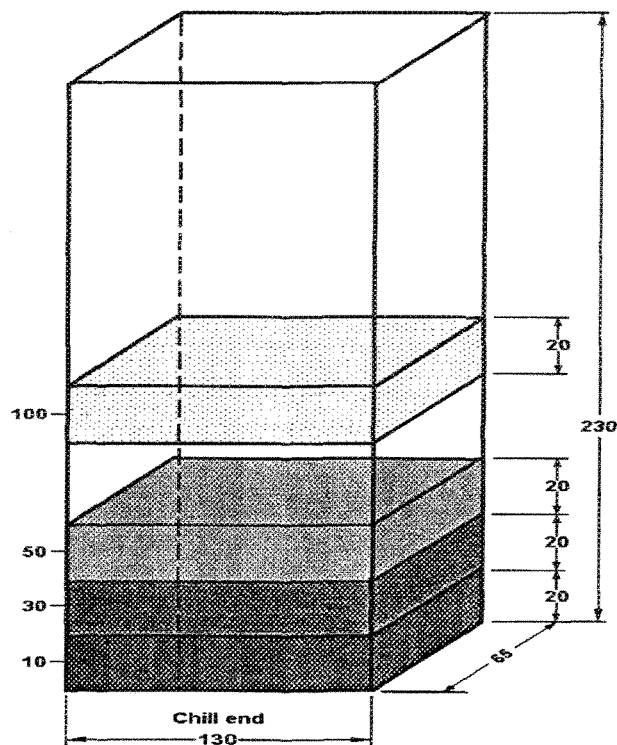


**Figure 4.2.** End-chill casting showing specimen blanks sectioning scheme (All dimensions are in mm).

**Table 4.3.** DAS values obtained at various levels of the end-chilled castings for the six alloys studied

Level #	Distance From Chill End (mm)	DAS ( $\mu\text{m}$ )
1	10	23
2	30	47
3	50	60
4	100	83

#### 4.2.2 Heat Treatment

The six castings prepared for each of the alloys listed in Table 4.1 were divided into two groups, *i.e.* group I that included: AW1, AW2, and AW5 castings, and group II that

included: AW3, AW4, and AW6 castings, and so on. The rectangular specimen blanks sectioned from the group I castings were subjected to T5 heat treatment as follows:

- 1) 5 hours of ageing at 155 °C;
- 2) air cooling.

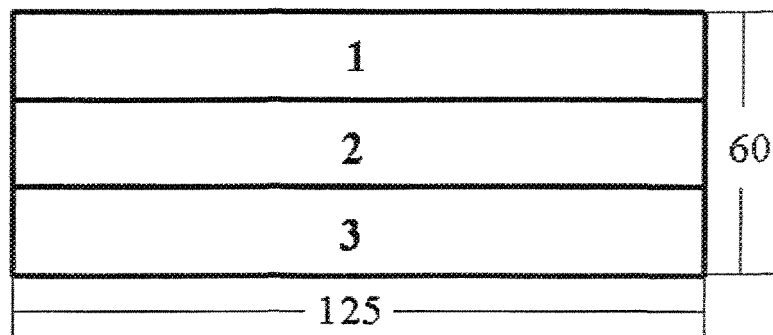
For the blanks of group II castings, T6 heat treatment was applied:

- 1) solution heat treatment for 8 hours at  $490 \pm 2$  °C;
- 2) quenching in warm water (60 °C);
- 3) immediate ageing for 5 hours at 155 °C;
- 4) air cooling.

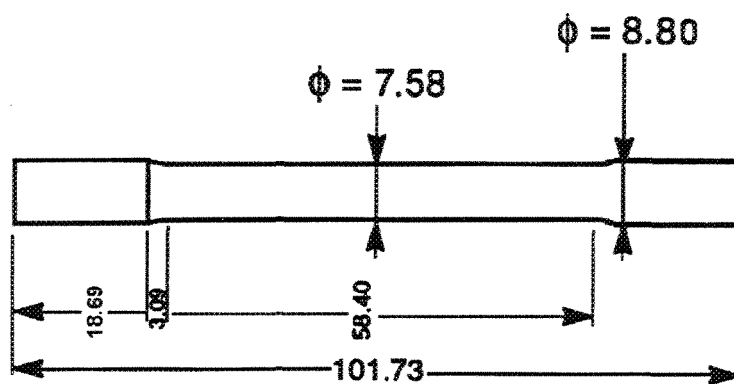
All heat treatments were conducted in an air-forced electric furnace (where the temperature could be controlled within  $\pm 2$  °C). The warm water used for quenching was changed frequently to ensure that the water temperature was always  $\sim 60$  °C.

#### **4.2.3 Tensile Testing**

Samples for tensile testing were machined from the heat-treated rectangular blanks. Each blank was cut into three longitudinal bars as shown in Figure 4.3(a). These bars were further machined into the form of test samples with precise dimensions (Figure 4.3(b)). The machined samples were polished with fine sandpaper to remove any machining marks from the sample surface.



[ a ]



[ b ]

**Figure 4.3.** a) Schematic diagram of blank used for preparing tensile test specimens, b) dimensions of the tensile test specimen (All dimensions are in mm).

Tensile tests were conducted at room temperature using a mechanical Instron Universal testing machine at a strain rate of  $2 \times 10^{-4}$  m/s. Prior to testing, a precision alignment device was used to minimize frame bending strains. Six tensile specimens were tested corresponding to each of the four levels (DAS values: 23, 47, 60, and 83  $\mu\text{m}$ ).

#### 4.2.4 Impact Testing

A data acquisition system was connected to a conventional pendulum impact machine to monitor the dynamic behavior of the test specimen and to measure the load and energy value as a function of time (shown in Figure 4.4). The total absorbed energy ( $E_t$ ) during impact testing was determined, as well as some specific parameters such as crack initiation and propagation energies, and the maximum load required to break the specimens.

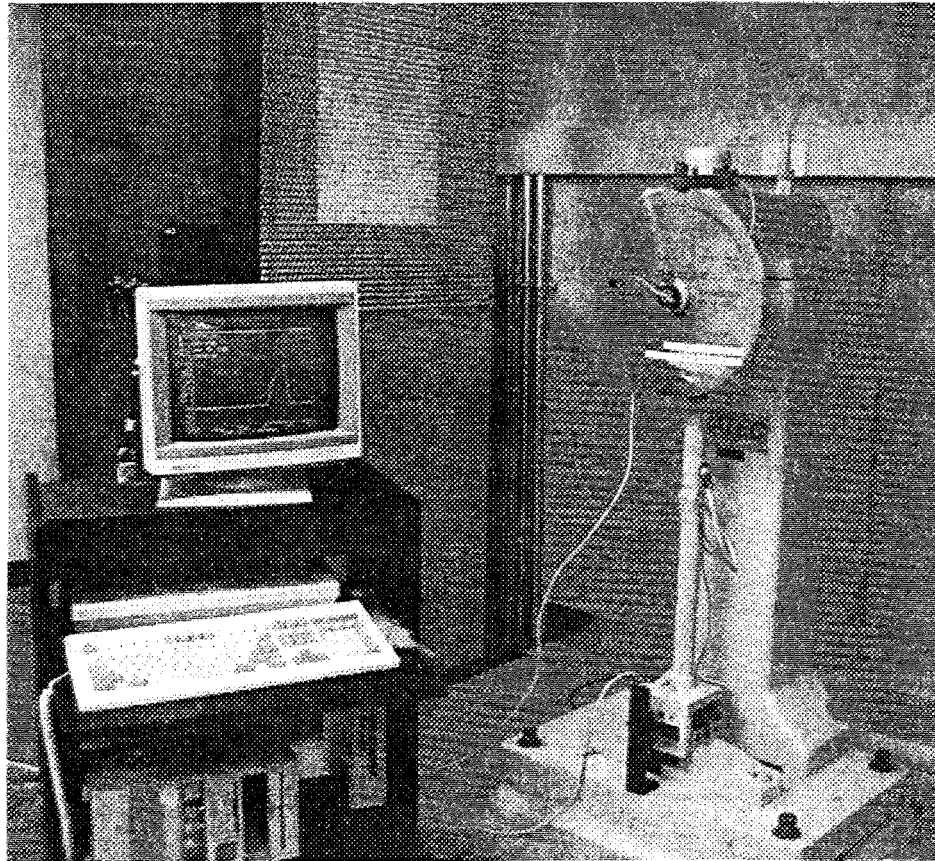


**Figure 4.4.** Impact machine connected to a data acquisition system.

Impact testing was performed on unnotched samples that were machined from rectangular blanks corresponding to the same six alloys studied. Each blank was sectioned into six small bars as shown in Figure 4.5(a). The impact test specimens were machined from these bars according to the dimensions shown in Figure 4.5(b). As before, the specimen surfaces were polished with fine sandpaper to remove any machining marks.

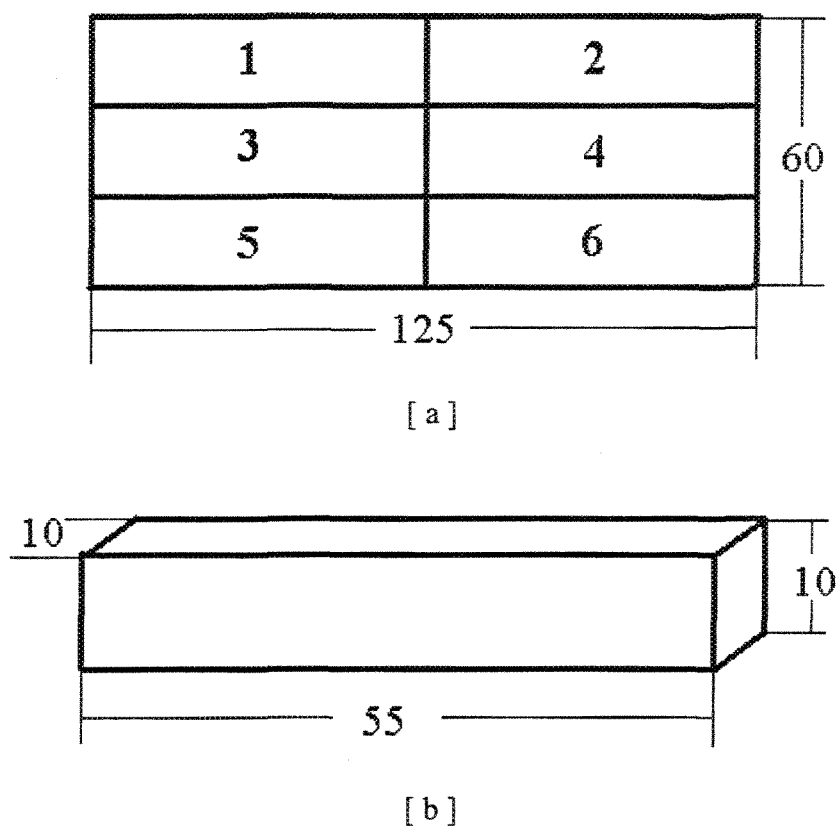


**Figure 4.5.** a) Schematic diagram of the blank used for preparing the impact testing specimens, b) dimensions of the impact testing specimen (All dimensions are in mm).

#### 4.2.5 Image Analysis

In order to emphasize the effect of the  $\text{CuAl}_2$  phase on the tensile properties of the studied alloys, the amount of undissolved  $\text{CuAl}_2$  particles in the test samples of level 1 and level 4 were measured after the T5 and T6 heat treatments. Samples for metallographic examination were sectioned from the broken tensile test specimens, away from the fractured surfaces. The sectioned samples were mounted in bakelite, and polished to a fine finish (1  $\mu\text{m}$  diamond paste). Optical micrographs were taken at magnifications of 750X.

Microstructural changes—mainly the amount of the undissolved  $\text{CuAl}_2$  phase for the highest and the lowest cooling rates applied, *i.e.* 23  $\mu\text{m}$  and 83  $\mu\text{m}$  DAS—were quantified using a Leco 2001 image analyzer in conjunction with an optical microscope. In each case, 25 fields were analyzed over the entire sample surface. From these readings, the average area percent of the undissolved  $\text{CuAl}_2$  phase was determined for each condition. In the same way, the percentage of porosity in these samples was also evaluated in order to study its contribution to the mechanical properties.

The eutectic Si particles characteristics, *viz.* particle size, roundness, area percent, in the AW (base alloy), CW (Sr-modified) and DW (Sr-modified and high Fe level) alloys, were also measured. For these measurements, 20 fields were analyzed over the whole sample surface at a magnification of 200X.

## 4.3 RESULTS AND DISCUSSION

### 4.3.1 Microstructure

The results of the present investigation suggest that microstructure has an important influence on the mechanical properties of 319 Al-Si-Cu alloys. The tensile and impact values vary as a function of the structural fineness, the morphology and the size of the microstructural constituents, as well as porosity. The microstructure is also affected by the type of heat treatment employed.

#### 4.3.1.1 T5 heat treatment

Typical microstructures of the base alloy (AW alloy) in the T5 heat treatment condition are presented in Figure 4.6. At a DAS of 23  $\mu\text{m}$ , the AW alloy exhibits the presence of small acicular eutectic silicon particles well dispersed throughout the aluminum matrix, along with fine eutectic (Al+CuAl<sub>2</sub>) particles, Figure 4.6(a). The microstructure shown in Figure 4.6(b), corresponding to a DAS of 83  $\mu\text{m}$ , reveals much coarser and larger Si and CuAl<sub>2</sub> particles than those observed in the 23  $\mu\text{m}$  DAS case.

Figure 4.7 presents the microstructures of CW alloy (Sr-modified) at different cooling rates. In the presence of Sr, the morphology of the Si particles has changed from a coarse, flake-like form to a fine fibrous one, which is reflected by the image analysis results shown in Table 4.4. In addition to the modification of the silicon phase, Sr-modification also leads to the formation of more of the block-like CuAl<sub>2</sub>, although dispersed CuAl<sub>2</sub> particles are also observed. In some cases, the CuAl<sub>2</sub> is segregated to certain regions away from the modified eutectic Si particles, as shown in Figure 4.7(b). From Table 4.4, it can also be

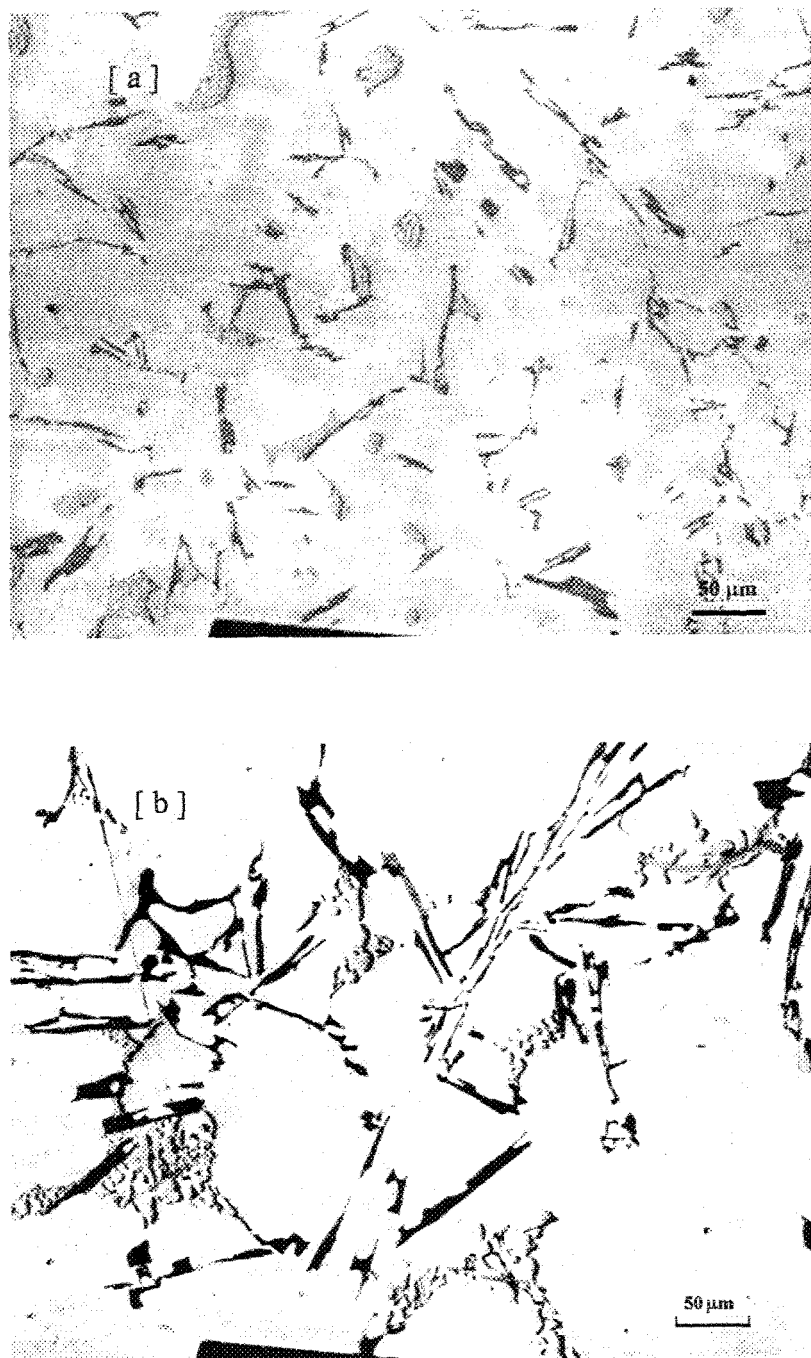


**Figure 4.6.** Optical micrographs showing microstructures of AW alloy after T5 heat treatment obtained at cooling rates corresponding to: a) 23  $\mu\text{m}$  DAS, b) 83  $\mu\text{m}$  DAS.

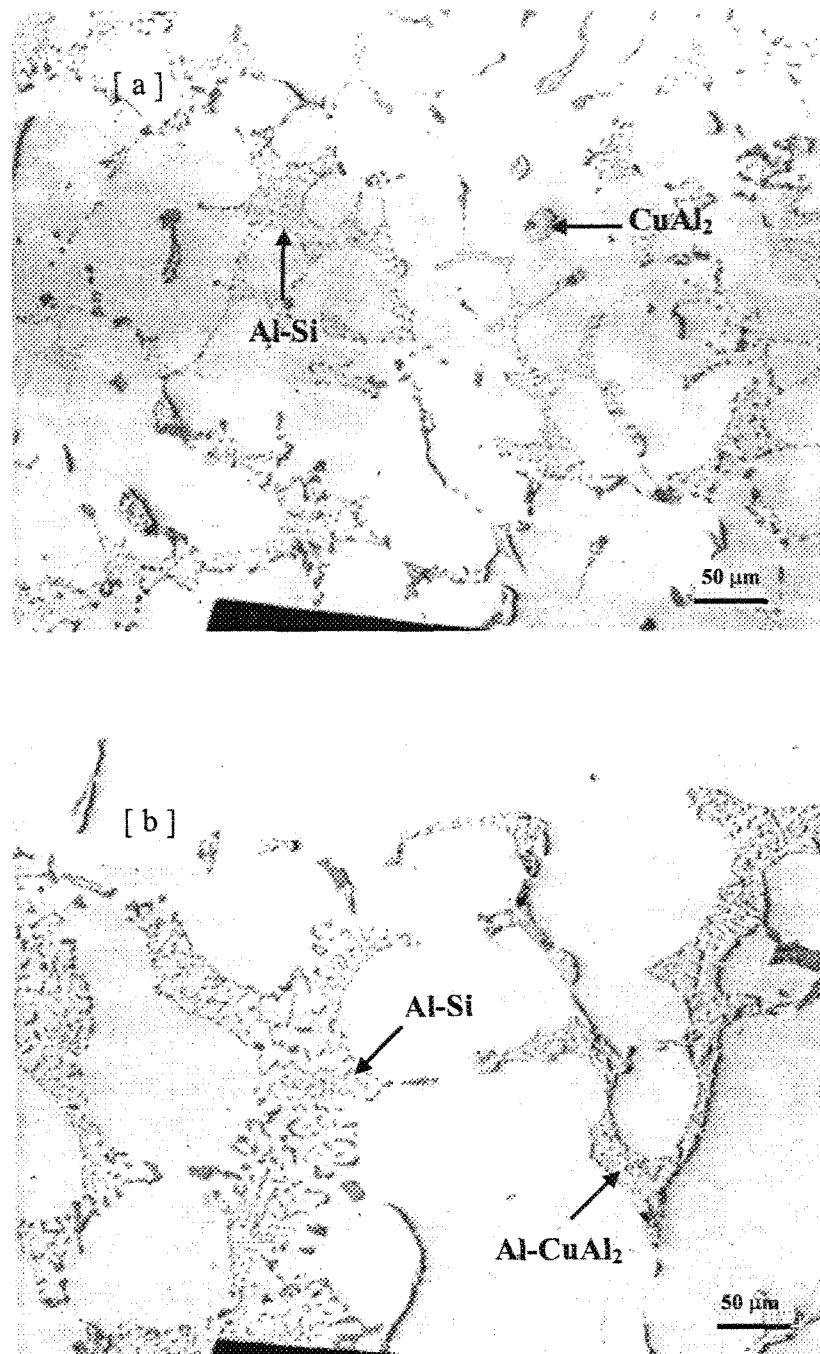


**Figure 4.7.** Optical micrographs showing microstructures of CW alloy after T5 heat treatment obtained at cooling rates corresponding to: a) 23 μm DAS, b) 83 μm DAS.

**Table 4.4.** Eutectic Si particle characteristics observed in AW, CW and DW alloy samples (T5 condition)

Alloy Code	DAS ( $\mu\text{m}$ )	Area %	Length ( $\mu\text{m}$ )	Aspect Ratio	Roundness
AW	23	$6.65 \pm 0.83$	$10.87 \pm 12.04$	$2.54 \pm 1.36$	$60.82 \pm 28.68$
	83	$7.15 \pm 1.07$	$15.00 \pm 18.82$	$2.54 \pm 1.42$	$58.50 \pm 32.03$
CW	23	$6.48 \pm 0.99$	$3.58 \pm 3.04$	$1.79 \pm 0.70$	$81.51 \pm 21.32$
	83	$5.73 \pm 1.36$	$4.81 \pm 5.89$	$1.91 \pm 0.80$	$80.36 \pm 22.04$
DW	23	$5.42 \pm 1.13$	$2.45 \pm 2.38$	$1.98 \pm 0.82$	$73.61 \pm 23.63$
	83	$6.47 \pm 1.45$	$3.30 \pm 3.78$	$1.86 \pm 0.72$	$75.63 \pm 22.15$

seen that, the presence of Fe (in the form of  $\beta\text{-Al}_5\text{FeSi}$  platelets) in the DW alloy leads to further refinement of the Si particles, in terms of the decrease in the average length.

The microstructure of DW alloy has an obvious characteristic that is not present in the AW and CW alloys, as shown in Figure 4.8: large needle-like  $\beta\text{-Al}_5\text{FeSi}$  intermetallics appear all over the matrix, and this is reflected in the tensile and impact behavior of the alloy.

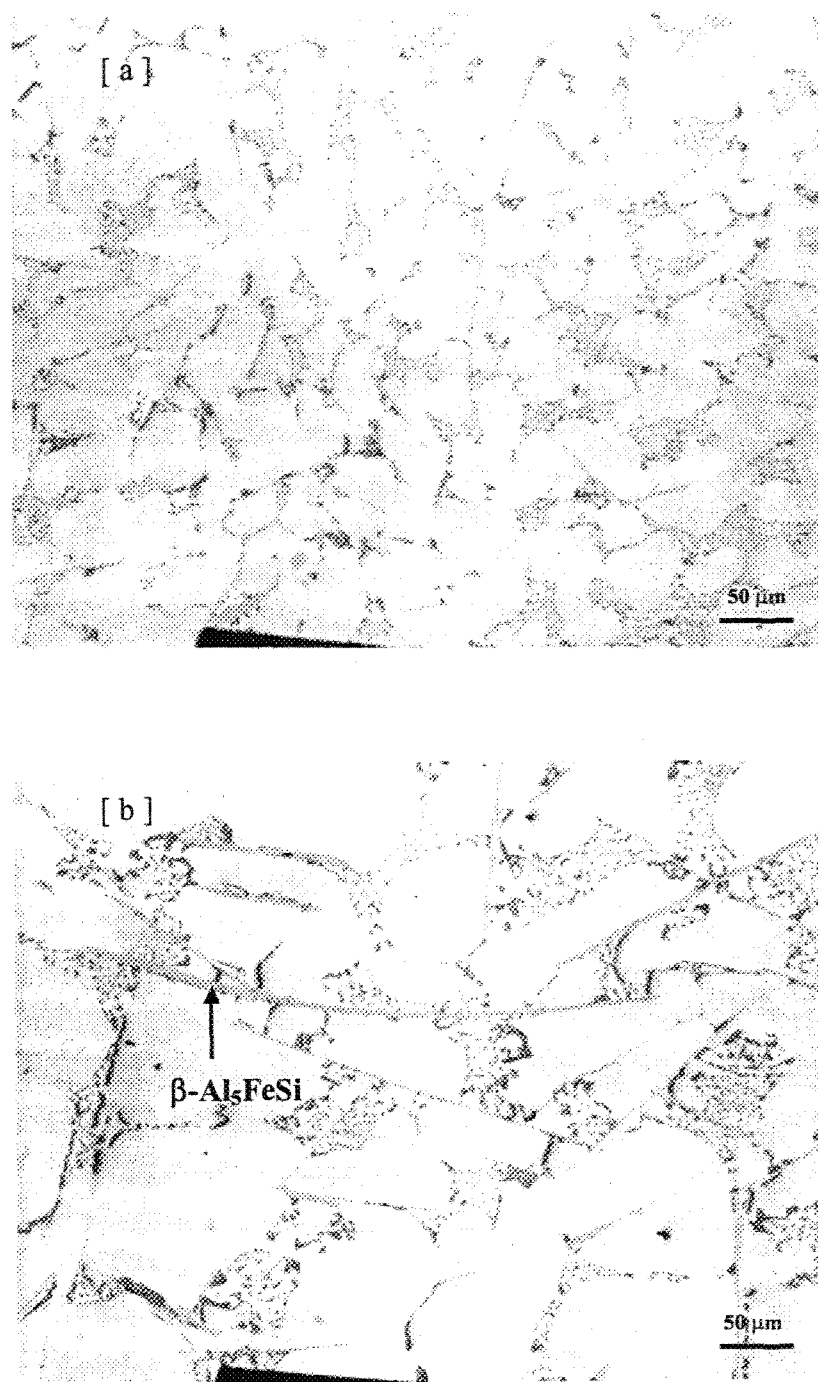


**Figure 4.8.** Optical micrographs showing microstructures of DW alloy after T5 heat treatment obtained at cooling rates corresponding to: a) 23  $\mu\text{m}$  DAS, b) 83  $\mu\text{m}$  DAS.

#### 4.3.1.2 T6 heat treatment

The T6 treatment consists of an extended solution treatment to reduce the angularity of interdendritic phases. The influence of solution treatment on the morphology of interdendritic Si particles in Al-Si alloys has been well documented.<sup>24,92</sup> As seen from Figure 4.9 (AW alloy), except for the dissolution of the  $\text{CuAl}_2$  phase particles, the Si particles underwent spheroidization and coarsening. It ought to be noted here that the solution temperature ( $490 \pm 2$  °C) was not high enough to cause complete fragmentation of the Si particles. Also, the image analysis data for the Si particles is very similar to that observed for the T5 heat-treated alloy, (*cf.* Table 4.4 and Table 4.5), in that the average length of the Si particles is not significantly changed. Figure 4.10 presents the microstructure of CW alloy (Sr-modified) at the highest and lowest cooling rates (23  $\mu\text{m}$  DAS and 83  $\mu\text{m}$  DAS). Fine fibrous silicon particles are observed well dispersed throughout the entire matrix. Compared to the morphology of the Si particles observed the T5 heat-treated CW alloy, the Si particles in this case display a slight spheroidization, accompanied by the dissolution of  $\text{CuAl}_2$  particles. The amounts of undissolved  $\text{CuAl}_2$  particles at the highest and lowest cooling rates for each studied alloy are listed in Table 4.6. However, the iron intermetallics did not exhibit marked detectable changes during solution treatment in the T6 heat treatment case (Figure 4.11).

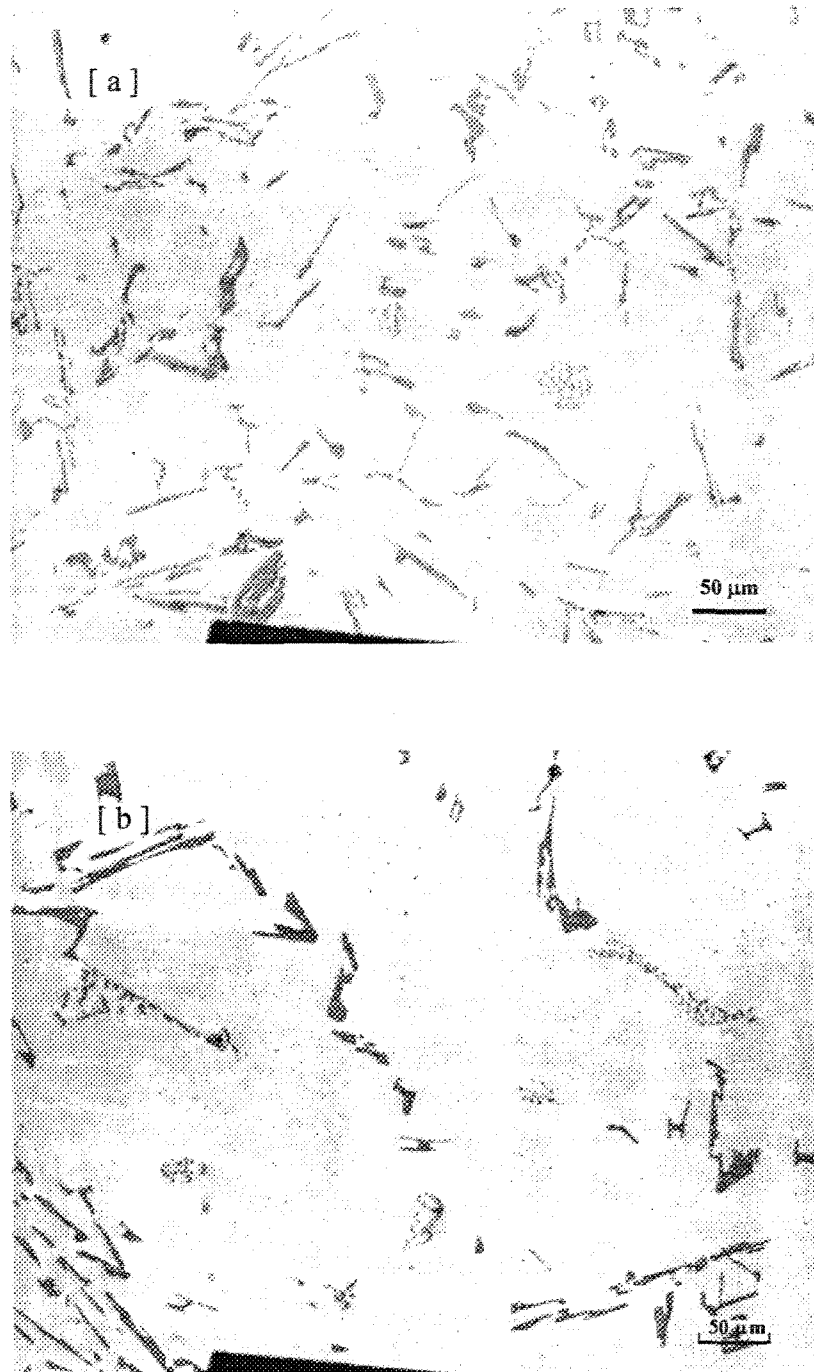


**Figure 4.9.** Optical micrographs showing microstructures of AW alloy after T6 heat treatment obtained at cooling rates corresponding to: a) 23 μm DAS, b) 83 μm DAS.

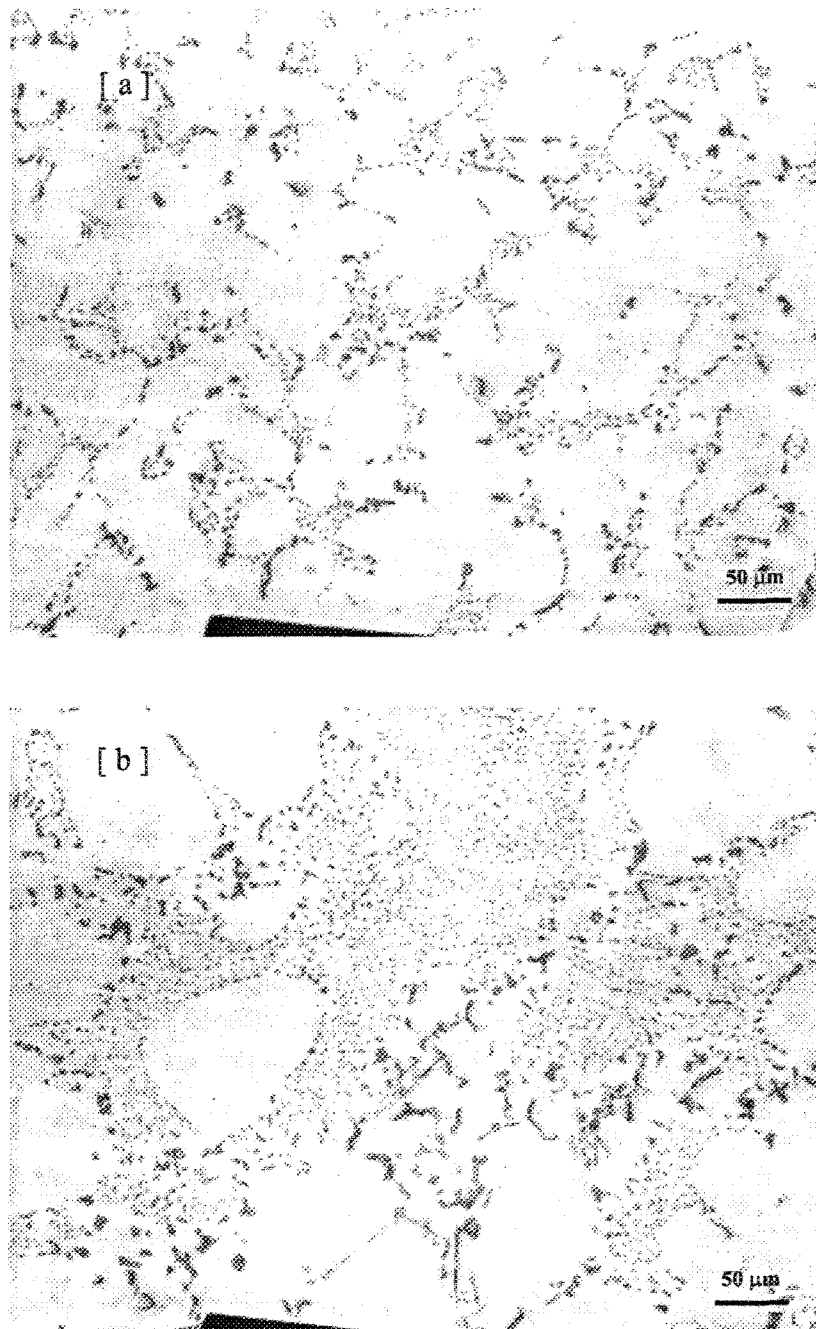


**Figure 4.10.** Optical micrographs showing microstructures of CW alloy after T6 heat treatment obtained at cooling rates corresponding to: a) 23  $\mu\text{m}$  DAS, b) 83  $\mu\text{m}$  DAS.

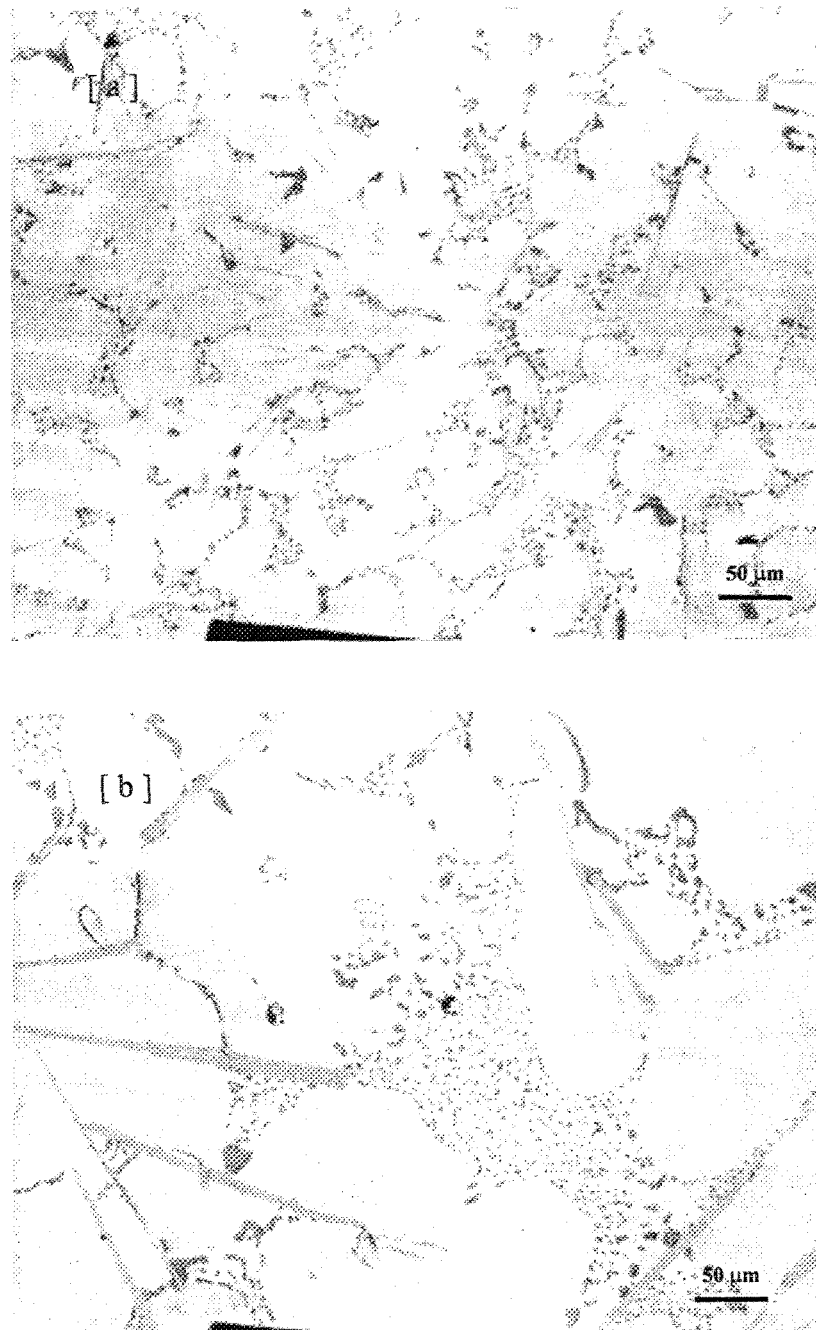


**Figure 4.11.** Optical micrographs showing microstructures of DW alloy after T6 heat treatment obtained at cooling rates corresponding to: a) 23  $\mu\text{m}$  DAS, b) 83  $\mu\text{m}$  DAS.

**Table 4.5.** Eutectic Si particle characteristics observed in AW, CW and DW alloy samples (T6 condition)

Alloy Code	DAS ( $\mu\text{m}$ )	Area %	Length ( $\mu\text{m}$ )	Aspt Ratio	Roundness
AW	23	$6.40 \pm 1.10$	$10.91 \pm 14.16$	$2.47 \pm 1.31$	$59.70 \pm 29.45$
	83	$6.92 \pm 1.60$	$14.75 \pm 17.24$	$2.61 \pm 1.50$	$57.81 \pm 31.58$
CW	23	$5.62 \pm 0.65$	$3.79 \pm 3.88$	$1.72 \pm 0.63$	$84.31 \pm 18.48$
	83	$6.69 \pm 1.99$	$4.85 \pm 4.96$	$1.78 \pm 0.72$	$82.82 \pm 19.64$
DW	23	$5.27 \pm 1.13$	$2.68 \pm 3.28$	$1.74 \pm 0.66$	$79.52 \pm 19.27$
	83	$5.90 \pm 1.75$	$3.75 \pm 5.47$	$1.79 \pm 0.67$	$76.09 \pm 21.27$

**Table 4.6.** Amount of undissolved  $\text{CuAl}_2$  phase observed at the highest and lowest cooling rates in the six studied alloys

Alloy Code	DAS ( $\mu\text{m}$ )	Amount of Undissolved $\text{CuAl}_2$ Phase			
		T5 Heat Treatment		T6 Heat Treatment	
		Area %	SD	Area %	SD
AW	23	1.69	1.05	0.57	0.61
	83	3.65	1.91	1.43	1.11
BW	23	1.41	0.89	0.46	0.29
	83	1.92	0.86	0.98	0.81
CW	23	1.53	1.06	0.64	0.67
	83	2.64	1.49	1.40	1.10
DW	23	1.32	0.77	0.41	0.35
	83	2.21	1.27	1.07	0.92
EW	23	0.86	0.49	0.40	0.35
	83	1.76	0.98	0.91	0.99
FW	23	1.25	0.91	0.41	0.36
	83	1.95	1.47	1.44	1.16

### 4.3.1.3 Porosity

Porosity in Al-Si castings occurs because of the negative pressure generated by solidification contraction, as well as the pressure from the evolution of dissolved hydrogen from the growing solid into the adjacent liquid. Emadi *et al.*<sup>93</sup> have indicated that Sr reduces the surface tension of the melt and increases the volumetric shrinkage, thus facilitating porosity formation. This viewpoint can be verified by comparing the area percentage porosity of AW and CW alloys in Table 4.7. As can be seen from the table, the porosity increases from 1.33% in the base AW alloy to 2.32% in the Sr-modified CW alloy (at 83  $\mu\text{m}$  DAS).

**Table 4.7.** Area percentage of porosity in the alloys studied

Alloy Code	DAS ( $\mu\text{m}$ )	Area % of Porosity (average value of T5 and T6)	
		Area %	Standard Deviation
AW	23	0.35	0.39
	83	1.33	2.59
BW	23	0.59	0.48
	83	1.70	2.10
CW	23	0.82	0.49
	83	2.32	3.01
DW	23	0.32	0.26
	83	1.92	2.62
EW	23	0.38	0.30
	83	1.56	2.49
FW	23	0.80	0.45
	83	1.83	3.18

It has been observed that a decrease in the cooling rate (*i.e.* increase in DAS) increases both the total amount of porosity and the average pore size in both modified and unmodified Al-Si alloy castings.<sup>94</sup> Fang and Granger<sup>95</sup> have drawn the same conclusion in the case of modified and unmodified A356 alloys for a given melt hydrogen content. At increasing solidification rates, less time is available for hydrogen to diffuse into the interdendritic spaces of the partially solidified metal, resulting in smaller pore sizes. A recent study by Liu *et al.*<sup>96</sup> found that the increase in porosity content in Sr-treated alloys is mainly due to the presence of SrO particles.

In addition, the higher temperature gradients present during rapid solidification tend to limit the length of the mushy zone, making feeding easier and retarding porosity formation. Castings cooled at higher rates tend to contain less (and more finely dispersed) porosity, which is consistent with the results presented in Table 4.7. For each studied alloy, the area percentage porosity at high cooling rates (*i.e.* 23  $\mu\text{m}$  DAS) is much smaller than at low cooling rates (*i.e.* 83  $\mu\text{m}$  DAS). In the case of FW alloy (containing 1.4% Fe), the percentage porosity at 23  $\mu\text{m}$  DAS is relatively higher due to the precipitation of  $\beta\text{-Al}_5\text{FeSi}$  platelets.

The effect of porosity on the mechanical properties of castings has been investigated in several studies. McLellan<sup>97</sup> found that increasing metal soundness in terms of porosity, results in a higher elongation to fracture in alloy A357. Another example of the deleterious effect of hydrogen porosity on the yield strength and ultimate tensile strength of sand cast 356-T6 aluminum castings was reported by Traenkner<sup>98</sup>, where both UTS and YS were found to decrease with the increase in porosity. Furthermore, Surappa *et al.*<sup>99</sup> showed that

the decrease in the elongation to fracture could be related to the projected area of the pores on the fracture surface.

### 4.3.2 Tensile Properties

The obtained ultimate tensile strength (UTS), yield strength (YS) and percent elongation (%El) values were analyzed with respect to the various parameters involved, viz. cooling rate or DAS, amount of undissolved  $\text{CuAl}_2$  phase, alloying elements, and applied heat treatment. These variables will be discussed in the following sections. The relationship between UTS and %El was also analyzed in the form of UTS vs. %El, as well as  $\log\text{UTS}$  vs.  $\log\%El$  plots. Such representations were found to be successful in providing a fairly reasonable interpretation of the obtained results.

#### 4.3.2.1 T5 heat treatment

The tensile properties of T5 heat-treated bars as a function of cooling rate are shown in Figure 4.12 for the six alloys studied.

In general, yield strength, ultimate tensile strength and percent elongation are found to decrease with a decrease in the cooling rate (*i.e.*, increase in DAS) regardless of alloy composition. With a decrease in DAS, a finer dispersion of smaller microconstituents and porosity can be achieved. For example, the size and shape of the eutectic silicon are smaller and less acicular. This observation, known as quench modification, indicates the refinement of eutectic silicon particles at high growth rates, resulting from the change in molecular attachment kinetics.<sup>100</sup>

The dependence of ultimate tensile strength on cooling rates is shown in Figure 4.12(a). The higher the cooling rate, the higher the UTS value. The variation in UTS with the variation in cooling rate and alloy composition can be explained in terms of the size and distribution of both the  $\beta$ -iron intermetallics and eutectic Si particles.

The UTS of the BW alloy (*i.e.* base alloy with 100 ppm Sr and 0.4%Fe) is the highest among the six studied alloys, for the range of applied cooling rates. It is reasonable to propose that, at the small amount of Fe present in the base alloy, the hard  $\beta$ -Al<sub>5</sub>FeSi platelets are uniformly dispersed within the aluminum matrix, improving the UTS values to a certain extent. The change in the morphology of the eutectic Si particles in Sr-modified alloys from a coarse, flake-like form to a fine fibrous one is also a parameter to consider in explaining why the UTS of CW (*i.e.* base alloy with 220 ppm Sr) is higher than the UTS values obtained from the other alloys (except for the BW alloy).

For a given value of DAS, high UTS values are obtained from BW and CW alloys (containing 100-220 ppm Sr). From this, it can be concluded that the segregation of the CuAl<sub>2</sub> phase (as discussed in the Chapter 3) has no considerable negative effect on the alloy UTS. The high iron content (~1.2%) of the DW, EW and FW alloys is, however, definitely harmful to the UTS, especially at low cooling rates (which favor the growth of large  $\beta$ -platelets). In Figure 4.12(a), as seen in the 60  $\mu$ m and 83  $\mu$ m DAS cases, the UTS values of these three alloys are lower than those exhibited by the base AW alloy. Thus, it may be suggested that when 319 alloy contains high Fe additions, the UTS is controlled mainly by the brittle  $\beta$ -iron particles. Modification with Sr may improve alloy properties through partial fragmentation of the  $\beta$ -phase. However, this effect depends mainly on the Fe content

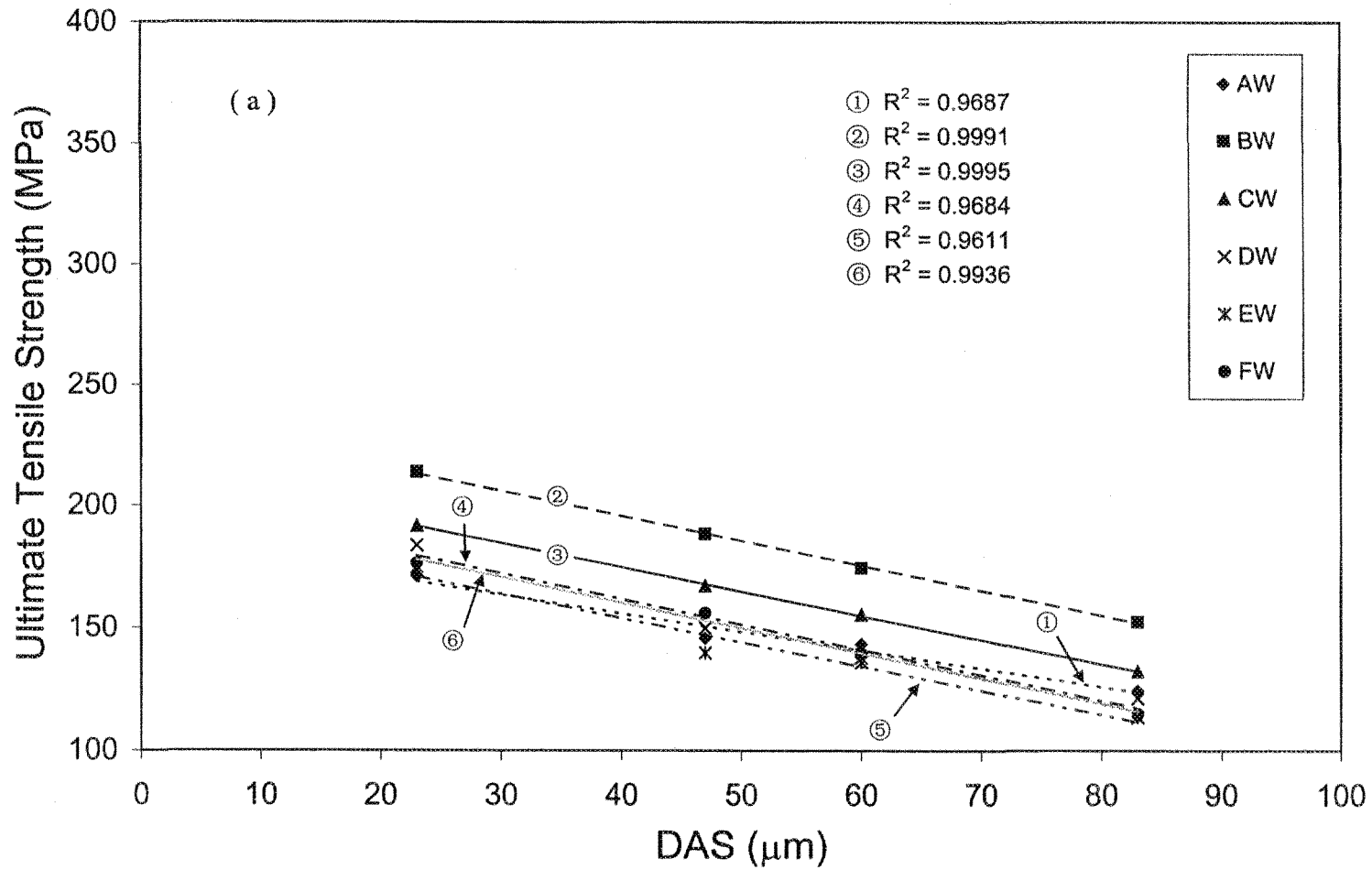


Figure 4.12. Tensile properties of the six alloys studied (T5 condition) as a function of DAS: a) Ultimate Tensile Strength, b) Yield Strength, c) % Elongation.

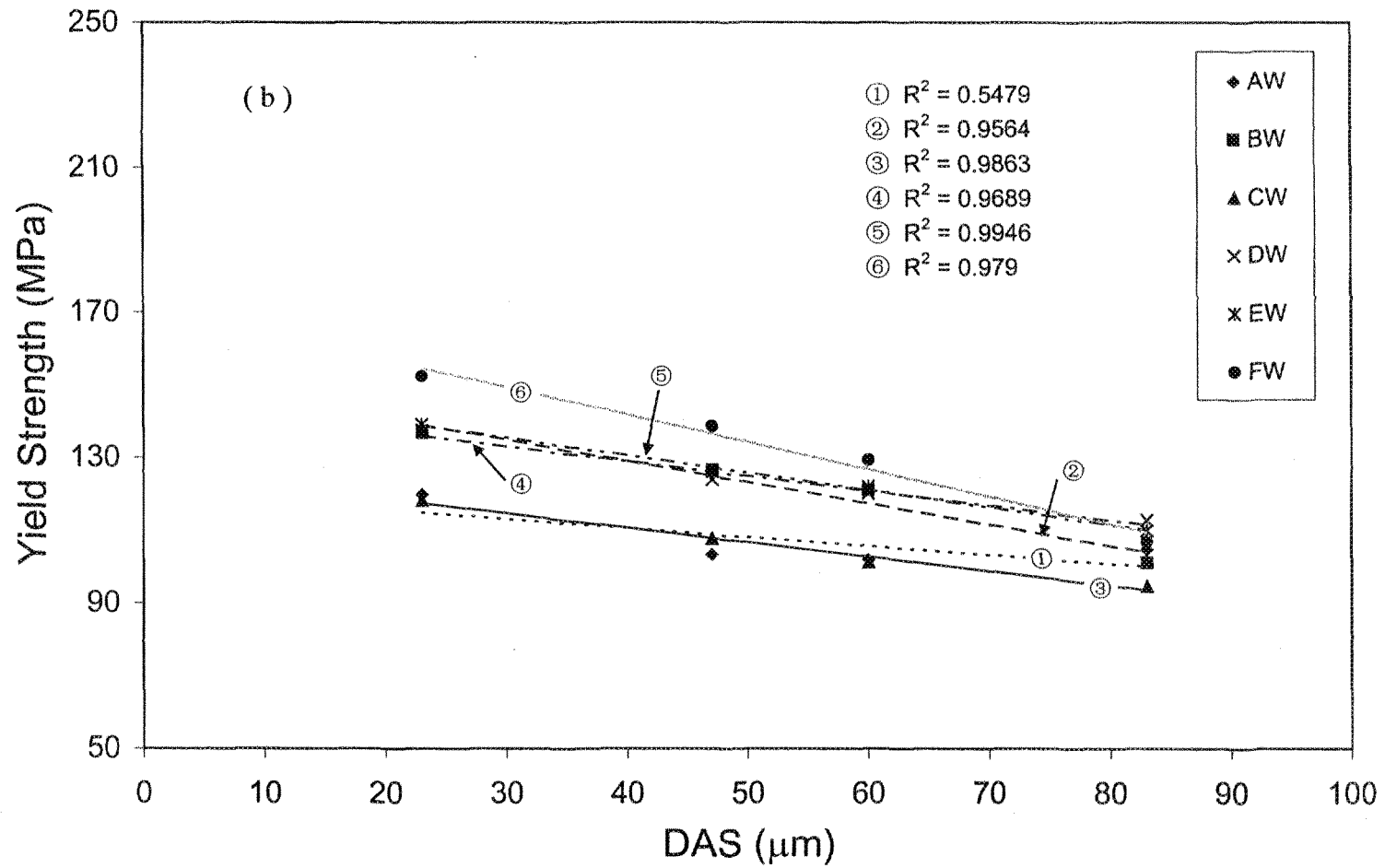


Figure 4.12. Tensile properties of the six alloys studied (T5 condition) as a function of DAS: a) Ultimate Tensile Strength, b) Yield Strength, c) % Elongation.

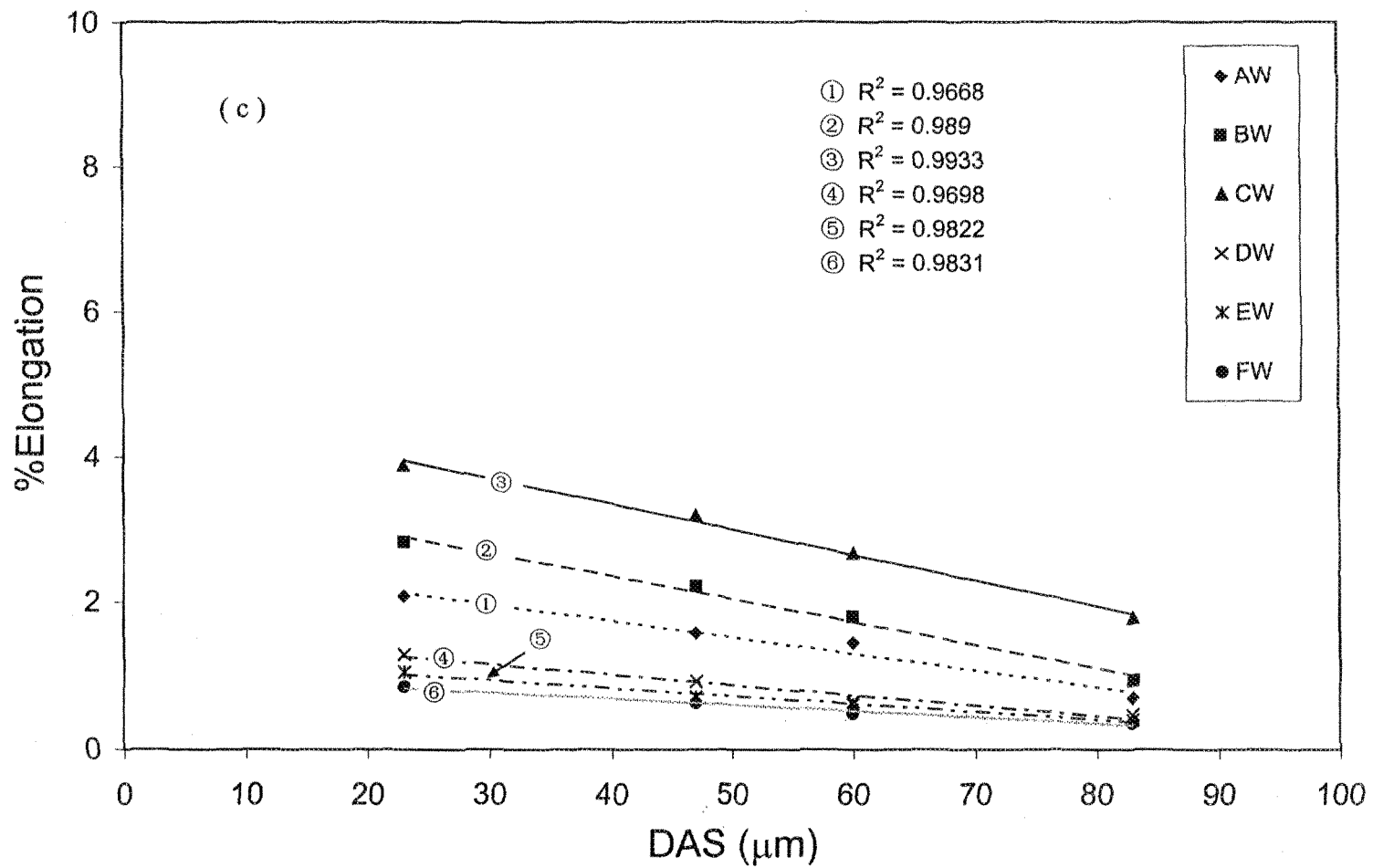


Figure 4.12. Tensile properties of the six alloys studied (T5 condition) as a function of DAS: a) Ultimate Tensile Strength, b) Yield Strength, c) % Elongation.

and cooling rate. It should be borne in mind that the UTS values obtained from all studied alloys fall within a narrow band of ~50 MPa width.

Figure 4.12(b) shows the relationship between yield strength and DAS, exhibiting behavior similar to that shown by the UTS vs. DAS relationship, in the sense that, with the decrease in the cooling rate (*i.e.* increase in DAS), yield strength decreases. For all alloys studied, the maximum decrease in YS was observed for FW alloy (*i.e.* from 152 MPa at 23  $\mu\text{m}$  DAS to 107 MPa at 83  $\mu\text{m}$  DAS, decrease by 29.6%). It also should be noted here that the yield strength of the FW alloy (base alloy with Sr, Fe, and P additions) is the highest, especially at high cooling rates, which is in contrast to the ductility behavior shown in Figure 4.12(c).

The correlation between yield strength and cooling rate observed in the present work is in accordance with the results reported by Boileau *et al.*<sup>101</sup> and Meyer *et al.*<sup>58</sup> According to Boileau *et al.*,<sup>101</sup> yield strength in heat-treated 319.2 alloys depends upon the type, size and distribution of precipitates. Under the T5 heat treatment, the precipitates are not expected to change significantly. Thus, the YS depends on the original phases in the solidified microstructure. It should be pointed out from Figure 4.12(b) that for the same cooling rate (*i.e.* same DAS value), the alloys with Fe additions (*i.e.* BW, DW, EW, FW alloys) are associated with higher YS values compared to AW and CW alloys, (containing ~0.1% Fe), especially at high cooling rates. According to the study of Ananthanarayanan *et al.*,<sup>102</sup> this can be explained that the addition of iron decreases DAS due to the action of AlFeSi needles acting as nucleation sites for silicon growth, resulting in minimizing the isothermal dendrite arm coarsening at the eutectic temperature. Based on these

observations, it may be concluded that a certain amount of iron intermetallics can contribute to the improvement in the yield strength of 319 alloys, especially at high cooling rates, which refine the size of the iron intermetallics.

From Figure 4.12(c), three main features can be observed:

- a) the ductility of CW alloy (base alloy with Sr-modification) is the best for all ranges of DAS studied;
- b) when the alloy has a high iron content (about 1.2%Fe, *i.e.* DW, EW, FW alloys), the decrease in elongation with increasing DAS is not significant;
- c) at a DAS of 23  $\mu\text{m}$ , representing the highest cooling rate, the decrease in percent elongation with the increase in iron content is more obvious than at a DAS of 83  $\mu\text{m}$ .

These observations are explicable in terms of Sr-modification, the precipitation of  $\beta$ -platelets and the segregation of the  $\text{CuAl}_2$  phases. When Sr is added, the silicon particles change from coarse acicular forms to much smaller and fibrous ones. The changes in the morphology of Si particles are expected to improve alloy ductility. However, for the three alloys with high Fe levels (*i.e.* DW, EW, FW), the brittle  $\beta\text{-Al}_5\text{FeSi}$  platelets formed during solidification are very harmful to the ductility. In addition, decreasing the cooling rate increases the size of these platelets and amount of porosity leading to further reduction in alloy ductility. Their negative effect is found to dominate the positive effect of Sr-modification, when one compares the BW and CW alloys. Also, it should be noted that the ductility of FW alloy (containing Sr, Fe, and P) is the lowest among the six alloys studied. This is due to the phosphorus oxide particles existing in the microstructure, acting as

nucleation sites for the  $\beta$ - $\text{Al}_5\text{FeSi}$  and  $\text{CuAl}_2$  phase particles, in addition to their diffusion through the  $\text{CuAl}_2$  particles themselves.

#### 4.3.2.2 T6 heat treatment

Figure 4.13 shows the tensile properties of the six alloys after T6 heat treatment, as a function of cooling rate (DAS). In general, the observed increase in UTS with increase in cooling rate is in accordance with the results obtained by other investigators.<sup>103,104</sup> Compared to the T5 heat-treated alloys (Figure 4.13(a)), the UTS levels of the T6 heat-treated alloys are significantly higher, with the maximum increase being observed in the CW alloy (base alloy with 220 ppm Sr), *i.e.* from 192 MPa to 304 MPa (increase by 58.3%) at the DAS value of 23  $\mu\text{m}$ . Due to the Sr-modification, the eutectic Si precipitates in fibrous morphology and the T6 heat treatment causes redistribution of copper into the aluminum matrix. Both factors contribute in enhancing the UTS.

From Figure 4.13(a), the difference in UTS between the BW (Sr-modified base alloy with 0.4%Fe) and AW (base) alloys can be interpreted in terms of the increase Fe level of the former, resulting in the formation of a certain amount of hard  $\beta$ - $\text{Al}_5\text{FeSi}$  platelets dispersed within the aluminum matrix, which contributes to an increase in the strength. The smaller  $\beta$ -platelet sizes resulting from the effect of Sr modification ameliorates the UTS of the BW alloy at all DAS values, although the effect is naturally more evident at larger DASs than at the lowest DAS of 23  $\mu\text{m}$  where the  $\beta$ -platelet sizes are already expected to be small due to the high cooling rate. These observations are in accordance with those of other investigators.<sup>105,106</sup>

Figure 4.13(a) also shows that, at Fe levels as high as 1.2%, the UTS values are lowered considerably, as depicted by the DW, EW and FW alloys. The larger-sized and larger amount of  $\beta$ -platelets formed at such Fe levels, and their relatively low bond strength with the matrix<sup>37</sup> explain the low UTS values observed. It is interesting to note that, in the case of the FW alloy (with Fe, Sr and P additions), the presence of P is somewhat useful in improving the alloy strength over that obtained for the DW alloy (with Fe and Sr additions), due to the P addition modifies the primary Si particles during solidification, resulting in the length of the primary  $\alpha$ -dendrite Si particles in FW alloy is shorter than in DW alloy.

The data on yield strength depicted in Figure 4.13(b) shows that the T6 heat-treated alloys display much higher yield strengths compared to the T5 heat-treated alloys. While a decrease in YS with increase in DAS is also observed in this case, the decrease in YS with DAS is quite sharp in some cases (*e.g.* for alloys EW and CW). This is due to that at the lowest cooling rate, there exists a lot of blocky  $\text{CuAl}_2$  or large sized  $\beta\text{-Al}_5\text{FeSi}$  particles in CW and EW respectively, resulting in much lower YS values compared to the case of the highest cooling rate.

Yield strength is more difficult to predict for T6 heat-treated materials. According to Samuel *et al.*,<sup>107</sup> Sr addition allows for the fragmentation and partial dissolution of a proportion of the  $\beta$ -iron intermetallics in the aluminum matrix. Such dissolution could affect the precipitation of the  $\text{CuAl}_2$  phase in 319 alloys, since  $\text{CuAl}_2$  particles precipitate along the long sides of the  $\beta$ -iron platelets. Meanwhile, Sr modification also leads to local segregation of  $\text{CuAl}_2$  blocky particles in areas away from the eutectic Si particle regions.

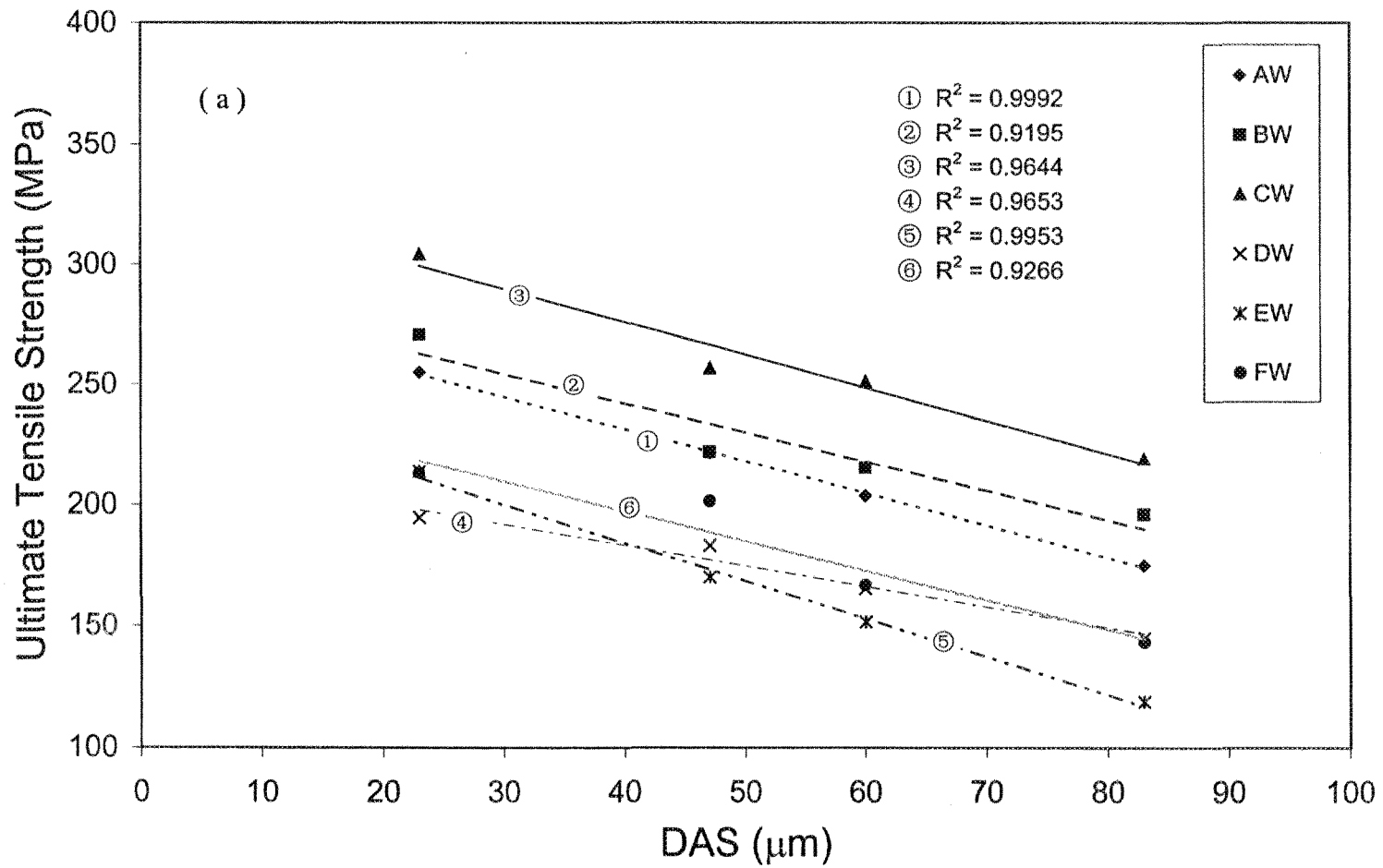


Figure 4.13. Tensile properties of the six alloys studied (T6 condition) as a function of cooling rate: a) Ultimate Tensile Strength, b) Yield Strength, c) % Elongation.

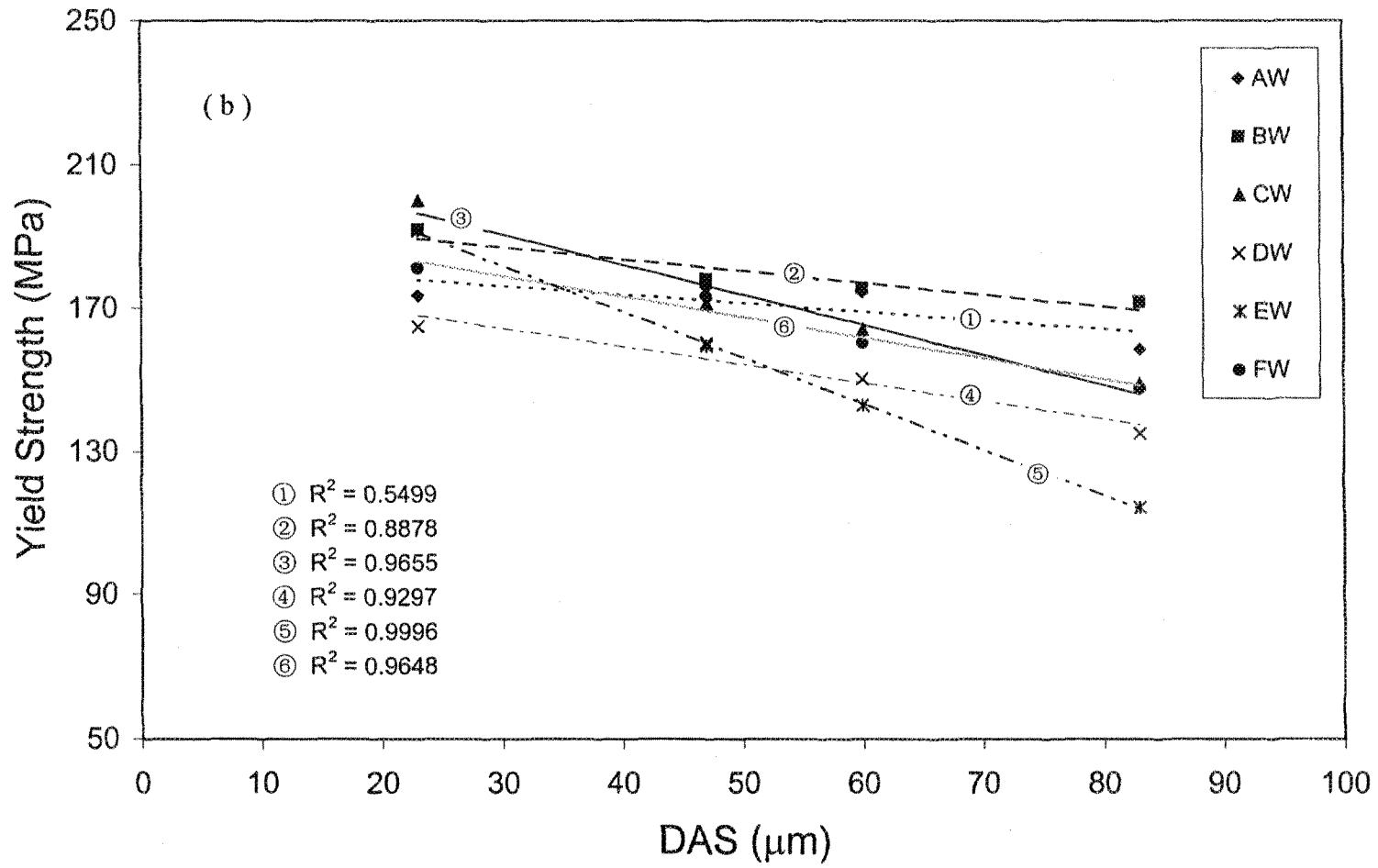


Figure 4.13. Tensile properties of the six alloys studied (T6 condition) as a function of cooling rate: a) Ultimate Tensile Strength, b) Yield Strength, c) % Elongation.

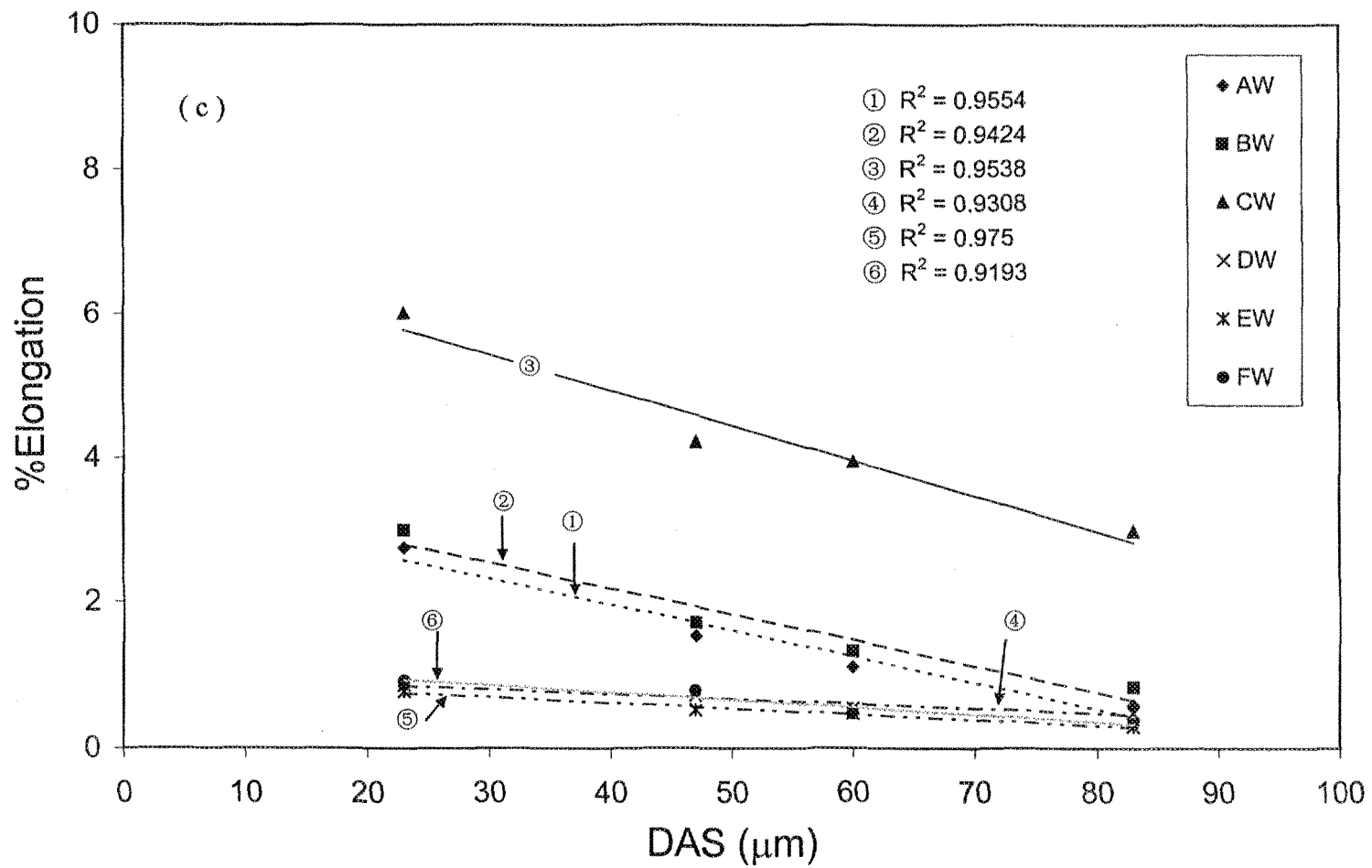


Figure 4.13. Tensile properties of the six alloys studied (T6 condition) as a function of cooling rate: a) Ultimate Tensile Strength, b) Yield Strength, c) % Elongation.

In contrast, yield strength is strongly related to the dislocation movement and pinning by precipitates. Therefore, yield strength in the heat-treated 319 alloy is determined by the type, size, and distribution of the precipitates. Also, the amount and size of the  $\beta$ -iron phase present in the alloy matrix would produce variations in the yield strength. Furthermore, the dissolution of phosphorus in the  $\text{CuAl}_2$  particles, and the presence of phosphorus oxide particles (acting as nucleation sites for the precipitation of  $\text{CuAl}_2$ ), and the amount of porosity observed in the alloy sample would also influence the YS values obtained.

Comparing Figure 4.13(c) to Figure 4.12(c), the maximum attainable increase in ductility in the T6 heat-treated alloys is achieved by the CW alloy (*i.e.* Sr-modified base alloy) at 23  $\mu\text{m}$  DAS value (*cf.* 6.01% with 3.89% in the T5-treated CW alloy). It is also seen that larger improvements in ductility are obtained for the CW alloy over the BW alloy (exhibiting the second highest ductility values) when the alloys are subjected to T6 treatment rather than T5 treatment.

This observation can be attributed to the dissolution of  $\text{CuAl}_2$  during solution heat treatment (instead of the presence of the segregated blocky  $\text{CuAl}_2$  particles), combined with the effect of fine Si particles caused by the modification with Sr. Again, the presence of high Fe levels ( $\sim 1.2$  wt%) in the DW, EW and FW alloys reduces the alloy ductility significantly due to the presence of an increased amount of large brittle  $\beta$ -iron platelets. Such alloys exhibit extremely low elongation between 0.3% and 0.9%, and no improvements are obtained either with increased cooling rates, Sr modification or P addition.

### 4.3.2.3 Correlation between ultimate tensile strength and %elongation

In order to seek a reasonable interpretation of the obtained tensile test results, the relationship between UTS and percent elongation for the two heat treatments (T5 and T6) employed were analyzed collectively (for all alloys) in the form of UTS vs. %El and logUTS vs. log%El plots, along the lines of the UTS vs. log%El plots used by Drouzy *et al.*<sup>108</sup> In their concept, quality index, Q, together with the probable yield strength YS, was developed to interpret tensile results when they observed that, as a particular batch of Al-7Si-Mg alloy samples was aged, the plot of ultimate tensile strength versus the logarithmic value of elongation (tensile ductility) followed a linear relationship.

The plots in Figure 4.14 show clearly that the increase in UTS is directly related to percent elongation, *i.e.* from high iron content and low cooling rate to high cooling rate and low iron content. Due to the data scatter caused by different variables, the  $R^2$  values are below unity. Both of these parameters control the size and amount of the formed copper intermetallic. In the case of high iron content and a low cooling rate, a sufficient number of precipitation sites (*i.e.*  $\beta$ -Al<sub>5</sub>FeSi platelets) and adequate solidification time are available for the CuAl<sub>2</sub> and Al<sub>7</sub>FeCu (insoluble) particles to precipitate during the solidification process.

The data scatter for the T5-treated alloys is greater than that observed for the T6-treated alloys. This is due to the fact that in the latter case, the microstructure is more homogeneous than in the case of the T5 heat-treated alloys. Also, the T6 heat-treated alloys display much higher strengths at the same ductility values. The  $R^2$  values obtained from the logUTS vs. log%El plot are slightly better than those obtained from the UTS vs. %El plot.

Other observations can be noted in Figure 4.14:

1. much higher strength-ductility combinations are obtained with T6 heat treatment under similar cooling rate conditions;
2. linear relationships in both plots;
3. the strength-ductility combinations fall into two main groups: corresponding to high cooling rate-low iron and low cooling rate-high iron combinations, the high cooling rate-low iron exhibiting the best properties, and the low cooling rate-high iron combinations showing the lowest properties.

According to the above facts, it can be concluded that the best mechanical properties are based on the conditions of high cooling rate, low iron content and T6 heat treatment.

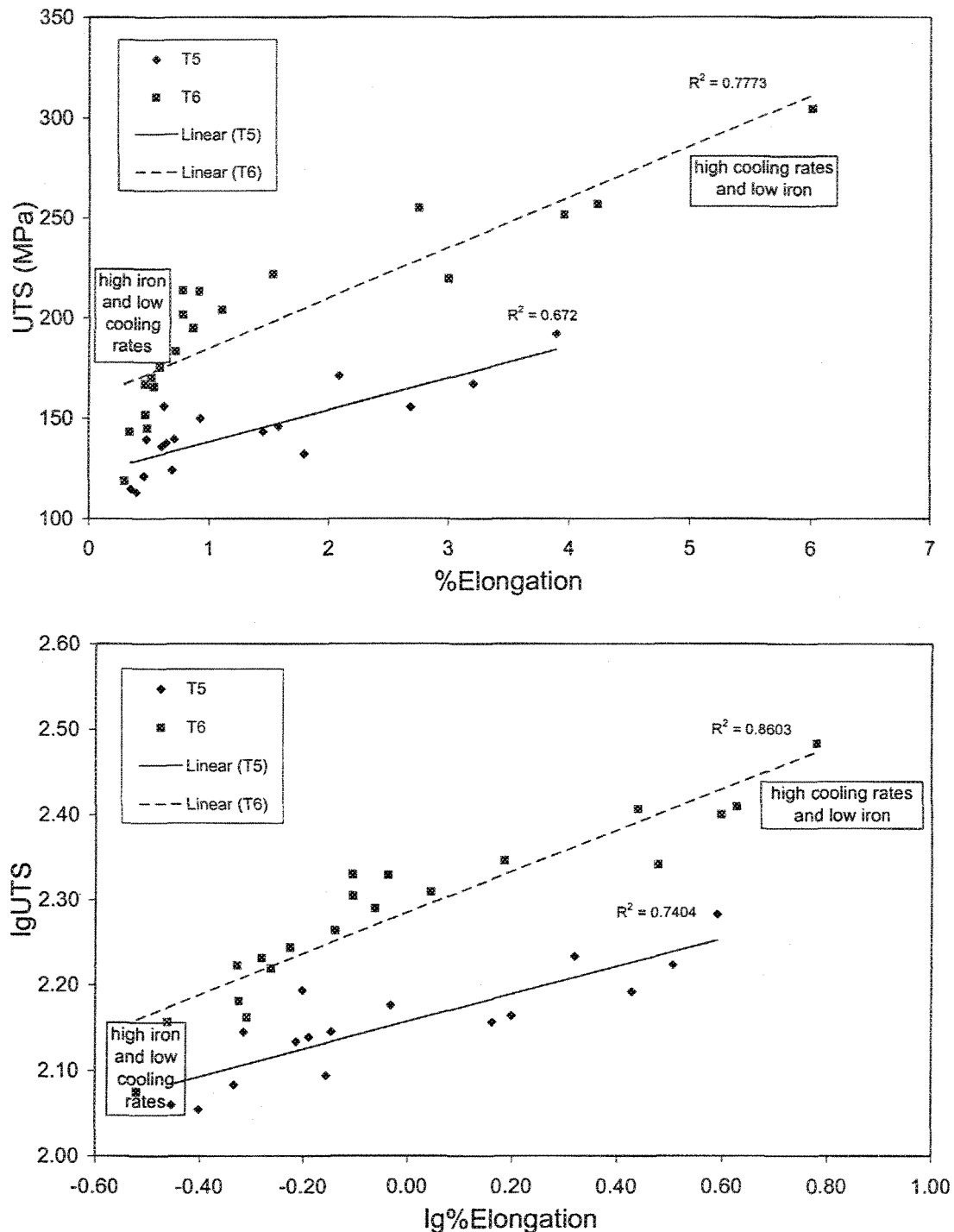


**Figure 4.14.** a) Plot of ultimate tensile strength vs. percent elongation for studied alloys with different solution heat treatments (T5 & T6), b) plot of  $\lg$ UTS vs.  $\lg$ %El for studied alloys with different heat treatments (T5 & T6).

### 4.3.3 Impact Properties

Impact tests were carried out for the six Al-Si-Cu 319 alloys in order to investigate the effect of various alloying elements, *i.e.* Sr, Fe, and P (individually or in combination), and heat treatment (T5 and T6) on the alloy toughness. The results are presented in the form of total energy vs. dendrite arm spacing (DAS) plots. At the same time, with the aim of seeking to establish the relationship between impact properties and tensile properties, the plots of total energy vs. percent elongation and total energy vs. ultimate tensile strength were also drawn.

#### 4.3.3.1 Load-time curves

Figure 4.15 presents two typical load-time curves obtained from the results of the instrumented impact testing. Figure 4.15(a) corresponds to the sample obtained from the level 1 blank of CW alloy (*i.e.* Sr-modified base alloy, 23  $\mu\text{m}$  DAS) after T6 heat treatment, while Figure 4.15(b) corresponds to the sample obtained from the level 4 blank of EW alloy (*i.e.* base alloy with 1.2% Fe, 83  $\mu\text{m}$  DAS) after T5 heat treatment. These two samples were selected for comparison purpose, being representative of the highest and lowest impact toughness values that were obtained among all the samples studied.

The shape of the load-time curve indicates the deformation and fracture history of the test piece. The interpretation of the curve can be done using concepts similar to those employed for a conventional tensile test. The curve can be subdivided into two zones: elastic and plastic zones, delineated by the dashed line in each case. The first load fluctuation on these curves is not a real effect of the material properties, since it is caused by the inertial loading of the hammerhead as a result of the acceleration of the specimen

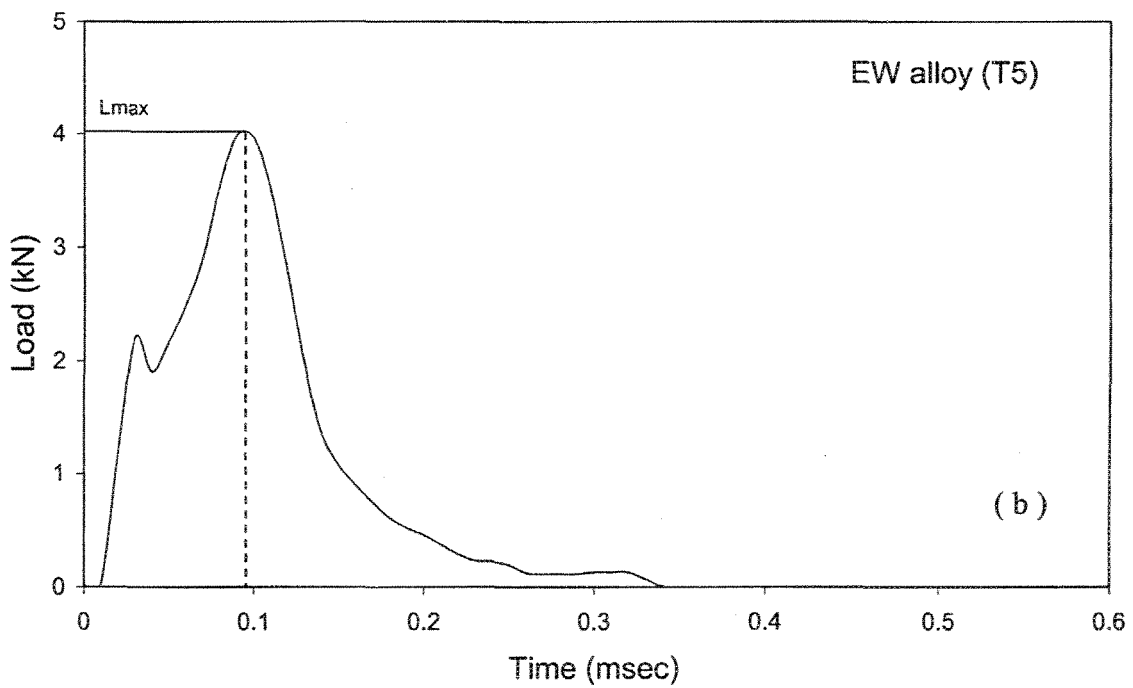
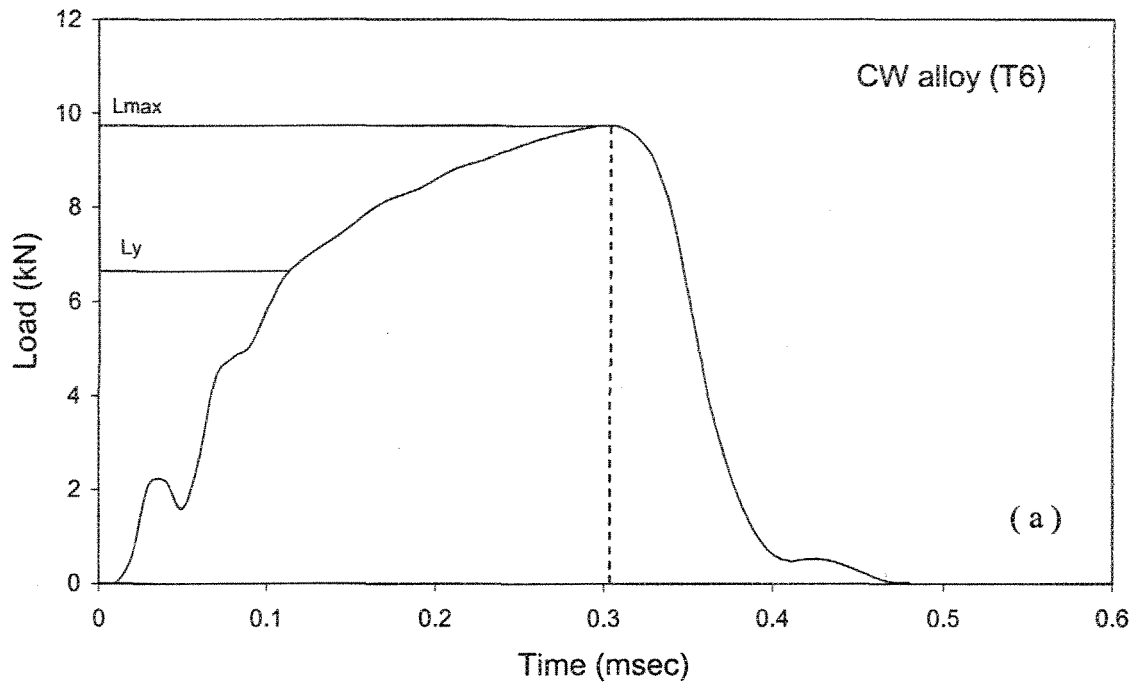


**Figure 4.15.** a) Load-time curve of T6 heat-treated CW alloy (at 23  $\mu\text{m}$  DAS),  
 b) load-time curve of T5 heat-treated EW alloy (at 83  $\mu\text{m}$  DAS).  
 $L_{max}$  : Maximum Load  $L_y$  : Yield Load

from rest. In Figure 4.15(a), the initial rise corresponds to the elastic zone (up to the yield load  $L_y$ ). At higher loads, prior to the maximum load  $L_{max}$ , the specimen deforms plastically, while after  $L_{max}$  the load decay is indicative of controlled crack propagation.

The shape of the load-time curve in Figure 4.15(b) indicates that when the 319 alloy has a high Fe content, the alloy exhibits a brittle nature. The load increases linearly with time to the maximum,  $L_{max}$ , and then decreases rapidly, indicating that the crack propagation, which leads to failure, is rather short. There is no evidence of obvious plastic deformation. Comparing Figure 4.15(a) and 4.15(b), the process of crack propagation is observed to be more sluggish in the T6 heat-treated material. Also, the maximum load value in this case is 9.75 kN, which is much higher than the one exhibited by the T5-treated EW alloy in Figure 4.15(b), *i.e.* 4.03 kN.

#### 4.3.3.2 T5 heat treatment

The Charpy impact test results for the T5 heat-treated alloys are listed in Table 4.8 in terms of the total absorbed energy ( $E_t$ ) and maximum load ( $L_{max}$ ) values obtained at each dendrite arm spacing/cooling rate. The impact strengths are relatively lower than those reported for 356 aluminum alloys.<sup>109</sup> In general, this is due to the presence of copper in the 319 alloys which drastically changes the fracture behavior. When the  $CuAl_2$  phase is present in the microstructure, the fracture is apparently no longer controlled only by the morphology of the eutectic Si particles (*i.e.* modified or unmodified).<sup>91</sup>

Figure 4.16 presents the impact properties of the studied alloys as a function of dendrite arm spacing (DAS). The failure process during an impact test can be divided into two parts, *i.e.* crack initiation and crack propagation. The total absorbed Energy  $E_t$  of a

**Table 4.8.** Impact test results of T5 heat-treated alloys

Alloy Code	DAS ( $\mu\text{m}$ )	Impact Test Data (T5 condition)		
		Total Absorbed Energy, $E_t$ (J)		Maximum Load $L_{\text{max}}$ (kN)
		Average $E_t$	Standard Deviation	
AW	23	5.33	0.69	6.39
	47	4.60	0.23	5.77
	60	4.03	0.37	5.26
	83	2.31	0.37	3.96
BW	23	3.88	–	–
	47	3.60	–	–
	60	3.37	–	–
	83	3.25	–	–
CW	23	7.55	0.65	6.36
	47	7.32	1.19	7.20
	60	6.08	0.84	6.28
	83	4.09	0.27	4.76
DW	23	5.55	0.69	5.55
	47	3.38	0.76	6.67
	60	2.64	0.18	5.32
	83	2.56	0.33	4.43
EW	23	3.00	0.89	5.16
	47	2.45	0.27	4.28
	60	2.36	0.16	4.56
	83	2.35	0.12	4.03
FW	23	3.99	0.45	6.27
	47	2.89	0.22	5.38
	60	2.55	0.07	4.77
	83	2.21	0.20	3.93

sample subjected to impact testing is the sum of the energy required for crack initiation,  $E_i$ , and the energy required for crack propagation,  $E_p$ , and can therefore be used as a parameter to describe the impact toughness of the sample material.

The dependence of total absorbed energy,  $E_t$ , on DAS is presented in Figure 4.16, where the  $E_t$  for each alloy is found to decrease with the increase in the DAS value (*i.e.* decrease in cooling rate). The decrease in the total absorbed energy from one alloy to another is more significant at the highest cooling rate (23  $\mu\text{m}$  DAS), compared to that observed at 83  $\mu\text{m}$  DAS. At the highest cooling rate, the reduced size of the microconstituents ( $\beta$ -iron intermetallics, Al-Si eutectic, and  $\text{CuAl}_2$  phase) and porosity content lead to a more homogeneous microstructure. Though Sr modification enhances the impact toughness (*cf.* CW and AW alloys), addition of iron is detrimental, so that at 1.2%Fe levels, neither increasing the cooling rate nor adding different alloying elements produces much improvement in the alloy toughness.

It is observed that the  $E_t$  values of CW alloy (Sr-modified base alloy) obtained at any DAS level are higher than those obtained from any other alloy. This observation may be explained as being due to the effective increase in the volume fraction of the plastic aluminum matrix when the Si particles are modified with Sr, leading to superior impact toughness. At low cooling rates, however, the segregation of the brittle  $\text{CuAl}_2$  particles counteracts the positive influence of the modified Si particles, lowering the impact energy. In comparison, in the base AW alloy, the stress concentration is relatively considerable due to the presence of the eutectic Si in the form of coarse, brittle acicular particles. Consequently, the impact toughness of the alloy is lower than that of the CW alloy.

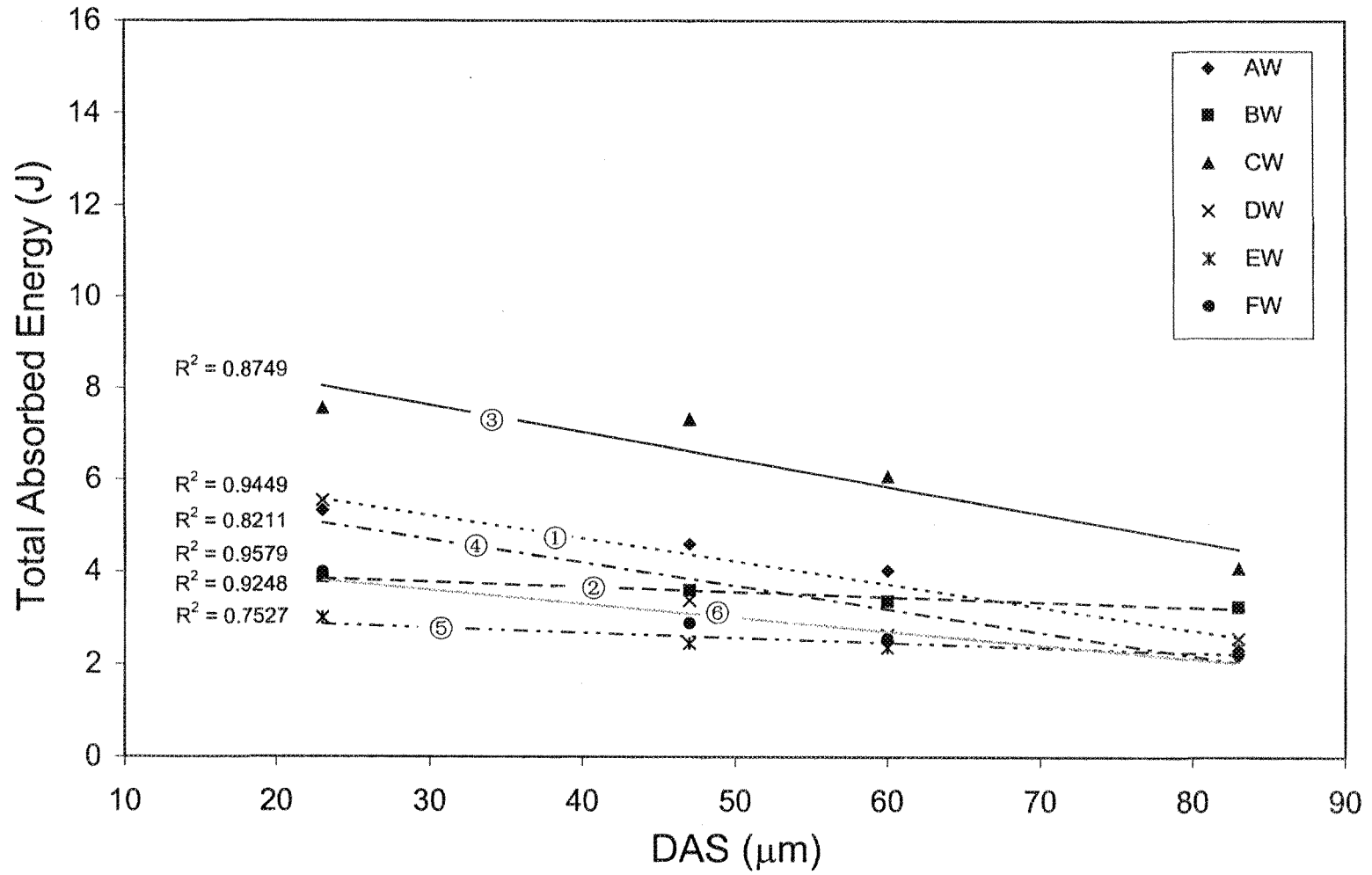


Figure 4.16. Total absorbed energy of the studied alloys as a function of DAS after T5 heat treatment.

As for DW, EW and FW alloys (containing ~1.2%Fe), the presence of the  $\beta$ -Al<sub>5</sub>FeSi platelets reduces the impact energy dramatically regardless of the cooling rate. The stress concentration occurring around the  $\beta$ -phase platelets due to their plate-like form provides additional crack initiation sites apart from the Si particles. In the FW alloy, the presence of the phosphorus in the form of phosphorus oxides – which act as nucleation sites for the blocky CuAl<sub>2</sub> phase – would provide that many more brittle CuAl<sub>2</sub> intermetallic particles to facilitate rapid crack initiation.

#### 4.3.3.3 T6 heat treatment

The values of total absorbed energy ( $E_t$ ) and the maximum load ( $L_{max}$ ) values obtained from the impact tests of the T6 heat-treated alloys are presented in Table 4.9.

In the T6 heat-treated condition, the microconstituents in the alloys are well distributed or dissolved in the aluminum matrix. Compared to the T5-treated alloys, there are less acicular particles acting as stress concentrators during the crack propagation process, leading to improved impact toughness. For example, at 23  $\mu$ m DAS, the  $E_t$  value of CW alloy (Sr-modified base alloy) is increased from 7.55 J (T5 heat treatment) to 14.54J (T6 heat treatment). It is interesting to note that the improvement in the impact toughness value due to the increase in the cooling rate is accompanied by an improvement in the maximum impact load sustained prior to crack initiation.

The dependence of  $E_t$  on DAS is shown in Figure 4.17. Impact toughness values of alloys solidified at high cooling rates are superior to those solidified at low rates. The significant increase in the impact toughness of CW alloy after T6 heat treatment is

**Table 4.9.** Impact test results of T6 heat-treated alloys

Alloy Code	DAS ( $\mu\text{m}$ )	Impact Test Data (T6 condition)		
		Total Absorbed Energy, $E_t$ (J)		Maximum Load $L_{\text{max}}$ (kN)
		Average $E_t$	Standard Deviation	
AW	23	10.45	1.97	9.63
	47	7.46	0.61	8.39
	60	6.16	0.41	7.53
	83	2.47	0.34	4.69
BW	23	8.14	–	–
	47	7.57	–	–
	60	6.78	–	–
	83	5.25	–	–
CW	23	14.54	2.56	10.04
	47	12.75	1.06	9.53
	60	8.19	0.60	8.16
	83	6.56	0.53	7.47
DW	23	4.34	0.37	7.56
	47	3.31	0.37	5.58
	60	3.19	0.47	5.34
	83	3.09	0.15	6.04
EW	23	3.34	0.60	6.44
	47	2.86	0.24	4.57
	60	2.67	0.23	5.02
	83	2.56	0.11	5.49
FW	23	4.14	0.43	7.21
	47	2.89	0.19	5.14
	60	2.73	0.37	5.68
	83	2.58	0.16	5.31

particularly noteworthy. As most of the block-like  $\text{CuAl}_2$  particles have been dissolved and redistributed within the aluminum matrix after T6 heat treatment, more copper is available to act as a strengthening agent (during aging), thus contributing to the significant increase in the  $E_t$  value of the alloy.

Comparing the  $E_t$  values of BW alloy (containing 0.4% Fe and Sr) and AW (base) alloy shows that the AW alloy has a higher  $E_t$  value at the highest cooling rate, whereas at the lowest cooling rate, the BW alloy shows higher values. This may be explained as follows: at the highest cooling rate, the Si particles in the base alloy are quench-modified, *i.e.* they appear as small particles that are much less acicular in nature. In the BW alloy, however, even given that the eutectic Si is Sr-modified, the existence of the brittle  $\beta\text{-Al}_3\text{FeSi}$  particles due to the higher Fe content of the alloy (0.4%) counteracts the beneficial effect of cooling rate.

At the lowest cooling rate, the Si particles in the unmodified AW alloy are very coarse and acicular. These serve as stress concentration sites and ease crack propagation, resulting in a low impact toughness value. In the case of the BW alloy, the main difference in microstructure is the size of the  $\beta$ -phase needles, which are larger in size in this case than those that precipitate at high cooling rates. Nevertheless, one observes that the impact toughness is still higher than that of the AW alloy. This could be attributed to the modification effect of Sr on both the Si particles and the  $\beta$ -phase needles.

Finally, at very high Fe levels ( $\sim 1.2\%$ ), the impact toughness is considerably lowered, as observed in the case of the DW, EW and FW alloys, with little or no influence of cooling rate or of element additions. Due to the brittle and hard nature of the iron microconstituents,

even after T6 heat treatment, no significant increase in the impact toughness of these alloys is achieved. Therefore, it can be concluded that a high Fe concentration is greatly detrimental to the impact properties of 319 alloys. Komatsu *et al.*<sup>110</sup> have pointed out that iron exerts a detrimental effect on the impact strength of Al-Si alloys due to the formation of FeAl<sub>3</sub> crystallites. The formation of these undesirable crystallites is not changed by solution heat treatment at 500 °C, resulting in low impact energy values.

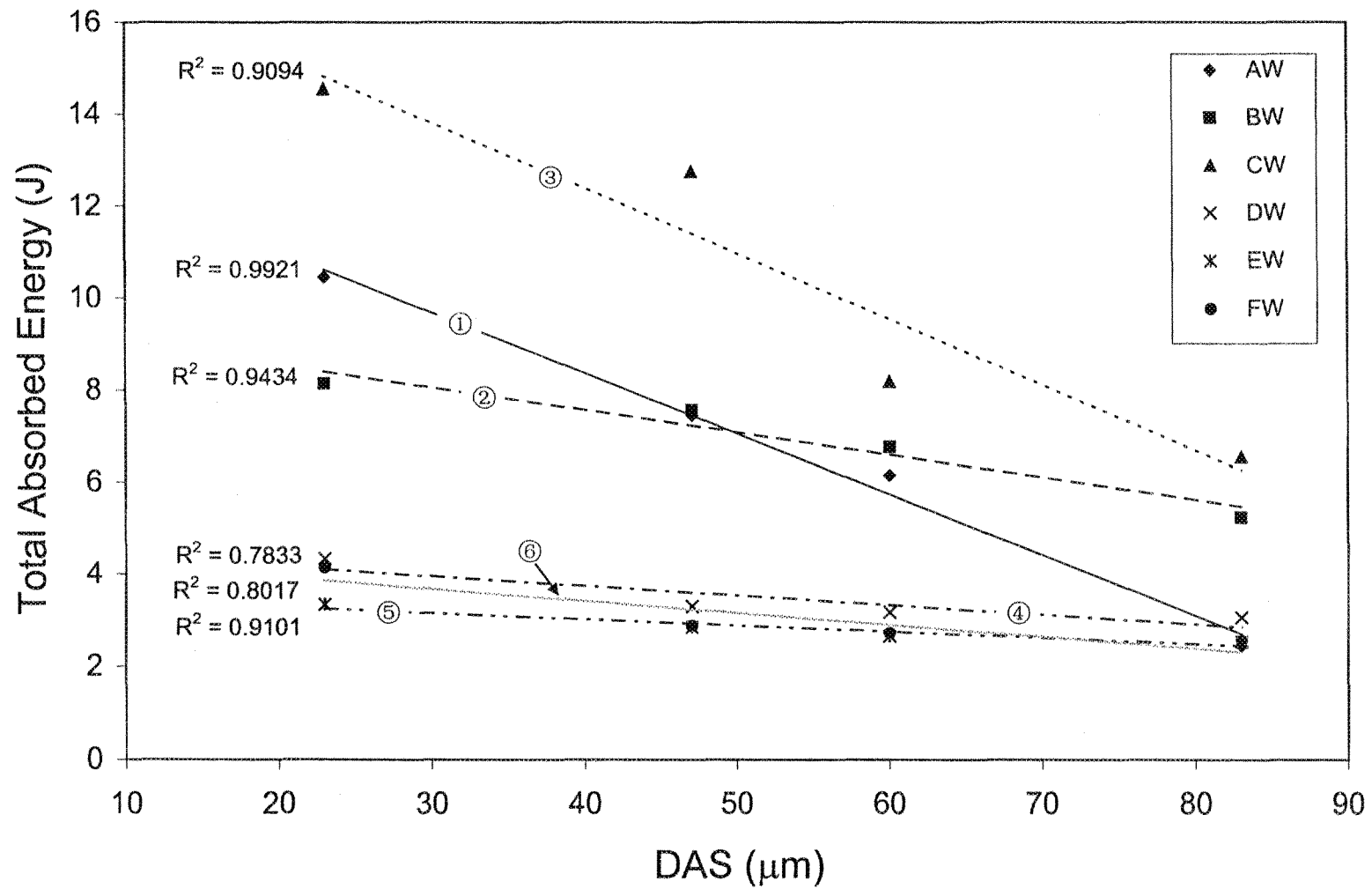


Figure 4.17. Total absorbed energy of the alloys studied as a function of DAS (T6 condition).

### 4.3.4 Relationship Between Tensile and Impact Properties

#### 4.3.4.1 T5 heat treatment

Figure 4.18 shows the relationship between total absorbed energy ( $E_t$ ) and percent elongation for the T5 heat-treated alloys. It is seen that with the increase in percent elongation, the total absorbed energy of impact testing ( $E_t$ ) increases for all alloys. The alloy samples with a high Fe content and obtained at low cooling rate are characterized by low  $E_t$  and low % Elongation values. Alloys with low Fe content and obtained at high cooling rates possess relatively high  $E_t$  and % Elongation values. Thus, the presence of a high Fe level is detrimental to both impact toughness and ductility.

For a given  $E_t$  value, the CW alloy (Sr-modified base alloy) possessed the best ductility, whereas the FW alloy (with Sr, P and high Fe additions) displayed the lowest ductility. The existence of a well-modified Al-Si eutectic and the low amount of  $\beta$ -Al<sub>5</sub>FeSi platelets in CW alloy in contrast to the large amount of brittle  $\beta$ -iron intermetallics and phosphorus oxides present in the FW alloy explain the observed results.

Figure 4.19 illustrates the dependence of the impact energy on the ultimate tensile strength of T5 heat-treated alloys. Generally, at a given UTS level, the  $E_t$  values of various alloys always decrease in the following order:

$$CW > AW > DW > FW, BW > EW,$$

except for some discrepancy observed at the low UTS values. From an analysis of the different alloying elements added to these alloys, it is reasonable to conclude that Sr modification has a positive effect on improving the impact energy, whereas both P and high Fe additions have a negative effect on  $E_t$ , due to the formation of (Al,P)O<sub>2</sub> and  $\beta$ -Al<sub>5</sub>FeSi

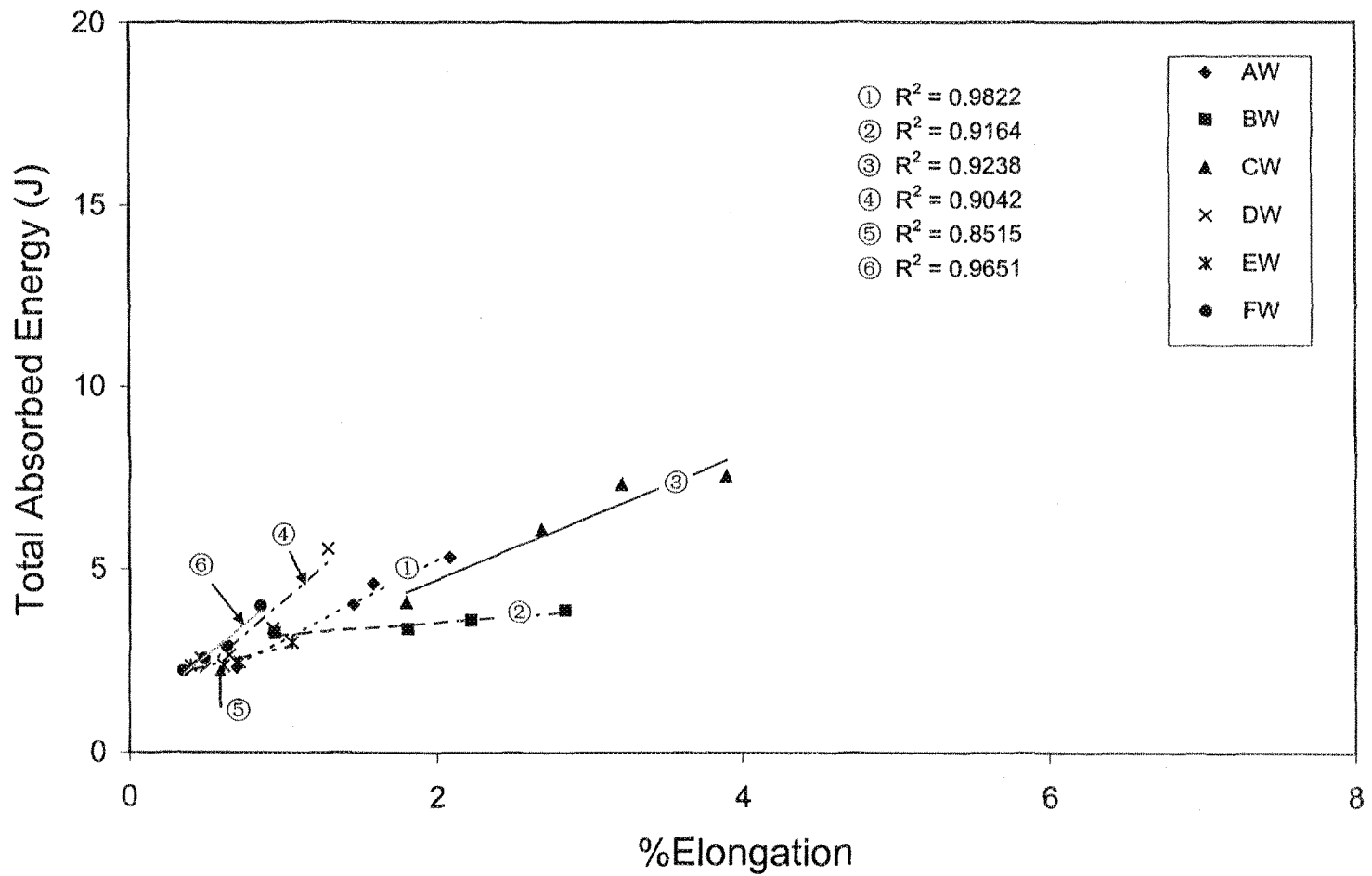
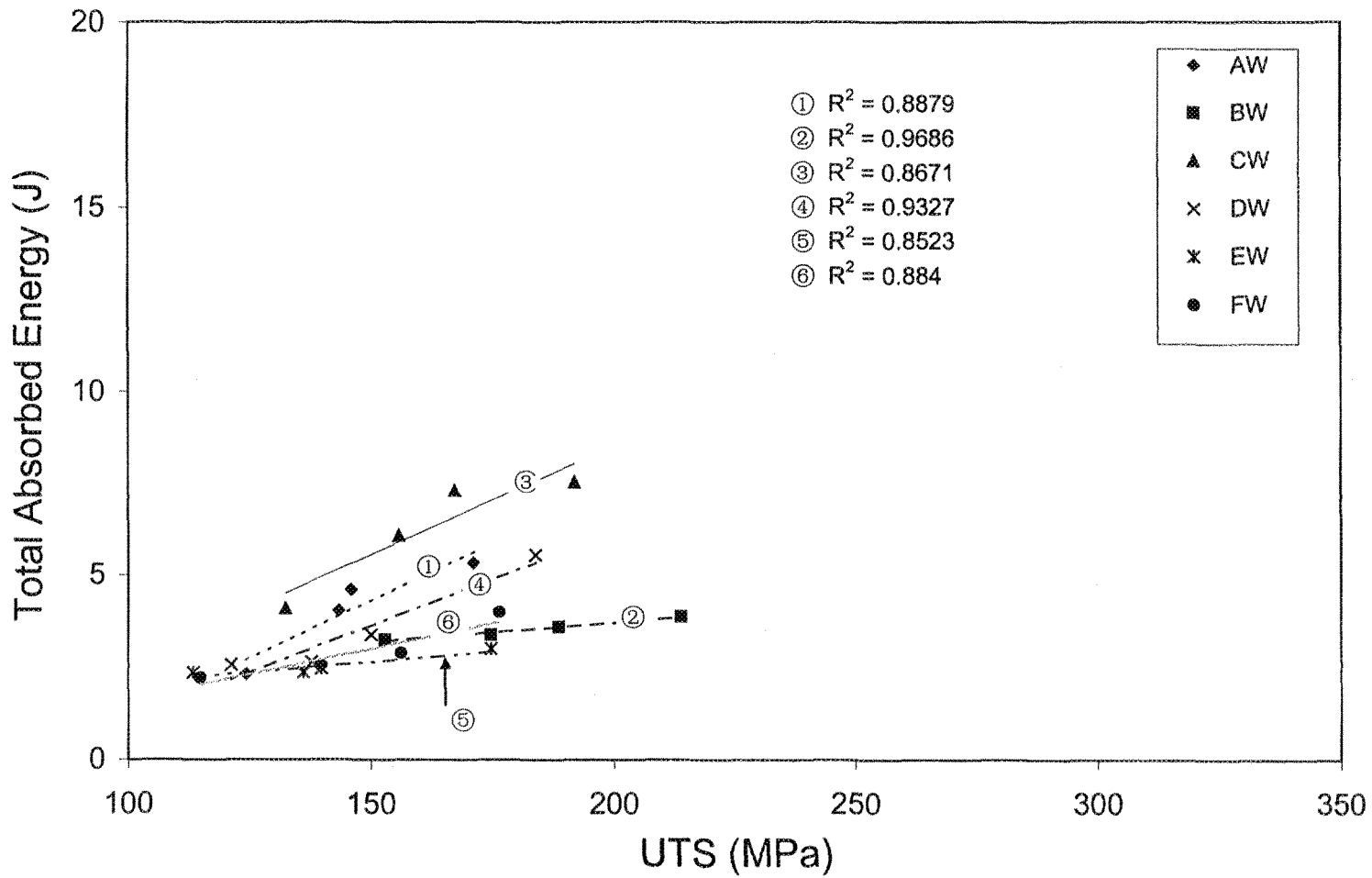


Figure 4.18. Relationship between %El and  $E_t$  for the six alloys studied (T5 condition).



**Figure 4.19.** Relationship between UTS and  $E_t$  for the six alloys studied (T5 condition).

phases during solidification, respectively. As Figure 4.19 shows, the Sr-modified CW alloys exhibits the best mechanical properties.

#### 4.3.4.2 T6 heat treatment

Figure 4.20 shows the relationship between  $E_t$  and percent elongation for the six alloys. The plots clearly depict that the increase in  $E_t$  and % Elongation in AW, BW and CW alloys are much higher than those observed for DW, EW and FW alloys, due mainly to the presence of high Fe levels in the latter alloys. The detrimental effect of iron on the mechanical properties can be clearly understood from the figure.

As mentioned previously, after T6 heat treatment, the microconstituents of all the studied alloys became more homogeneous and a large proportion of intermetallics underwent dissolution and redistribution. This process is very effective for AW, BW and CW alloys in improving their mechanical properties, but is limited by the presence of a high Fe content in the DW, EW and FW alloys. In these high Fe-containing alloys, the persistence of the plate-like  $\beta$ - $\text{Al}_5\text{FeSi}$  phase even after T6 heat treatment lowers the impact toughness and ductility. This observation is consistent with that of Grand<sup>35</sup> who reported that increasing the iron content from 0.5 to 1.2% in an Al-13%Si casting alloy dramatically reduced its mechanical properties, particularly ductility, due to the formation of the  $\beta$ -iron phase platelets.

Comparing AW and BW alloys, it is interesting to note that their lines intercept at a certain % El value. At low cooling rates, modified eutectic Si particles in the BW alloy enhance the  $E_t$  value and the ductility to some extent, compared to the (unmodified) AW alloy. At high cooling rates, however, the Si particles in the AW alloy are quench-modified

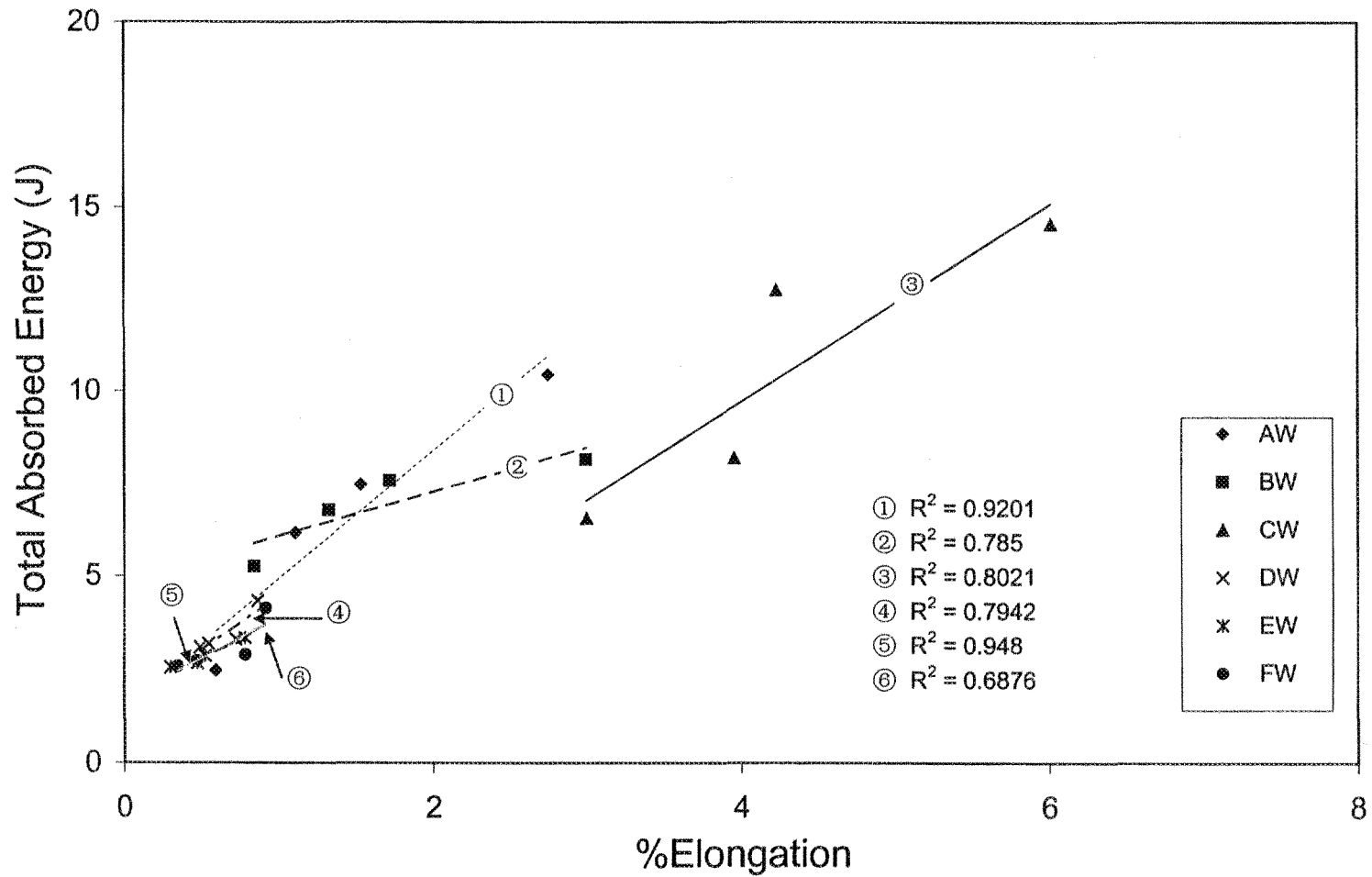


Figure 4.20. Relationship between  $E_t$  and %El for the six alloys studied (T6 condition).

and the segregation of  $\text{CuAl}_2$  particles is also prevented due to the shortened growth time, resulting in the relatively higher toughness and ductility values. In the BW alloy, the 0.4% Fe addition results in the formation of a larger amount of  $\beta\text{-Al}_5\text{FeSi}$  platelets than in the AW base alloy. These platelets precipitate before the  $\text{CuAl}_2$  phase during solidification, providing more nucleation sites for the  $\text{CuAl}_2$  particles in the BW alloy. The increased precipitation of  $\beta\text{-Al}_5\text{FeSi}$  and  $\text{CuAl}_2$  particles lower the impact energy of the BW alloy below that of the AW alloy at high cooling rates.

Figure 4.21 shows the plots of impact energy ( $E_t$ ) versus ultimate tensile strength (UTS) for the six alloys studied (at various cooling rates). It is found that after T6 heat treatment, both the impact energy and UTS improve significantly. Compared to Figure 4.19, the UTS value of the CW alloy is seen to increase from 192 MPa in the T5 condition to 310 MPa after T6 treatment. This is attributed to the effective increase in the volume fraction of the aluminum matrix due to Sr modification that results in very fine Si particles. At the same time, extended solution heat treatment (T6) enabled the blunting of sharp edges in the eutectic silicon particles, especially in unmodified castings produced at low solidification rates.<sup>109</sup> All of these factors explain why the trend lines of AW and CW alloys have bigger slopes than those observed in Figure 4.19 in the T5 case.

As for DW, EW and FW alloys (containing high Fe and P), the influence of T6 heat treatment on the UTS is greater than the influence on the impact energy. The impact energies for these three alloys fall in a very narrow band ( $E_t \approx 3.45 \pm 0.9$  J). On account of the presence of a large amount of  $\beta\text{-Al}_5\text{FeSi}$  phase particles in the alloys, the impact energy is not improved significantly even on changing the heat treatment from T5 to T6 type.

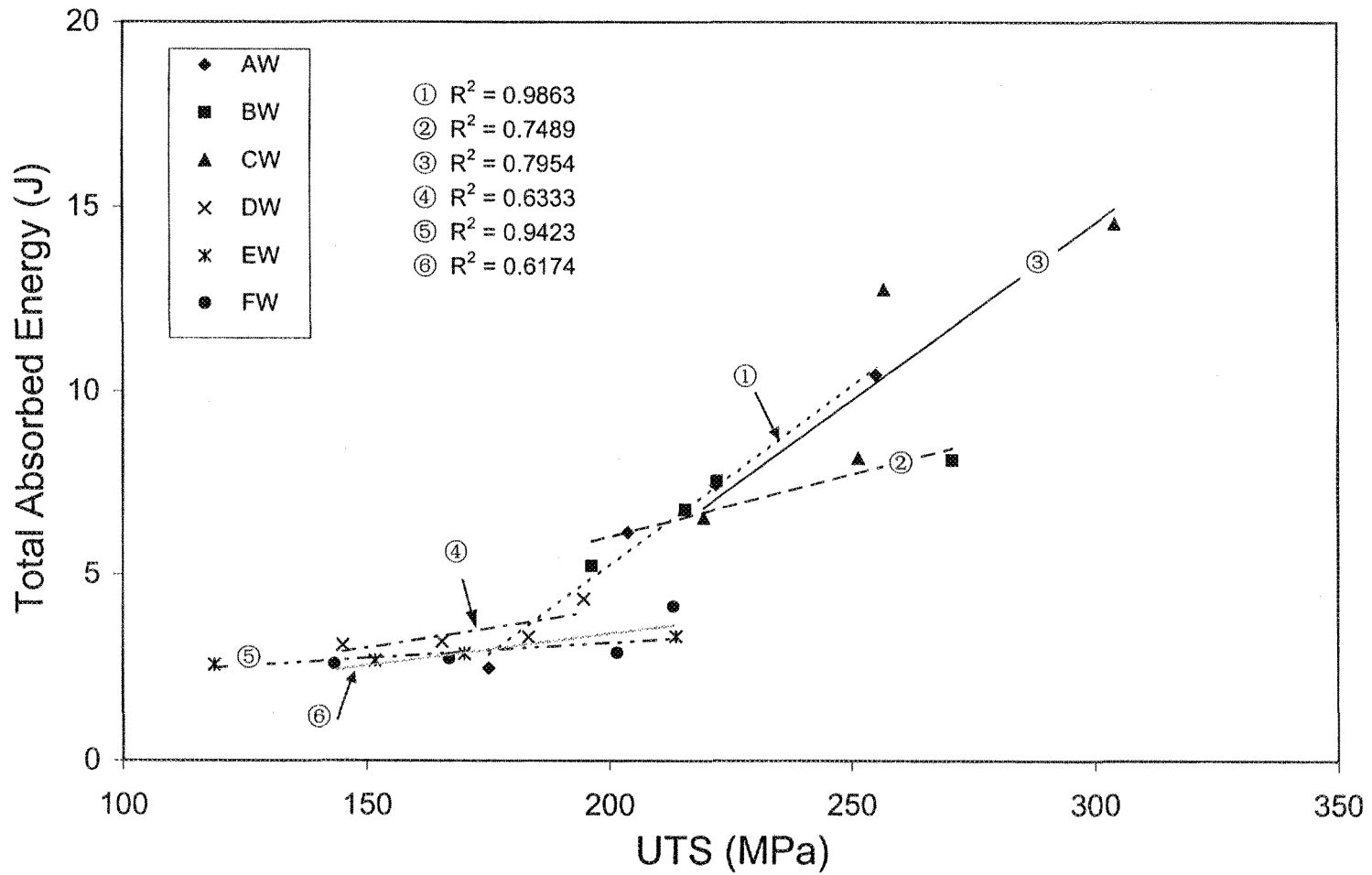


Figure 4.21. Relationship between  $E_t$  and UTS for the six alloys studied (T6 condition).

**CHAPTER 5**  
**FRACTOGRAPHY**

## CHAPTER 5

# FRAC TOGRAPHY

### 5.1 INTRODUCTION

Fractography is defined as the study and documentation of fracture surfaces.<sup>111</sup> The purpose of fractography is to analyze fracture features and attempt to relate the topography of the fracture surface to the cause and/or basic mechanisms of fracture.<sup>73</sup> In addition to metallography, fractography is used in upgrading materials specifications, improving product design, and analyzing failures for improving product reliability.<sup>74</sup>

A backscattered electron mode of operation is normally employed for fractographic purposes. The backscattered electron image offers an improved image contrast, despite the fact that it is accompanied by a loss of resolution. Backscattered electrons are electrons with high energy (equivalent to that provided by the accelerating voltage, which is usually in the range of 20-25 kV). The electrons escape from as deep as 300 Å in the specimen. Due to scatter within the specimen, the resultant source is much larger in diameter than the incident-beam diameter.<sup>112</sup> The fractographs presented in this chapter are backscattered electron images, which were found suitable to bring out the various features observed on the fracture surfaces of the studied alloys.

Al-Si alloys are essentially a combination of the high-strength brittle silicon phase and the low-strength ductile aluminum matrix, containing, in addition, other microstructural

constituents such as iron intermetallic phases, porosity, inclusions, etc. For Al-Si-Cu 319 alloys, while it is natural to assume that the Si particles play an important role in the fracture behavior, the contribution of other microstructural aspects ( $\beta$ -Al<sub>5</sub>FeSi, CuAl<sub>2</sub>, etc.) must also be considered. Consequently, the alloying and melt processing parameters (e.g. strontium modification), the heat treatment applied, and the solidification rates (viz. dendrite arm spacings involved), which directly affect the microstructure, will also be discussed.

In this chapter, the fracture behavior of AW (base) alloy and DW (modified base alloy with 1.2% Fe addition) alloy samples obtained after T5 and T6 heat treatments have been presented, with particular attention paid to the role of various microconstituents with respect to crack initiation and crack propagation in these alloys.

## 5.2 FRACTOGRAPHY RESULTS

Backscattered electron microscopy was used to examine the fracture surfaces of selected impact-tested samples. For each alloy, samples obtained at the lowest and highest cooling rates were examined (*i.e.* at DASs of  $\sim 23 \mu\text{m}$  and  $\sim 83 \mu\text{m}$ ). By taking both the T5 and T6 conditions into account, a total of eight fracture surfaces were examined as follows:

$$2 \text{ alloys} \times 2 \text{ cooling rates} \times 2 \text{ solution treatment conditions} = 8 \text{ samples}$$

In each case, several backscattered images were taken – from the edge, as well as from the central region of the fractured surface – in order to observe the crack initiation and crack propagation characteristics. In addition, interesting features appearing on the fracture surface were also noted.

### 5.2.1 T5 Heat Treatment

Figure 5.1(a) shows a general view of the fracture surface revealing the progress of the crack through the matrix of the base AW alloy sample obtained at the highest cooling rate (*i.e.*, 23  $\mu\text{m}$  DAS), in which acicular Si particles and undissolved  $\text{CuAl}_2$  particles can be observed. It is well known that the cracking of Si particles in samples with small DAS occurs preferentially at grain boundaries and the fracture path is predominantly intergranular. In samples with large DAS, particle cracking is concentrated at the cell boundaries and the fracture mode is transgranular, *viz.*, along the cell boundaries.<sup>113</sup> The high magnification fractograph of Figure 5.1(b), taken from the center of the same sample surface, shows how the crack propagates through the fracture of the Si and  $\text{CuAl}_2$  particles.

In the backscattered (BS) image of Figure 5.2, another interesting fracture feature observed on the surface is the presence of a coarse pore formed during solidification which initiated the fracture, indicating that porous areas favor the fracture path.

Figure 5.3 is taken from the central region of the fracture surface of the AW alloy sample at 83  $\mu\text{m}$  DAS, exhibiting cracked  $\alpha$ -iron script,  $\text{CuAl}_2$  and Si particles. The presence of cracks within these particles confirms how crack propagation is facilitated when such intermetallics are present in the microstructure. More details about the fracture behavior of  $\text{CuAl}_2$  particles at the edge of the same alloy sample are presented in Figure 5.4. It is also possible to see a large sized  $\beta$ - $\text{Al}_5\text{FeSi}$  platelet present in the microstructure, due to the low cooling rate. During impact loading upon application of a high deformation rate, the  $\beta$ -platelet at the edge of the sample was broken into several small fragments.

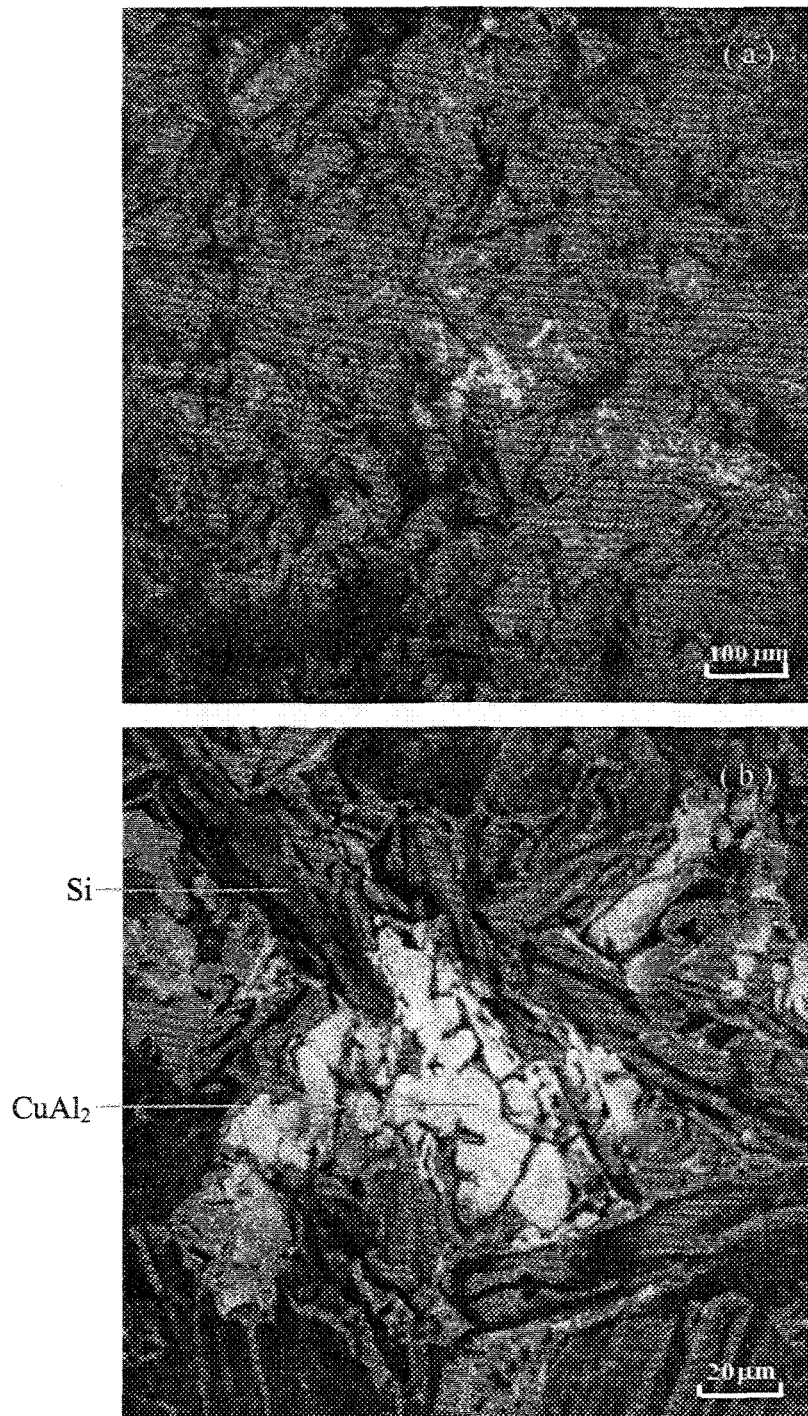


**Figure 5.1.** (a) BS micrograph showing fracture surface of AW base alloy (DAS 23 μm, unmodified, T5 condition, center), (b) high magnification BS showing the fracture of Si and CuAl<sub>2</sub> particles in (a).

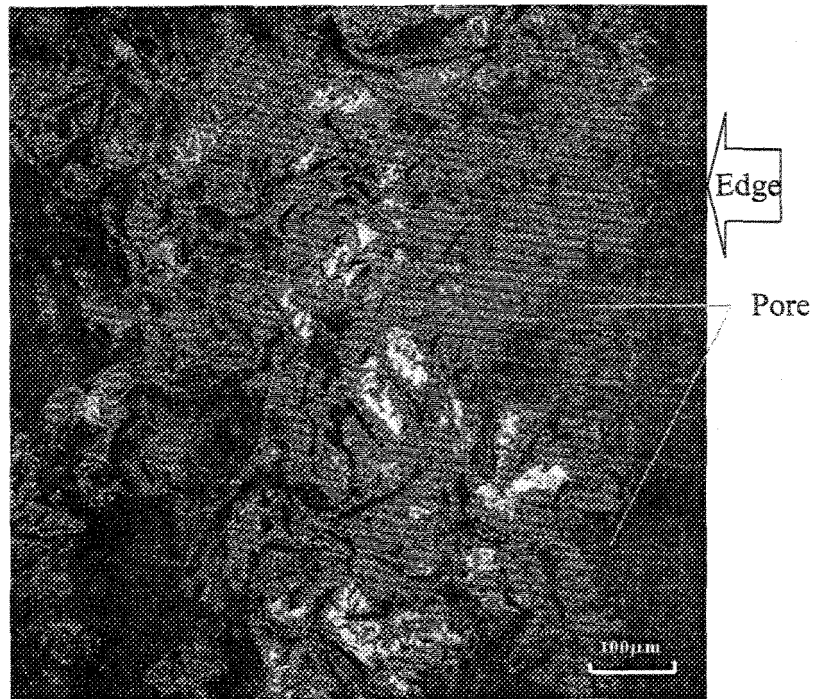


**Figure 5.2.** BS micrograph showing fracture surface of AW base alloy (DAS 23 μm, unmodified, edge).

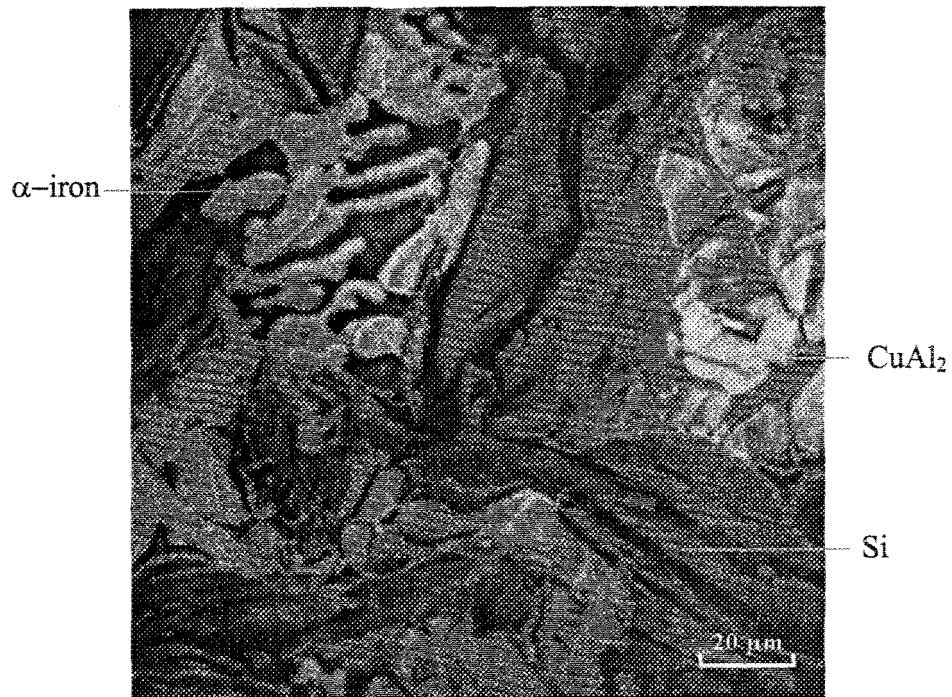


**Figure 5.3.** High magnification BS micrograph showing fracture surface of AW base alloy (DAS 83 μm, unmodified, center).

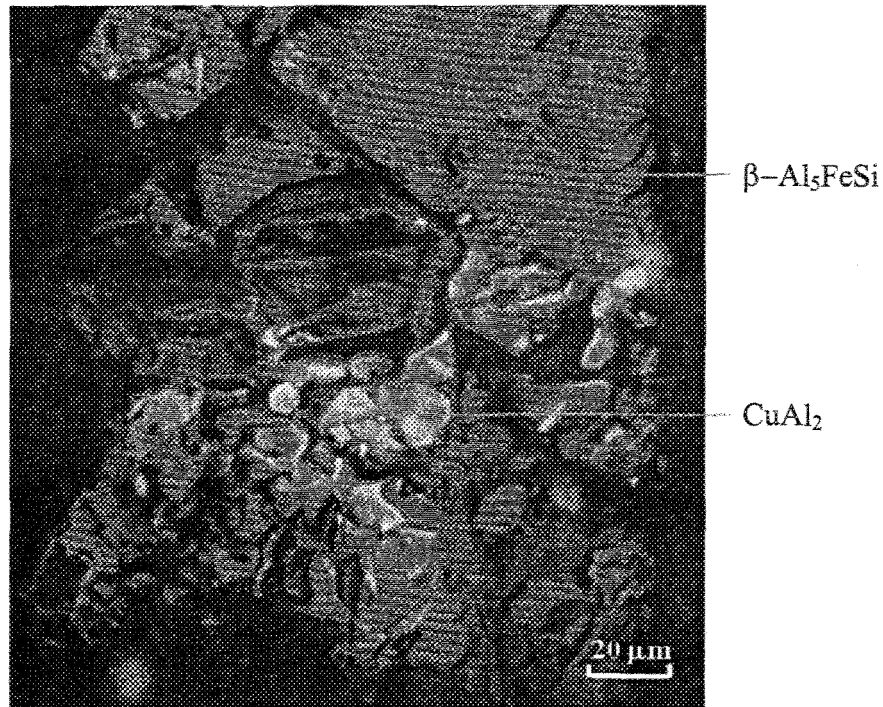


**Figure 5.4.** High magnification BS micrograph showing fracture surface of AW base alloy (DAS 83  $\mu\text{m}$ , unmodified, edge).

In the case of the DW alloy sample (modified 319.2 alloy containing 1.2% Fe) obtained at the highest cooling rate, the backscattered electron images, Figure 5.5 and Figure 5.6, reveal considerably different characteristics. For low DAS, the Si particles are isolated (marked) and the grain boundaries offer the most significant obstacle to slip bands in this alloy sample. The preferential cracking of particles at either cell or grain boundaries seems to be determined by the relative ability of each type of boundary to offer a significant obstacle to plastic deformation. However, keeping in mind the effect of Sr (in the modified alloy) on the transformation of the  $\text{CuAl}_2$  particles from eutectic to block-like form, the resulting fracture would be of a brittle nature, as can be seen from Figure 5.5.

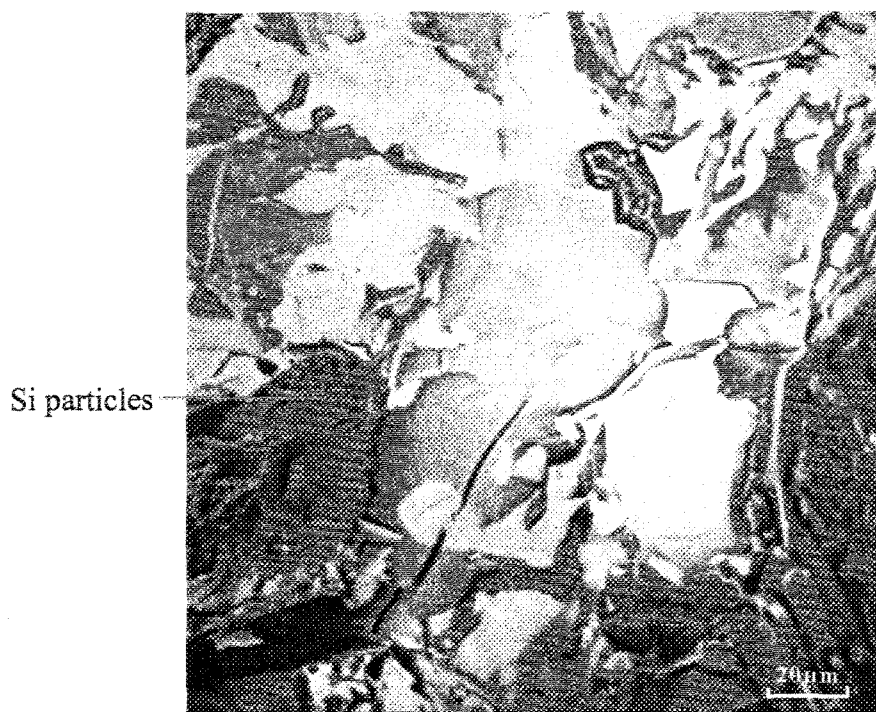


**Figure 5.5.** BS micrograph showing fracture surface of DW alloy (1.2% Fe, DAS 23 μm, Sr-modified, center).

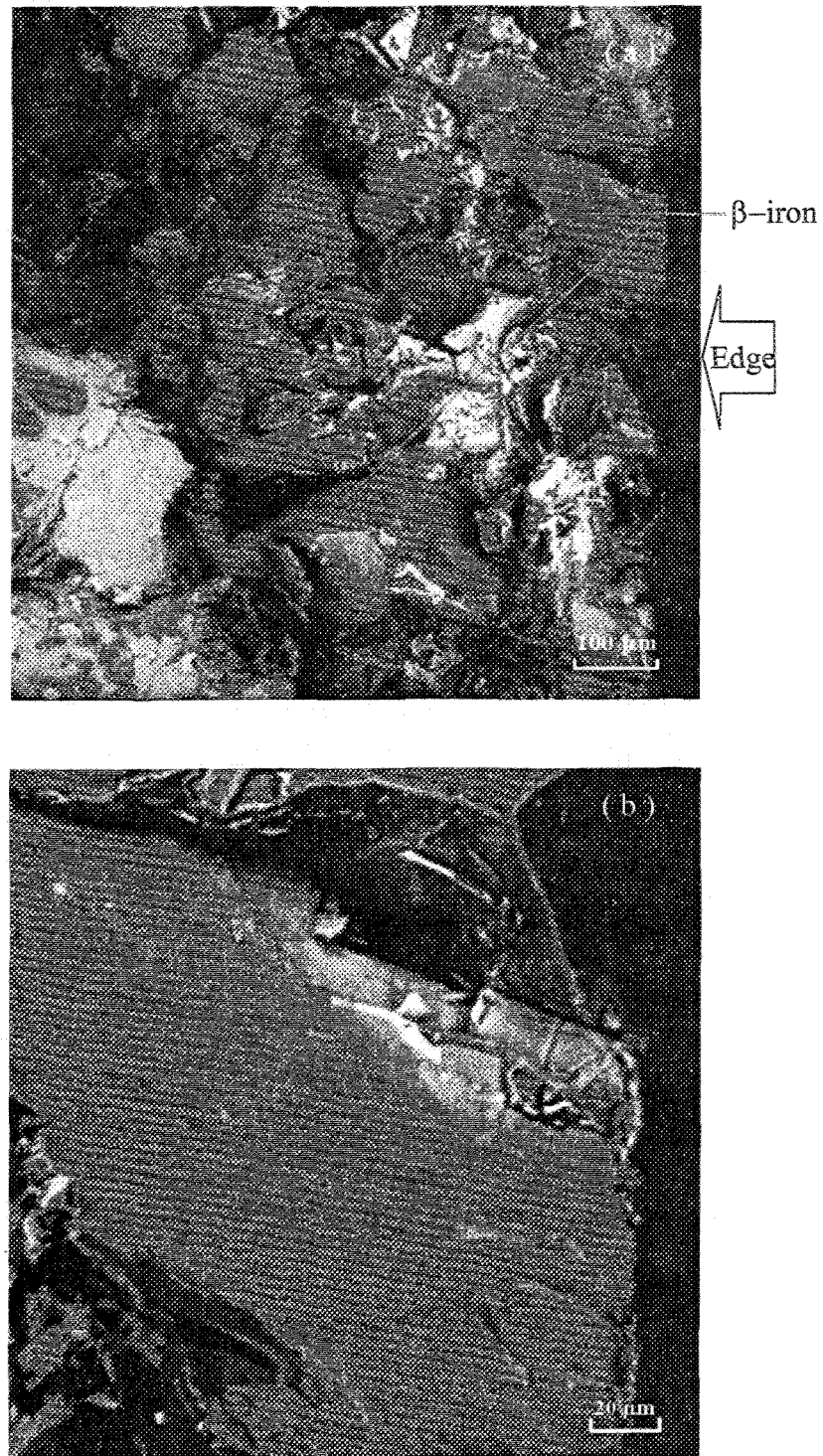


**Figure 5.6.** BS micrograph showing fracture surface of DW alloy (1.2% Fe, DAS 23 μm, Sr-modified, center).

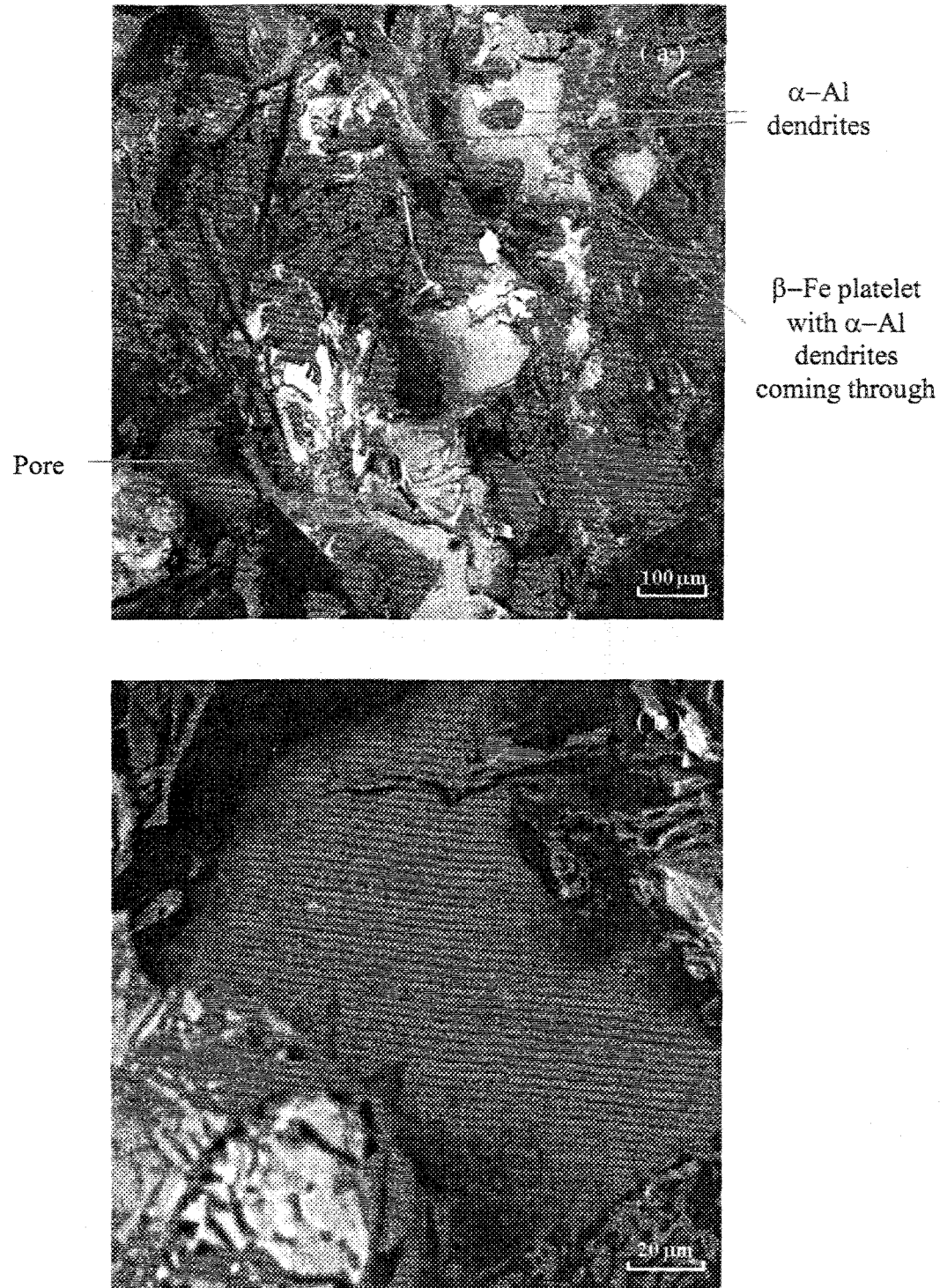
It is interesting to see that the toughness of the unmodified low-iron AW base alloy is more or less equal to that of the Sr-modified DW alloy (containing  $\sim 1.2\%$  Fe) at a DAS of  $23 \mu\text{m}$  (*cf.* 5.33 J for AW alloy with 5.55 J for DW alloy). This observation allows us to conclude that modification with Sr and consequent spheroidization of the Si particles would improve the alloy toughness due to the increase in the volume fraction of  $\alpha\text{-Al}$ . This, in turn, would compensate for the loss in energy caused by the presence of large brittle  $\beta$ -phase platelets. It should be pointed out that the bright region (marked A) in Figure 5.6 corresponds to the  $\text{Cu}_2\text{FeAl}_7$  phase. According to section 3.3.6, this phase is insoluble even after 100 h of solution heat treatment at  $505^\circ\text{C}$ .

Figure 5.7(a) shows the fracture surface of the DW alloy (DAS  $\sim 83 \mu\text{m}$ ). The cleavage fracture of the  $\beta$ -phase at the start of crack initiation accelerates the crack formation. For a high value of DAS, the cell boundaries are well defined by a dense array of Si particles and thereby provide an easy path for the crack propagation, leading to an intercellular type of fracture. A high magnification image of the cleavage of the  $\beta$ -phase platelet observed in Figure 5.7(a) is presented in Figure 5.7(b).

From Figure 5.8(a) and Figure 5.2, the effect of Sr modification on the  $\beta\text{-Al}_5\text{FeSi}$  phase is evident. The deterioration of the  $\beta$ -phase caused by Sr addition would likely result in the fragmentation of the  $\beta$ -platelets to some extent. The effect of Sr addition on the wearing off the  $\beta\text{-Al}_5\text{FeSi}$  particles chiefly depends on the size of the  $\beta$ -iron platelets. Furthermore, the high magnification BS image, Figure 5.8(b), reveals coarse pores on the fracture surface of DW alloy, resulting from the low cooling rate.



**Figure 5.7.** (a) BS micrograph showing fracture surface of DW alloy (1.2% Fe, DAS 83 μm, Sr-modified, edge), (b) high magnification BS showing cleaved  $\beta$ -Al<sub>5</sub>FeSi platelet observed in (a).



**Figure 5.8.** (a) BS micrograph showing fracture surface of DW alloy (1.2% Fe, DAS 83  $\mu\text{m}$ , Sr-modified, center), (b) high magnification BS showing the pore observed in (a).

It is also interesting to note from the smooth surface of the  $\beta$ -platelets in Figure 5.7 that the  $\beta$ -platelets not modified by Sr can be cracked by cleavage quite easily, as evidenced by the low impact energy of corresponding DW alloy sample (*i.e.* 2.56 J).

In summary, Sr-modified high Fe-containing 319.2 alloy would expect to exhibit a mixed fracture mode. This is also confirmed by comparing the impact energies of the four DW alloy sample corresponding to the various dendrite arm spacings.

### 5.2.2 T6 Heat Treatment

Figure 5.9(a) shows the edge of the fractured AW alloy sample (DAS  $\sim 23 \mu\text{m}$ ) after T6 heat treatment. A comparison with the fractograph shown in Figure 5.1(a) (same alloy, T5 condition) shows that most of the  $\text{CuAl}_2$  phase has dissolved into the surrounding matrix. Crack initiation is facilitated by the existence of insoluble  $\beta\text{-Al}_3\text{FeSi}$  particles. In contrast, the coalesced void which nucleates on the Si phase are characteristic of ductile fracture. Figure 5.9(b) is the high magnification micrograph of Figure 5.9(a), revealing the cleavage of partially spheroidized Si particles as well as the undissolved Cu phases through which crack propagation takes place.

The high-magnified backscattered electron image of the same alloy, Figure 5.10, reveals that the intergranular crack propagation continues with the rupture of the brittle Si particles, the  $\text{CuAl}_2$  and  $\beta\text{-Al}_3\text{FeSi}$  intermetallics.

The BS micrographs shown in Figure 5.11 reveal the nature of crack propagation in the center of the same AW alloy sample ( $83 \mu\text{m}$  DAS – lowest cooling rate). In Figure 5.11(a), the fracture surface consists of undissolved Cu phase particles and partially

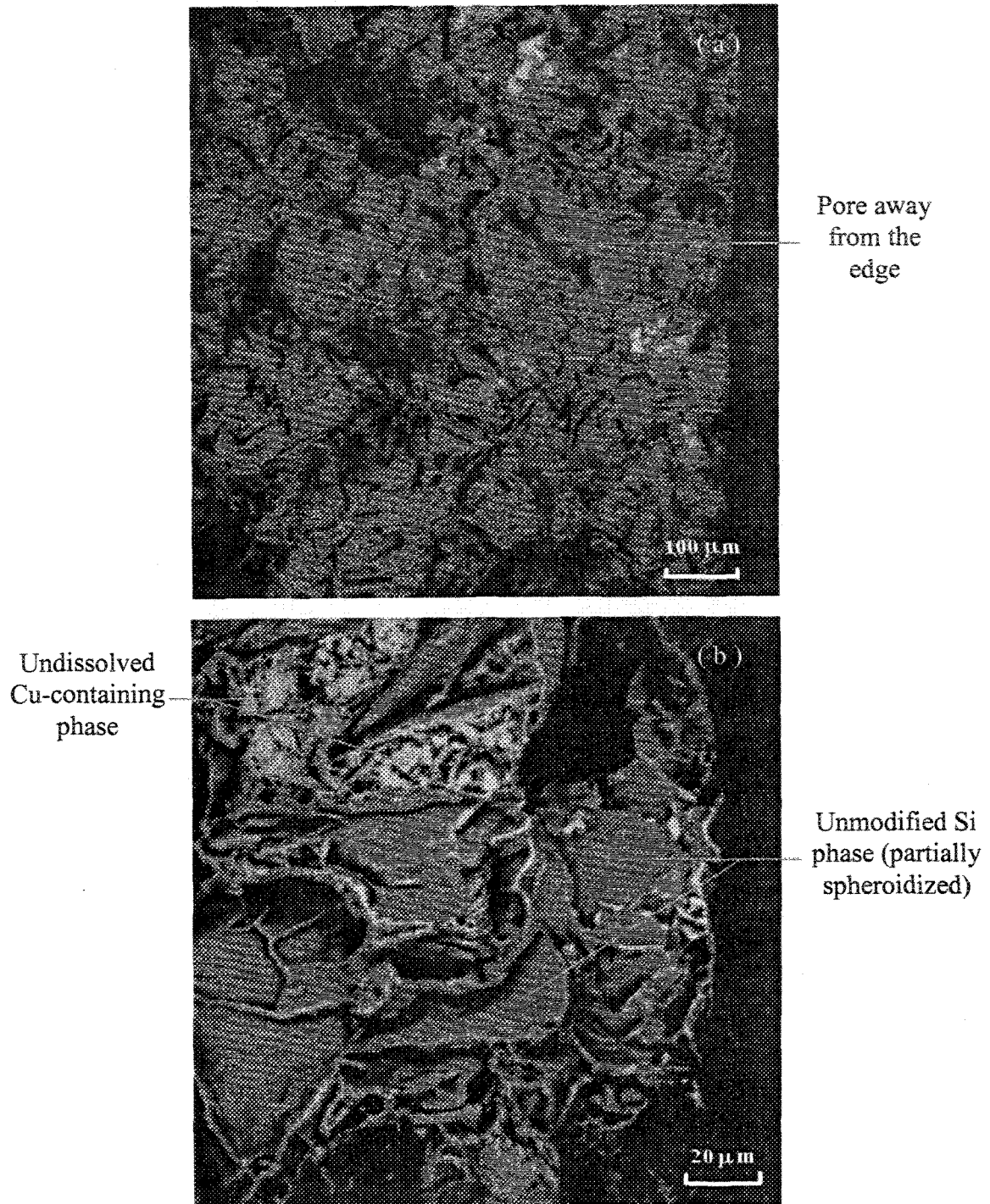


**Figure 5.9.** (a) BS micrograph showing fracture surface of AW base alloy (DAS 23 μm, unmodified, T6 condition, edge), (b) high magnification BS showing the crack initiation passing through the undissolved Cu-containing phase and fibrous Si particles.

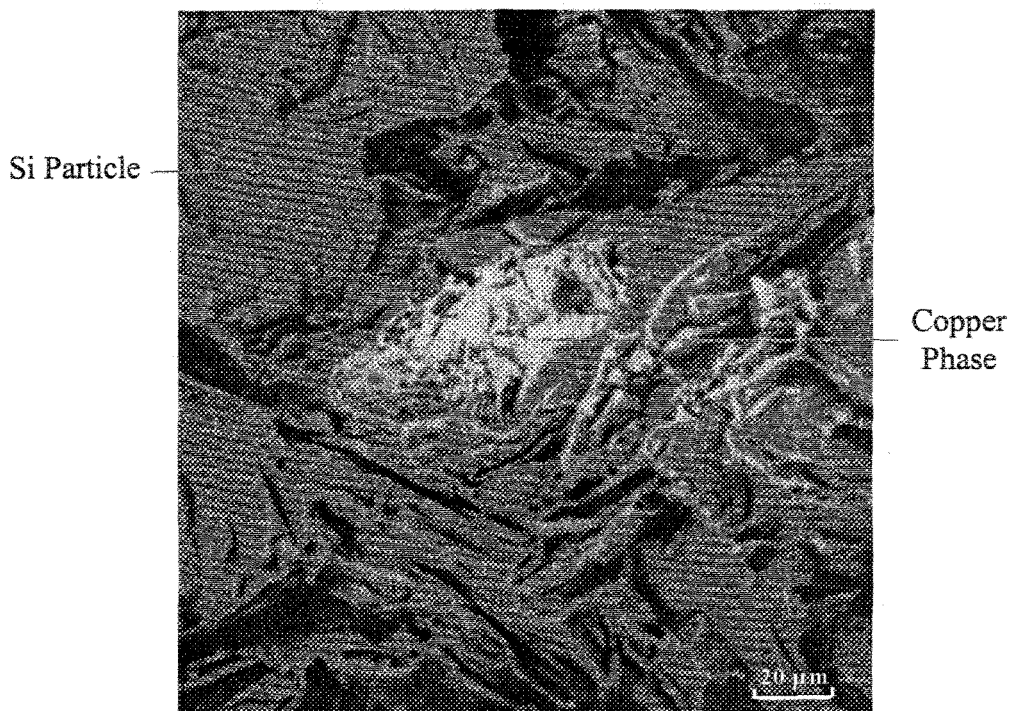


**Figure 5.10.** High magnification BS micrograph showing fractured intermetallics in AW base alloy (DAS 23  $\mu\text{m}$ , unmodified, T6 condition, center).

fragmented acicular Si particles, due to the temperature of the solution heat treatment, 490°C, not being high enough to completely spheroidize the Si particles. Comparing Figure 5.11(b) and Figure 5.10, (obtained at the same magnification), it is observed that the size of the eutectic copper phase particle in Figure 5.11(b) is much larger than that seen in Figure 5.10, due to the fact that the low cooling rate provides much nucleation time for the formation of the  $\text{CuAl}_2$  phase. The brittle nature of the  $\text{CuAl}_2$  phase particle facilitates crack propagate through the particle.

In the non-Sr-modified AW alloy, the effect of the cooling rate on the fracture surface is evident in that the sample obtained at the highest cooling rate (23  $\mu\text{m}$  DAS) exhibits a more ductile fracture mode than that obtained at the slowest cooling rate (83  $\mu\text{m}$  DAS).

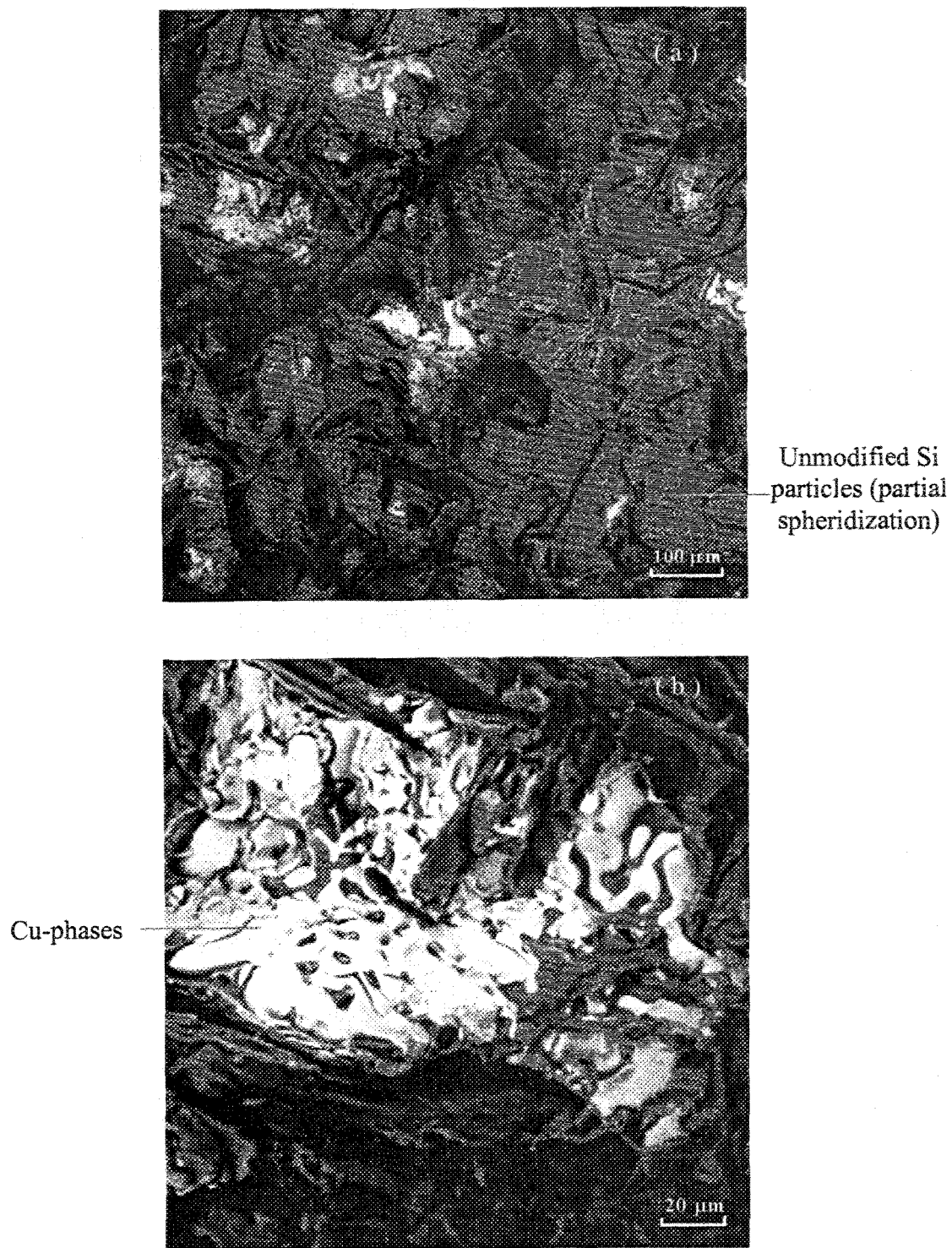


**Figure 5.11.** (a) BS micrograph showing fracture surface of AW base alloy (DAS 83  $\mu\text{m}$ , unmodified, T6 condition, center), (b) high magnification BS showing crack propagation through the undissolved  $\text{CuAl}_2$  phase.

At the high iron level (1.2%) and highest cooling rate, the BS fractographs of the Sr-modified DW alloy, Figure 5.12(a), showed that crack initiation occurred at the edge of the sample by the fragmentation of the  $\beta$ -phase, clearly seen in the high magnification image of Figure 5.12(b). Due to the high deformation rate and high load strength associated with the impact testing, the  $\beta$ -platelet at the edge of the sample fragmented into smaller segments, rather than undergoing cleavage as observed in the interior region of the  $\beta$ -platelet, away from the sample edge. In addition to the modification of the silicon phase, there is a tendency to form more block-like  $\text{CuAl}_2$  in the presence of strontium, due to the segregation of the  $\text{CuAl}_2$  phase to certain regions of the sample (away from the Al-Si eutectic regions). All of these factors coupled with the brittle nature of the  $\text{CuAl}_2$  particles likely contribute to the very low impact strength of the alloy. Another interesting point to be noted in Figure 5.12(a) is the worn-out nature of the  $\beta$ -iron particles in the Sr-modified alloy, resulting in the surface being more reminiscent of brittle type fracture. All these fracture characteristics contribute to the considerable decrease in the impact energy of the sample (*cf.* 4.34 J with 10.45 J in the AW alloy at 23  $\mu\text{m}$  DAS).

Obviously, at high Fe levels and at the lowest cooling rate, even in the Sr-modified DW alloy, the fracture still occurs mainly by cleavage of the brittle  $\beta\text{-Al}_5\text{FeSi}$  platelets, Figure 5.13(a). The high magnification BS image of the DW alloy sample given in Figure 5.13(b) clearly shows how crack initiation begins with the fragmentation of the  $\beta$ -phase, followed by cleavage. In some instances, the crack also propagates through the

fragmentation of  $\text{Cu}_2\text{FeAl}_7$  particles which have precipitated on the sides of the  $\beta$ -platelets during solidification, Figure 5.14.

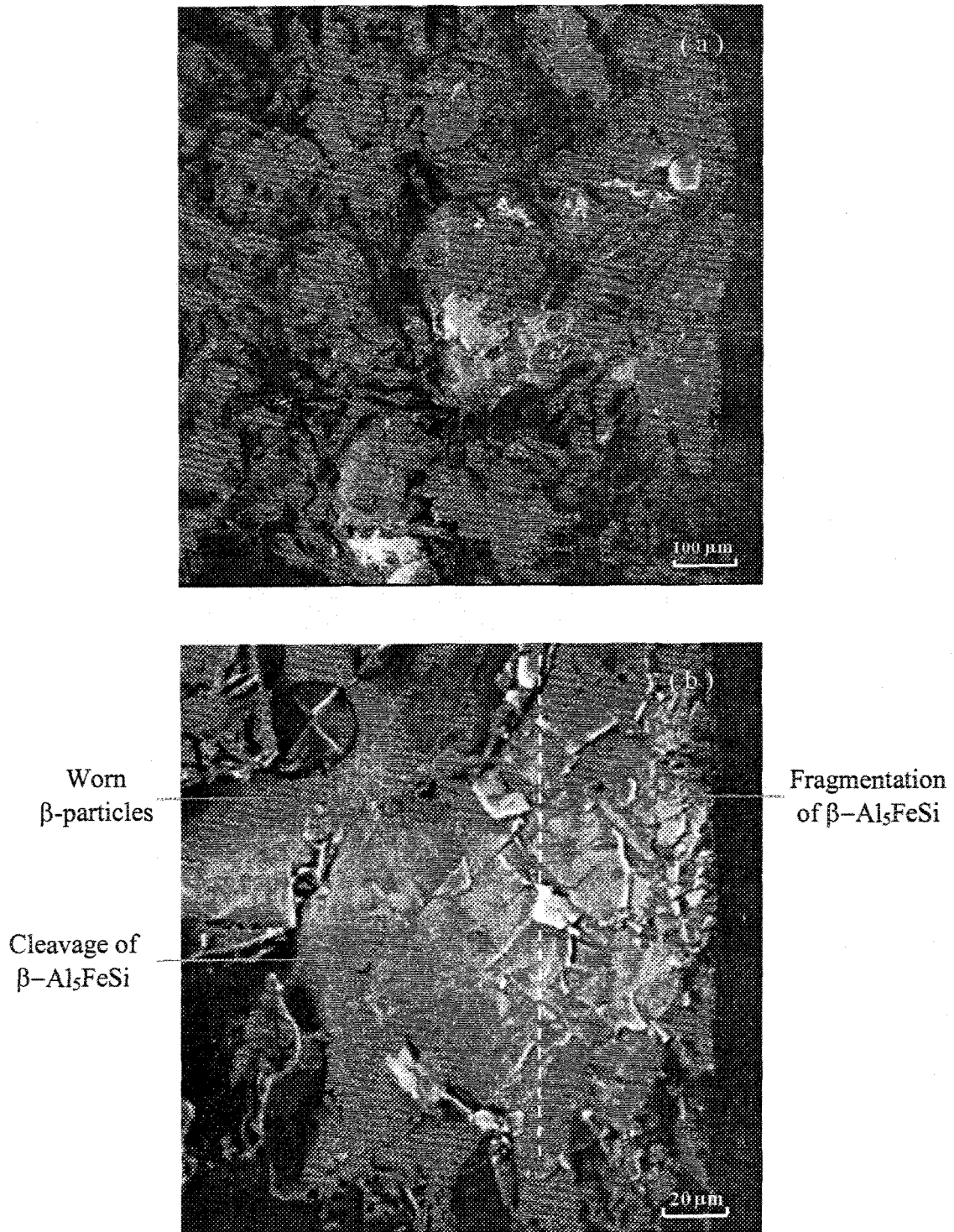


**Figure 5.12.** (a) BS micrograph showing fracture surface of DW alloy (1.2% Fe, DAS 23 μm, Sr-modified, T6 condition, edge), (b) high magnification BS showing fragmentation of β-Al<sub>5</sub>FeSi during crack initiation.

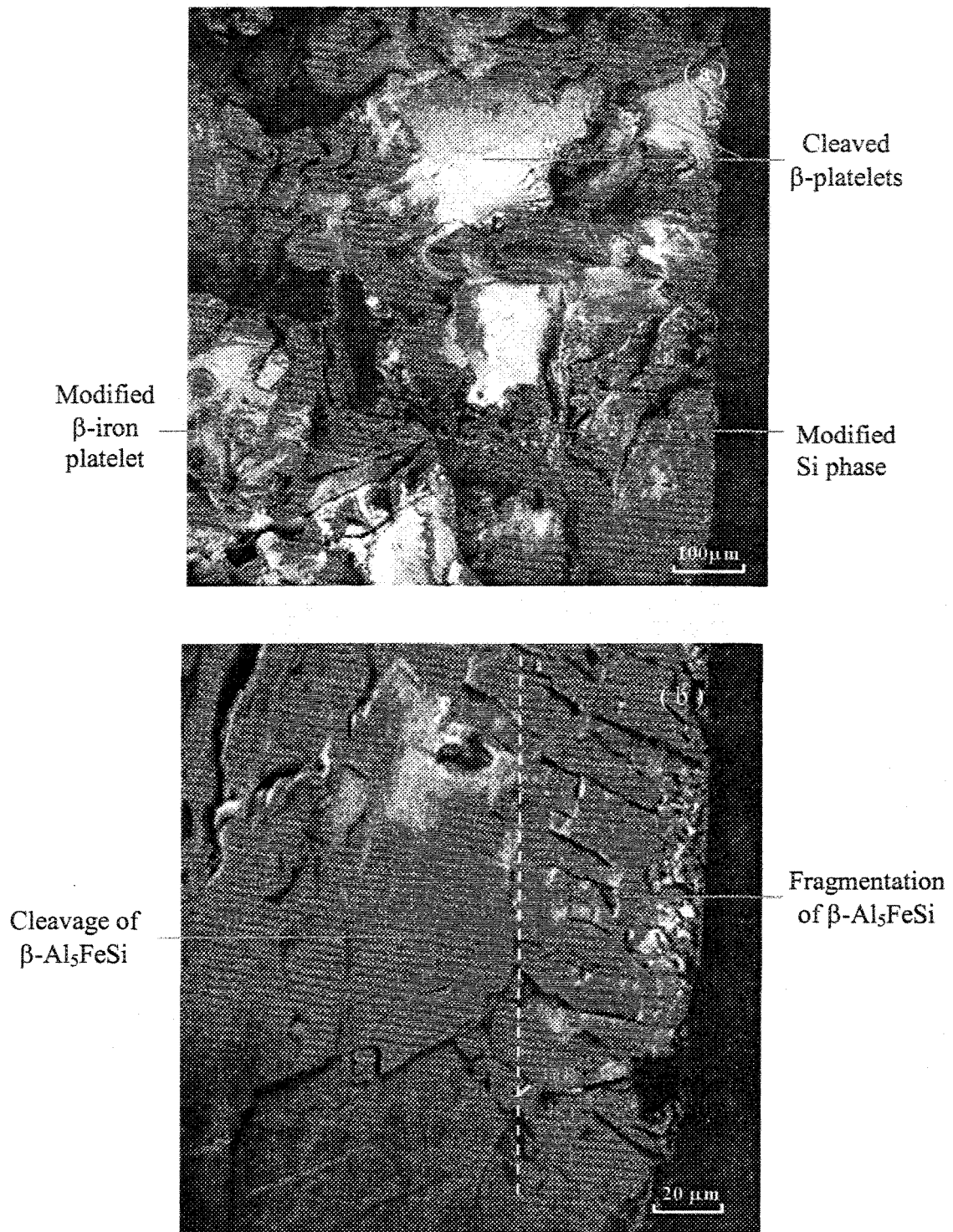


**Figure 5.13.** (a) BS micrograph showing fracture surface of DW alloy (1.2% Fe, DAS 83  $\mu\text{m}$ , Sr-modified, T6 condition, edge), (b) high magnification BS showing fragmentation of  $\beta\text{-Al}_5\text{FeSi}$  during crack initiation.

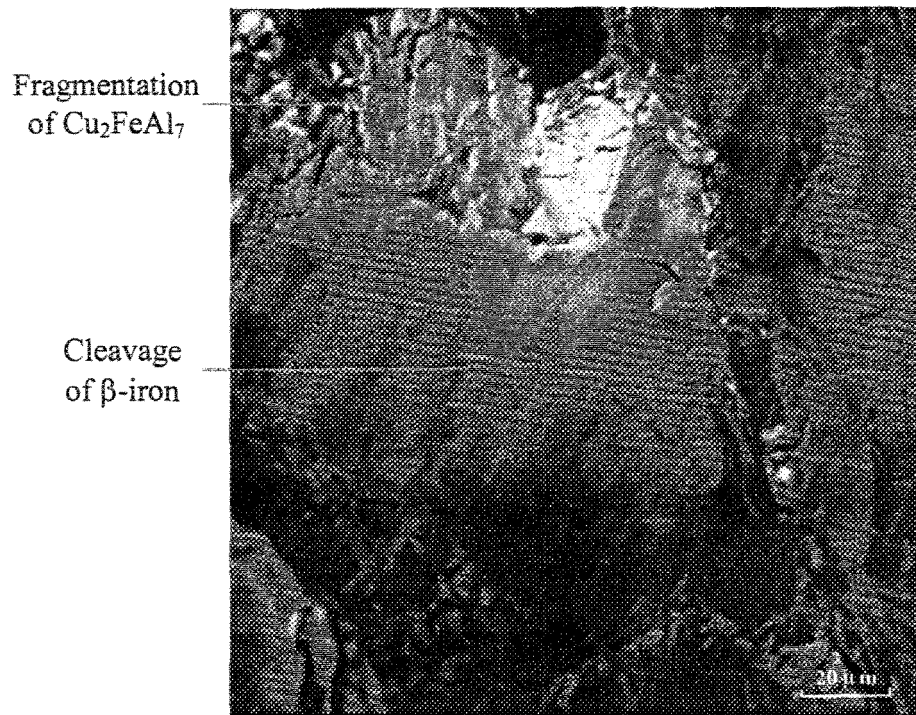


**Figure 5.14.** BS micrograph showing fragmentation of  $\text{Cu}_2\text{FeAl}_7$  on the fracture surface of DW alloy (1.2% Fe, DAS 83  $\mu\text{m}$ , Sr-modified, T6 condition, center).

**CHAPTER 6**  
**CONCLUSIONS**

## CHAPTER 6

### CONCLUSIONS

A study of the effect of Sr, Fe and P additions on the precipitation and dissolution of the  $\text{CuAl}_2$  phase in 319 type Al-Si-Cu alloys (following different solution heat treatment times at 505 °C) was carried out, using optical microscopy, image analysis and electron probe microanalysis. The effect on mechanical properties was also investigated through a study of the tensile and impact properties. Based on the results obtained, the following conclusions can be made:

#### Microstructure

1. The addition of Sr leads to the segregation of the copper phase in regions away from the Al-Si eutectic. This results in:
  - i) an increase in the amount of blocky  $\text{CuAl}_2$  in the as-cast alloy (*cf.* ~17.7% with 2.60% in the unmodified alloy).
  - ii) a slowing down of the rate of  $\text{CuAl}_2$  dissolution on account of the  $\text{CuAl}_2$  segregation during solidification.
2. The addition of Fe results in the dispersion of the  $\text{CuAl}_2$  phase and hence accelerates its dissolution during solution heat treatment. The precipitation of the  $\beta\text{-Al}_3\text{FeSi}$

phase provides nucleation sites for the precipitation of the copper phase which, in turn, reduces the severity of  $\text{CuAl}_2$  segregation. In this case, the blocky  $\text{CuAl}_2$  form as small particles which can be greatly beneficial in enhancing the  $\text{CuAl}_2$  dissolution during solution heat treatment.

3. The negative effect of phosphorus addition is due to the formation of  $(\text{Al,P})\text{O}_2$  oxide particles which act as nucleation sites for the precipitation of the  $\text{CuAl}_2$  phase.
4. The  $\text{CuAl}_2$  phase particles are more or less completely dissolved in the Al matrix after 100 hours of solution heat treatment in all the alloys studied, except in the case of the 319 alloy containing both P and Sr (*i.e.* H4T1 alloy). As both the precipitation of AlP particles and the presence of Sr in the H4T1 alloy lead to the severe segregation of the  $\text{CuAl}_2$  phase during solidification, the dissolution of the  $\text{CuAl}_2$  phase is slowed down considerably during solution heat treatment. The introduction of Fe to the alloy can, to some extent, assist in neutralizing the negative effect of phosphorus.
5. The mechanism for the dissolution of the  $\text{CuAl}_2$  phase during solution heat treatment can be proposed as follows: (i) separation of the  $\text{CuAl}_2$  particles from the  $\beta\text{-Al}_5\text{FeSi}$  platelets, (ii) necking of the  $\text{CuAl}_2$  particles followed by spheroidization, (iii) dissolution of the spheroidized  $\text{CuAl}_2$  particles by radial diffusion of Cu atoms into the surrounding aluminum matrix.

## Mechanical Properties

### Tensile Properties

6. Tensile properties, viz., ultimate tensile strength (UTS), yield strength (YS) and percent elongation (%El) decrease with a decrease in the cooling rate (*i.e.* increase in DAS) regardless of alloy composition, in both T5 and T6 conditions.
7. Strontium modification leads to a change in the morphology of the eutectic Si particles from a coarse flake-like form to a fine fibrous one. Thus, the Sr-modified alloys display much higher UTS and ductility values compared to the non-modified alloys.
8. Iron has a detrimental effect on the UTS and ductility in terms of the  $\beta$ -Al<sub>5</sub>FeSi platelet size. At iron contents beyond 1.2 wt%, no obvious improvement in ductility can be observed with an increase in the cooling rate.
9. The negative effect of phosphorus addition, due to the formation of (Al,P)O<sub>2</sub> oxide particles which act as nucleation sites for the precipitation of the block-like CuAl<sub>2</sub>, is reflected in the lower UTS value of FW alloy compared to DW alloy at ~23  $\mu$ m DAS in T5 condition (*cf.* 176 MPa vs. 184 MPa).
10. Iron addition increases YS in the alloys studied, *i.e.*, the presence of iron can harden the alloy to some extent. The correlation between YS and cooling rate is more complex in the T6 condition than in the T5 condition, as it is also a function of the homogeneity of the alloy composition and CuAl<sub>2</sub> dissolution.

11. Compared to the T5 condition, the UTS, YS and %El increase significantly in the T6 condition (except for the %El values of the 1.2% Fe-containing DW, EW and FW alloys), since the T6 heat treatment assists in homogenizing the alloys, changing the morphology of the interdendritic phases, and dissolving precipitation-hardening constituents such as  $\text{CuAl}_2$ . However, Fe levels beyond 1.2 wt% reduce alloy ductility significantly due to the presence of a large amount of the brittle  $\beta$ -iron platelets. Even after T6 heat treatment, no apparent effect on %El in the three high Fe-containing alloys can be observed.

#### Impact Properties

12. An increase in the DAS value leads to a decrease in the total absorbed energy (Et) for all alloys studied. Strontium modification and spheroidization of the Si particles can compensate for the loss in impact energy caused by the presence of ~1.2% Fe addition, resulting in similar Et values being observed for the unmodified AW alloy and DW alloy at the same cooling rate.
13. Strontium addition results in changing the morphology of the Si particles from acicular to fibrous. This lessens the stress concentration during impact testing and effectively increases the volume fraction of the aluminum matrix, so that the Sr-modified CW alloy displays a higher impact energy than the AW base alloy at any given DAS.
14. Iron addition leads to an increased precipitation of  $\beta$ - $\text{Al}_5\text{FeSi}$  platelets, which, due to their acicular nature, also act as crack initiation sites in addition to the brittle Si

particles, and dramatically reduce the impact properties, regardless of the cooling rate.

15. The phosphorus added to FW alloy is distributed within the segregated  $\text{CuAl}_2$  particles during solidification. However, the formation of phosphorus oxides, which act as nucleation sites for the  $\text{CuAl}_2$  phase, can accelerate cracking of the  $\text{CuAl}_2$  particles.
16. Compared to the T5 heat treatment, the T6 treatment helps in the even distribution of the microconstituents and their dissolution into the aluminum matrix, thereby reducing the amount of acicular particles (Si and  $\beta\text{-Al}_3\text{FeSi}$ ) present in the matrix. Also, as most of the block-like  $\text{CuAl}_2$  particles are dissolved and redistributed within the aluminum matrix, more Cu is available to act as a strengthening agent during aging. Consequently, the impact toughness is greatly improved.

### **Fracture Mechanism**

The fracture surface of the impact tested samples corresponding to AW and DW alloys were examined, to determine the fracture behavior in Al-Si-Cu alloys. The two alloys were respectively selected to compare the fracture behavior in the unmodified base 319 alloy with that of the Sr-modified alloy containing a high percent of Fe. Such a comparison helped to bring out the influence of Sr and Fe addition on the nature of the crack initiation and crack propagation behavior.

17. In the T5 condition, the unmodified 319 AW base alloy undergoes crack initiation mainly through the fracture of acicular Si particles. Cracks propagation takes place through the mechanism of void coalescence (where the voids result from the fracture of the Si particles), except when  $\beta$ -iron and  $\text{CuAl}_2$  intermetallics are present, in which case the latter take priority in the fracture propagation process.
18. In the DW alloy (Sr-modified 319 alloy with  $\sim 1.2\%$  Fe), in both T5 and T6 conditions, crack initiation occurs through the fragmentation of  $\beta\text{-Al}_5\text{FeSi}$  intermetallics, Si particles, and  $\text{CuAl}_2$  particles. The existence of coarse pores also facilitates crack initiation, reducing the impact energy of the tested sample. Thereafter, crack propagation occurs through the cleavage of  $\beta\text{-Fe}$  platelets (rather than by their decohesion from the matrix). Cracks also propagate through the fracture of undissolved  $\text{CuAl}_2$  or other insoluble intermetallics such as  $\text{Cu}_2\text{FeAl}_7$ , as well as through brittle Si particles.
19. After T6 heat treatment, in the DW alloy, most of the  $\text{CuAl}_2$  phase particles are dissolved into the aluminum matrix, which minimizes the detrimental effect on impact energy caused by the brittle nature of these particles. The fibrous nature of the modified Si particles and those undergoing spheroidization during T6 heat treatment, as well as the fragmentation of the  $\beta\text{-Fe}$  phase due to Sr modification decrease the chances for crack propagation to occur through these particles.

## SUGGESTIONS FOR FURTHER WORK

The work carried out in the present study on the segregation and dissolution of  $\text{CuAl}_2$  phase in 319 alloys with respect to various metallurgical factors (*i.e.*, cooling rate, iron content, Sr modification and heat treatment) has provided some important results in relation to the copper phases present in these alloys. Based on these results, it is suggested that the study could be extended to other casting methods such as lost foam casting, where the use of different types of chills could be explored as another parameter.

Likewise, in the context of the mechanical properties, these could be extended to include a study of the fatigue properties of these alloys, which would provide very useful information in regard to the use of 319 alloys in critical components.

## REFERENCES

1. J. F. Major, A. Makinde, P. D. Lee, B. Chamberlain, T. Scappaticci, and D. Richman, "The Lincoln Mark VIII Cast Al Suspension Control Arm," *SAE Paper #940874*, SAE International, Warrendale, PA, 1994.
2. C. M. Sonsino, and J. Ziese, "Fatigue Strength And Application of Cast Aluminum Alloys With Different Degrees of Porosity," *International Journal of Fatigue*, Vol. 15(2), March 1993, pp. 74-84.
3. L. Bäckerud, G. Chai, and J. Tamminen, *Solidification Characteristics of Aluminium Alloys, Vol. 2: Foundry Alloys*, AFS/Skanaluminium, Des Plaines, IL, USA, 1990, pp. 71-84.
4. M. A. Moustafa, F. H. Samuel, H. W. Doty, and S. Valtierra, "Effect of Mg and Cu Additions on the Microstructural Characteristics and Tensile Properties of Sr-modified Al-Si Eutectic Alloys," *International Journal of Cast Metals Research*, Vol. 14, 2002, pp. 235-253.
5. J. E. Hatch (Ed.), *Aluminum: Properties and Physical Metallurgy*, American Society for Metals, Metals Park, Ohio, USA, 1984, p. 143.
6. J. E. Davis (Ed.), *Aluminum and Aluminum Alloys*, ASM Specialty Handbook<sup>®</sup>, ASM International, Materials Park, Ohio, USA, 1993.
7. M. Hansen, *Constitution of Binary Alloys*, Second Edition, McGraw-Hill Book Company, Inc., New York, 1958, pp. 84-90.
8. M. H. Mulazimoglu, N. Tenekedjev, B. Closset and J. Gruzleski, "Microstructure and Thermal Analysis of Strontium Treated Aluminium-Silicon Alloys," *American Foundrymen's Society, Inc.*, USA, 1995, pp. 23-40.
9. L. F. Mondolfo, *Aluminum Alloys: Structure and Properties*, Butterworths, London-Boston, 1976.

10. M. F. Hafiz and T. Kobayashi, "A Study on the Microstructure – Fracture Behavior Relations in Al-Si Casting Alloys," *Scripta Metallurgica et Materialia*, Vol. 30, 1994, pp. 475-480.
11. R. W. Smith, *Solidification of Metals*, Publication 110, Iron and Steel Institute, 1968, p. 224.
12. P. B. Crosley and L. F. Mondolfo, "Modification of Aluminum-Silicons," *Modern Castings*, Vol. 49, 1966, pp. 89-100.
13. M. D. Hanna, S. Lu, and A. Hellawell, "Modification in the Aluminum Silicon System," *Metallurgical Transactions A*, Vol. 15A, 1984, pp. 459-469.
14. P. D. Hess and E. V. Blackman, "Strontium as a Modifying Agent for Hypoeutectic Aluminum-Silicon Alloys," *AFS Transactions*, Vol. 84, 1975, pp. 87-90.
15. J. E. Gruzleski, F. Paray, S. G. Shabestari, and M. H. Mulazimoglu, "Applications of Strontium in Cast and Wrought Aluminum Alloys," *All3: le Magazine de l'Aluminium* Vol. 2, no. 1, 1996, pp. 23-33.
16. S. Lu and A. Hellawell, "The Mechanism of Silicon Modification in Aluminum Silicon Alloys: Impurities Induced Twinning," *Metallurgical Transactions A*, Vol. 18A, 1987, pp. 1721-1733.
17. J. E. Gruzleski, M. Pekguleryuz, and B. Closset, in *Proceedings of the Third International Solidification Conference* (Sheffield, U.K.), Institute of Metals, 1987.
18. Y. Tsumura, A. Sakakibara, K. Toyoda, and M. Ishikawa, "The Mechanism of Incubation Period of Modification Effect on Al-Si Alloy," *Journal of the Japan Institute of Light Metals* (in Japanese), Vol. 30, 1980, pp. 239-245.
19. A. M. Samuel, P. Ouellet, F. H. Samuel, and H. W. Doty, "Microstructural Interpretation of Thermal Analysis of Commercial 319 Aluminum Alloy with Magnesium and Strontium Additions," *AFS Transactions*, Vol. 105, 1997, pp. 951-962.
20. D. Argo and J. E. Gruzleski, "Porosity in Modified Aluminum Alloy Castings," *AFS Transactions*, Vol. 96, 1988, pp. 65-74.
21. G. K. Sigworth, S. Shivkumar, and D. Apelian, "The Influence of Molten Metal Processing on Mechanical Properties of Cast Al-Si-Mg Alloys," *AFS Transactions*, Vol. 97, 1989, pp. 811-824.

22. H. Beumler, A. Hammerstad, B. Wieting and R. DasGupta, "Analysis of Modified 319 Aluminum Alloy," *AFS Transactions*, Vol. 96, 1988, pp. 1-12.
23. M. Djurdjevic, T. Stockwell, and J. Sokolowski, "The Effect of Strontium on the Microstructure of the Aluminium-Silicon and Aluminium-Copper Eutectics in the 319 Alloy," *International Journal of Cast Metals Research*, Vol. 12(2), 1999, pp. 67-73.
24. S. Shivkumar, S. Ricci, Jr., B. Steenhoff, D. Apelian, and G. Sigworth, "An Experimental Study to Optimize the Heat Treatment of A356 Alloy," *AFS Transactions*, Vol. 97, 1989, pp. 791-810.
25. S. Shivkumar, S. Ricci, Jr., and D. Apelian, "Effects of Solution Parameters and Simplified Supersaturation Treatments on Tensile Properties of Cast Al-Si-Mg Alloys," *AFS Transactions*, Vol. 98, 1990, pp. 913-922.
26. B. A. Parker, D. S. Saunders, and J. R. Griffiths, "The Quantitative Evaluation of Microstructure of a Strontium-Modified Al-Si-Mg Alloy Following Prolonged Solution Treatment," *Metallurgical Forum*, Vol. 5, 1982, pp. 48-53.
27. J. E. Gruzleski and B. M. Closset, *The Treatment of Liquid Aluminum-Silicon Alloys*, American Foundrymen's Society, Inc., Des Plaines, IL, 1990.
28. R. Kiusalaas, "Relation Between Phases Present in Master Alloys of the Al-Ti-B Type," Ph.D. Thesis, University of Stockholm, Sweden, 1986.
29. F. H. Samuel, A. M. Samuel, and H. W. Doty, "Factors Controlling the Type and Morphology of Cu-Containing Phases in 319 Al Alloy," *AFS Transactions*, Vol. 104, 1996, pp. 893-901.
30. O. Reiso, H. Øverlie, and N. Ryum, "Dissolution and Melting of Secondary Al<sub>2</sub>Cu Phase Particles in an AlCu Alloy," *Metallurgical Transactions A*, Vol. 21A, 1990, pp. 1689-1695.
31. A. M. Samuel, J. Gauthier, and F. H. Samuel, "Microstructural Aspects of the Dissolution and Melting of Al<sub>2</sub>Cu Phase in Al-Si Alloy During Solution Heat Treatment," *Metallurgical and Materials Transactions A*, Vol. 27A, 1996, pp. 1785-1798.
32. J. Gauthier, P. Louchez, and F. H. Samuel, "Heat Treatment of 319.2 Al Automotive Alloy: Part 1, Solution Heat Treatment," *Cast Metals*, Vol. 8(1), 1995, pp. 91-106.

33. J. Gauthier, P. Louchez, and F. H. Samuel, "Heat Treatment of 319.2 Al Automotive Alloy: Part 2, Aging Behavior," *Cast Metals*, Vol. 8(1), 1995, pp. 107-114.
34. W. B. Pearson, *Handbook of Lattice Spacings and Structures of Metals and Alloys*, Vol. 2, Pergamon Press, Oxford, 1967.
35. L. Grand, "Influence of Some Impurities on the Quality of Aluminum Alloys," *Fonderie*, Vol. 217, Mar. 1964, pp. 95-100.
36. S. Hajas, "Effect of Iron Contamination on the Mechanical Properties of Aluminum Casting Alloys," *Chemical Abstracts*, Vol. 73, 1970, No. 133571.
37. L. F. Mondolfo, *Manganese in Aluminum Alloys*, The Manganese Centre, France, 1990.
38. A. Couture, "Iron in Aluminum Casting Alloys – A Literature Survey," *AFS International Cast Metals Journal*, Vol. 6(4), Dec. 1984, pp. 9-17.
39. S. Murali, K. S. Raman and K. S. S. Murthy, "The Formation of  $\beta$ -FeSiAl<sub>5</sub> and Be-Fe Phases in Al-7Si-0.3Mg Alloy Containing Be," *Materials Science and Engineering A*, Vol. 190A, 1995, pp. 165-172.
40. O. Vorren, J. E. Evensen, and T. B. Pedersen, "Microstructure and Mechanical Properties of AlSi(Mg) Casting Alloys," *AFS Transactions*, Vol. 92, 1984, pp. 459-466.
41. A. Franek, J. Pazdernik, and A. K. Hanna, "On the Morphology of the Eutectic and Phases in Aluminum-Silicon 12-Iron and Aluminum-Silicon 20-Iron Alloys," *World Aluminum Abstracts*, Vol. 7, 1974, No. 53-0036X.
42. H. Iwahori, H. Takamiya, K. Yonekura, Y. Yamamoto, and M. Nakamura, *Casting* (in Japanese), Vol. 60, No. 9, 1988, pp. 590-595.
43. J. Igléssis, C. Frantz and M. Gantois, "La croissance par propagation de plans de macle des composés eutectiques dans le système ternaire Al-Fe-Si," *Mémoires scientifiques de la revue de métallurgie*, Fév. 1978, pp. 93-100.
44. A. Griger, V. Stefaniay, A. Lendvai and T. Turmezey, "Possible Modification of Cast Structure by Continuous Casting Technology in AlFeSi Alloys, Part III: Intermetallic Phases", *Aluminum*, Vol. 65, No. 10, 1989, pp. 1049-1056.

45. A. M. Samuel, F. H. Samuel and H. W. Doty, "Observations on the Formation of  $\beta$ - $\text{Al}_5\text{FeSi}$  Phase in 319 Type Al-Si Alloys," *Journal of Material Science*, Vol. 31, 1996, pp. 5529-5539.
46. M. R. Ghomashchi, "Intermetallic Compounds in an Al-Si Alloy Used in High Pressure Die-Casting," *Zeitschrift für Metallkunde*, Vol. 78, 1987, pp. 784-787.
47. G. L. Armstrong, "Alloy Selections for Automotive Aluminum Castings," *SAE Technical Paper*, No. 780249, Society of Automotive Engineers, 1978, 7 pages.
48. A. Pennors, A. M. Samuel, F. H. Samuel and H. W. Doty, "Precipitation of  $\beta$ - $\text{Al}_5\text{FeSi}$  Iron Intermetallic in Al-6%Si-3.5%Cu (319) Type Alloys: Role of Sr and P," *AFS Transactions*, Vol. 106, 1998, pp. 98-105.
49. C. W. Meyers, "Solution Heat Treatment Effects on Ultimate Tensile Strength and Uniform Elongation in A357 Aluminum Alloys," *AFS Transactions*, Vol. 94, 1986, pp. 511-518.
50. G. E. Totten and D. S. Mackenzie, "Aluminum Quenching Technology: A Review," *Materials Science Forum*, Vols. 331-337, 2000, pp. 589-594.
51. H. D. Brody and M. C. Flemings, "Solute Redistribution in Dendritic Solidification," *TMS-AIME*, 1966, pp. 496-502.
52. W. Bonfield and P. K. Dutta, "Precipitation Hardening in an Al-Cu-Si-Mg Alloy at 130 to 220°C," *Journal of Materials Science*, Vol. 11, 1976, pp. 1661-1666.
53. J. H. Sokolowski, X.-C. Sun, G. Byczynski, D. O. Northwood, D. E. Penrod, R. Thomas, and A. Esseltine, "A Metallurgical Study of the Heat Treatment of Aluminum Alloy 319 (Al-6Si-3.5Cu) Castings," *Journal of Materials Processing Technology*, Vol. 53(1-2), 1995, pp. 385-392.
54. N. Crowell and S. Shivkumar, "Solution Treatment Effects in Cast Al-Si-Cu Alloys," *AFS Transactions*, Vol. 103, 1995, pp. 721-726.
55. G. E. Dieter, Jr., *Mechanical Metallurgy*, 2<sup>nd</sup> edition, Metallurgy and Metallurgical Engineering Series, McGraw-Hill, New York, 1976.
56. R. DasGupta, C. Brown, and S. Marek, "Effect of Increased Magnesium Content on the Mechanical Properties of Sand-Cast 319 Aluminum Alloy," *AFS Transactions*, Vol. 97, 1989, pp. 245-253.

57. J. Dornauf and A. M. Frankfurt, "Silicon-Aluminum Cast Alloys," *Chemical Abstracts*, Vol. 22, 1928, p. 210.
58. P. Meyer, D. Massinon, and P. Guerin, "Influence of Microstructure on the Static and Thermal Fatigue Properties of 319 Alloys," *SAE Paper #970705*, SAE International, Warrendale, PA, 1997.
59. A. M. Samuel and F. H. Samuel, "A Metallographic Study of Porosity And Fracture Behavior in Relation to the Tensile Properties in 319.2 End Chill Castings," *Metallurgical Transactions A*, Vol. 26A, 1995, pp. 2359-2372.
60. M. F. Hafiz and T. Kobayashi, "Mechanical Properties of Modified and Nonmodified Eutectic Al-Si Alloys," *Journal of the Japan Institute of Light Metals*, Vol. 44(1), 1994, pp. 28-34.
61. N. Komatsu, M. Nakamura, and Y. Yamamoto, "Relationship between Si Crystallized Form and Impact Strength of Al-Si Alloys," *Journal of the Japan Institute of Light Metals*, Vol. 19(9), 1969, pp. 398-408.
62. M. Tsukuda, H. Masoyuki, T. Suzuki, and S. Koike, "The Effects of Si, Mg, Fe on the Mechanical Properties of Al-Si-Mg Alloys for Castings," *Journal of the Japan Institute of Light Metals*, Vol. 28(3), 1978, pp. 109-115.
63. J. M. Boileau, J. W. Zindel, and J. E. Allison, "The Effect of Solidification Time on the Mechanical Properties in a Cast A356-T6 Aluminum Alloy," *SAE Paper #970019*, SAE International, Warrendale, PA, 1997.
64. M. Richard, "La résilience des alliages d'aluminium moulés," *Fonderie*, Vol. 404, Dec. 1980, pp. 397-400.
65. M. Tsukuda, "Problems on Modification of Al-7%Si-0.8%Mg Alloy by Sb," *Journal of the Japan Institute of Light Metals*, Vol. 30(2), pp. 65-71.
66. M. Drouzy, M. Richard, and S. Jacob, "Globulisation par traitement thermique du silicium de l'A-S13," *Fonderie Fondeur d'Aujourd'hui*, Vol. 30, Dec. 1983, pp. 25-29.
67. M. Tsukuda, S. Koike, and M. Hurada, "The Heat Treatment of Al-7%Si-0.3%Mg Alloy," *Journal of the Japan Institute of Light Metals*, Vol. 28(1), 1978, pp. 8-14.
68. S. Shivkumar, L. Wang, and C. Keller, "Impact Properties of Al-Si-Cu Alloys," *Journal of Materials Engineering and Performance*, Vol. 3(1), 1994, pp. 83-90.

69. B. M. Closset, "Modification and Quality of Low Pressure Al-Si Castings," *AFS Transactions*, Vol. 96, 1988, pp. 249-260.
70. A. Wickberg, G. Gustafsson, and L. E. Larsson, "Microstructural Effects on the Fatigue Properties of a Cast Al7SiMg Alloy," *SAE Paper #840121*, SAE International, Warrendale, PA, 1984.
71. J. A. Odegard and K. Pedersen, "Fatigue Properties of an A356 (Al7SiMg) Aluminum Alloy for Automotive Applications-Fatigue Life Prediction," *SAE Paper #940811*, SAE International, Warrendale, PA, 1994.
72. B. Skallerud, T. Iveland, and G. Harkegard, "Fatigue Life Assessment of Aluminum Alloy with Casting Defects", *Engineering Fracture Mechanics*, 44(6), 1993, pp. 857-874.
73. J. L. McCall, "Failure Analysis by Scanning Electron Microscopy," *MIMC Report*, Metals and Ceramics Information Center, Dec. 1972.
74. W. W. Gerberich, "Microstructure and Fracture," *Metals Handbook, Vol. 8: Mechanical Testing, 9<sup>th</sup> Edition*, American Society for Metals, Metals Park, OH, 1985, pp. 476-491.
75. V. Kerlins and A. Phillips, "Modes of Fracture," *Metals Handbook, Vol. 12: Fractography, 9<sup>th</sup> Edition*, American Society for Metals, Metals Park, OH, 1987, pp. 12-71.
76. Z. Ma, "Effect of Fe-Intermetallics and Porosity on Tensile and Impact Properties of Al-Si-Cu and Al-Si-Mg Cast Alloys," Ph.D. Thesis, Université du Québec à Chicoutimi, 2002.
77. R. C. Voigt and D. R. Bye, "Microstructural Aspects of Fracture in A356," *AFS Transactions*, Vol. 99, 1991, pp. 33-50.
78. J. H. Horng, D. S. Jiang, T. S. Lui, and L. H. Chen, "The Fracture Behaviour of A356 Alloys with Different Iron Contents under Resonant Vibration," *International Journal of Cast Metals Research*, Vol. 13, 2000, pp. 215-222.
79. E. Kato, "Relationship Between Fracture Process of Al-Si Alloy Castings and Shape of Iron Compounds," *Journal of Japan Institute of Light Metals (in Japanese)*, Vol. 45(1), 1995, pp. 9-14.

80. C. Villeneuve and F. H. Samuel, "Fragmentation and Dissolution of  $\beta$ -Al<sub>5</sub>FeSi Phase During Solution Heat Treatment of Al-13%Si-Fe Alloys," *International Journal of Cast Metals Research*, Vol. 12, 1999, pp. 145-160.
81. A. M. Samuel, F. H. Samuel, C. Villeneuve, H. W. Doty, and S. Valtierra, "Effect of Trace Elements on  $\beta$ -Al<sub>5</sub>FeSi Characteristics, Porosity and Tensile Properties of Al-Si-Cu (319) Cast Alloys," *International Journal of Casting Metals Research*, Vol. 14, 2001, pp. 97-120.
82. C. H. Cáceres, C. J. Davidson, and J. R. Griffiths, "The Deformation and Fracture Behavior of an Al-Si-Mg Casting Alloy," *Materials Science and Engineering A*, Vol. A197, 1995, pp. 171-179.
83. Q.G. Wang, C.H. Cáceres, and J.R. Griffiths, "Transgranular and Intergranular Fracture in Al-Si-Mg Casting Alloys," *Advances in Fracture Research – International Conference on Fracture*, Vol. 5, 1997, pp. 2511-2518.
84. A. M. Samuel and F. H. Samuel, "A Metallographic Study of Porosity and Fracture Behavior in Relation to Tensile Properties in 319.2 End Chill Castings," *Metallurgical and Materials Transactions*, Vol. 26A, 1995, pp. 2539-2372.
85. A. Berry, G. Byczynski, M. Djurdjevic, and J. Sokolowski, "Integrated Dynamic Control System for Ford's Windsor Aluminum Plant Casting Processes," *Industrial Research Chair in Light Metals Casting Technology*, Report, September 12, 1996.
86. P. N. Crepeau, "Effect of Iron in Al-Si Casting Alloys: A Critical Review," *AFS Transactions*, Vol. 103, 1995, pp. 361-366.
87. E. Kato, H. Nomura, and N. Oshiro, "Effect of Phosphorus on Solidified Structure of Hypoeutectic Al-Si Alloys," *Journal of Japan Institute of Light Metals* (in Japanese), Vol. 47, No. 12, 1997, pp. 667-671.
88. S. Shivkumar, S. Ricci, Jr., and D. Apelian, "Influence of Solution Treatment on Tensile Properties of Sr-modified Al-Si-Mg Alloys," *Proceedings of the International Symposium on Production and Electrolysis of Light Metals*, B. Closset (Ed.), Pergamon Press, New York, 1989, pp. 173-182.
89. G.D. Scott, B.A. Cheney, and D.A. Granger, "Fracture Toughness and Tensile Properties of Directionally Solidified Aluminum Foundry Alloys," *Technology for Premium Quality Castings*, E. Dunn and D.R. Durham (Ed.), The Metallurgical Society, 1986, pp. 123-151.

90. M. Tsukuda, S. Koike, and M. Hurada, "The Heat Treatment of Al-7%Si-0.3%Mg Alloy," *Journal of the Japan Institute of Light Metals* (in Japanese), Vol. 28, No. 1, 1978, pp. 8-14.
91. F. Paray, B. Kulunk and J. E. Gruzleski, "Impact Properties of Al-Si Foundry Alloys," *International Journal of Cast Metals Research*, Vol. 13, 2000, pp.17-37.
92. D. Apelian, S. Shivkumar and G. Sigworth, "Fundamental Aspects of Heat Treatment of Cast Al-Si-Mg Alloys," *AFS Transactions*, Vol. 97, 1989, pp. 727-742.
93. D. Emadi, J. E. Gruzleski, and J. M. Toguri, "The Effect of Na and Sr Modification on Surface Tension and Volumetric Shrinkage of A356 Alloy and Their Influence on Porosity Formation," *Metallurgical Transactions B*, Vol. 24B, Jan. 1993, pp. 1-9.
94. A. K. Gupta, B. K. Saxena, S. N. Tiwari, S. L. Malhotra, "Review: Pore Formation in Cast Metals and Alloys," *Journal of Materials Science*, Vol. 27, 1992, pp. 853-862.
95. Q. T. Fang and D. A. Granger, "Porosity Formation in Modified and Unmodified A356 Alloy Castings," *AFS Transactions*, Vol. 97, 1989, pp. 989-1000.
96. L. Liu, A. M. Samuel, F. H. Samuel, H. W. Doty, and S. Valtierra, "Influence of Oxides on Porosity Formation in Sr-treated Al-Si Casting Alloys," *Journal of Materials Science*, 2002, in Press.
97. D. L. McLellan, "Tensile Properties of A357-T6 Aluminum Castings," *Journal of Testing and Evaluation*, Vol. 8(4), 1980, pp. 170-176.
98. F. O. Traenkner, "A Checklist for the Mechanical Properties of Aluminum Castings," *Modern Casting*, Vol. 70(10), 1982, pp. 36-37.
99. M. K. Surappa, E. W. Blank, and J. C. Jaquet, "Effect of Macro-Porosity on the Strength and Ductility of Cast Al-7Si-0.3Mg Alloy," *Scripta Metallurgica*, Vol. 20, 1986, pp. 1281-1286.
100. R. Elliott, "Growth Kinetics in Aluminium Silicon Eutectic Alloys," *Proceedings of 2nd International Conference on Molten Aluminum Processing*, American Foundrymen's Society, Inc. Des Plaines, IL, 1989, pp. 10-(1-24).
101. J. M. Boileau, P. C. Collins, and J. E. Allison, "The Effect of Solidification Time and Heat Treatment on the Tensile and Fatigue Properties of a Cast 319 Aluminum Alloy," *Proceedings of 5<sup>th</sup> International Conference on Molten Aluminum Processing*, American Foundrymen's Society, Inc. Des Plaines, FL, 1998, pp. 158-172.

102. L. Ananthanarayanan and F. H. Samuel, "Thermal Analysis Studies on the Effect of Cooling Rate on the Microstructure of 319 Aluminum Alloy," *AFS Transactions*, Vol. 100, 1992, pp. 383-391.
103. R. S. Archer and L. W. Kempf, "Modification and Properties of Sand-Cast Aluminum-Silicon Alloys," *AIME Transactions*, Vol. 73, 1926, pp. 581-621.
104. M. Drouzy and S. Jacob, "Mechanical Properties of Die Cast AS10U4 Alloy – Influence of Iron Content," *Fonderie*, Vol. 240, Feb. 1966, pp. 50-54.
105. W. Bonsack, "Discussion on the Effect of Minor Alloying Elements on Aluminum Casting Alloys," *ASTM Bulletin 117*, 1942, pp. 45-51.
106. I. Alfaro, J. Martinez, and C. Hernaiz, *Chemical Abstracts*, Vol. 71, 1969, No. 6152.
107. F. H. Samuel, P. Ouellet, A. M. Samuel, and H. W. Doty, "Effect of Mg and Sr Additions on the Formation of Intermetallics in Al-6 Wt Pct Si –3.5 Wt Pct Cu-(0.45) to (0.8) Wt Pct Fe 319-Type Alloys," *Metallurgical and Materials Transactions A*, Vol. 29A, No. 12, 1998, pp. 2871-2884.
108. M. Drouzy, S. Jacob, and M. Richard, "Interpretation of Tensile Results by Means of Quality Index and Probable Yield Strength," *AFS International Cast Metals Journal*, Jun. 1980, pp. 43-50.
109. S. Shivkumar, L. Wang, and C. Keller, "Impact Properties of A356-T6 Alloys," *Journal of Materials Engineering and Performance*, Vol. 3(1), 1994, pp. 83-90.
110. N. Komatsu, M. Nakamura, and Y. Yamamoto, "Metallurgical Structure and Impact Strength of Al-Si Alloys," *Technical Report of Toyota R&D Center*, TR-11, 1975.3, pp. 1-46 (in Japanese).
111. B. L. Gabriel, *SEM: A User's Manual for Materials Science*, American Society for Metals, Metals Park, OH, 1985, p. 97.
112. The ASM Committee on Fractography by Electron Microscopy, "The Scanning Electron Microscope and Its Application to Fractography", *Metals Handbook, 8<sup>th</sup> Edition, Vol. 9: Fractography and Atlas of Fractographs*, American Society for Metals, Metals Park, OH, 1978, pp. 49-53.
113. Q. G. Wang and C. H. Cáceres, "The Fracture Mode in Al-Si-Mg Casting Alloys," *Materials Science and Engineering A*, Vol. A241, 1998, pp. 72-82.